3-21-2019

Investigation of Endwall Vortex Manipulation in High Lift Turbines Caused By Active Endwall Forcing

Horatio J. Babcock

INVESTIGATION OF ENDWALL VORTEX MANIPULATION IN HIGH LIFT TURBINES CAUSED BY ACTIVE ENDWALL FORCING

THESIS

Horatio J. Babcock, Second Lieutenant, USAF

AFIT-ENY-MS-19-M-202

DEPARTMENT OF THE AIR FORCE
AIR UNIVERSITY

AIR FORCE INSTITUTE OF TECHNOLOGY

Wright-Patterson Air Force Base, Ohio

AFIT-ENY-MS-19-M-202

INVESTIGATION OF ENDWALL VORTEX MANIPULATION IN HIGH LIFT TURBINES CAUSED BY ACTIVE ENDWALL FORCING

THESIS

Presented to the Faculty

Department of Aeronautics and Astronautics

Graduate School of Engineering and Management

Air Force Institute of Technology

Air University

Air Education and Training Command

In Partial Fulfillment of the Requirements for the

Degree of Master of Science in Aeronautical Engineering

Horatio J. Babcock, BSME

Second Lieutenant, USAF

March 2019

AFIT-ENY-MS-19-M-202

INVESTIGATION OF ENDWALL VORTEX MANIPULATION IN HIGH LIFT TURBINES CAUSED BY ACTIVE ENDWALL FORCING

Horatio J. Babcock, BSME

Second Lieutenant, USAF

Committee Membership:

Dr. Mark F. Reeder
Chair

Dr. Marc Polanka
Member

Major Levi Thomas
Member

Abstract

With the increased demand for lighter, more fuel efficient and smaller gas turbine engines, the impetus to reduce the weight and size of the turbine has become apparent. One approach to reduce this weight is to reduce the number of blades in the turbine. However, to maintain power output, each blade must be capable of supporting a greater amount of lift. While several high-lift turbine profiles have been detailed in literature, most of these profiles have increased endwall losses, despite their desirable mid-span characteristics. To mitigate this endwall loss, a number of active and passive flow approaches have been studied and reported. The current effort documents significant manipulation and reduction in strength of endwall flow features via active control in the AFRL Low Speed Wind Tunnel Test Facility. The manipulation of the pressure side leg of the horseshoe vortex, formed at the leading edge of the turbine profile, has been shown to reduce overall pressure loss near the endwall in certain active flow control conditions. The active flow took the form of a localized low-momentum pulsed jet directly under the pressure side leg of the horseshoe vortex. Total pressure loss measurements have been collected and mapped at six planes within and beyond the passage. To supplement the total pressure loss measurements, high speed stereographic particle image velocimetry data were collected to study the effects of localized forcing of the endwall flow structure. The combination of the velocity measurements at several planes throughout the passage and the total pressure loss measurements led to a deeper understanding of the fluid dynamic mechanisms responsible for the reduction in endwall losses.

Acknowledgements

First and foremost I would like to thank my Fiancée Claire for her unending support in this endeavor. The late nights and long hours could not have been easy for her and I appreciate her patience with me as I have worked towards the completion of this thesis.

I want to thank Dr. Chris Marks, Molly Donovan, and Nathan Fletcher for their unending support during the collection and processing of the data contained herein. Their expertise and patience have not gone unnoticed and I would like to sincerely thank them for their continued support.

I would also like to thank my thesis advisor, Dr. Mark Reeder, for his assistance in setting this project up and for his wealth of knowledge in terms of low speed aerodynamics and fundamental fluid dynamics. He has been a continued support and I and truly grateful.

I would also like to thank my research sponsor, AFRL Aerospace Systems Directorate, for their assistance in allowing me to pursue this research endeavor.

Last, but certainly not least, I would like to thank my friends and family for their patience with me as I have worked on this document and throughout the completion of my master's degree. I know I have been hard to reach at times but I thank you for your understanding and patience.

Horatio J. Babcock

Table of Contents

Page

List of Figures

Page

List of Tables

Page

Nomenclature

BL	boundary layer
BR	blowing ratio
B_x	axial chord length
CFD	computational fluid dynamics
c	airfoil true chord
C_μ	coefficient of momentum
C_x	axial direction
C_y	axial normal direction
f	forcing frequency
F^+	non-dimensional frequency, $F^+ = \frac{f*c}{U_\infty}$
F^+_{SSL}	non-dimensional frequency, $F^+ = \frac{f*SSL}{U_{avg}}$
FSTI	free stream turbulence intensity
GTE	gas turbine engine
HV	horseshoe vortex
ILES	Implicit Large Eddy Simulation
LE	leading edge
LPT	low pressure turbine
MR	mass ratio
P_t	total pressure
PS	pressure side
PSHV	pressure side horseshoe vortex

PV	passage vortex
RANS	Reynolds-averaged Navier-Stokes
Re	Reynolds number $Re_{C_x} = \frac{\rho U_\infty C_x}{\mu}$
SPIV	stereoscopic particle image velocimetry
SS	suction surface
SSL	suction surface length
SSCSV	suction side corner separation vortex
SSHV	suction side horseshoe vortex
TDAAS	Turbine Design and Analysis System
u	streamwise velocity
U	velocity
v	pitchwise velocity
VGJ	vortex generating jets
w	spanwise velocity
x	streamwise direction
y	surface normal direction
Zw	Zweifel loading coefficient $Zw = 2\frac{S}{B_x}\cos^2\ \beta_2 \left[\frac{u_1}{u_2} tan\beta_1 + tan\beta_2\right]$

Greek

β	gas flow angle
δ	boundary layer height $u(\delta) = 0.99\ U_\infty$
μ	dynamic viscosity

ρ	density of air
γ	total pressure loss coefficient

Subscript

∞	freestream condition
avg	average condition
in	inlet condition
out	outlet condition

INVESTIGATION OF ENDWALL VORTEX MANIPULATION IN HIGH LIFT TURBINES CAUSED BY PERIODIC FORCING

I. Introduction

In the aviation industry today, the vast majority of the fuel consumption occurs in aircraft powered by one or more gas turbine engines (GTE). A GTE may vary in design from application to application, but is generally comprised of five main sections; the inlet or diffuser, the compressor and or fan, the combustor, the turbine, and the exhaust nozzle. Given the expansive use of GTEs in the aviation industry, any technological advancement in the components of the engine that may reduce weight, size, complexity, part count and or increase efficiency is worth considering for new designs.

With that being said, in gas turbine engine design there is an increasing demand for weight reduction in the aviation industry. With reduced weight, an aircraft can carry more fuel or additional payload. For reference: a Boeing 747's engines comprise approximately 4.2% of gross takeoff weight and the C-17 Globemaster's engines comprise approximately 2.2% of gross takeoff weight[1]–[3]. A reduction in weight without any other penalty for either of these aircrafts' engines would prove to be monetarily beneficial. Furthermore, it has been shown that the lower the weight of a vehicle, the higher the overall fuel efficiency is[4].

The focus of this research is to fundamentally study ways to improve the efficiency of new high-lift low pressure turbine designs. Current components of non-high-lift LPT's have been studied extensively and have been improved upon such that

efficiencies of 90% are not uncommon[5]. The low pressure turbine of a GTE can constitute up to one-third of an engine's overall weight but, in a high-bypass engine can provide the power for up to 80% of the engines thrust[6]. With the aforementioned desire of industry to reduce weight, the LPT becomes an increasing attractive component to improve.

One way to reduce LPT weight is to reduce the total number of blades. In some LPT's the blade count can approach 2,000 individual blades[7]. By reducing the number of blades in an LTP not only is weight reduced, but complexity and maintenance cost are as well. The reduction of LPT blades requires that each new blade produce a greater amount of power from the fluid. In order to produce greater power, greater aerodynamic loading and subsequently greater pressure differentials are often required. With the increased difference in pressure comes an increase in the tendency for aerodynamic loss. In order to combat some of this loss, extensive work has gone into new blade design for LPT's.

McQuilling[8] has shown that blade designs with high lift characteristics are capable of producing adequate lift and possessing favorable flow properties at typical engine operation conditions. However, McQuilling's profile design is susceptible to large magnitudes of endwall loss[9]. In turbomachinery research, when performed in a stationary, incompressible, low-speed linear cascade wind tunnel, an indicator of efficiency is the presence of total pressure loss. A design with less total pressure loss is by definition more efficient. Therefore, the measurement, and comparison of, total pressure losses between designs is useful in quantifying the relative efficiencies of each. The blade design described by McQuilling, the L2F, would allow for 38% fewer blades while maintaining a similar geometry to those found in use presently[8]. This L2F blade design will be used

further in the accompanying study and will be referenced simply as “L2F”. In a 2000 blade turbine that equates to a blade reduction of over 750 blades. Figure 1 is a comparison of the L2F to the Pratt and Whitney Pack B profile found in use in industry.

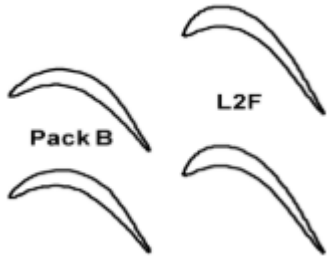

Figure 1. L2F Profile Compared to Pack B[10]

In the L2F flow field, like other turbine profiles, the creation and presence of a horseshoe vortex formed by the junction of the endwall and the leading edge of the profile is inevitable. The interaction of these vortices with the endwall, and one another, is responsible for the generation of significant losses associated with the L2F. The vortices are described in Section 2.2. The primary vortex of interest is the pressure side leg of the horseshoe vortex formed at the leading edge of the profile. The vortex extends across the passage where in interacts with a strong corner separation on the suction surface of the adjacent profile. In this paper, the combination of the corner separation vortex and the pressure side leg of the horseshoe vortex will be referred to as the passage vortex (PV). Figure 2, from a NASA report[11] and also presented by Sharma and Butler[12], shows some of relevant secondary flows present in a turbine passage. This figure will be discussed in greater detail in Section 2.2.

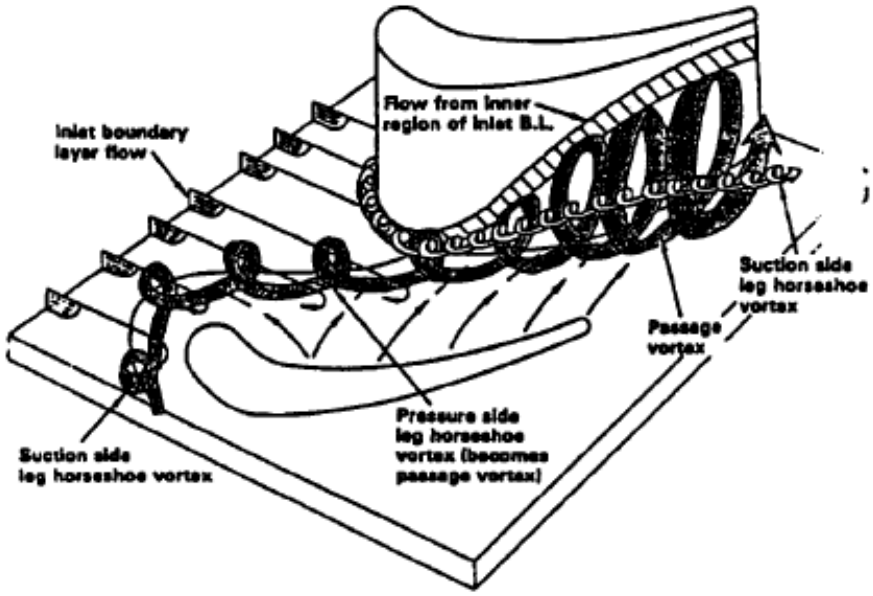

Figure 2. Passage Vortex Development of Sharma and Butler[11]

Several methods for reducing the strength of the endwall vorticies have been studied. The methods fall primarily into one of two categories: passive flow control or active flow control. Passive flow control is flow manipulation that is always present, whereas active flow control may be "turned on and off based upon operational requirements[13]". The focus of this research is the method of active flow control by way of localized endwall normal forcing. The hypothesis is that by forcing the pressure side leg of the horseshoe vortex a significant reduction in vortex strength and a relocation of the vortex within the passage is possible. This, in turn, would reduce the loss generation along the endwall. It is thought that there exists a certain forcing frequency at which the effect of endwall normal forcing is maximized. Steady jet forcing will also be utilized to investigate the mass flow requirements necessary for a given loss reduction or location shift.

This study investigates the effects of endwall forcing by utilizing a combination of total pressure loss measurements taken at a number of locations throughout and downstream of the passage along with stereoscopic particle image velocimetry measurements and high speed flow-vis data sets, taken within the passage only, to better understand the effects that periodic, and steady, endwall forcing has on the strength, structure, and location of the endwall vortical structures. This study also provides a better understanding of the fluid dynamic phenomena that result from the implementation of pulsing an endwall-normal jet as opposed to the phenomena resulting from steady endwall blowing. The study can then, in turn be used to further assess the loss generation mechanisms present within, and downstream of, the LPT passage.

The research contained herein was performed in The Air Force Research Laboratory (AFRL) Low Speed Wind Tunnel (LSWT) Test Facility. This test facility has been instrumental in the advancement of similar turbomachinery research, some of which has been previously mentioned[8], [10], [14]–[17]. Further, a reduction in fuel consumption can yield substantial energy and capitol savings for a budget, which in FY 2010, allotted over 80% of total energy costs for aviation fuel[18]. One overarching goal of the present study therefore, is to reduce the operating costs, reduce aircraft engine weight, and improve aircraft effectiveness for the USAF.

II. Literature Review

Chapter Overview

The purpose of this chapter is to provide the reader with a brief discussion of the previous research relevant to the current effort. The chapter will first discuss the design of the turbine profile, the L2F, in Section 2.1. Section 2.2 will discuss prior efforts associated with the fundamental fluid dynamic phenomena present within a turbine passage. Section 2.3 will discuss previous techniques that have been studied and implemented in industry and academia in order to manipulate, disrupt and mitigate the aerodynamic loss associated with vortical flow phenomena. Finally Section 2.4 will discuss the methods and measurement techniques used to quantify these phenomena. This chapter will serve as the foundational background upon which the present research has been based.

2.1 - L2F Design and Characteristics

The desire for high lift blades was suggested by Curtis et al. [19] and has been a driving force for much of the following work in this field. Building on the work of Curtis et al. and others, the L2F design was created in conjunction with the Air Force Research Laboratory's Propulsion Directorate using a Matlab based *Turbine Design and Analysis System* (TDAAS)[8], [20].

The L2F is a high-lift research turbine blade profile that is designed such that the number of blades within an LPT can be reduced. This new L2F design also attempted, and did, address the Reynolds lapse issues found within LPT's in service at the time of the profiles creation[8]. Reynolds lapse phenomena is described as an increase in total pressure loss with a decreasing Reynolds number and can been seen when plotting passage loss

versus Reynolds number. By convention the Reynolds Number, Re is defined in Equation (1) [14], [21]–[23]

$$Re = \frac{\rho U_\infty C_x}{\mu} \quad \textbf{(1)}$$

where ρ is the density of the fluid, U_∞ is the free stream velocity, C_x is the axial chord length, and μ is the dynamic viscosity.

The performance of an LPT at varying Reynolds numbers is of great importance in modern design and validation. The LPT is required to produce a maximum amount of power to the compressor and or fan during a sea-level take off where Reynolds numbers are high, but yet also spends the majority of its operation at altitude where the Reynolds numbers within the engine are far lower. The L2F was designed such that the operation of the LPT at these varied conditions produce the most amount of power in the most efficient manner while still reducing the overall blade count within an LPT.

The L2F was not the first high-lift turbine produced using the TDAAS system. In fact, the naming convention, L2F, stands for level 2 increase, front loaded profile. Previous studies had been performed on designs such as the L1M and L1A (level one mid loaded and aft loaded respectively)[20]. The L2F has better Reynolds lapse performance with much higher loading than either the L1M or L1A, as expected by the naming convention. In comparison, the L1A shows a 17% increase in loading level over the Pack B[24] where the L2F showed the aforementioned 38%. These assessments were made both experimentally and through the use of computational fluid dynamics.

2.2 - Fundamental Fluid Dynamics

However, as successful as the L2F was, there are still loss production features present within the LPT passage. One loss mechanism often manifests by way of vortical structures formed by boundary layer junction flow at the leading edge of the turbine blade. These losses are known as endwall losses and will be investigated in detail throughout this study. A discussion of the importance of vortices, vortical flow, and endwall losses, as well as a qualitative discussion thereof is contained in this section.

The study of vortices is in no sense a new endeavor. While our means to observe these fascinating phenomena have improved, the actual understanding and overall study of vortices can be traced back to the 16th century when Leonardo Da Vinci wrote;

> "*So moving water strives to maintain the course pursuant to the power which occasions it, and if it finds an obstacle in its path, completes the span of the course it has commenced by a circular and revolving movement*[25]".

While not called a vortex at that time, the rotational aspect of fluid motion was still acknowledged by man. The presence of vortex-like shapes can be seen on pottery and other art of even earlier time periods as well[25]. Today, the study of vortex flows have vastly outgrown the drawings of Da Vinci. In the early 1960's Küchemann explained that:

> "*Vortex motions are still described as the sinews and muscles of fluid motions and the classical subject finds ever newer applications…*[26]".

The research contained herein is a clear example of the importance of man's fascination and desire to understand further this classical subject in a new application, in particular the manipulation of these flow features and the resulting effects that said manipulation has on overall performance of an LPT.

In order to fully appreciate the effects that vortex manipulation has on overall performance it is useful to first discuss the fundamental physics revolving around the generation, propagation, and dissipation of vortices in general. An example of vortex generation is the vortices on the end of aircraft wings, called horseshoe vortices, which are formed by high energy (high pressure) air under a wing escaping from the edge of the finite wing and interacting with the lower energy fluid above the wing creating flow circulation. This vortex that is formed creates added pressure drag to the aircraft because the streamwise flow of the fluid entrained in the vortex is slower than the surrounding freestream fluid flow.

Another instance of vortex generation, and the impetus of this research, is the vortex that is formed by the separation of boundary layer flow at a vertical junction at an otherwise horizontal flow field. This vortex is formed when the boundary layer is forced to separate to move around the obstruction. Figure 3 is an image of such a vortex generation. The shapes are added for clarity of the figure.

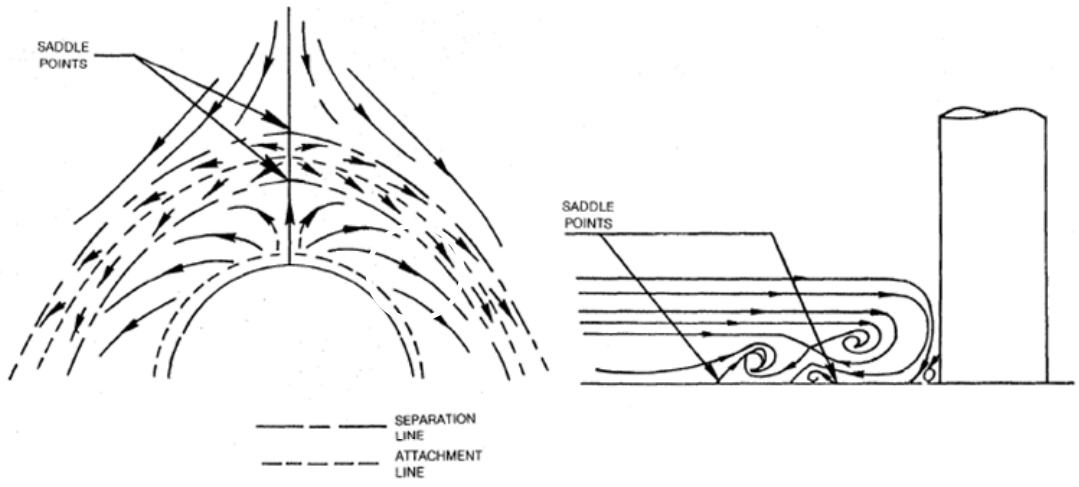

Figure 3. Visualization of the vortex structure of laminar juncture flow[27]

The generation of this junction vortex is of particular importance for this research, for this is the physical representation of how the vortices found within the turbine passage are created when incoming boundary flow intersects with the leading edge of a turbine blade. Figure 4, as presented previously in Chapter 1, shows an early, but accurate, model of this vortex and endwall flow structure as seen in the passage. This interaction is not a vis-à-vis comparison, the cylinder in Figure 3 is clearly dissimilar to the contoured edges of the profile in Figure 4, but the fundamental physics driving the formation of the two vortices is the same.

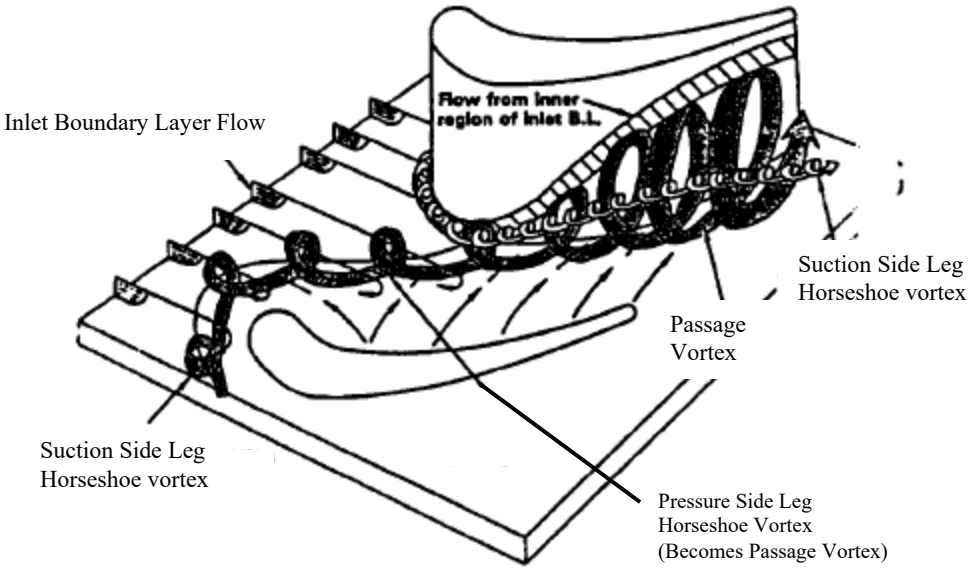

Figure 4. Adapted Endwall Flow Model of Sharma and Butler[11]

These vortices are produced by three dimensional effects and are identified as follows. The horseshoe vortex (HV) is created at the leading edge of a turbine blade at its junction point with the endwall. This vortex is created by the roll up of the boundary layer at this junction location. The HV has two legs, a suction side leg, (SSHV) and a pressure side leg (PSHV). The SSHV has been observed to dissipate quickly within the L2F passage but, the PSHV is directed by the overall pressure gradient within the passage and exits the passage near the suction side leg of the adjacent L2F. The suction side also produces a second vortex as a result of the separation caused by the high-lift nature of the L2F. This vortex is known as the suction side corner separation vortex (SSCSV). This corner separation vortex has the same rotational direction as the PSHV and, when interacting therewith, produces significant additional pressure loss in the passage. The combination of these two vortices will be referred to as the passage vortex in this report. The passage vortex (PV) is often found in the corner aft area as shown in Figure 4. Each of these generated

vortices have a predominately streamwise orientation and the literature often refers to this situation as “secondary flow” phenomena.[21]

Figure 5 is a CFD simulation representation of the vortical structures present in the turbine passage. The figure plots Q-criterion, a representation of rotation within a flow, to show the location of the vortical structures within the flow. Equation (2) contains the formulation of Q-criterion as described by Cummings et al.[28]

$$Q = \left|\vec{\zeta}\right|^2 - \left|\vec{S}\right|^2 \qquad \textbf{(2)}$$

where $\vec{\zeta} = \left(\nabla\vec{V} - \nabla\vec{V}^T\right)/2$ and is described as the rate of rotation and $\vec{S} = \left(\nabla\vec{V} + \nabla\vec{V}^T\right)/2$ is the rate of shearing. Q-Criterion is used to easily identify the location of vortices by stating where Q is greater than or equal to zero. That is, positive values are flow regions that are controlled by rotation whereas negative values are representative of strain-dominated flow[15].

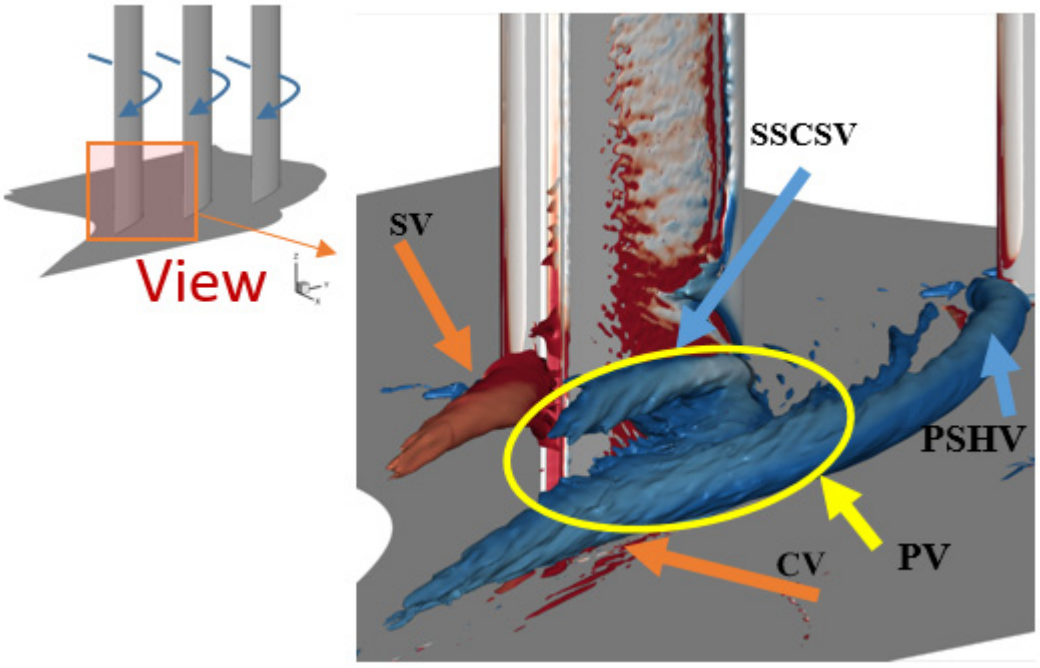

Figure 5. Endwall Flow Structures. Isosurfaces of Q=10 colored based on vorticity. Red is positive. Blue is negative. – Adapted from Veley et al.[29]

Figure 5 provides insight into a specific experiment that provides visualization of the vortical structures present within a turbine passage of interest as described previously. The pressure side leg of the horseshoe vortex (PSHV) and suction side corner separation vortex (SSCSV) in the figure represent the two vortical structures that interact to form the passage vortex (PV). The interaction of these co-rotating vortices generate loss within the L2F passage. The passage vortex, and the loss associated therewith, is the primary focus of this study. In a broad sense, this loss motivated the entire study of secondary flows as the net result is a reduction of efficiency and reduction in flow turning which could, in principle, be mitigated with a better design. The suction side leg of the horseshoe vortex

(SSHV) was observed to dissipate quickly within the passage and is not shown in the figure. The corner vortex is labeled CV in the figure and forms at the trailing edge of the blade, this vortex is not of significant interest in this study. Finally the Shed Vortex (SV) is formed due to separation on the pressure side of the L2F profile. This vortex has a rotational direction that is opposite from the PSHV and is responsible for large magnitudes of loss. This shed vortex occurs regardless of present pressure loss mitigation techniques applied herein and will therefore be present in much of the data presented in subsequent chapters. Finally, the separation seen on the blade above the SSCSV is not of interest in this study.

The presence and interaction of the pre-described vortices is one form of loss generation in a high-lift turbine passage. Lyall postulated that turbulence shear and subsequent turbulence dissipation caused by these vortices is responsible for majority of the total pressure loss throughout the passage[9]. The interaction of these vortices, and the loss associated therewith, is known in the broader sense as endwall flow loss. Much research has been done in order to mitigate and understand the causes of these losses. As a general summary, the cause of this loss is due to friction between the flow and the boundary surfaces and flow mixing both downstream and within the passage[9]. Understanding loss generation in turbomachinery is as important as the understanding of the flow features[30]. That is, loss reduction is of critical importance to the turbomachinery community because the preventing loss increases efficiency, which improves power output.

2.3 - Flow Control Overview

If one is able to manipulate these loss producing structures, it is likely that an overall efficiency increase is possible. There has been much work in the field of vortex manipulation and flow control. One way that aerodynamic loss can be mitigated is by reducing the strength and presence of the passage vortex. Methods for vortex manipulation are often separated into two categories: passive flow control and active flow control.

Passive flow control is performed in a manner such that the means of vortex manipulation is always present. This means that regardless of flow characteristics, the vortex-disturbing feature will be affecting the flow in some manner. Passive flow control is also the simplest means of vortex manipulation. Fences, profile contours, and endwall contouring have all been studied and have shown varying levels of aerodynamic loss mitigation[16], [22], [31]. However, the constant presence of passive flow control can be disadvantageous if the flow conditions change, altering the performance of the flow control device[13]. For example, differing Reynolds numbers, have been shown to effect the performance of some passive flow control devices turbulence conditions[10].

Active flow control, by contrast, requires "energy to be expended in order for control to take place."[32] However, active flow control may be adjusted to optimize performance at a given flow condition if needed. Past studies of active flow control in turbomachinery have investigated steady endwall and pulsed blowing[13], [17]. This blowing has been implemented in many regions of the passage and can greatly vary in intrusiveness. With the added flexibility of active flow control comes increased complexity and increased cost[13]. This increased cost can come in two forms: the capitol cost of manufacture, and also the performance cost of routing engine bleed air to manipulate the

vortex. It is worth noting though, that this bleed air may also be useful for cooling of the passage but, the effectiveness of this cooling is out of the scope of this research endeavor. While there is promise in past active flow control research, much is still unknown about the effects of active flow control in test conditions similar to real world application and further work is necessary[13]. This research aims to further investigate the effectiveness of pulsed and steady, localized, endwall normal jets in reducing the size and strength, or changing the location, of the passage vortex and other endwall vortical structures.

2.3.1 - Passive Flow Control

Several types of passive flow control has been documented in literature with varying degrees of effectiveness. This section will focus upon three types of passive flow control and the effectiveness thereof. The passive controls are, boundary layer fences, profile contouring and endwall contouring.

2.3.1.1 - Fences

The first type of passive flow control that will be discussed herein is the simplest case of a boundary layer fence. A boundary layer fence is an intentional structure placed along a surface within the passage to impede flow in a given direction. These fences can be found on the suction surfaces of blades, as shown by Kawai and Adachi in 1988[31] or along the endwall as shown by the same authors a year later[33]. The discussion here will pertain to boundary layer fences placed along the endwall because they are most similar to the research performed in this study. It is thought, that the endwall normal jets may behave in a way similar to endwall fences.

Boundary layer fences are designed such that the effect that they have on the flow features produces a net reduction in aerodynamic loss. Kawai and Adachi, in the later study, placed fences along the endwall of a cascade wind tunnel, similar to the one used in the present research. This study showed that the most effective heights for these fences are 1/3 of the incoming boundary layer[33]. The effective height of the fence is likely related to the tradeoff effects of added skin friction drag and flow effects that was incurred due to the addition of this fence to the flow field. That is, a fence must be large enough to disturb the boundary layer, but not so large that the net reduction in loss seen by this disturbance is mitigated by the added loss incurred by friction. Further, if a fence is sufficiently large, the flow will behave as if this fence is now a blade within the flow, removing all benefit of the fence. Additional research by Kawai and Adachi[34] clearly identified the physical effect that the fences had on the flow features. In this application the fence affects the passage vortex by impeding its motion to the suction surface and thus mitigating the endwall cross flow loss carried by the vortex. In the study, Kawai and Adachi[34] showed a reduction in local endwall losses of 25% when their fence was used.

Chung, Simon and Buddhavarapu[35] also studied the effects of boundary layer fences in turbines with a focus on film cooling applications and found the endwall fence was useful in keeping the passage vortex from contacting the adjacent suction wall. Chung and Simon[36] later showed that a fence was useful to reduce “hot spot” created by the passage vortex “washing away” the cooling fluid on the suction side of an adjacent blade. Additional film cooling and fence research was performed by Aunapu et al.[37] where the fence described by Chung and Simon was used to further verify the effectiveness of an endwall boundary layer fence. Aunapu et al.[37] found that the boundary layer fence was

successful in keeping the passage vortex from contacting the suction surface. The fence lifted the PV in such a way that it was washed downstream by the passage flow.

The findings of all of these researchers yielded similar conclusions in terms of the effects of a boundary layer fence in that, an idealized fence is an effective means for diverting flow within a turbine passage capable of reducing the size and strength of a passage vortex. This work was corroborated by Moon and Koh[38] and, more recently, by Kumar and Govardhan[39] using computational fluid dynamics to solve numerically the Navier-Stokes equations describing a flow with and without boundary layer fences. Moon and Koh found that the 1/3 boundary layer height fence provided the most effective means of reducing secondary flow and subsequent losses, concurrent with Kawai and Adachi[33]. Kumar and Govardhan[39] went further to describe a linearly varying boundary layer fence where the trailing edge height was the aforementioned 1/3 boundary layer height, but whose leading edge was only 1/6 of the incoming boundary layer height.

2.3.1.2 - Profile Contouring

The next form of passive flow control to be discussed is profile contouring. Profile contouring is defined here by additions made to the blade in the endwall region of the flow. These modifications take the form of additions to the profile of a bulb of a prow and were first introduced by Sauer and Wolf[40]. A sample bulb of a prow can be seen in Figure 6 adapted from US Patent US6058864A. The bulb is labeled "5" in the figure Further work by the Sauer et al. in 2001[41] focused on optimizing the size and shape of the bulb. Figure 7 shows example overhead view of the profiles used. The shaded region of the figure is the location of two different sizes of bulbs on a generic research profile.

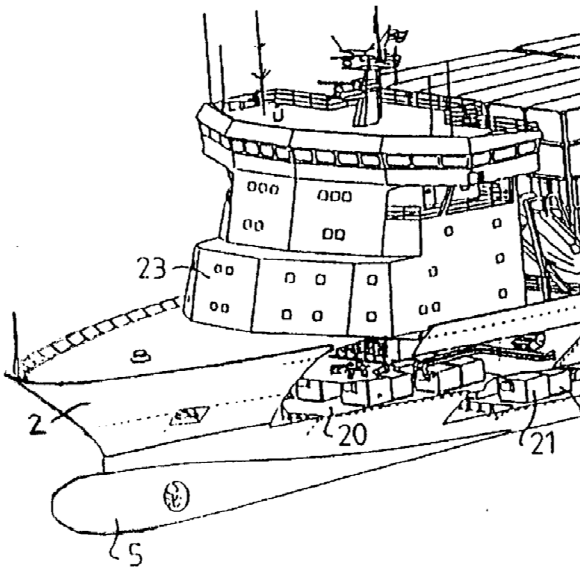

Figure 6. Sample of a Bulb of a Prow[42]

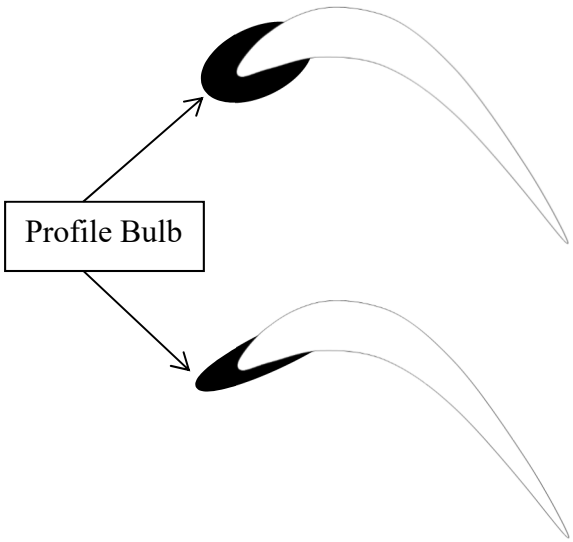

Figure 7. Bulb(s) location on generic research profile similar to Sauer et al.[41]

Sauer et al. showed that an optimized bulb interacts with the incoming boundary layer and intensifies the horseshoe vortex formed at the leading edge of the blade. This

intensified vortex, in particular, the suction side leg, now moves away from the suction side surface. This separation of the passage vortex from the profile boundary layer was expected to reduce passage losses. To this end, the authors documented an endwall loss reduction from approximately 4% endwall loss at baseline conditions to the new 2% endwall loss with the passive flow features applied. Endwall loss is defined as the summation of the loss in region near the endwall.

Building on the work of Sauer et al, Mahmood and Acharya[43] studied the effects of an edge fillet as opposed to a bulbous prow shape. After preliminary screening, the researches chose two promising endwall fillets for detailed flow measurements. The endwall fillets were chosen based upon a preceding study by the same researchers where a study of fillets on heat transfer was performed. Each fillet attached to the endwall and blade at the same locations. The maximum height of the fillet was one inlet boundary layer thickness or 10% span. The maximum height point was located on the stagnation location of the blade. The fillets extended downstream a maximum distance of 29.9% of the axial chord. The fillets intersected with the suction surface at 56.6% of the suction surface total length, and intersected with the pressure surface at 32.2% of the pressure surface length. However, one fillet was linear from blade to endwall and the second was parabolic. The parabolic fillet can be seen in Figure 8, a 2-D overhead view on the left and a 3-D profile on the right, adapted from Mahmood and Acharya[43]. The profiles of Mahmood and Acharya had a larger planform and wrap further around the blade profile. However, the best loss reduction produced by the modified blades was on the order of 14%. Using fillets described in literature, Lethander et al.[44] was also able to conclude, that endwall fillets

can also be used to provide thermal benefits as well as flow control and pressure loss reduction.

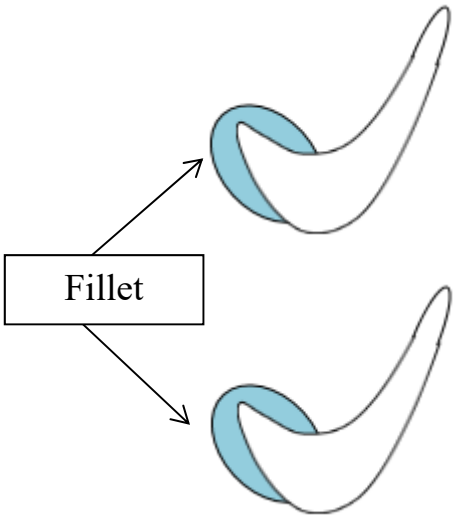

Figure 8. Location of Fillets and Sample 3-D profile – Similar to Mahmood and Acharya[43]

Research into profile contouring was also performed by AFRL on the research L2F profile design mentioned in a Section 2.1. Work by Lyall et al.[10] documented a reduction in endwall pressure loss of approximately 23% with a substantial fillet of the endwall region. This filleted endwall essentially changed the profile shape at the endwall to provide better endwall flow performance characteristics. An overhead, 2-D view, of the fillet can be seen in Figure 9, and a 3-D view can be seen in fig as reproduced from the same article.

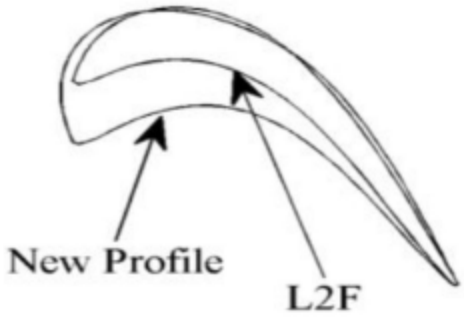

Figure 9. 2-D Profile Contour of L2F - Lyall et al.[10]

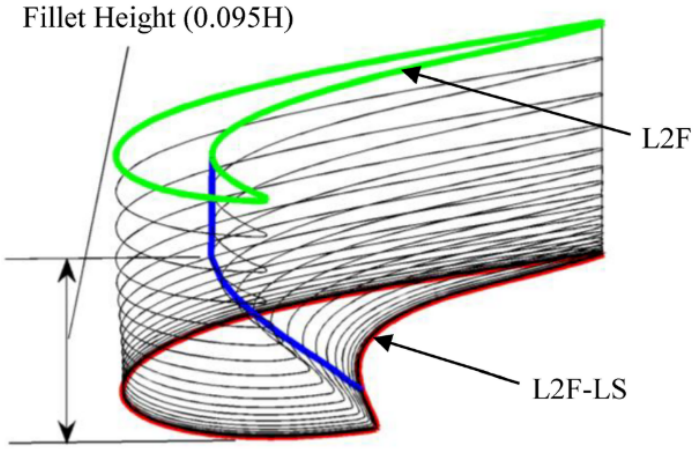

Figure 10. 3-D Profile Contour (L2F-EF) of L2F - Lyall et al.[10]

The design methodology behind the L2F profile contour stemmed from loss associated with increased stagger angle. By reducing the stagger angle Lyall et al. was able to reduce losses by 20%[10]. Further, the effectiveness of the new endwall fillet was achieved due to a design that was able to take advantage of the reduced endwall loss properties of the low stagger variant of the L2F and the general profile success of the L2F.

Additional work was performed with the L2F and profile contours. Research by Bear[15] studied the effects of differing profile contours for the L2F. The three contours

used by Bear were L2F-EF, L2F-EB, and L2F-EF2. The L2F-EF is a combination of the low stagger variant of the L2F postulated by Lyall and shown in Figure 10. The L2F-EB is a modification of the L2F-EF using a bulb design in a similar fashion as those discussed by Sauer and Wolf[40]. However, the shape of the bulb was modeled after a low-stagger variant of the L2F. Finally, the L2F-EF2 is a modification of the L2F-EF where the leading edge of the fillet is directed towards the incoming flow. The L2F-EF, L2F-EB, and L2F-EF2 showed an overall passage loss reduction, compared to a non-contoured baseline case, of 5.2%, 3.2% and 4.7% respectively when tested at 100,000 Re_{C_x}[15]. These loss values can be used as baselines to which active flow control may be compared.

2.3.1.3 - Endwall Contouring

The final form of passive flow control to be discussed here is the complex case of endwall contouring, in particular, non-axisymmetric endwall contouring applied to the hub of the rotor in a GTE. Endwall contouring is the application of curvature to an endwall with the intent of modifying the static pressure field, thus altering the secondary flow[45]. Axisymmetric contouring is no newer a technology than profile contouring or endwall fences with research initiating as early as the 1960's[46]. In their ASME journal article Harvey et al.[47] provides a thorough review of the work regarding endwall contouring prior to the advent, and efficient application of CFD. With that being said, it has been due to new developments in computational systems that has afforded researched the ability to greatly improve the three dimensional nature of an effective endwall contour seen in the literature of this century. Hartland et al[45] studied the implementation of specific curving of the endwall to reduce secondary flow and the losses associated therewith. These researchers found that an application of specific endwall contours resulted in substantial

secondary loss reductions, on the order of 30% or more due to the altered nature of the static pressure field[45].

Hartland et al.[45] claimed that this non-axisymmetric contouring will eventually become as prevalent a tool in the toolbox of the turbomachinery designer as the implementation of airfoil lean and skew. To that end, further research in this field has led to further improvements in particular with higher loaded turbine profiles. Knezevici et al.[48] further studied the effects of endwall contouring, in particular the underlying physics of the boundary layer flow and the secondary kinetic energy associated therewith. It was found that the presence of endwall contouring reduces the strength of cross passage flow, weakening the passage vortex and its roll-up. This weaker PV results in less fluid entrained in secondary flow and thus less secondary loss.

Praisner et al.[49] continued this research effort and studied the benefits of endwall contouring on the high lift profiles studied in this decade. Researchers used CFD and a family of high-lift and conventional profiles to further numerically investigate the effectiveness of endwall contours[49]. Their results were consistent with the preceding findings of the successes of endwall contours.

Researchers at AFRL recently applied endwall contouring to the L2F profile using a CFD contouring optimization procedure. The optimization process used a system of Bezier curves to define the endwall shape. The shape was optimized such that the low speed flow near the leading edge was forced towards the suction surface prior to the flow entering the passage. This optimized contour was tested numerically and experimentally and results were yet again promising[16]. Figure 11 shows these contours from an inlet flow direction view. The contours had maximum contour values of 10.9% axial chord and minimum

values of 13.5% axial chord Experimental passage total pressure loss reduction was 7.8% while the endwall specific losses were 19.9%. These reductions in loss were similar to those found numerically of 8.2% passage loss reduction and 22.9% endwall loss reduction. The contours used in the research had more aggressive features as compared to other work in the field.

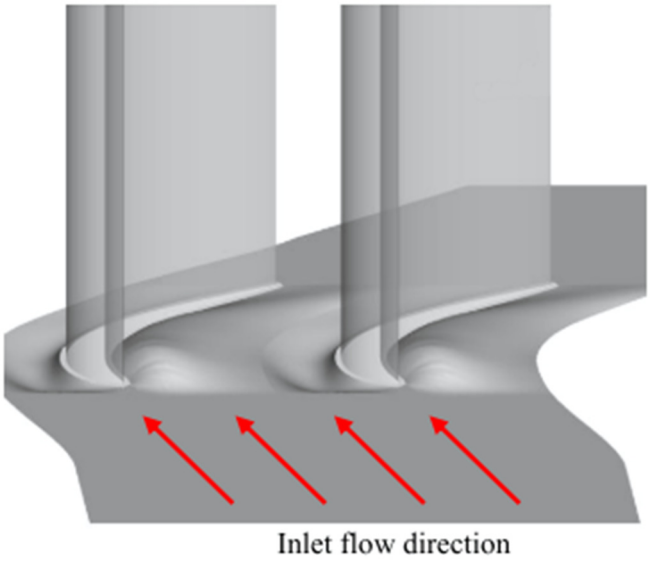

Figure 11. Endwall Contours - Dickel et al.[16]

2.3.2 - Active Flow Control

Active flow control, aims to accomplish similar, and or better, effects of the passive flow control previously discussed, by using pulsed or steady jets of air to manipulate the flow within a passage. Many of the studies reviewed here investigated the effects of steady and pulsed jets concurrently, comparing them to each other and to a baseline condition. Pulsed jets and steady jets are inherently different in their application but are capable of producing similar flow manipulation. However, researchers have shown that the same flow

control effects can be achieved by using a pulsed jet, often with a duty cycle at or below 50% as opposed to the 100% duty cycle of a steady jet[50]. Duty cycle here is defined as the proportion of time the jet is on in a given period. This finding implies that the "cost," as measured by the total amount of air required to manipulate the flow, of pulsed jets is less than the steady jet control of the same maximum flow rate.

McManus et al. studied pulsed jet configurations that matched the volumetric flow rate of a separate pulsed configuration and also jets that matched the jet to cross flow velocity and found that the pulsed condition showed a significant, as defined by a reduction in power required, improvement as compared to the steady jets with a fixed mass flow rate[50].

The first type of blowing or forcing discussed here will be the use of vortex generator jets (VGJ). A VGJ is a compound directional jet placed along the surface of the profile aimed at energizing the boundary layer flow to assist in reducing separation at low Reynolds number operation conditions[51]. Multi-directional jets were chosen in favor of wall normal jets because the two small horseshoe vortices that may be formed using wall normal jets are replaced with one large vortex. This singular large vortex more effectively energizes the boundary layer and aids in delaying separation of flow over the aft portion turbine profiles at low Reynolds number operating conditions[51]. Studies have shown that these VGJs are capable of drastically reducing boundary layer separation on turbine blades operating at low Reynolds number flight conditions[52], [53]. Low Reynolds numbers are defined here as less than 50,000 Re. However, the performance of a VGJ is related to the blowing ratio used for the steady jet, and there is a minimum value necessary for effective operation which varies based upon passage flow conditions. For the optimum

pulsed case a minimum blowing ratio of 1 was required. In steady cases the blowing ratio could be as high as 5. Equation (3) defines the blowing ratio,

$$B = \frac{(\rho U)_{jet}}{(\rho U)_{local}} \quad (3)$$

where $(\rho U)_{jet}$ is the jet density and velocity and$(\rho U)_{local}$ is the local density and velocity.

As mentioned previously, much of the work in industry and academia couples steady and pulsed jets research. The work by Bons et al.[51] found the pulsed VGJs achieved results similar to those of the steady jets but had an order of magnitude reduction in mass flow required[51]. Later work by Bons et al.[54] studied the effects of the non-dimensional pulsing frequency and found that frequencies ranging from $0.1 < F^+ < 7.7$ produced loss reductions of up to 60% as compared to the baseline $F^+ = 0$ case[54]. Equation shows the non-dimensional pulsing frequency referred to by Bons

$$F^+ = \frac{f * c}{U_\infty} \quad (4)$$

where f is the pulsed frequency in Hz, c is the true chord length, and $U_\infty$is the incoming freestream velocity. This non-dimensional pulsing frequency is not the same as the one presented in the current study.

Following the work on VGJs, research into the effectiveness of endwall manipulation was performed. Benton et al[55] initially showed that, by using a combination of VGJs in the midspan and forcing jets near the endwall, pressure loss reductions on the order of 20% were possible. This loss reduction was accomplished by moving the PV away from the suction surface and reducing crossflow. An example of

Benton's suction surface jet layout can be seen in Figure 12. The figure is representative of a far more intrusive active flow control experiment. The text in the figure represents the location of the jets relative to the axial chord of the blade. The jets are spaced 2.5 jet diameters, on center, from each other. The legend indicates which jets are in use in the given experiment. The jets are oriented such that the momentum injection is direct with the incoming flow direction, not counter to it.

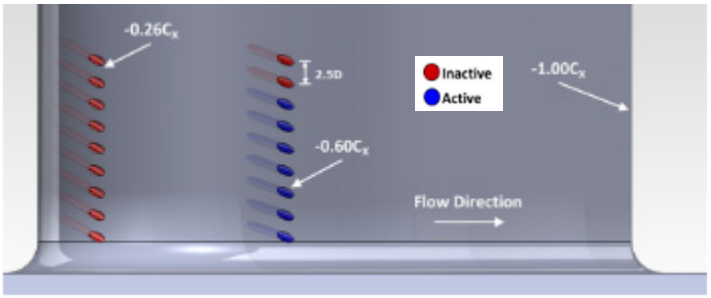

Figure 12. Suction Surface Jet Location – Modified from Benton et al[55]

Benton et al.[56] further went on to investigate the effects of pulsing frequency and duty cycle for pulsed jets on an L2F turbine profile. It was shown that the frequency of the pulsed jets played a significant role in the behavior of the PV. As the frequency of blowing is increased, the passage vortex is disturbed such that it no longer returns to its baseline state. Rather, the vortex traces a path above the endwall. The area that this path encompasses reduces in size as the forcing increases from $F^+ = 0$ to $F^+ = 1.0$. The non-dimensional frequency here, is not the same at the F^+ presented in Equation (4). Rather Equation (5) is the non-dimensional frequency reported by Benton et al.[56]

$$F^+ = \frac{f}{\bar{U}_{FC}/SSL_{FC}} \qquad (5)$$

where f is the pulsing frequency, $\overline{U}_{FC}/SSL_{FC}$ is the "effective time scale of the freestream flow between the jet injection point and the blade trailing edge."

Higher frequencies do not seem to show a noticeable change in the path mapped by the vortex location. However, one specific frequency, $F^+ = 0.4$, displayed a behavior of increased randomness in location within the passage. It was postulated that this increased randomness of the vortex location is due to the pulsed jet frequency actuating natural instabilities in the flow. Moreover, for a 50% duty cycle, the total pressure loss reduction for the $F^+ = 0.4$ case was 13% with 22% less mass flow compared to the $F^+ = 1.2$ case where a 15% total pressure loss reduction was achieved but only a 6% mass flow reduction was realized. When the duty cycle was reduced to 35%, the loss reduction and mass flow reduction were negatively affected, for the $F^+ = 0.4$ frequency case only an 11% loss reduction was seen with a mass flow reduction of 20%.

The final study discussed here, Fletcher et al.[17], is a direct precedent to the present study. Fletcher et al [17], building on an ILES study of a single configuration [57] that showed potential for strong vortex manipulation along the endwall, investigated the effects of endwall normal jets. These jets, in contrast to those of Benton and Bons which were placed at a compound angle within the turbine blade, were placed within the passage endwall, normal to the flow incoming flow, at a location of 7% C_X from the leading edge of the L2F profile along the pressure side horseshoe vortex liftoff line described in a previous study of the L2F PV development. Figure 13 shows the location of these jets, along the PSHV liftoff line, which are only located in a centralized location on the endwall.

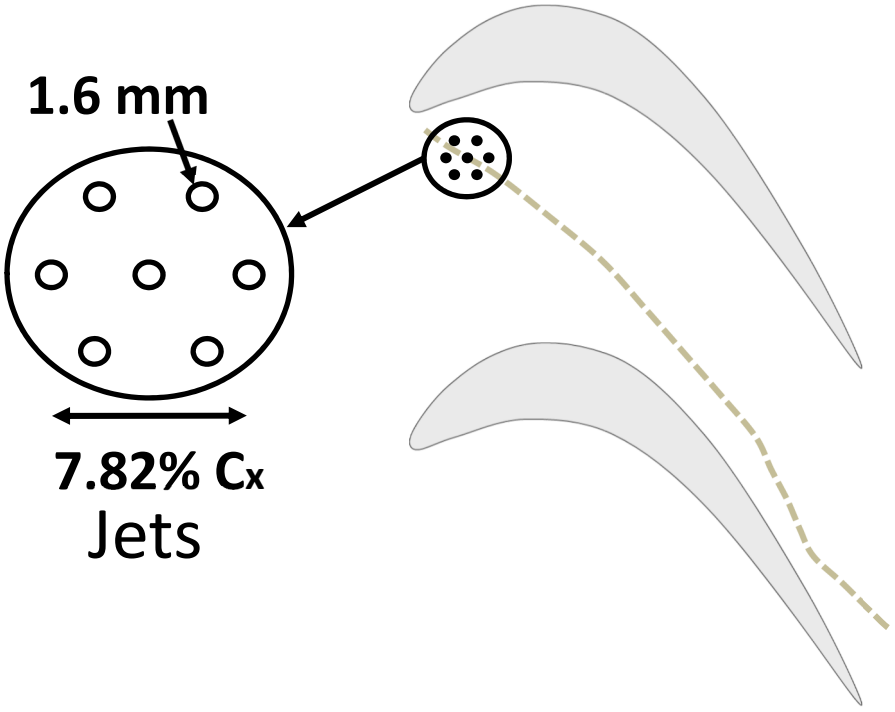

Figure 13. Endwall Jet Location – Presented by Donovan et al.[23]

Fletcher et al.[17] demonstrated that there existed an apparent optimum blowing frequency that produced the greatest pressure loss reduction. According to Fletcher this frequency was $F_{SSL}^{+} = 1\ or\ 1.2$ depending on the duty cycle (45% or 55%). Fletcher also concluded that a localized frequency of $F_{SSL}^{+} = 0.4$ related to the natural occurring oscillation of the PV reported by Veley et al[14] and Gross[58]. Moving forward, these frequencies, $F_{SSL}^{+} = 0.4$ and 1.2 are used in the present work to study the effects of pulsed normal jets on the location and shape of the passage vortex generated by the L2F. The non-dimensional frequency of F_{SSL}^{+} is discussed in greater detail in Section 2.4.4

2.4 - Measurement Techniques

Many of the previously discussed quantitative research endeavors were performed using similar measurement metrics. In order to provide a concise description of the major mathematical methods used, a compilation of said metrics, are contained in the following sub-sections. The measurement tools are total pressure loss (Section 2.4.1), via Kiel probes, hot-wire and hot-film anemometry (Section 2.4.2), and stereoscopic particle image velocimetry (Section 2.4.3). There is also a brief section, Section 2.4.4, on relevant parameters regarding specific parameters previously discussed that will be further used in the analysis section of this document.

2.4.1 - Total Pressure Loss

Total pressure loss historically has been qualified by pitot static probes. The total pressure in a fluid flow can be defined as the dynamic pressure plus the static pressure. A useful way for comparing total pressures is shown in Equation (6). This comparison is known as the total pressure loss coefficient, γ.

$$\gamma = \frac{P_{t,in} - P_{t,local}}{\frac{1}{2}\rho U_{in}^2} \quad (\mathbf{6})$$

where $P_{t,in}$ is inlet total pressure, $P_{t,local}$ is local total pressure, ρ is density, and U_{in}^2 is the square of the inlet freestream velocity. The vast majority of low-speed cascade wind tunnel testing considers density to be a constant due to the incompressible flow assumption due to operation conditions of M << 0.3. A note, in some work this pressure loss coefficient is denoted as, *Y*. Also, when the average loss is reported it is sometimes signified as $\bar{\gamma}$ *or* $\bar{Y}$ depending on the specific author. In this report $\bar{\gamma}$ is described by Equation (7).

$$\bar{\gamma} = \frac{1}{s}\int_{-\frac{1}{2}s}^{\frac{1}{2}s} \gamma \, dy \qquad (7)$$

where s is the pitchwise distance between profiles and y is the pitchwise direction. This $\bar{\gamma}$ is the pitchwise area averaged total pressure loss coefficient. Finally a passage total pressure loss coefficients can be calculated by taking the spanwise average of $\bar{\gamma}$ to use for comparison of passage total pressure losses. Recall that pressure loss has been used by many of the authors in Section 2.3 and the change in pressure loss is how efficiency has traditional been quantified.

2.4.2 - Hot-film and Hot-wire Anemometry

Hot-wire or hot-film anemometry is often used to calculate the velocity of a flow. Hotwire anemometry is an intrusive measurement but allows for precise collection of velocity conditions throughout a flow field. However, the work by Veley[59] used platinum hot-film sensors to calculate the location the PV as it oscillated within the passage. Veley reported that the oscillation centered near a nominal frequency of 22 Hz or $F^+ = 0.4$ based upon a limited data acquired in a time series. A more rigorous approach is to use hot-film sensors and spectrum analysis to find a time averaged spectrum of frequencies present within the passage. As such, this section will discuss the theory regarding the use of a spectral analyzer in conjunction with hot-film sensors.

The hot-film sensors work much like a hot wire sensor where a voltage difference is placed across a platinum wire of know resistance and thermal conductivity. As fluid moves across the wire the fluid draws heat from the wire, the voltage difference changes because of this reduction in heat and the measured voltage change can be used to determine the velocity of the fluid at the location of the sensor.

By using a hot-film sensor to determine the change in velocity of a fluid, it is possible to determine the location of the pressure side leg of the horseshoe vortex with an array of hot-film sensors. By taking the velocity data from the sensors a Spectrum Analyzer may be used to determine a time averaged spectrum of a given signal based upon a larger data set. This time averaged data set can allow for a better understanding of behavior of the vortical structures. For further information regarding hot-films and their use in unsteady flows see Veley et al.[14]. The signal is then reported in terms of power spectral density (PSD). A PSD plot displays the relative power of a signal occurring at a given frequency. This transformation of a signal in the time domain to a signal in the frequency domain is performed by way of a Fourier Transform. This transformation is valid for all real world signals[60]. Equation (8) shows the transformation to frequency domain

$$S_x(f) = \int_{-\infty}^{\infty} x(t) e^{-j2\pi f t} dt \qquad (8)$$

where $x(t)$ is the x signal in the time domain, $S_x(f)$ is the x signal in the frequency domain and j is the imaginary unit. This process can be reversed using Equation (9)

$$x(t) = \int_{-\infty}^{\infty} S_x(f) e^{j2\pi f t} df \qquad (9)$$

The computation of a Fourier Transform, in its purest mathematical form, is not possible digitally, so a Discreet Fourier Transform (DFT) is performed. The computation of a DFT is accomplished by integrating the signal numerically[60]. Several difficulties

arise, such as the evaluation of an infinite integral, when calculating the DFT so a simplification is again made in the form of a Fast Fourier Transform (FFT). An FFT introduces assumptions that allow for fewer computations while still retaining the quality of the information within a given signal. This FFT is a discrete approximation, valid only for a specified period of time, of the true Fourier Transform. For the analysis herein, the assumptions made in calculation of the FFT are not influential enough to require calculation of a more exact frequency transformation. Following the transformation and calculation of the FFT a subsequent stable average is performed over a set number of samples and is reported in terms of the PSD previously discussed.

2.4.3 - Particle Image Velocimetry

PIV data collection is obtained by first seeding a flow of interest. The seeded flow is then illuminated by a high power laser sheet and a photo of the flow, showing the light scattered by the seeding particles, is taken. The flow is illuminated again and a second image is taken again. By comparing the change in location of seed particles between the first and second image and knowing the time between illuminations, the velocity of the flow can be determined. Stereoscopic Particle Image Velocimetry is a newer technology which uses two cameras, set at an angle to the flow, to obtain three velocity components as opposed to the two velocity components collected in two dimensional PIV.

The use of single camera PIV is a seasoned endeavor. It has been shown that there is a vast amount of information that may be gained quickly from the use of high-powered lasers and high speed cameras. One author lists several uses of PIV including “high quality visualization of the flow, rapid acquisition of data and measurements of flow relative to

moving boundaries –i.e. blades….”[61]. Further the use of PIV allows for calculations of intricate flow properties.

In a 2005 review of the first 20 years of particle image velocimetry Adrian provides a brief summary of the advent and advances of PIV technology[62]. Adrian also describes the then-common system of the use of a single camera coupled with a Nd:YLF laser and mentions the use of the “now relatively common” SPIV systems but cautions that there is, at that time, developments needed to refine the out-of-plane components[62].

A few years following Adrian’s review, Beresh et al.[63] performed a comparison of PIV camera and flow configurations that intersected along a common line in a well-established jet. The comparison showed that while the streamwise components agreed well with their uncertainties the cross plane stereographic data had slightly lower, albeit significant, mean velocities and turbulent stresses. Beresh et al. also called for an improvement in software for calculation of uncertainties in PIV measurements. Since this call for improved software, several new commercially available systems have been modified and the accuracy of PIV has improved. With this increase in accuracy the use of SPIV has increased. SPIV allows for collection of three velocity components found within a flow and greatly increases the attainable knowledge in a low field from a single data set collection. Work by Veley et al. and Bear et al. have provided insight into the flow features present within the passage of the LSWT test facility[14], [22].

Even with improved PIV software difficulties still exist in generating consistent seeding of the flow. Inconsistent seeding can result in increased error in PIV measurements. Several methods for seeing flow have been used but leave residue on tunnel surfaces

degrading the accuracy of the equipment. Clean seeding research has shown in some instances that solid particles of dry ice can be used to seed the flow[64].

The research contained herein builds upon the SPIV setup and procedure as performed previously in the Low Speed Wind Tunnel test facility at AFRL. For a detailed review of the current SPIV setup see Section 3.5. Researchers have used similar setups to produce satisfactory results for flows in various orientations to the measurement plane of interest[21], [22], [29][23].

2.4.4 - Relevant Parameters

One relevant parameter discussed will be the non-dimensional frequency as it will be used herein. This is slightly different than the non-dimensional frequency previously discussed in section 2.3.2 as different non-dimensionalizing quantities are used. When creating a non-dimensional frequency a reference length scale is needed. The author has chosen to remain consistent with Fletcher et al. [17] and non-dimensionalize by the suction surface length as shown in Equation (10)

$$F_{SSL}^{+} = \frac{f * SSL}{U_{avg}} \quad (10)$$

Also remaining consistent with Fletcher et al. [17] are the definitions of mass ratios and the coefficient of momentum. The mass ratio is the calculation of the mass of the injected air from the jets compared to the mass of the passage for one half of the span. The mass ratio is given by Equation (11) and the momentum coefficient, C_{μ}, which is the influx of momentum from the jets normalized by the momentum flux of one half passage is shown in Equation (12)

$$MR = \frac{1}{2}\overline{\left(\frac{U_J}{U_{in}}\right)}\left(\frac{\pi N D_J^2}{HScos(\alpha_{in})}\right) * 100 \quad (11)$$

$$C_\mu = \frac{1}{2}\overline{\left(\frac{U_J}{U_{in}}\right)^2}\left(\frac{\pi N D_J^2}{HScos(\alpha_{in})}\right) * 100 \quad (12)$$

where U_J and U_{in} are the jet velocity and tunnel inlet velocity respectively, N is the number of active jets, D_J is jet diameter, H is the span, S is the pitch and α_{in} is the inlet flow angle. The inlet flow angle for the test contained herein is 35° and there are seven active jets.

Finally, Fletcher et al. [17] defined Blowing ratio as shown in Equation (**13**)

$$BR = \frac{\overline{U_{Jet,max}}}{\overline{U_{in,}}} \quad (13)$$

where $\overline{U_{Jet,max}}$ is the average maximum jet velocity and $\overline{U_{in}}$ is the average inlet velocity. This is different than Equation (3) as densities are not included in the calculation. For this study, the blowing ratio as defined by Equation (13) will be used.

Summary

This chapter has served as a concise overview of the motivation for the present study as well as a more in-depth look at previous work performed in and about the field of vortex flows in turbomachinery. A discussion of the history of vortex investigation, dating back to the 16th century was followed by the underlying physics that drive the generation of vortical structures in junction regions of boundary layer flow. Following the fundamental physical discussion, past flow control work was present as a foundation for the present study. This flow control was achieved in several ways but overall was discussed

as either a passive or active approach. Finally a brief overview of the measurement techniques that have been employed for the study of similar flow phenomena was presented. Such measurement techniques varied in complexity from simple surface-oil flow visualization to hi-speed stereoscopic particle image velocimetry or detailed computational fluid dynamic studies.

III. Methodology

3.1 - Wind Tunnel Overview

All experiments herein were performed using the Air Force Research Laboratory's Low Speed Wind Tunnel (LSWT) Test Facility. This tunnel is designed in a linear cascade configuration with a net turning angle of 95°. The hub in a linear cascade is equivalent to an infinite hub radius. Figure 14, shows the tunnel from an overhead perspective view in the laboratory with critical components detailed. The inlet straightens the incoming flow to provide a uniform flow field to use in experimental tests. Located directly behind the inlet is a tubular grid turbulence generator which produces an approximate 3% freestream turbulence intensity, measured by hotwire anemometry[9], in the incoming flow. The flow then passes through a cascade row of seven L2F blades contained within the test section. Following the test section the flow is exhausted from the tunnel back to ambient conditions. The tunnel is operated by a fan near the exhaust which draws the fluid through the tunnel.

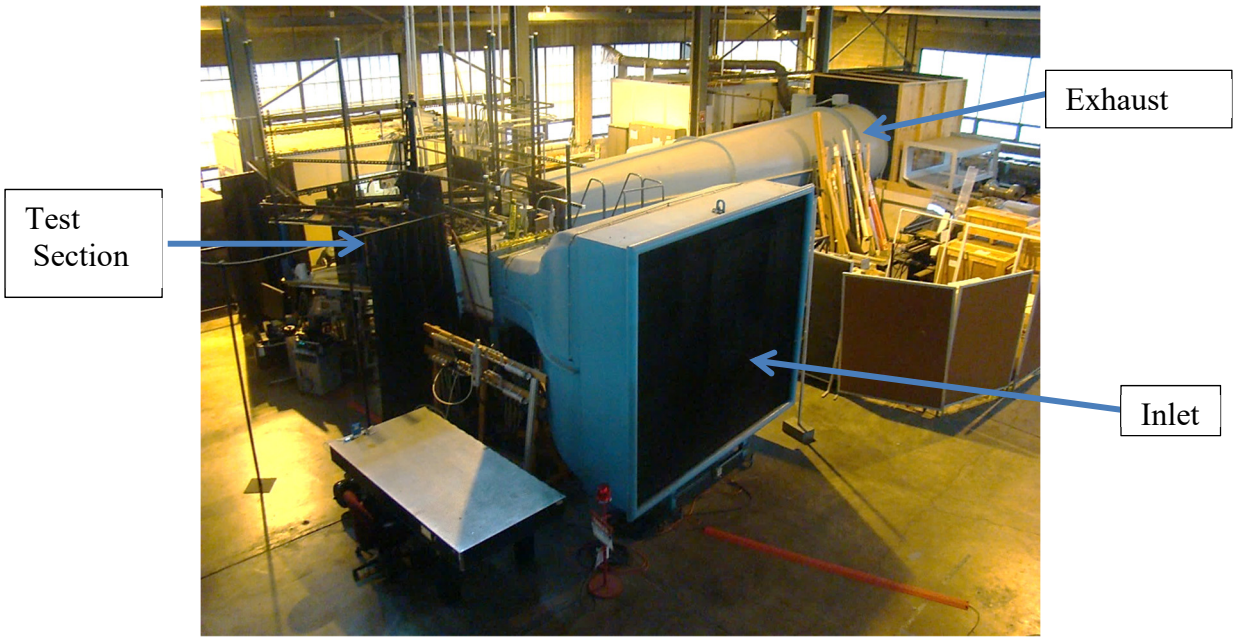

Figure 14. LSWT Test Facility

Figure 15 gives a top schematic of the test section of the tunnel. This schematic allows for a detailed understanding of the test section in which the L2F blades are contained. In order to ensure a clean boundary layer for this secondary flow study a splitter plate is mounted 4.8 times the axial chord upstream of the cascade. The leading edge of this plate is elliptical to ensure a clean boundary layer is generated. This plate also extends downstream 4.27 times the axial chord. This plate, along with providing a surface for a clean boundary layer formation, also acts as an artificial endwall.

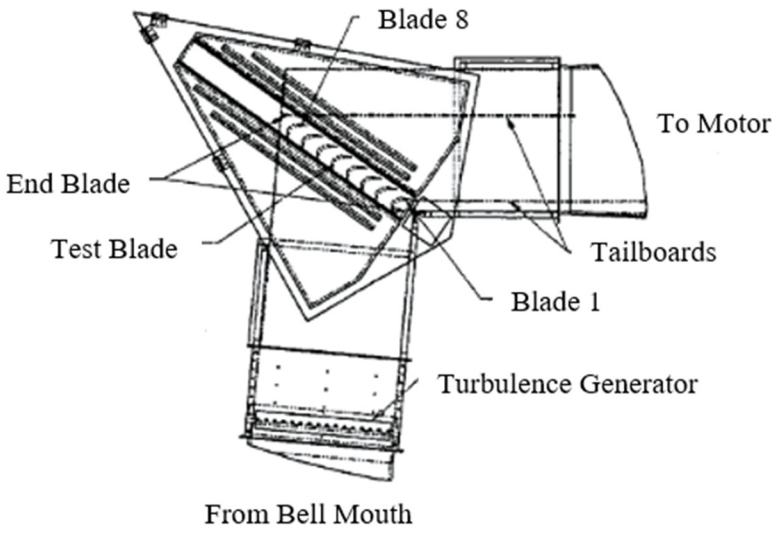

Figure 15. LSWT Top-View Schematic – Adapted from Bons et al[51]

Finally, Figure 16 is a larger detailed test section schematic. This figure provides further information about the location where the active flow control investigated in this study is applied. The passages where the active flow control, discussed in Section 3.2, was applied are marked with stars.

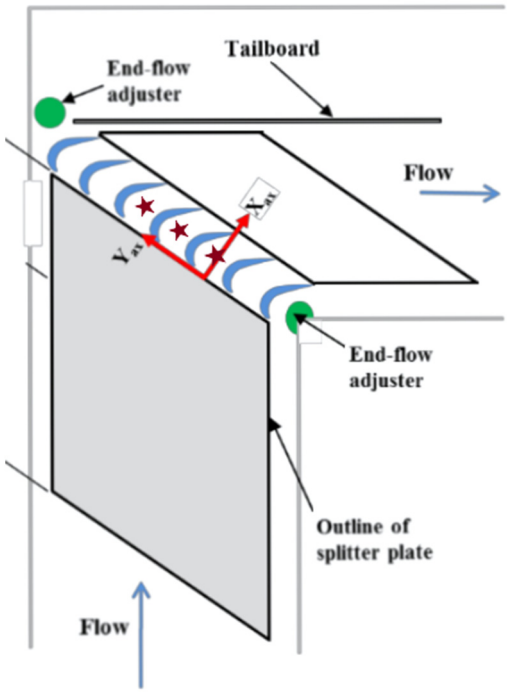

Figure 16. LSWT Test Section Top-View Schematic (Not-to-Scale)

The stationary blade profiles used are AFRL's L2F design. Seven blades were used in this cascade, creating six passages. In this configuration the blades have a 15.24 cm axial chord and an aspect ratio (AR) of 4.17. Further details of the LSWT, and L2F, can be found in Table 1.

Table 1. LSWT and L2F Characteristics

Axial Chord, C_x	15.24cm
Pitch/Axial, S/C_x	1.221
Span/Axial Chord, (Aspect Ratio) H/C_x	4.17
Inlet Flow Angle (from axial direction), α_{in}	35°
Predicted Mean Profile Exit Angle, α_{ex}	-58.1°
Freestream Turbulence Intensity	3%
Boundary Layer Thickness ($\delta_{99\%}$)	14mm

All tests were performed at a Reynolds number of 100,000 based upon inlet velocity, measured via a pitot static probe, and axial chord length. The inlet velocity was adjusted from test to test to meet the 100,000 Reynolds number testing condition. For reference, inlet velocity varied from 10.1 m/s to 10.8 m/s.

Repeatability of the LSWT has been shown to be approximately 1% in inlet conditions. A repeatability study was not performed with this research effort and the reliability of the tunnel was based upon previous work and repeatability studies by prior researchers[8], [9], [15].

3.2 - Pulsed and Steady Jet Blowing

Periodic forcing of the pressure side leg of the horseshoe vortex was achieved by way of seven localized jets. The jets are applied to three of the six passages created by the L2F blades in the cascade. A schematic of the test section set-up is shown in Figure 17. All lines are directly connected pneumatic fittings with minimal overall length to ensure that

the response lag time of the jets was as small as possible. The secondary tank was used to minimize fluctuations in pressure from the building air supply. The tank pressure was held constant for each given frequency test. As an additional data point, added after characterization, but upstream of the secondary tank, an OMEGA mass flow meter, model number FMA-A2322 with accuracy of $\pm$ 1% was used to estimate mass flow into the secondary tank.

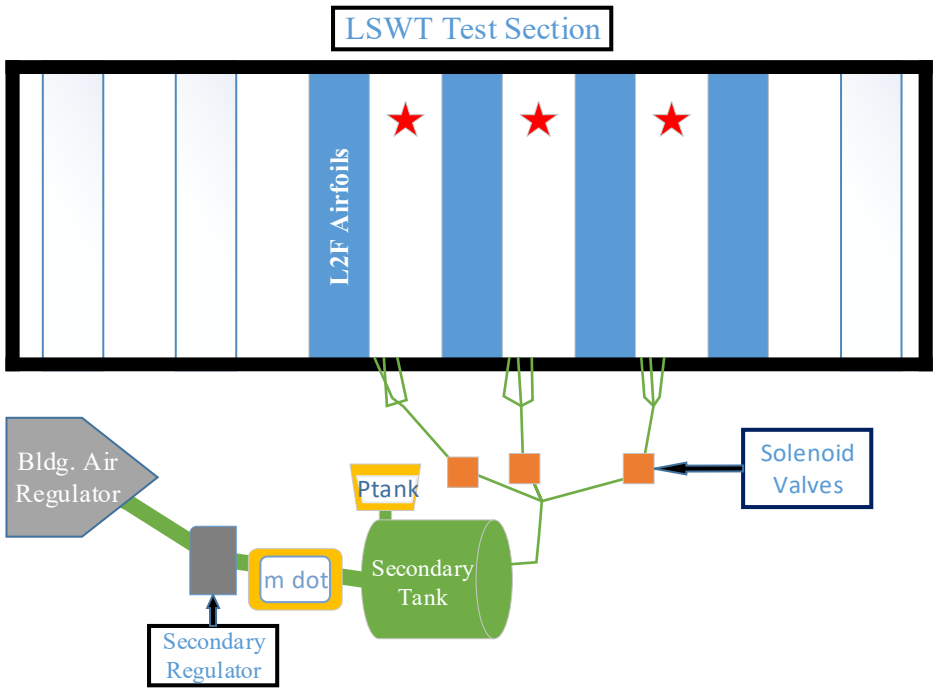

Figure 17. Schematic of Pulsed Jet Experimentation

Each jet has a diameter of 1.60mm and is arrayed in a circle with an overall diameter of 11.9mm or 7.8% axial chord. The jet location is centered 7% axial chord downstream of the leading edge and is shown in Figure 18. Table 2 contains the location of the jets relative to the axial chord, C_x. The location of these jets was described in Fletcher et al.[17] as

placed along the traced location of the liftoff line of the pressure side leg of the horseshoe vortex based on surface oil flow visualization. This location is similar to the location of disturbance selected by Gross[58].

Table 2. Axial Location of Wall Mounted Jets.

Jet #	x/C_x	y/C_x
1	0.063	0.497
2	0.083	0.448
3	0.083	0.51
4	0.094	0.479
5	0.12	0.488
6	0.12	0.51
7	0.133	0.479

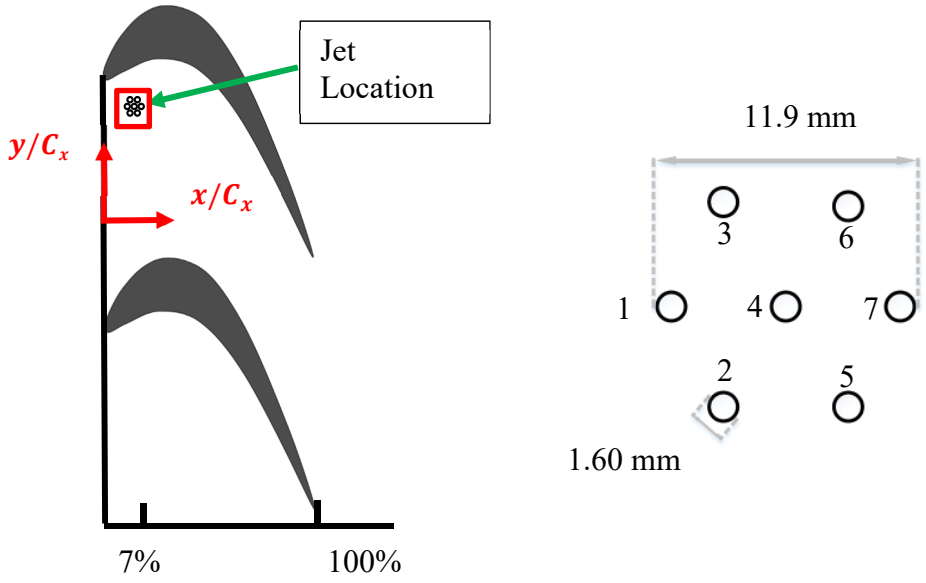

Figure 18. Location of Wall Mounted Jets and Jet Layout

The jets were characterized using a constant temperature hot-wire anemometry system as detailed by Fletcher et al[17]. The use of a miniature hotwire allowed for the

velocity of the jet, 1.5mm above the exit, to be measured. The center jet, number 4 according to Figure 18, of the center passage was used for the characterization. This characterization allowed for repeatable, less than 5% variation of, blowing ratios, pulsing frequencies, and velocities for each set of jets.

Figure 19 shows the on-off behavior of the jet adapted from Fletcher et al[17]. Pulsed jet operation was performed by way of a commercially available IOTA ONE solenoid valve controller manufactured by Parker. The signal from the IOTA ONE was used to trigger three Parker solenoid valves, with orifice size of 2.94mm, one in each of the middle three passages as shown by a star in Figure 16 and again in Figure 17, to create pulsed jets with effective duty cycles of 50%. In order to achieve an effective duty cycle of 50%, the jets were set at a 45% on, 55% off cycle time. Two frequencies of pulsing, 65 Hz and 22 Hz, were studied in these experiments. The average mass flow for the 65 Hz case was 44.8 SLPM and 40.1 SLPM for the 22 Hz case. The velocity of the exit jet was found to be approximately 45 m/s for the pulsed jets conditions.

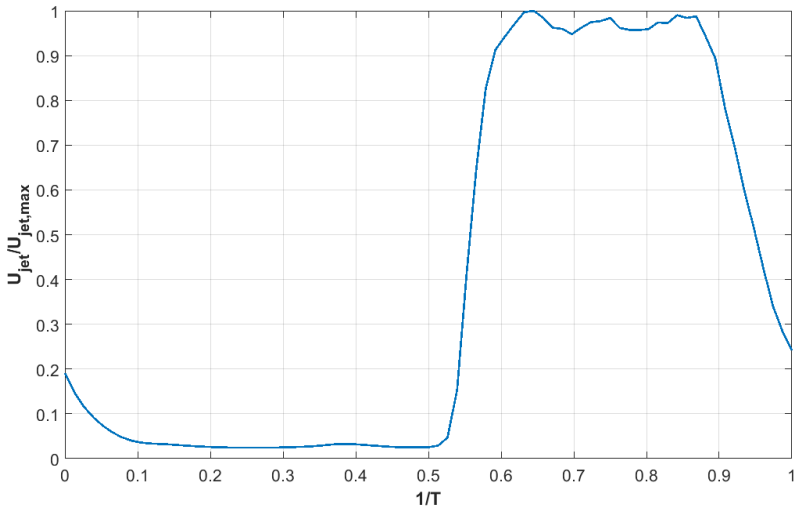

Figure 19. Non-Dimensionalized Jet Pulsing Behavior for Single Cycle at 65 Hz

Steady jets were applied using the same jet locations but the solenoid valves had been removed. Steady jet mass flows of 45.7 SLPM and 68.7SLPM were used to allow comparison between the effects of the pulsed frequencies and the associated mass flow. These results will be discussed in Sections 4.2 and 4.4. The velocity of the jets for the steady case can be approximated as half of the pulsed case, or approximately 23.0 m/s, based upon the assumption of equivalent mass flows. Table 3 shows a summary of the approximate blowing conditions applied in this research as well their relative non-dimensional parameters of interest. The values with asterisks are for reference only and were not directly measured in the present study.

Table 3. Blowing Condition Summary

Forcing Case	F^{+}_{SSL}	Effective Duty Cycle (% On)	Required Mass Flow (SLPM)	Max Jet Velocity (m/s)	BR	MR	C_{μ}
22 Hz	0.4	50	40.1	46.0	4.38	0.056	0.212
65 Hz	1.2	50	44.7	46.1	4.39	0.060	0.232
45.7 SLPM	--	100	45.7	23.0*	2.19*	0.063*	0.134*
68.7 SLPM	--	100	68.7	36.8*	3.48*	0.010*	0.344*

3.3 – Characterization of the Passage Vortex by way of Spectral Analysis of Hot-Film Sensors

Expanding upon the work of Veley, et al.[29] this report aims to provide further understanding of the baseline condition of the vortical structures in the passage. In order to understand the spectra of frequencies present within the passage surface mounted hot-film sensors will be used**.** These sensors are the same as the ones used by Veley[59] and a schematic, reproduced from the same report, can be seen in Figure 20.

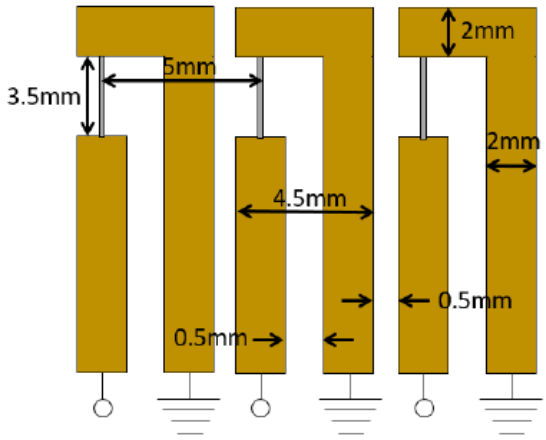

Figure 20. Schematic of Hot-film sensor - Veley[59]

The hot-films were paired with a TSI IFA 300 constant temperature anemometer system. The hot-film sensors were prepared in-house and consisted of a 3mm by 0.3mm platinum sensor created for measuring the passing flow features generated by high lift turbine blade. A high pass filter of 0.1 Hz and a low pass filter of 2 kHz was applied to the signal prior to the collection of averages. The hot-film sensors operated at approximately $100°C$ and had a set overheat ratio of 1.2. The hot-film sensors, when used in this surface mounted application, are used in a constant temperature mode to infer fluctuations of local velocity and thus infer the presence of the PSHV. Individual time series were not saved by the spectral analyzer and only the final spectral average was reported. The results from these tests are presented in Section 4.1. Sensors were placed, as shown in Figure 21, at the leading edge of the profile and throughout the passage, similar again to the work of Veley[59]. A single sensor, not shown in the figure, was also placed under the passage, out of the flow, in order to measure tunnel vibrations. The attempt to measure tunnel vibrations was made to address the source of the low frequency signal.

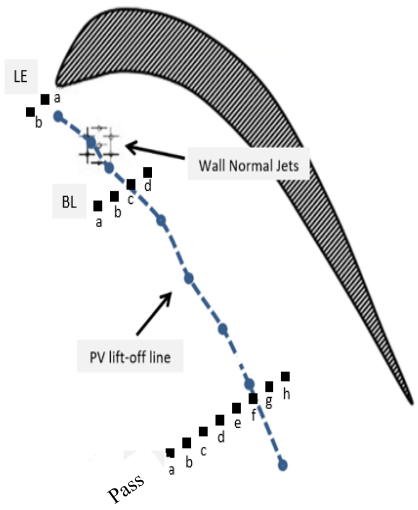

Figure 21. Location of Hot-Film Sensors

The work by Veley et al.[14] collected hot-film data for two consecutive 30-second intervals. The data collected from the intervals was divided into five second segments and Fast Fourier Transforms were performed on each of the now 12 individual spectral averages. Following the FFT, a Power Spectral Density calculation for each of 12 spectral averages was performed. A stable average, where each sample is given equal weighting, was then performed between the 12 spectral averages and the resulting average PSD was used to draw conclusions.

In this study a Data Physics Spectral Analyzer is used to perform a more intensive study of the baseline condition of the passage vortex. The Spectrum Analyzer was used in conjunction with Signal Calc Mobilizer software provided with the Abacus system manufacturer. A systematic variation of the number of spectral averages collected and averaged was performed to investigate the behavior of the passage vortex. Sample rates were fixed based upon frequency resolution. A frequency span of 1,000 Hz with a distance

between adjacent frequency points of 0.1563 Hz was set in order to capture an accurate representation of analog signal. These frequency settings resulted in a time of capture duration per sample of 6.4 seconds with a time between sample points of 390.6 μsec. Stable averages were performed, using the in tunnel sensors, for varying number of Spectral averages. The times required to collect each data set are shown in Table 4. The spectral averages here are comparable to the 12, five second spectral averages, of Veley et al.[14] which were captured over a single 60 second interval. By collecting and averaging large data sets the spectral content of the flow is better resolved than simply collecting 12 samples. For the sampling system, a Hanning window was used. The collected test data from the Data Physics Software was exported to MATLAB where the stable averages of the power spectral density voltages were plotted versus their accompanying frequencies for each of the sampling sets.

Table 4. Spectral Analysis Sampling Conditions

Spectral Averages (#)	10	20	50	100	200	400
Time (H:MM:SS)	0:01:04	0:02:08	0:05:20	0:10:20	0:21:20	0:42:20

3.4 - Total Pressure Loss Measurements

Total pressure loss measurements, for downstream regions, were taken via a custom, in-house-designed, total pressure rake. The rake, shown in two views, in Figure 22**,** consists of five vertically mounted Kiel probes plumbed to five corresponding All-Sensor model 1 INCH-G-4V pressure transducers with $\pm 0.25\%$ precision. The sensors had a vertical displacement between centers of 50.8 mm. Kiel probes were used in all tests because Kiel probes are less sensitive to incoming flow directions as compared to Pitot

probes. Lyall reports offsetting the Kiel probes up to 30° from the incoming flow and reports only a 0.15% error in such flow conditions[9].

Figure 22. Total Pressure Rake Location and Travel

An in-house LabVIEW program and interface is used to automatically traverse the probes in the pitch and span directions. The arrows in Figure 22 represent pitch motion and spanwise motion. This motion of the rake, circled in Figure 22, containing the five probes leads to a grid of 900 (30 total measurements in pitch by 30 total measurements span) individual total pressure measurements in the downstream planes. This relates to a measurement area of 18.61cm in the pitch direction and 25.4 cm in the span direction for the out of passage measurements. The test take approximately 25 minutes to complete. In order to measure freestream conditions, a pitot static probe is mounted upstream of the cascade well outside of any wall boundary layer region. The difference in total pressures, divided by the incoming dynamic pressure gives the pressure loss coefficient, as given by Equation (6), for each point. The local pressure loss coefficients can then be computed for each region at varying locations downstream of the passage. For in-passage total

pressure measurements a single Kiel probe was mounted in-line with the exit flow and was swept through the passage, in the pitch and span wise directions, in a manner similar to that of the pressure rake. The Kiel probe was plumbed to a singular Druck pressure transducer, model number LPM 4581 and the total pressure was recorded. The Kiel probe can be seen, again in two views, in Figure 23**.** The close proximity of the probe to the pressure surface of the adjacent blade is necessary to map as much of the endwall region of the passage as possible. The approximate region of data collection is shown by the box of Figure 23**.**

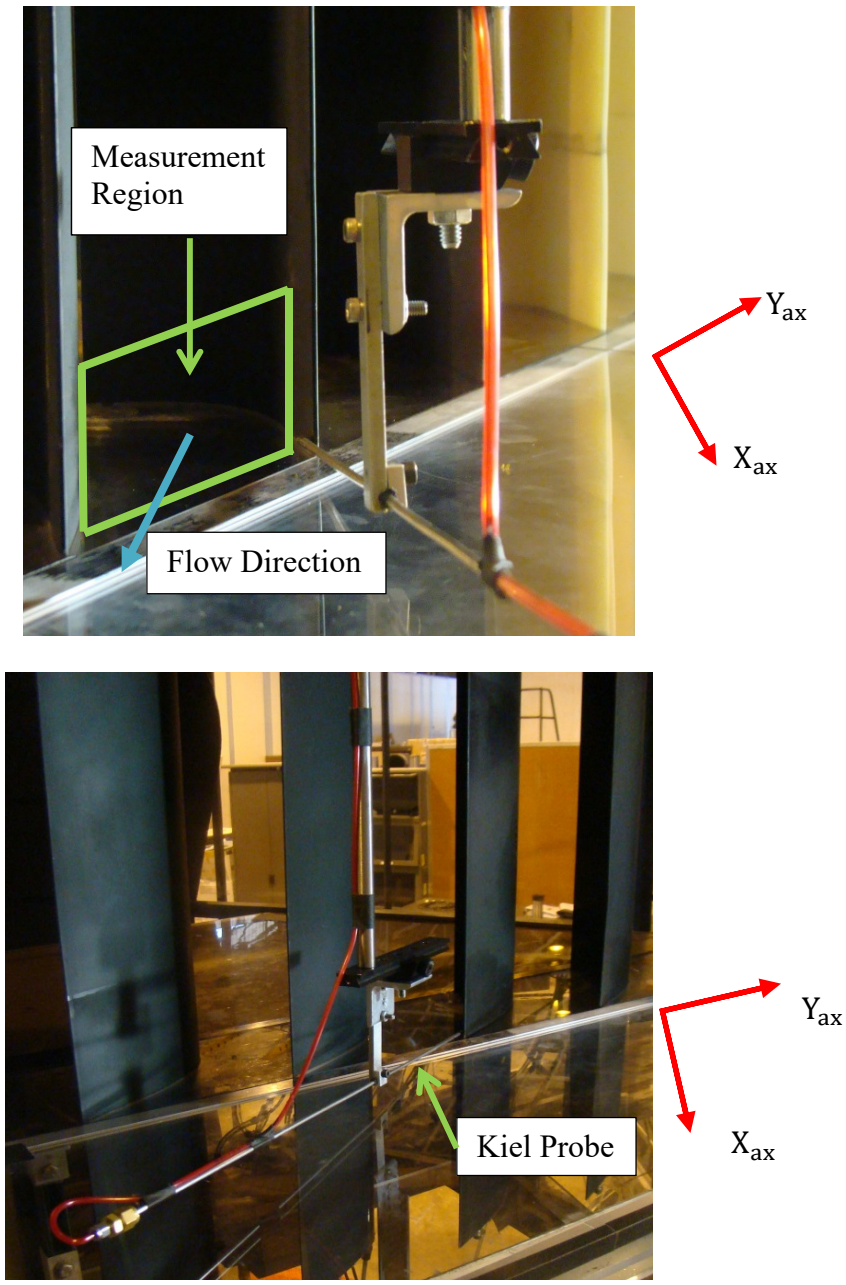

Figure 23. Location and Travel of Kiel Pressure Probe

Figure 24 shows the location of the planes of interest. Figure 25 is a secondary representation of the measurement location of the out of passage planes. The planes indicated by dashed lines are the out of passage measurement planes and are 105%, 125% and 150% of the axial chord length downstream of the leading edge. The in passage planes

are 75%, 85% and 95% of the axial chord downstream of the leading edge. All planes are oriented parallel to the pitchwise axis. Table 5 contains the number of data points and the size of the measurement region for all planes of interest described in Figure 24. The location of the planes has also be quantified in the table as well.

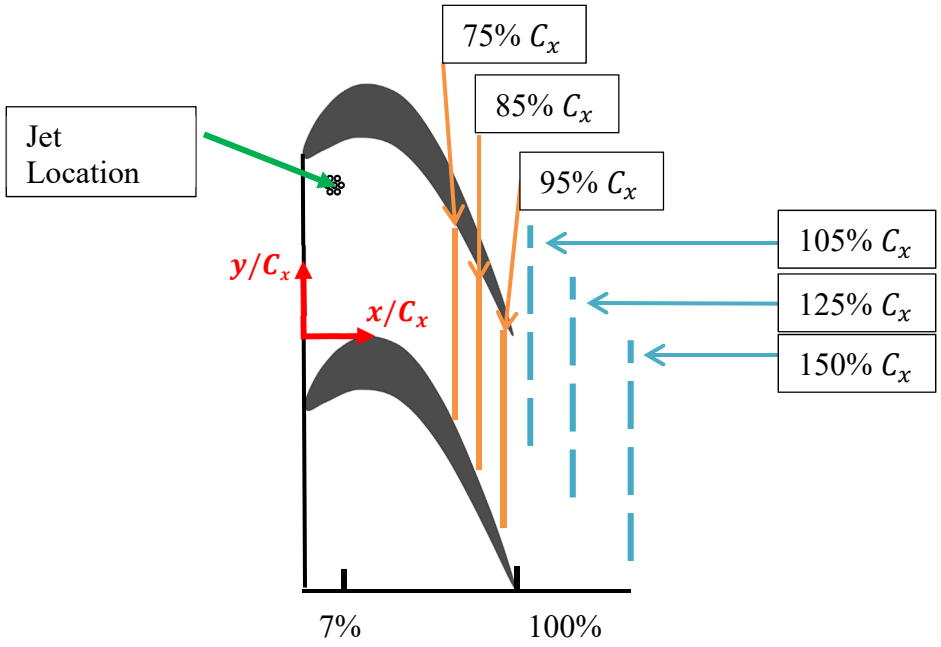

Figure 24. Location of Total Pressure Measurement and SPIV Planes

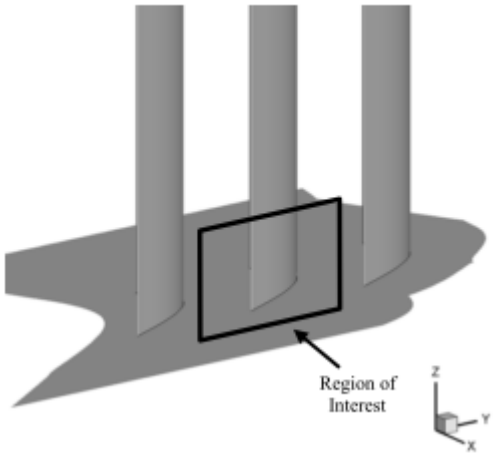

Figure 25. Representation of Region of Interest

Table 5. Pressure Plane Measurement Specifics

Plane (% Cx)	Length (cm)		Location		Data Points	
	Pitch	Span	y/S	z/H	Pitch	Span
150	18.6	25.4	-1.34 → -0.34	0 → 0.41	30	30
125						
105						
95	16.1	13.5	-0.85 → 0.01	0 → 0.23	26	16
85	15.2	11	-0.68 → 0.14	0 → 0.19	25	13
75	14.9	8.5	-0.53 → 0.27	0 → 0.15	24	10

As with the repeatability of the LSWT, the uncertainty in pressure loss measurements has been well documented in previous research efforts in the same facility with similar flow conditions as those studied herein[8], [9], [15]. Based upon previous work, the response time of the pressure transducers and the accuracy of the Kiel probes is sufficient for the current study. Further, it has been previously reported that the instrumentation used in the present study shows only a 1% variation in individual data points and area integrated losses over the course of several days [15]. For further reference regarding the Kiel Probes see reference [9]. For reference regarding transducer response see reference [8].

3.5 - Stereoscopic Particle Image Velocimetry and Flow-Visualization

Stereoscopic Particle Image Velocimetry (SPIV) and high-speed flow-visualization (flow-vis) was performed throughout the passage. Measurements were taken at 75%, 85% and 95% axial chord, corresponding with previous in-passage total pressure measurement planes, illustrated in Figure 24.

Figure 26 is an overhead schematic of the SPIV and flow-vis set up. The region of interest is the location where the actual measurements will be made. The purpose of this set-up is to acquire three components of velocity in the location notes as the "Region of Interest / Cal" in the figure. By obtaining the three components of velocity, vorticity can be derived and plotted in order to show the location and strength of the vortical endwall structures in high-speed. The camera angles can be seen as the deviation from the X axis in the representative fields of view. The physical setup can be seen in Figure 27.

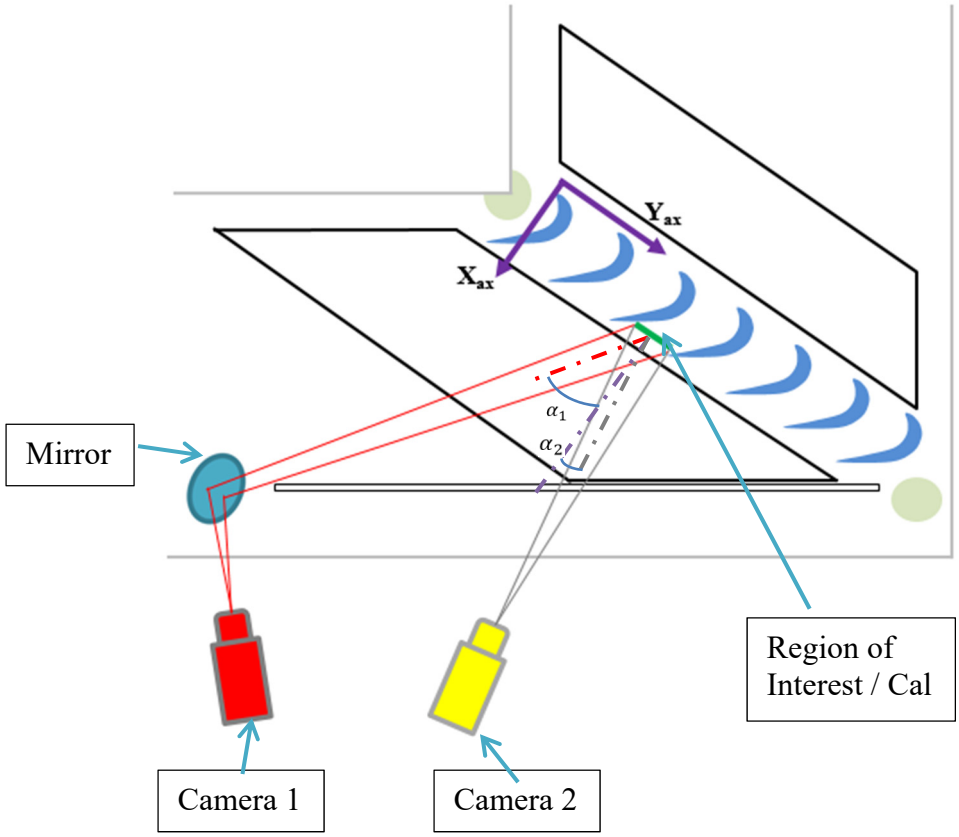

Figure 26. SPIV Overhead Schematic

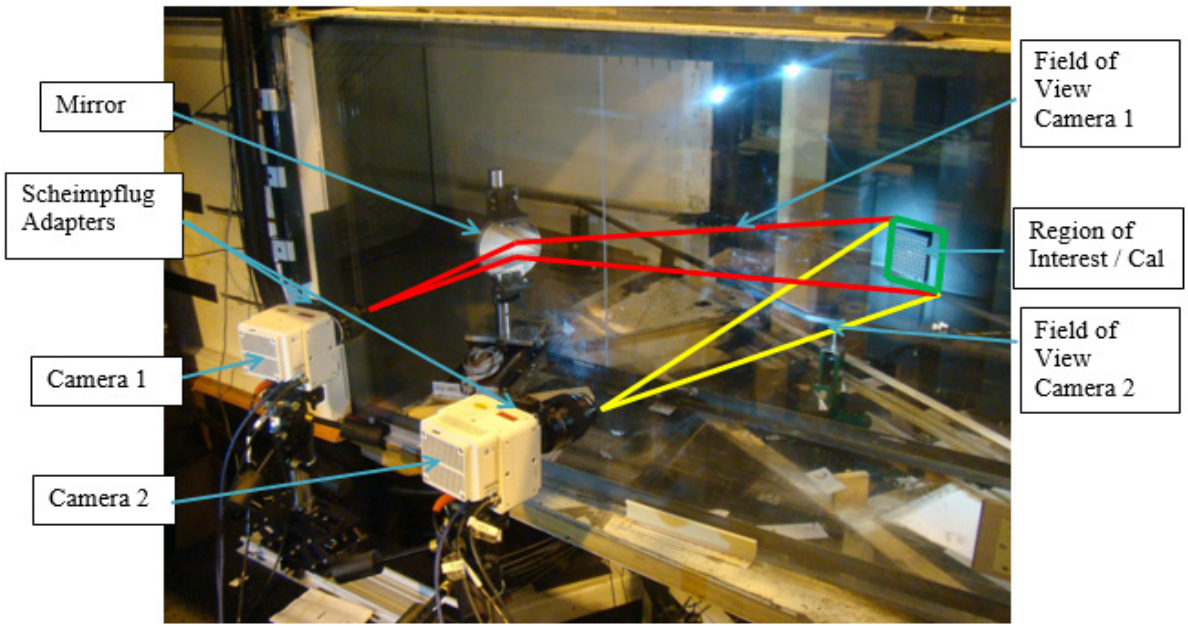

Figure 27. SPIV Experimental Set-up

A commercially available SPIV computer software package from LaVision, DaVis, was used as the hub for SPIV and flow-vis data collection. The DaVis software, version 8.4.1, was used in conjunction with a programmable timing unit, also from LaVision, to trigger two Ametek Phantom 640L CMOS cameras in sync with a laser light source. The IOTA ONE used to actuate the solenoid valves for the pulsed jets, was also used to trigger the programmable timing unit such that the collection of data began in the same portion of the pulsing phase for every case. The Phantom cameras were both fitted with Scheimpflug adapters and Nikon 105mm f/2.8 lenses. The Scheimpflug adapters were adjusted in each plane to ensure uniform focus across the plane. Also, 527nm $\pm$ 3nm wavelength bandpass filters were mounted to the lenses to so that only the wavelength of light of the laser is

reaches the camera sensor. A Photonics Industries dual Nd:YLF laser, fitted with LaVision sheet spreading optics, was used as the light source. The thickness of the laser sheet, in all test cases, was approximately 2mm, the maximum width possible from the sheet spreading optics.

A LaVision calibration plate, provided with the DaVis program, was placed in the passage and was used to calibrate the cameras and laser for each plane. The calibration plate is outlined in the "Region of Interest / Cal" in Figure 27. Table 6 contains the calibration angles recorded for each plane described in Figure 24. The calibration angles are the angles at which the camera is oriented relative to the calibration plate. These angles are also shown as α_1 and α_2 for camera 1 and 2 respectively in Figure 26. The angles of note are those in the y-direction. These angles are the best possible angles achievable with the current LSWT configuration. The ideal angles, that provide the minimum magnitude of error, as prescribed by LaVision are between $30°$ and $35°$[65].

Table 6. SPIV Camera Calibration Angles

Plane	Camera 1 Angles (deg)			Camera 2 Angles (deg)		
	X	Y	Z	X	Y	Z
95	-1.45	-32.41	-1.44	-3.68	40.44	-1.06
85	0.94	-33.60	-1.63	-0.95	39.57	1.64
75	0.71	-34.72	-1.66	-2.24	21.23	0.41

Camera one, seen at left in Figure 27, was focused on the calibration plate through a mirror placed within the tunnel. This mirror was positioned and secured such that the majority of the surface and stand was behind the tailboard to avoid creating a disturbance in the flow through the test section. Camera two, focused directly on the plate. Following

calibration of the cameras to the plane of interest, the laser was aligned with the center of the calibration plate. The plate was removed and the tunnel was then seeded using a commercially available fog generator, placed well upstream of the tunnel inlet. Each camera's lens was mildly adjusted, as needed, to focus upon the particles illuminated by the laser sheet. This adjustment is needed due to the difference in thickness between the calibration plate and the laser. A self-calibration of the system was subsequently performed using the DaVis software. This software calibration adjustment is designed to account for any laser sheet misalignment. The calibration images are shown in Figure 28, for reference. The labels on the figure are the location of the calibration plate relative to the origin of the SPIV set-up. The origin is located at the point labeled 1 in the figure. The images are of the same side of the calibration plate, but due to the camera angles the views appear different. The magnification factor for each plane is reported in Table 7 as a measure of calibration also.

Table 7. Magnification Factor Values

Measurement Plane	Magnification Factor (Pixel/mm)
75	9.629
85	9.891
95	10.485

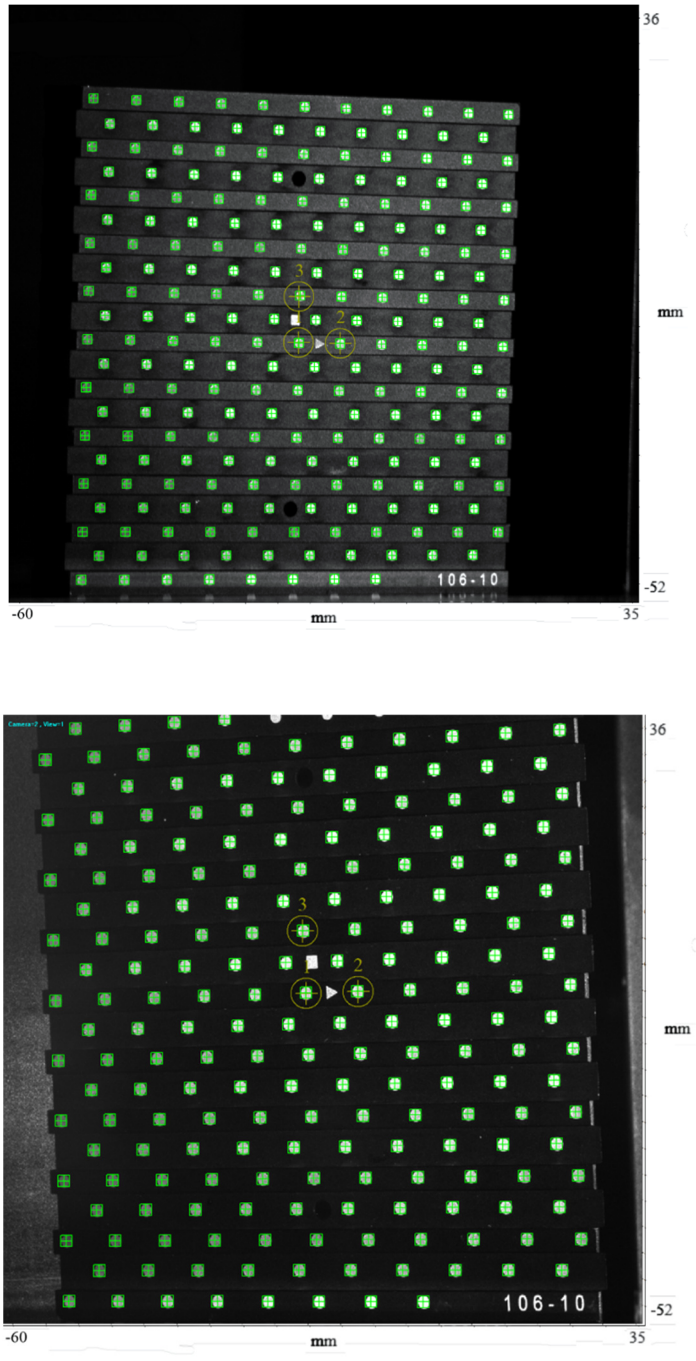

Figure 28. Calibration Images, Camera 1 (top) Camera 2 (bottom)

For SPIV data collection of baseline and steady jet forcing, 5000 images were recorded at a sampling rate of 2.5 kHz. Previous researchers have used similar settings in

their studies[59] [23]. The parameters used to capture flow-vis images were similar; however, only one camera, camera 1, was used with a singular laser pulse and a sampling frequency of 5 kHz.

In order for each pulsed run to contain only full pulsed periods, the sampling rate and number of images was adjusted. A full pulsing period, or cycle, here is described as the time, and thus number of SPIV images collected, between jet actuations. These adjustments are only required for pulsed forcing cases. For the 22 Hz forcing case, sampling occurred at 2.486 kHz and 4994 images were recorded. The number of images per period, or jet cycle, can be found by dividing the sampling frequency by the pulsing frequency yielding samples per pulse. This calculation results in 113 images per period for the 22 Hz case. For the 65 Hz case, sampling occurred at 2.47 kHz and 4940 images were collected, resulting in 38 images per period.

In order to more fully refine the temporal events occurring within a 65 Hz period one must take more images per jet cycle. To obtain more images separate data sets were collected because of the capture rate limitations of the SPIV hardware. A delay was added to postpone the start of data collection a specific time following the pulse of the solenoid. In order to have a set number of photos similar to the 22 Hz case a 1/3 period and 2/3 period delay was added on successive 65 Hz tests. This delay essentially tripled the number of images per jet cycle. The 1/3 period delay was 5.128 milliseconds and the 2/3 delay was 10.256 milliseconds. Figure 29 is a visual representation of this delay setup. The square wave is the initial signal from the IOTA ONE. The initial image pairs are taken with no delay from the IOTA ONE signal. The second data set of image pairs are shifted later in the pulse cycle due to an initial start delay of 5.128 milliseconds. The final set of image

pairs are shifted later still due to an initial start delay of 10.256 milliseconds. These delays ultimately allowed for 114 images per period when the three sets of data are combined. The number of periods however, did not change. These sampling conditions allowed for near-time resolved data and were held constant for all measurement planes.

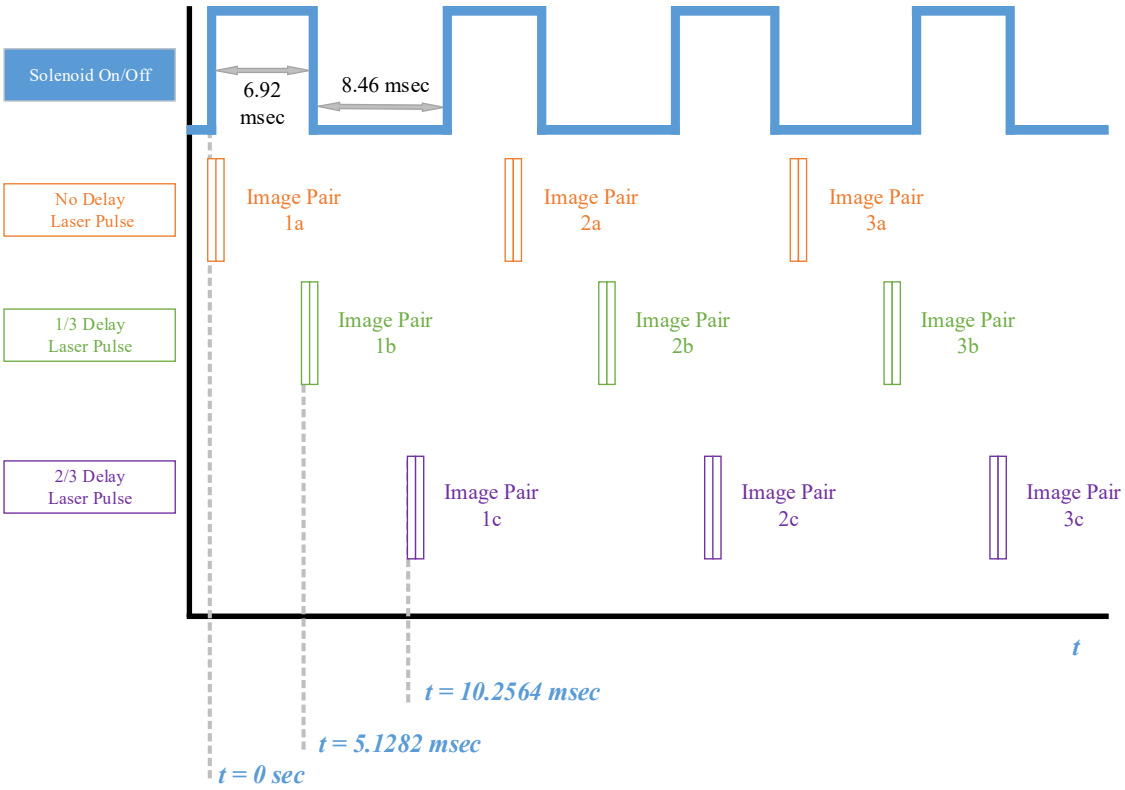

Figure 29. Sample Delay for SPIV at 65 Hz

In order to ensure sufficient particle movement between pulses, the time between each laser pulse was varied with plane location. Measurements in the 95% plane had a dt of 20 μsec, the 85% plane had a dt of 40 μsec and the 75% dt was 35 μsec.

To conclude this discussion of the SPIV set-up a brief error analysis and discussion is necessary. The topic of error analysis in PIV is quite extensive especially when

considering fluctuating velocity components. Several authors have discussed this topic, and for further information the reader is directed to their reports[63], [66], [67], among others. As an approximation for the error found in the current experiment, procedures outlined in literature were used to estimate that the error in the velocity[66]. The particle displacement was typically 5 to 8 pixels depending on the plane. The error is approximated by using a particle displacement with accuracy of 0.05 pixels, and an average passage velocity of 20 m/s for a five pixel displacement. For a given image the error is approximated as 0.2 m/s. The laser pulse durations were short and the laser is thus expected to not be a significant source of error. In areas of the flow where the velocity was expected to be steady, aside from FSTI, an approximate 3.5% standard deviation in velocity was found. The measured 3.5% variation in velocity relates closely to the reported 3% FSTI, as measured by a hotwire, of the tunnel. A final parameter used to qualify the SPIV data was image correlation values. The correlation value is a measure of the similarity in peaks of adjacent images. For this study a correlation value of 0.60 was used as an approximate lower cut-off for an acceptable data set as recommended by the supplier of the SPIV software, LaVision. For further details regarding the error analysis of the SPIV data see Appendix H. and there are several key parameters that are often studied to determine the error of a specific set of data.

IV. Analysis and Results

Chapter Overview

This chapter is intended to present the results found from in-depth study of the tests described in the previous section in order to investigate the effects of active forcing on the strength and coherence of the passage vortex both within and beyond the passage. This chapter is divided into five sections. Section 4.1 will focus on the spectral analysis of hot-wire anemometry data and provides insight to the unperturbed spectral content of the passage vortex in the LWST configuration. Section 4.2 builds upon the knowledge gained from the spectral analysis and investigates total pressure loss as mapped throughout the passage by Kiel probes in varying locations. Section 4.3 uses the results from a previously performed Implicit Large Eddy Simulation (ILES) solution to investigate the most effective way to present stereographic particle image velocimetry data for flows that are angled, rather than normal, to a measurement plane. A detailed derivation and discussion are included as well. Section 4.4 presents the average velocity data from the SPIV measurements data in order to further discuss the location of the vortical endwall structures and provide a discussion regarding the formation of loss in the passage. Finally, Section 4.5 presents and discusses the averages of near time resolved SPIV data in an attempt to more fully describe the effects of localized endwall forcing of the pressure side leg of the horseshoe vortex.

4.1 - Results of Spectral Analysis

The purpose of this section is to further resolve the natural baseline passage vortex oscillation prior to the application of flow control. Sampling occurred at a Reynolds

number of 100,000 with no flow control present. Refer to Table 4 for all tested spectral average sampling conditions. Figure 30, Figure 31, and Figure 32 show the averages taken from the passage hot-films for 20, 200, and 400 spectral averages respectively. The legends refer to the location of the sensor positions with labels previously described in Figure 21 in Chapter 3. The figures plot the spectra content in terms of the reported voltage supplied to each of the hot-film sensors. The average voltage values ranges from 0 to 0.005V and is plotted against the frequency range of 0 to 200 Hz. The peaks and bands shown relate to an change in voltage measured by the sensors while running in constant temperature mode. This change in voltage can be used to infer the presence of a vortical structure in this experimental configuration. The entire range of 0 to 1000Hz can be seen in Appendix A.

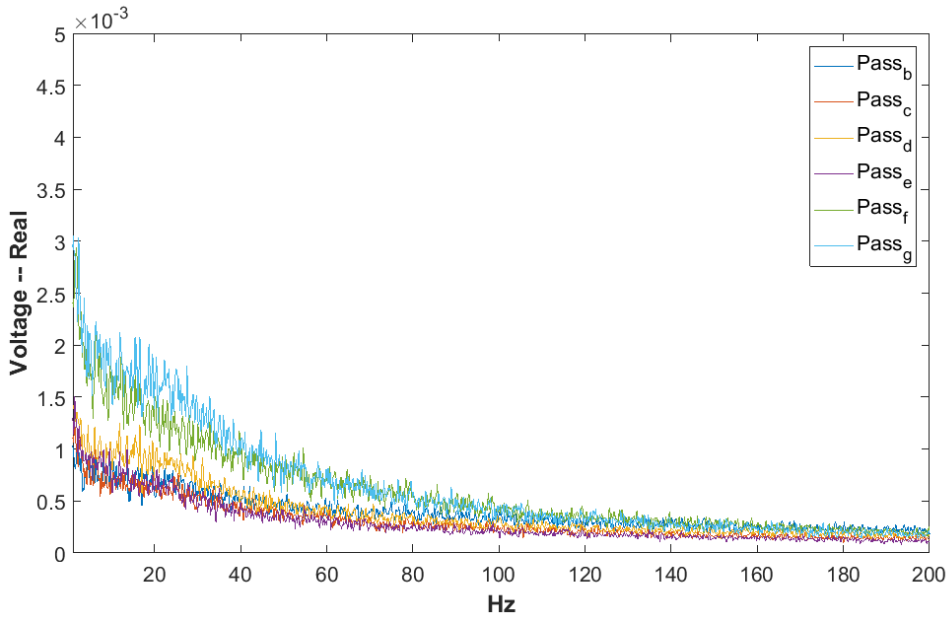

Figure 30. Hot-Film Stable Average of 20 Spectral averages

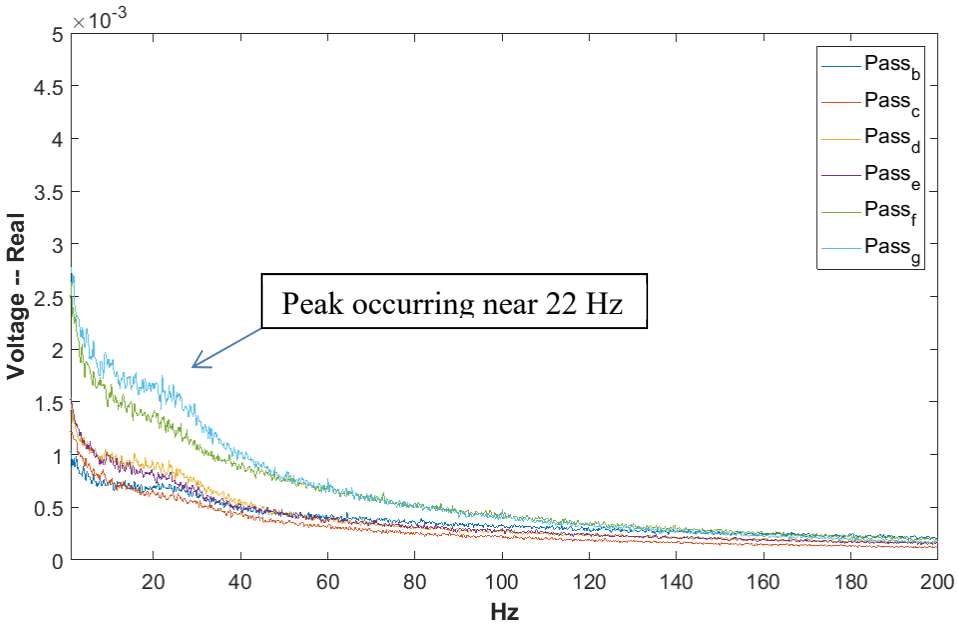

Figure 31. Hot-Film Stable Average of 200 Spectral averages

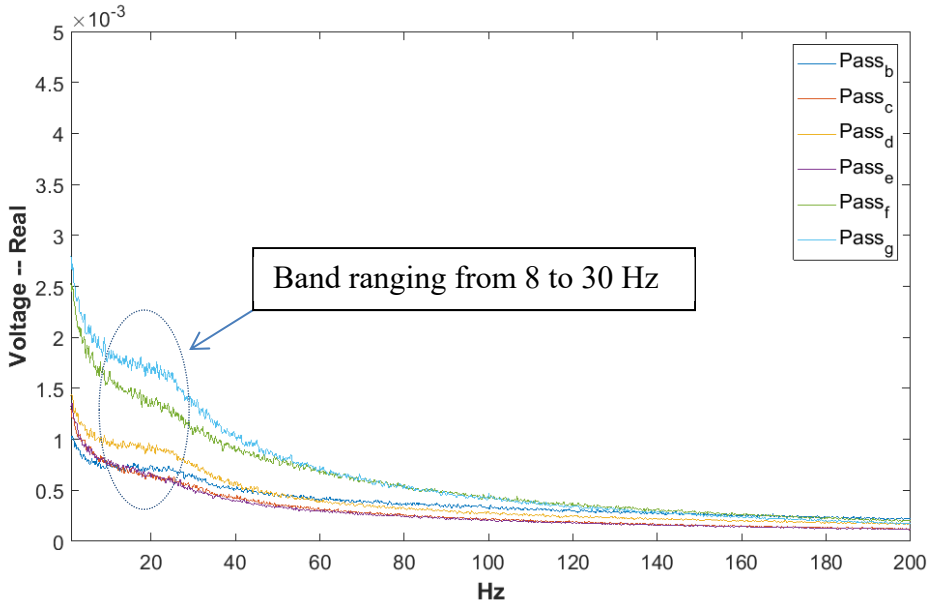

Figure 32. Hot-Film Stable Average of 400 Spectral averages

Figure 30, Figure 31, and Figure 32 show that as more spectral averages are accrued, the spectral output is smoother and a band of frequencies begins to form between

8 and 30 Hz. It can also be seen in Figure 31 that a small peak residing near 22 Hz occurs. The presence of the frequency band implies that while the oscillation of passage vortex is centered near 22 Hz, the true behavior of the vortex is more unsteady. These results, the natural oscillation of the passage vortex near 22 Hz, are consistent with the work of Veley[29], [59]. However the conclusions of Veley were drawn on a collection of data with only 12 individual spectral averages. The present study has taken, in some instances, 400 spectral averages. The 400 average result shows a decrease in the magnitude of the peaks but a consistent band remains. The presence of the peak near 22 Hz validates conclusion reached by Veley and Gross[58] that the natural frequency of oscillation of the PV occurs near 22 Hz for the tested conditions. It further validates the selection of 22 Hz as a blowing frequency of interest. Appendix A also contains the figures that show stable averages for 10, 20, 50, 100, 200 and 400 spectral averages for the sake of completeness. Note that the sensors at the leading edge did not show any peaks or bands of frequencies in the spectra, which eliminates upstream tunnel characteristics as a source of the peaks occurring in Figure 30, Figure 31, and Figure 32.

A sample leading edge sensor plot is shown in Figure 33. The lack of a frequency band near 22 Hz in these sensors implies that the frequency spectra present in the passage is truly generated by the profiles and is not a remnant of an upstream tunnel phenomena. The spikes that are seen at 60, 180 and 300 Hz are consistent with electrical noise and are not considered real phenomena. All other leading edge plots can be seen in Appendix A. Further, Appendix A contains a brief discussion of the low frequency signal, below 3-5 Hz and rules out the presence of tunnel vibration as the cause of this signal phenomena.

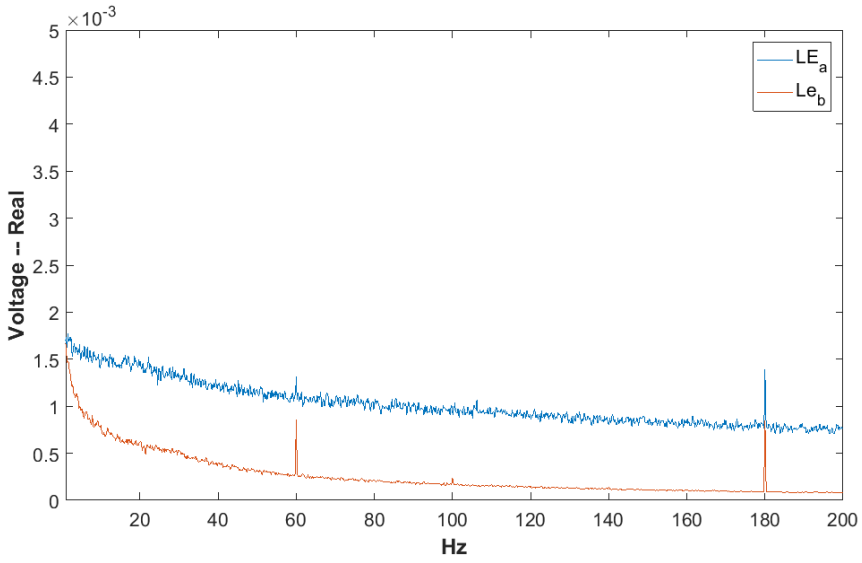

Figure 33. Hot-Film Stable Average 200 Spectral averages at Leading Edge Sensors

4.2 - Results of Total Pressure Loss Measurements

The next section of data to be discussed is the results of the in and out of passage total pressure loss measurements. Total pressure loss measurements allow for one to map out the regions of loss throughout, and downstream of the turbine passage. This section presents data in several different ways. Total pressure loss coefficient will be mapped at three in passage locations and three out of passage locations in order to show the shape and location of the loss structures, primarily the PSHV, SSCSV, PV, and SV. The values of the pressure loss coefficient, γ, range from nearly zero to as high as 1.8. Since γ is only a scaling factor to represent the regions of loss theses values that are greater than unity are not unreasonable. It is also important to note that these values are only for local regions of the flow and not the entire passage. In the largest measurement planes only 40% of the span can be seen. Finally, several previous efforts have shown loss coefficient values, defined the same way as this report, with values greater than unity[22]. Overall passage

loss has been calculated in the 150% plane and will be presented for each forcing case. Overall pressure loss is defined as the summation of the loss mapped in the region outlined by one pitch and the bottom half span of the passage. Overall pressure loss is a highly useful way of quantifying the effectiveness of the specific forcing condition and will be used to compare the overall effectiveness of each case to the baseline condition.

In order to place the flow control effects on total pressure loss into context it is useful to first describe and discuss a baseline case. The baseline conditions is one where there is no active flow control applied. Recall the Reynolds number for all tests is 100,000. Figure 34 and Figure 35 show the map of the total pressure loss for the baseline condition at the 85% plane and the 150% plane as indicated previously in Figure 24. The forthcoming figures also have labeled appropriate loss features for clarity.

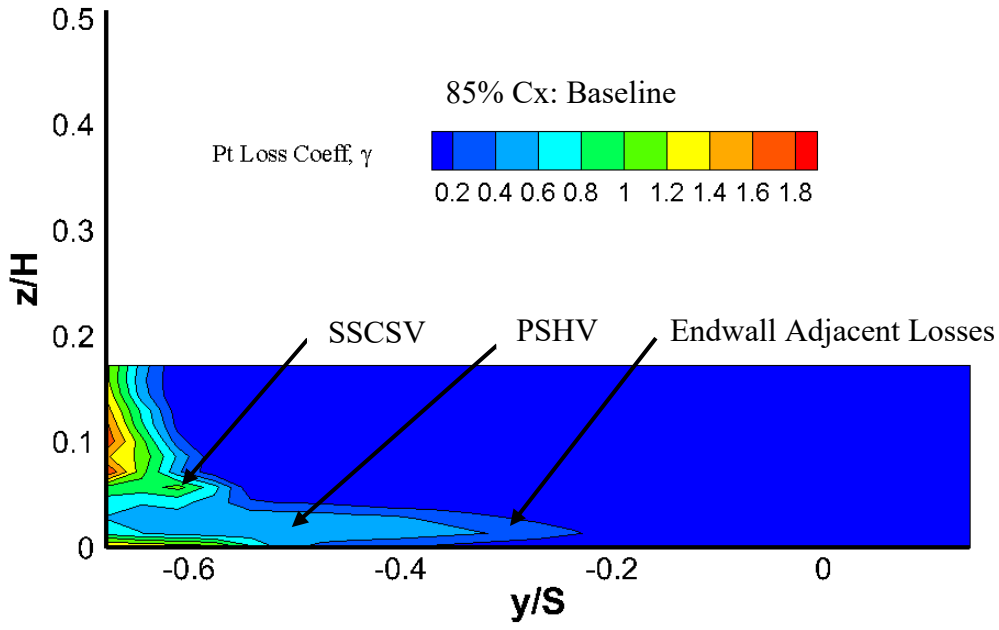

Figure 34. Baseline 85% Cx Total Pressure Loss Coefficient Map

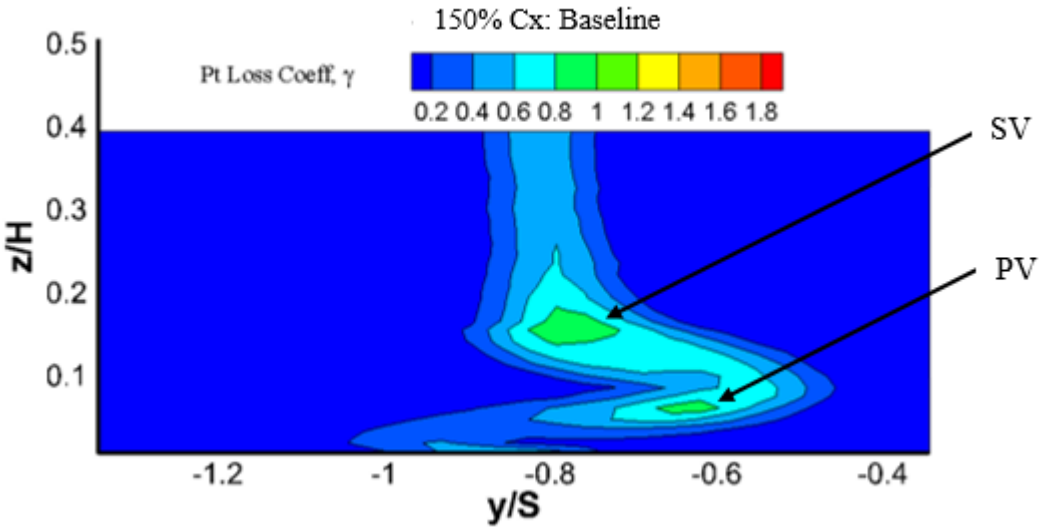

Figure 35. Baseline 150% Cx Total Pressure Loss Coefficient Map

In Figure 34 three loss features can be seen. A small core denoted as the suction side corner separation vortex (SSCSV). A region of loss along the endwall extending to approximately -40% pitch labeled as the pressure side leg of the horseshoe vortex (PSHV). There is also a significant amount of endwall adjacent loss that can be seen extending nearly to -20% pitch or y/S = -0.2. Endwall adjacent losses, are define in this research, as losses that occur within approximately 5% span of the physical endwall. The origin for the pitch measurements is the trailing edge of top blade. See Figure 24 for pictorial representation of the location of the origin. In Figure 34, the left edge of the plot ends along the suction surface of the adjacent blade. The loss along the suction surface (y/S ≈ -0.70) is due to the separation of the flow from the L2F and is not of primary interest in this study. The shed vortex (SV) is generated by separation occurring pressure side of the L2F profile.

This loss feature is not focused upon in this research. However, the second loss feature, the passage vortex (PV), which recall is a combination of the SSCSV and the PSHV can be seen near 8% span and -60% chord. This loss feature is targeted in this research and the location and movement of the vortex is of primary importance. In Figure 35 two loss features can be seen. The shed vortex (SV) is shown at approximately 20% span and -80% pitch and the passage vortex is located at -65% pitch and approximately 8% span. Finally, In Figure 34 the vertical axis only extends from approximately z/H = 0 to 0.18 and the plot in Figure 35 maps to z/H of 0.40. This is due to the fact that the loss structures grow in size as they propagate downstream.

The total pressure maps that were shown in Figure 34 and Figure 35 are representative of the plots that have been collected in the 75%, 85%, 95%, 105%, 125% and 150% Cx planes. However, it is difficult to demonstrate the growth of the loss features by only presenting two dimensional maps. In order to further discuss the effects of the jets both within and downstream of the passage a close-up view of the baseline case for the region between blades can be seen in Figure 36 and the region beyond the blades can be seen in Figure 37. Again, relevant loss features have been highlighted. For clarity, loss coefficient values less than 0.1 have been blanked in the following figures. Also, the grey regions in the figure are the surfaces of the L2F profiles.

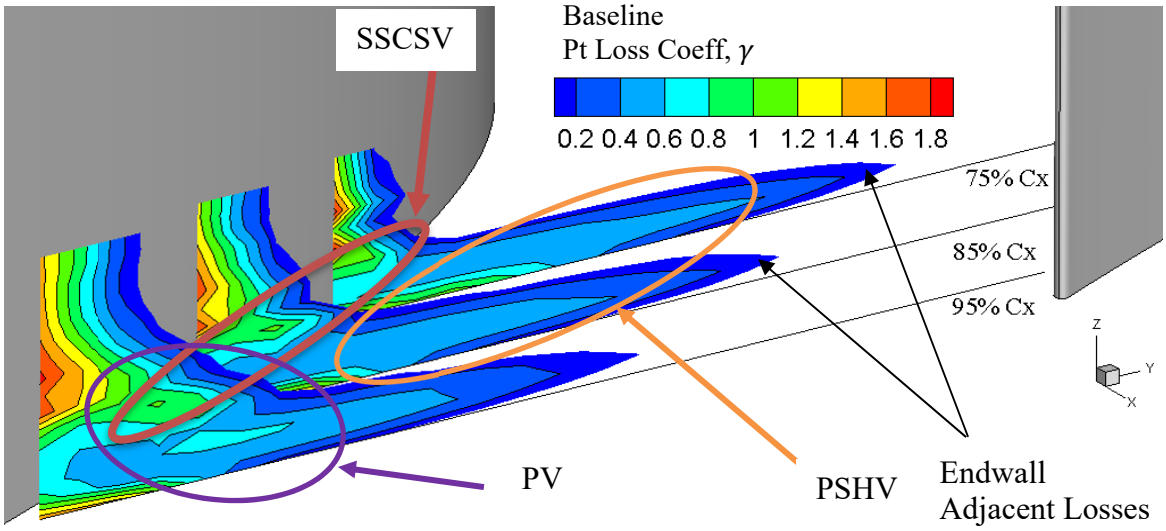

Figure 36. In-Passage Map of Baseline Total Pressure Loss Coefficient

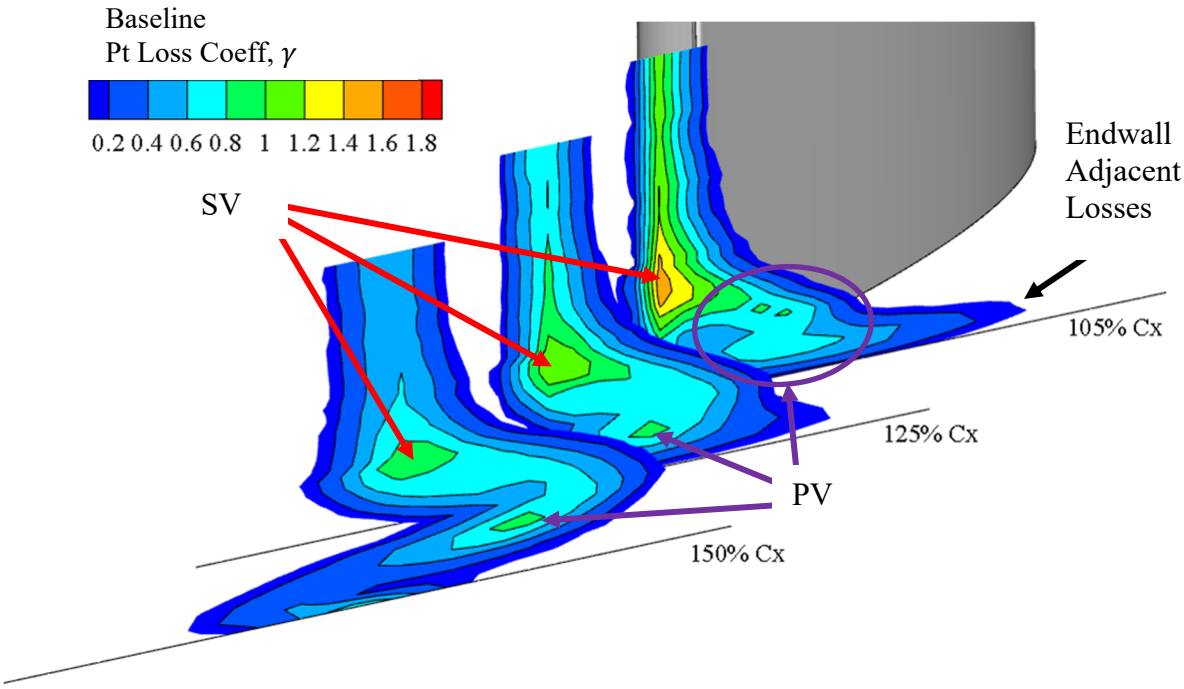

Figure 37. Out-of-Passage Map of Baseline Total Pressure Loss Coefficient

While the in-passage and out-of-passage figures can be useful, a total understanding of the flow is most often best obtained by displaying a Global 3-D perspective. As such, Figure 38 shows a sample 3-D perspective of the global maps that will be used to present each of the blowing cases for comparison. Table 8 shows the location and pressure loss coefficients of the vortices for the baseline case. Note the location and size of the PSHV as it moves from the 75% Cx plane to the 95% Cx plane where it interacts with the SSCSV and combines to form the PV in downstream planes. Also note how the loss along the endwall dissipates as the passage vortex lifts from the endwall in the later planes. Further, in the following figures the top of the profile will no longer be seen in order to focus on the loss structures. This method of presenting the data will be used throughout this section. In some rare cases though, the individual in-passage or out-of-passage plots will be used to show relevant features. Appendix B contains all of the individual plots for each active flow and baseline case as shown in Figure 34 and Figure 35. Appendix B also contains the separate in-passage and out-of-passage measurements for each case. This layout of the data allows for closer examination of the features.

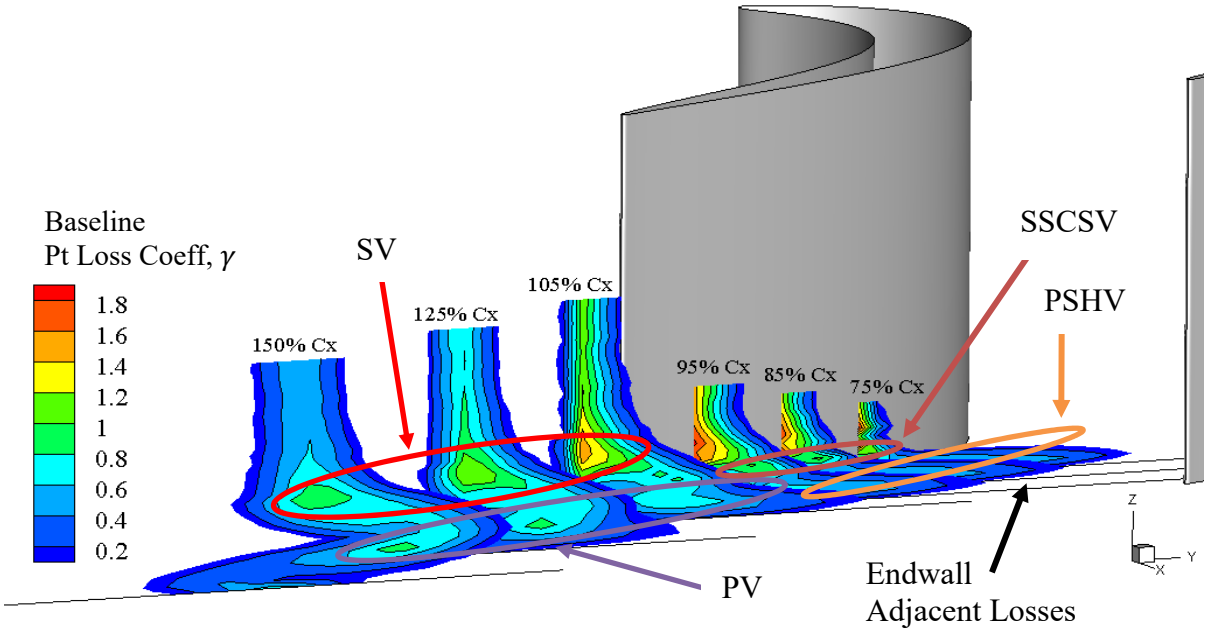

Figure 38. Global Map of Baseline Total Pressure Loss Coefficient

Table 8. Baseline Vortex Locations and Magnitudes

Measurement Plane	Shed Vortex (SV)			Suction Side Corner Separation Vortex (SSCSV)		
	y/S	z/H	Mag. (γ)	y/S	z/H	Mag. (γ)
75% Cx	--	--	--	-0.512	0.049	1.095
85% Cx	--	--	--	-0.613	0.060	0.978
95% Cx	--	--	--	-0.748	0.071	1.032
105% Cx	-0.968	0.131	1.486	-0.833	0.084	0.817
125% Cx	-0.643	0.141	1.156	--	--	--
150% Cx	-0.776	0.159	0.914	--	--	--

Measurement Plane	Pressure Side Horseshoe Vortex (PSHV)			Passage Vortex (PV)		
	y/S	z/H	Mag. (γ)	y/S	z/H	Mag. (γ)
75% Cx	-0.329	0.009	0.532	--	--	--
85% Cx	-0.515	0.016	0.522	--	--	--
95% Cx	-0.700	0.031	0.639	--	--	--
105% Cx	-0.819	0.033	0.740	--	--	--
125% Cx	--	--	--	-0.518	0.046	0.870
150% Cx	--	--	--	-0.629	0.063	0.867

While the presentation of the global maps is useful for displaying the movement of the loss features through and downstream of the passage. It can be helpful to use an area averaged loss measurement to compare loss in the similar regions of the flow. For the following figure styles, 150% plane has been used used to discuss and evaluate loss reduction further.

Figure 39 is a x-y plot of the pitchwise area-averaged loss coefficient, $\bar{\gamma}$, as defined in Equation (7), for the baseline condition. The dependent variable is plotted on the x-axis so the loss may be seen as a function of vertical location. Each data point in Figure 39 is the average loss, caluclated across the pitch, generated in that row of data. While the forgoing contour plots clairfiy trends, x-y plots ocassionaly yield better quantitative information.

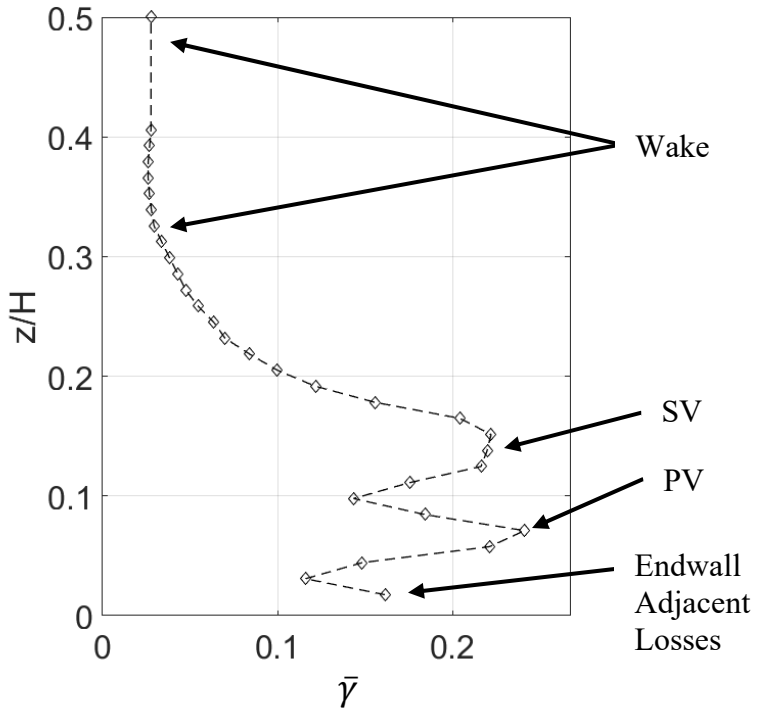

Figure 39. Baseline Pitchwise Area-Averaged Loss Coefficient

The loss features of importance have been labeled in Figure 39. The loss found above 30% span is related to the wake generated by the blade and is not studied in the present research. The shed vortex is shown by the upper loss region and the passage vortex is shown by the regions of high loss below the SV. The endwall adjacent losses are shown at the bottom of the plot. The combination of the mapped pressure loss coefficients and the area-averaged loss coefficients will allow for a detailed understanding of the effects of the endwall normal forcing of the pressure side leg of the horseshoe vortex.

The first forcing case to be studied is 22 Hz, chosen because the PV has been shown to oscillate naturally at or near that frequency. Recall that relevant forcing parameters can be seen in Table 3 in Section 3.2. However, some relevant parameters have been repeated

here for reference. Recall also, that these values are approximate averages and values with asterisks are for reference only and were not directly measured.

Table 9. Relevant Forcing Parameters

Forcing Case	F^{+}_{SSL}	BR	MR	C_{μ}
22 Hz	0.4	4.38	0.056	0.212
65 Hz	1.2	4.39	0.060	0.232
45.7 SLPM	--	2.19*	0.063*	0.134*
68.7 SLPM	--	3.48*	0.010*	0.344*

Figure 40 is a map of the global pressure loss for the 22 Hz blowing case as compared to the baseline case. Comparing the features in Figure 40 three noticeable differences are present. First, for the in-passage plots, note how the endwall adjacent loss has grown and now extends farther across the endwall. Second, in the 105% plane the PV has also decreased magnitude. Finally, the core magnitude of the passage vortex is smaller, by approximately 10% in maximum magnitude, in the 150% plane for the 22 Hz case but has remained in a similar location relative to, and a similar distance from, the shed vortex. The location of the vortices and their relative pressure loss coefficients, for the 150% Cx plane can be seen in Table 10. Also in Table 10 the separation of the major vertical structures is shown.

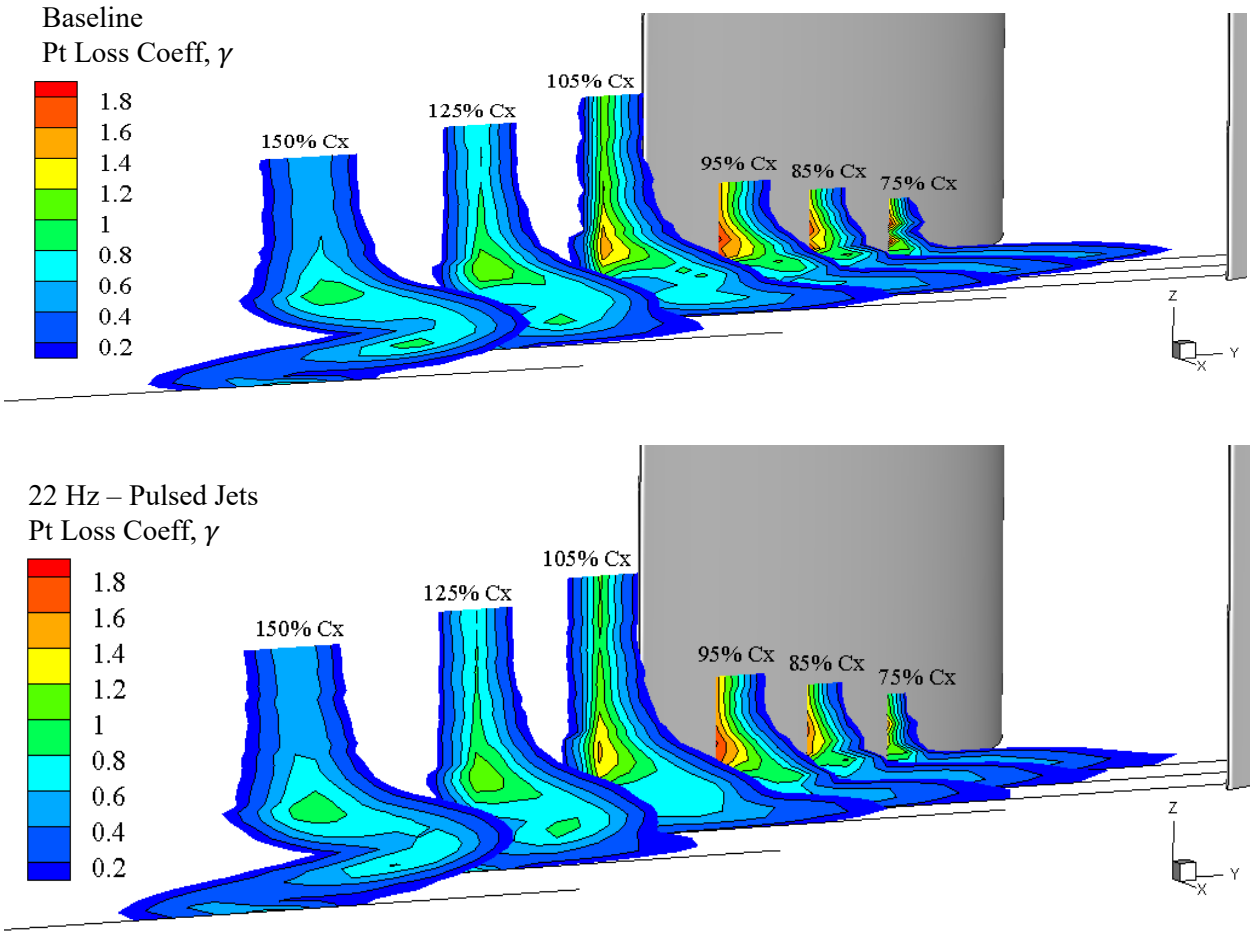

Figure 40. Global Map Comparison of Baseline (Top) and 22 Hz Pulsed Jets (Bottom) Total Pressure Loss Coefficient

Table 10. 150% Cx Vortex Location and Magnitude

Forcing Case	Shed Vortex			Passage Vortex			Vortex Separation		
	y/S	z/H	Mag. (γ)	y/S	z/H	Mag. (γ)	y/S	z/H	Total (mm)
Baseline	-0.775	0.159	0.912	-0.626	0.063	0.883	-0.148	0.096	67.134
22 Hz	-0.799	0.156	0.884	-0.658	0.063	0.794	-0.141	0.093	64.557
65 Hz	-0.798	0.152	0.895	-0.615	0.080	0.748	-0.182	0.072	56.891
45.7 SLPM	-0.778	0.157	0.920	-0.609	0.074	0.813	-0.169	0.082	61.050
68.7 SLPM	-0.785	0.152	0.906	-0.599	0.085	0.763	-0.186	0.067	54.677

Finally, Figure 41 is a comparison of the area-averaged loss coefficients of the baseline and 22 Hz forcing case. In Figure 41 the decrease in loss in the 22 Hz case in the region of the PV but the increase in loss along endwall can be seen more clearly. The combination of the loss reduction from the PV but the increase in loss along the endwall results in minimal overall loss reduction for the condition as a whole.

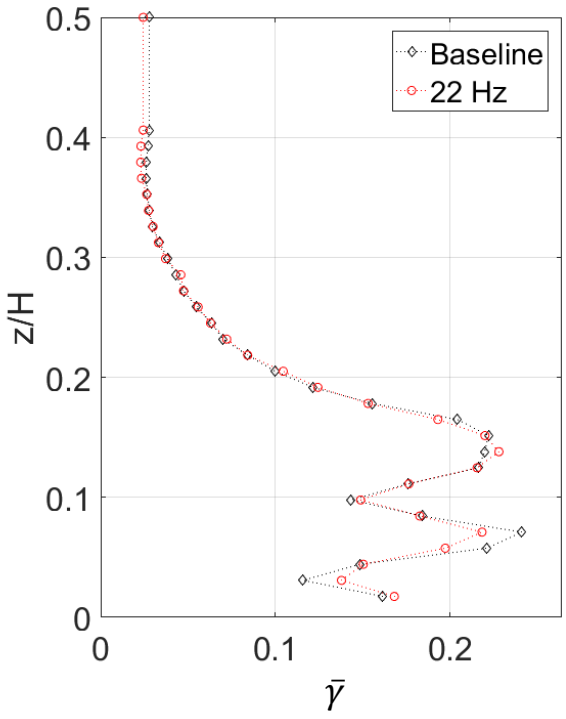

Figure 41. Baseline – 22 Hz Pitchwise Area-Averaged Loss Coefficient Comparison

The next case to be studied is the 65 Hz Pulsed Jet case. Recall that 65 Hz was chosen based upon previous research[17] that showed 65 Hz to be an optimum frequency where the effects of the forcing are most prominent on the PV. Recall relevant forcing parameters in Table 9. For the following discussions, only the global map of the case to be studied will be presented. Refer to the baseline condition in Figure 38 for comparisons.

Figure 42 is the global plot of the loss coefficient throughout the passage for the 65 Hz pulsed jet case. As with the 22 Hz case, note the strength of the PV. The reduced strength of the vortices can be followed from the 75% plane all the way to the 150% plane where the PV loss has reduced by over 15%. Also, the passage vortex has shifted off the endwall, a distance of approximately 2% span. Finally, the separation of the vortices has reduced by 15% as well. Refer to Table 10 for further quantitative values of the location and strength of the vertical structures of interest. The shift of position of the PV was important to this research. The shifted and weakened vortex results in less loss throughout the passage. However, noting the in passage planes, there is a large section of endwall adjacent losses that span across the passage that was not present in the baseline or 22 Hz case.

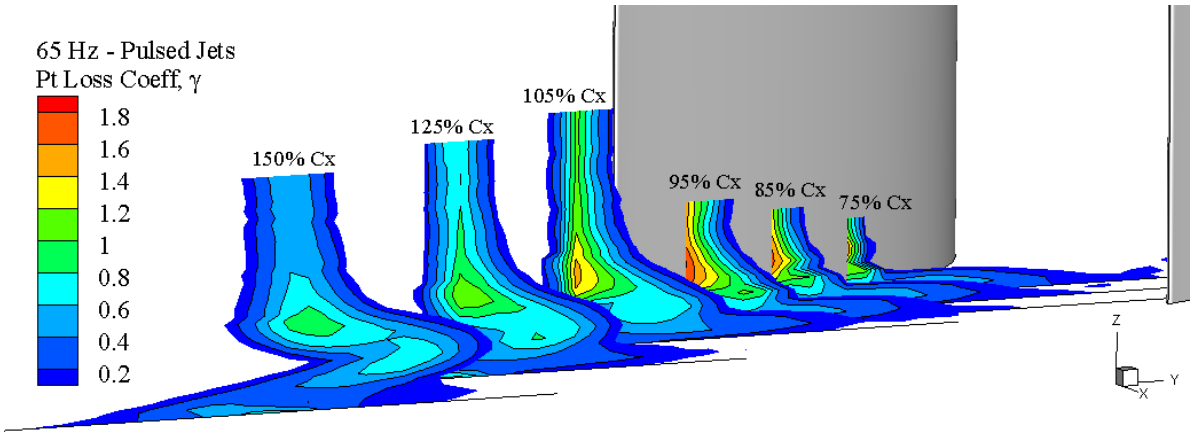

Figure 42. Global Map of 65 Hz Pulsed Jets Total Pressure Loss Coefficient

Figure 43 is the in-passage planes for this forcing case. This loss generation counteracts the loss reduction produced by the weakening and shifting of the passage vortex and results in the overall loss reduction of the 65 Hz case, as compared to the baseline, to be 2.2%.

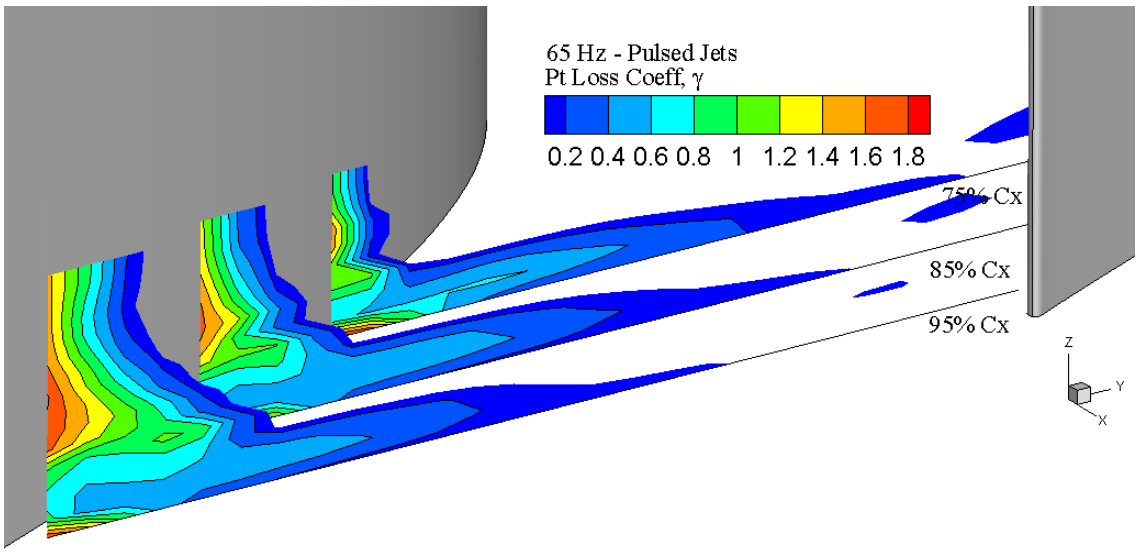

Figure 43. In-Passage Map of 65 Hz Pulsed Jets Total Pressure Loss Coefficient

Further, Figure 44 shows the area averaged loss of the 65 Hz case compared to the baseline to further demonstrate the effects of the pulsed frequency on the strength of the passage vortex. The reduction of the loss generated by the passage vortex, the lack of change in the wake region and the shed vortex and the increase in loss in the endwall region of the flow are again seen here.

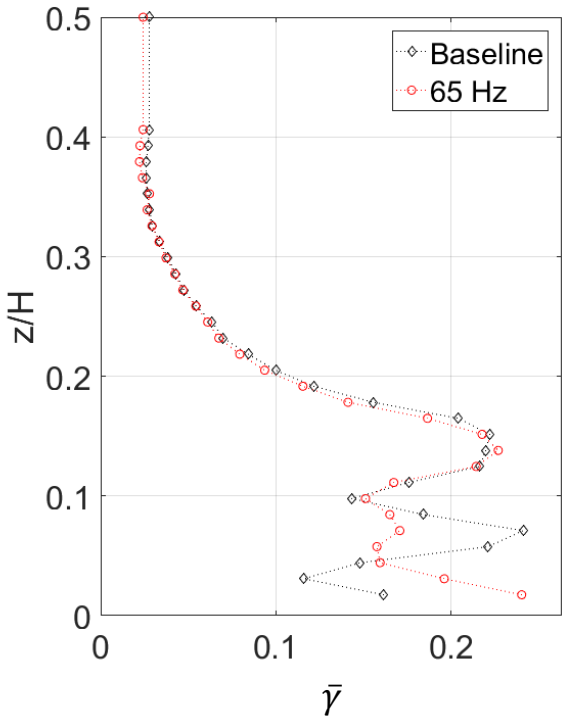

Figure 44. Baseline – 65 Hz Pitchwise Area-Averaged Loss Coefficient Comparison

Moving to the steady blowing cases, the first steady case to be investigated is the 45.7 SLPM case. 45.7 SLPM was chosen because it closely represents the average mass flow measured throughout initial testing the 65 Hz cases. For other forcing parameters, see Table 9. Figure 45 is the global map of the loss coefficient for the 45.7 SLPM steady jet case. In Figure 45 loss generation can be seen along the endwall throughout the passage. This loss is greater than the loss present in the 22 Hz case but less than that in the 65 Hz case. The steady jets in this case had a similar effect of the 22 Hz case reducing the strength of the PV by 7.9% and shifting the PV off the endwall by 1.2% span. For additional vortex information refer to Table 10. As a result of this weakening of the PV, coupled with the increase in endwall adjacent loss, an overall reduction of passage loss of 0.3% was realized.

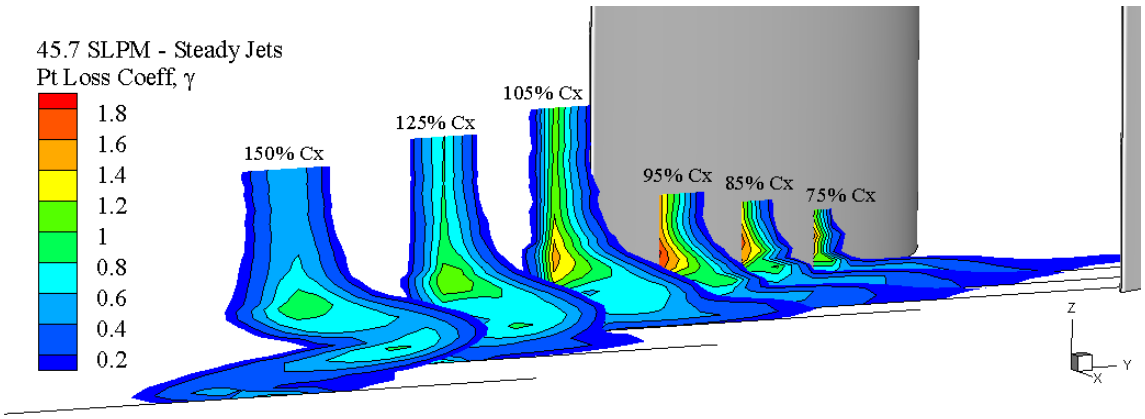

Figure 45. Global Map of 45.7 SLPM Steady Jets Total Pressure Loss Coefficient

Figure 46 is the area-averaged loss comparison for 45.7 SLPM steady case. Figure 46 shows the loss reduction generated in the region of the PV in the outer planes but also shows the increased loss in the region near the endwall in the passage.

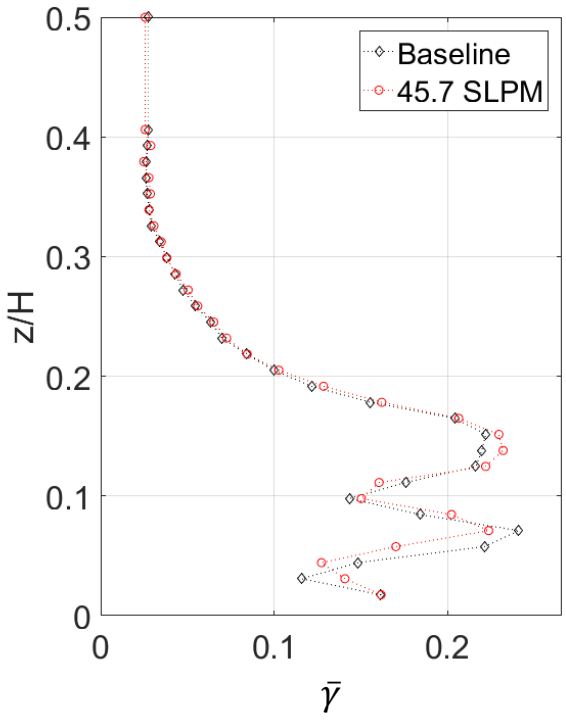

Figure 46. Baseline – 45.7 SLPM Pitchwise Area-Averaged Loss Coefficient Comparison

The final case to be investigated is the 68.7 SLPM steady jet case. 68.7 SLPM was chosen because the mass flow is 50% greater than the 45.7 SLPM case, further forcing conditions can be seen in Table 9. A 50% increase was selected to ensure a sizeable difference could be measured between the two steady cases.

Figure 47 is the global map of the 68.7 SLPM steady jet case. In Figure 47 several features can be distinguished. First and foremost the PV in the 150% plane has significantly reduced in magnitude. This reduction in magnitude is approximately 13.5%. The location of the PV has also changed significantly with a separation reduction of the vortices of 18.6%. The PV is now farther from the endwall, 2.3 % higher than the baseline case, and

has also shifted towards the SV. The reader is referred to Table 10 for further details regarding the location of the vortices. Finally, it is important to note the large losses generated along the endwall. These losses are no longer contained within the passages as with previous cases but now can be seen traveling all the way to the 150% plane. The generation of this loss, coupled with the loss reduction realized by the weakening and shifting of the PV produces a net pressure loss reduction of 1.8% for the 68.7 SLPM forcing case.

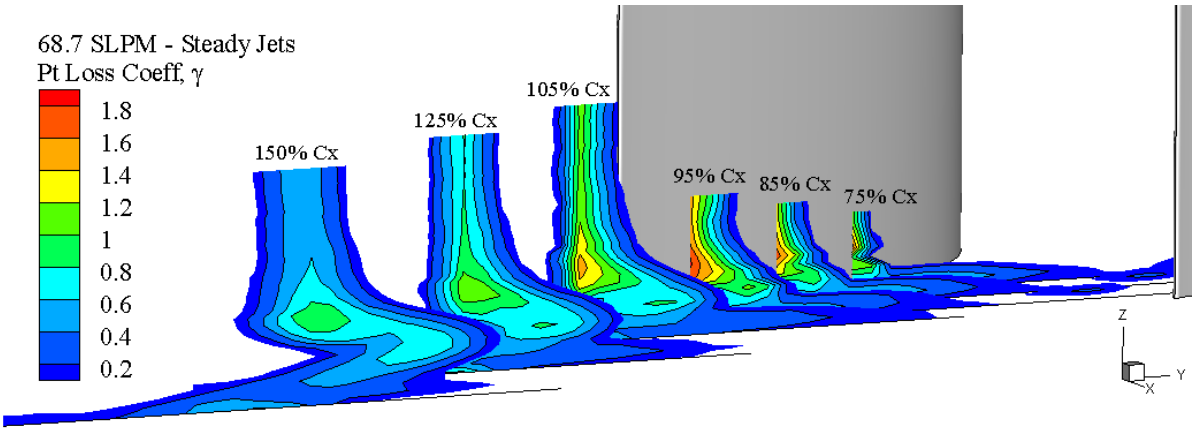

Figure 47. Global Map of 68.7 SLPM Steady Jets Total Pressure Loss Coefficient

Figure 48 is a comparison of the area-averaged losses of the 68.7 SLPM steady case compared to the baseline condition. As with the previous cases, note the loss reduction in the region associated with the PV, the minimal change in the wake and SV region and the loss generation in the endwall region.

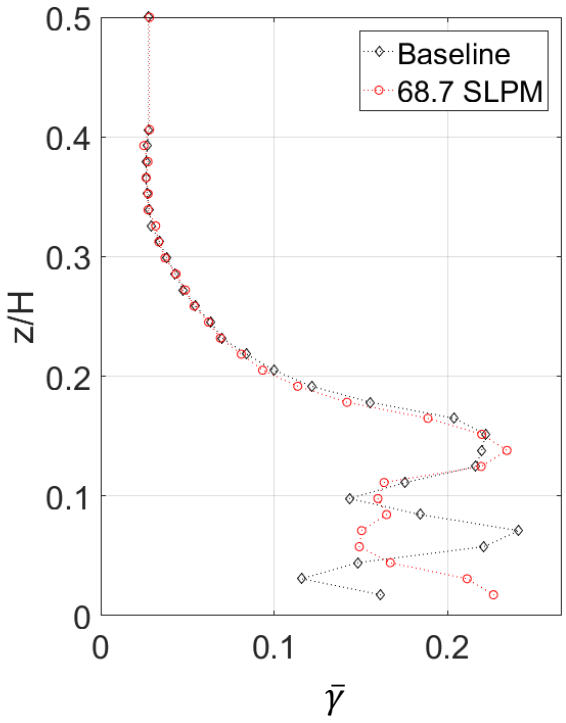

Figure 48. Baseline – 68.7 SLPM Pitchwise Steady Jet Area-Averaged Loss Coefficient Comparison

To begin concluding this section, and compare the effectiveness of each forcing condition, Figure 49 is each area-averaged loss plotted for comparison to one another. For an individual comparison of one case another see Appendix B. Using Figure 49 several comparisons between forcing cases can be made. First, compare the effectiveness of the reduction in strength of the passage vortex for each case. Figure 49 clearly shows how the passage vortex is more effectively reduced in strength by the 65 Hz pulsed case as compared to the 22 Hz pulsed case. The same can be said for the 68.7 SLPM steady case and the 45.7 steady case as well. The greatest loss reduction for the PV can be seen using the 68.7 SLPM case followed closely by the 65 Hz case. The 45.7 SLPM case was

least effective reducing the loss associated to the PV. Second, endwall adjacent loss generation is greatest in the 65 Hz case followed by the 68.7 SLPM case. The 45.7 SLPM case had the least endwall adjacent loss generation compared to the baseline.

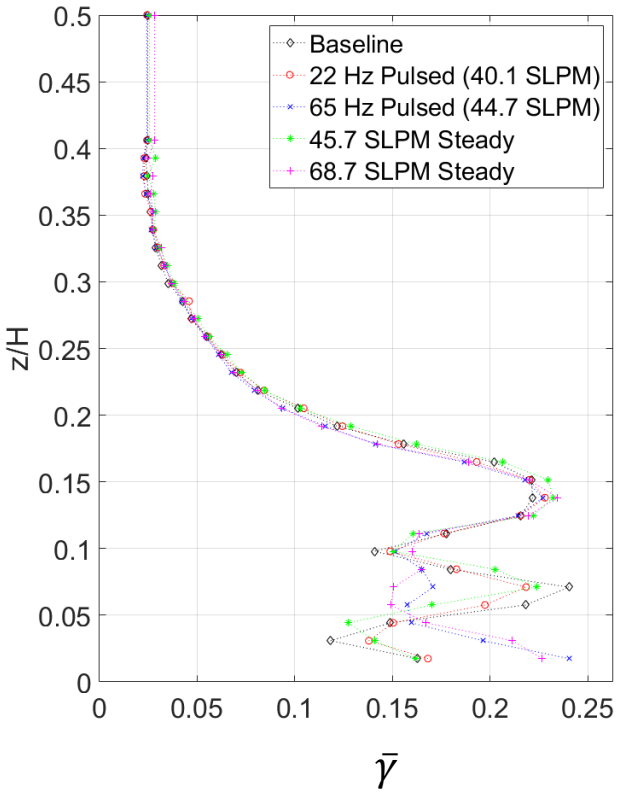

Figure 49. Area-Averaged Loss Coefficient Comparison

For further comparison of the active flow control effects on the PV Figure 50 is presented. Figure 50 is a pictorial representation of the location of the PV and SV for each forcing case. Note how the application of the active forcing caused a lifting of the PV off from the endwall. Also see how the SV location is minimally effected by the forcing cases. It can be said that the location of the PV relative to the endwall appears to play a role in loss generation. To this end, Figure 51 is a plot of the loss generated vs the

height of the PV off from the endwall. Figure 51 further reinforces the apparent correlation of loss reduction and PV height from the endwall in the 150% Cx plane.

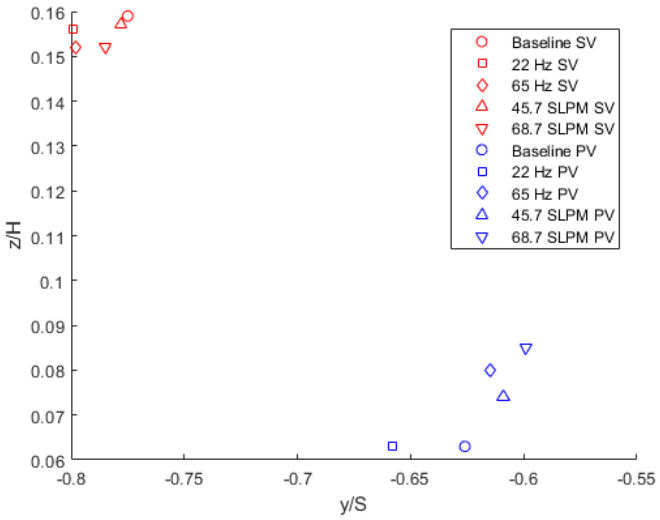

Figure 50. Vortex Locations in the 150% Cx Plane

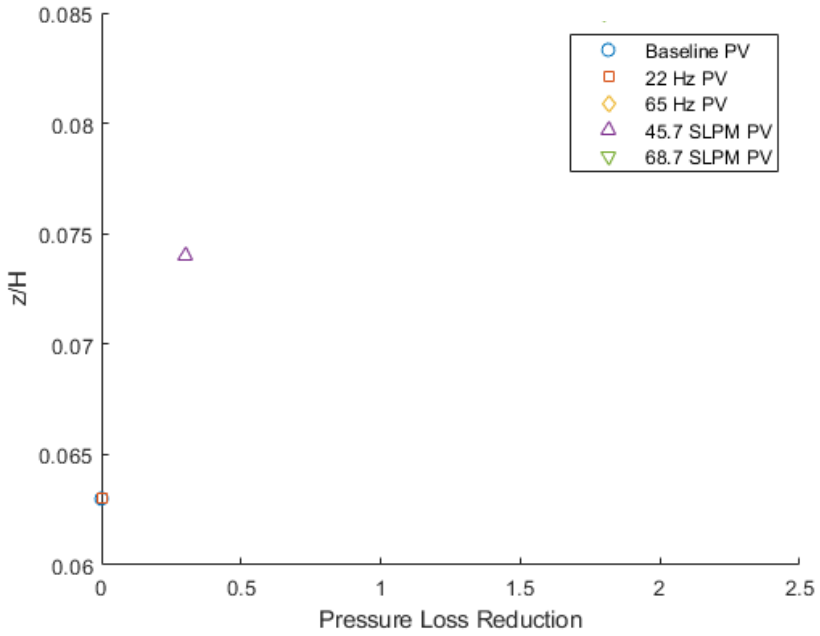

Figure 51. Loss Reduction v. PV Height from Endwall

As mentioned previously, the reduction in loss throughout the passage appears to be a function of the separation of the PV and SV. Figure 52 is a representation of this relation. Notice how as the separation of the PV and SV reduces, the loss associated with the magnitude of the pressure loss coefficient of the passage vortex also reduces implying that the separation of the vortical structures can play a part in loss generation associated with the PV.

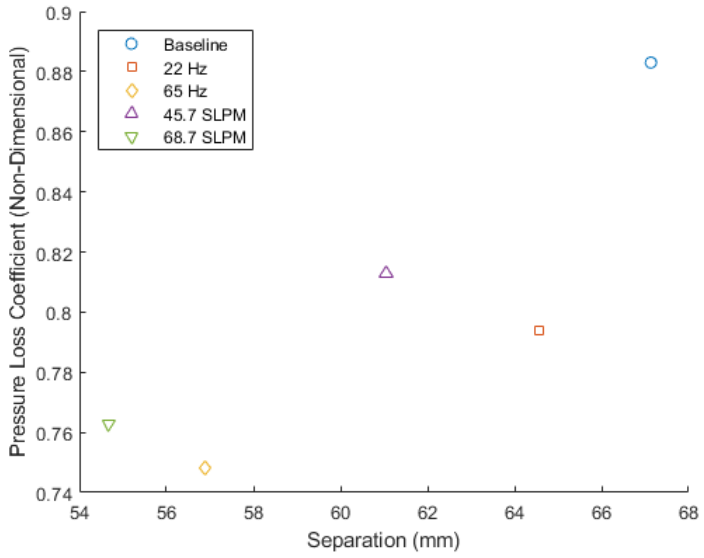

Figure 52. PV and SV Separation v. PV Pressure Loss Coefficient Magnitude

As a final overall comparison of the loss reduction and the cost, as measured by overall mass flow, associated with each case, Table 11 is presented. As a summary from Table 11, the most effective case for reducing the loss was the 65 Hz case followed closely by the 68.7 SLPM steady case, the 45.7 SLPM case showed the next highest reduction in loss and the 22 Hz case showed no reduction. However, the 68.7 SLPM case required the greatest mass flow to achieve the resultant loss reduction compared to the 65 Hz case. The conclusion that the approximate tripling of the natural frequency of PSHV oscillation

produces greater loss reduction concurs with previous work[17]. For comparison of effectiveness, recall from Section 2.3.1.2 that the passive flow control method of profile filleting produced a loss reduction from 3.2% to 5.2% for similar flow conditions.

Table 11. Summary of Forcing Cases, Computed in 150% Cx Plane

Forcing Case	Loss Reduction (%)	Required Mass Flow (SLPM)
22 Hz	0.0	40.1
65 Hz	2.2	44.7
45.7 SLPM	0.3	45.7
68.7 SLPM	1.8	68.7

4.3 - Discussion of Streamwise Vorticity Derivation and ILES Application

In order to further show the location and strength of the vortical endwall structures, stereoscopic particle image velocimetry has been conducted on the three in-passage planes where total pressure loss measurements had been initially taken. These measurements were compared to a previously performed Implicit Large Eddy Simulation solution. The ILES solution was conducted and described by Gross et al[58]. The simulation was performed at 100,000 Reynolds number and was modeled as near to the experimental conditions present in the LSWT facility as possible. Two simplifications of note included in the code are negligible surface roughness and no incoming turbulence intensity. While this does not allow for a direct vis-a-vis comparison of the ILES data to experimentally calculated data the error resulting from this simplification should be minimal. Refer to Gross[58] for further details regarding the ILES solution set up.

Figure 53 shows the X-velocity component compared to the ILES X-velocity. Figure 54 shows the Y-velocity component compared to the ILES Y-velocity. Finally, Figure 55 shows SPIV collected Z-velocity. The three collected SPIV velocity components are for the baseline 85% Cx plane as are the corresponding ILES simulation results. Figure 53, Figure 54, and Figure 55 all present similar velocity shapes and magnitudes within approximately 15% of the ILES solution. The ILES solution extends much higher in the spanwise direction than the SPIV data due to limitations of the SPIV system.

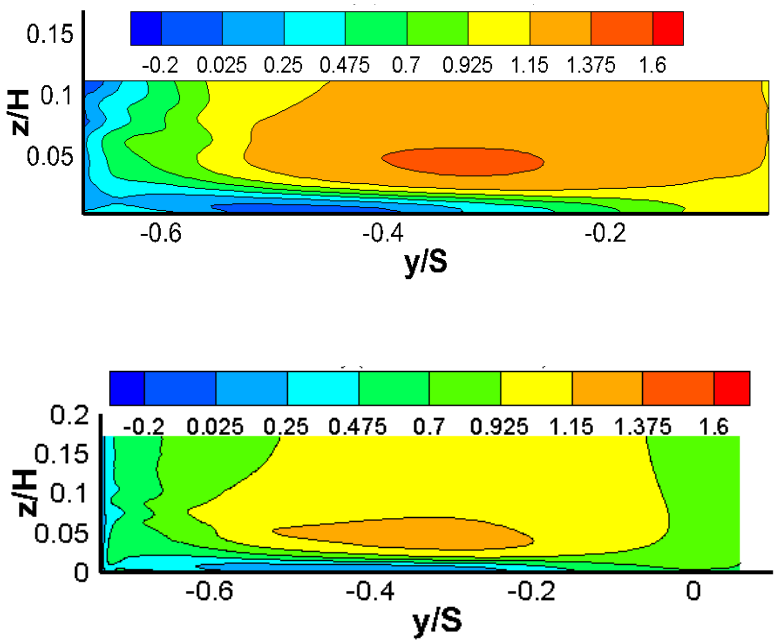

Figure 53. 85% Cx Non-Dimensional X-Velocity Comparison: SPIV (top), ILES (bottom)

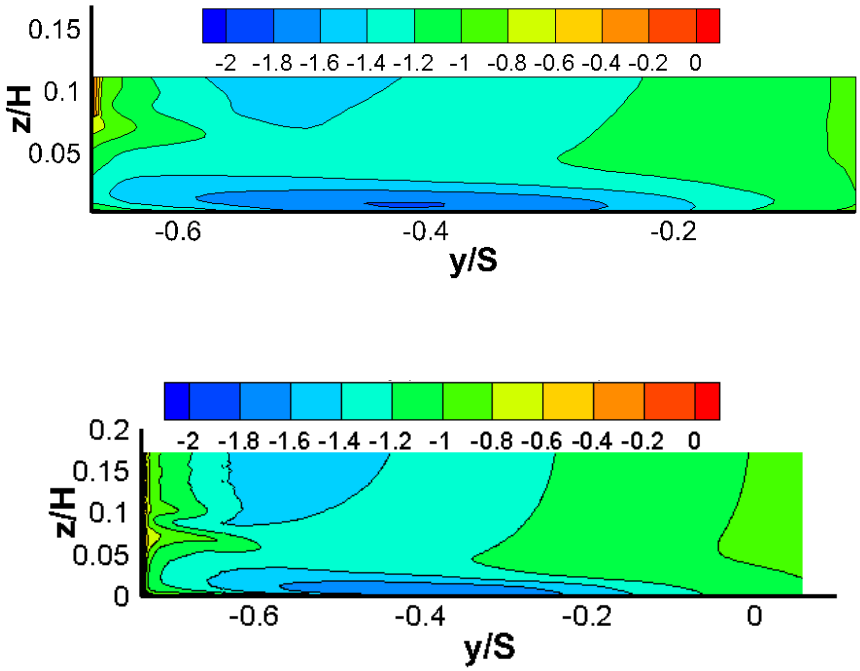

Figure 54. 85% Cx Non-Dimensional Y-Velocity Comparison: SPIV (top), ILES (bottom)

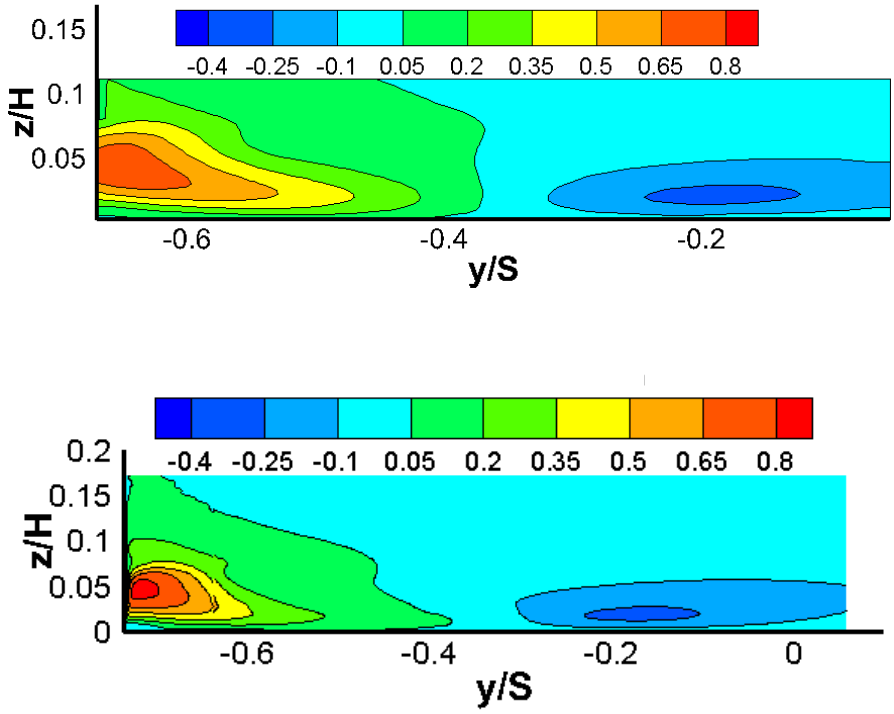

Figure 55. 85% Cx Non-Dimensional Z-Velocity Comparison: SPIV (top), ILES (bottom)

The collection of these three velocity components allows for the direct calculation of x-vorticity. Figure 56 is a comparison of the SPIV and ILES x-vorticity from the 85% plane. However, this x-vorticity misrepresents the shape of the vorticies due to the deviation of the flow direction compared to the measurement plane. To this end, an initial discussion must be made regarding the presentation of the SPIV data in the following section.

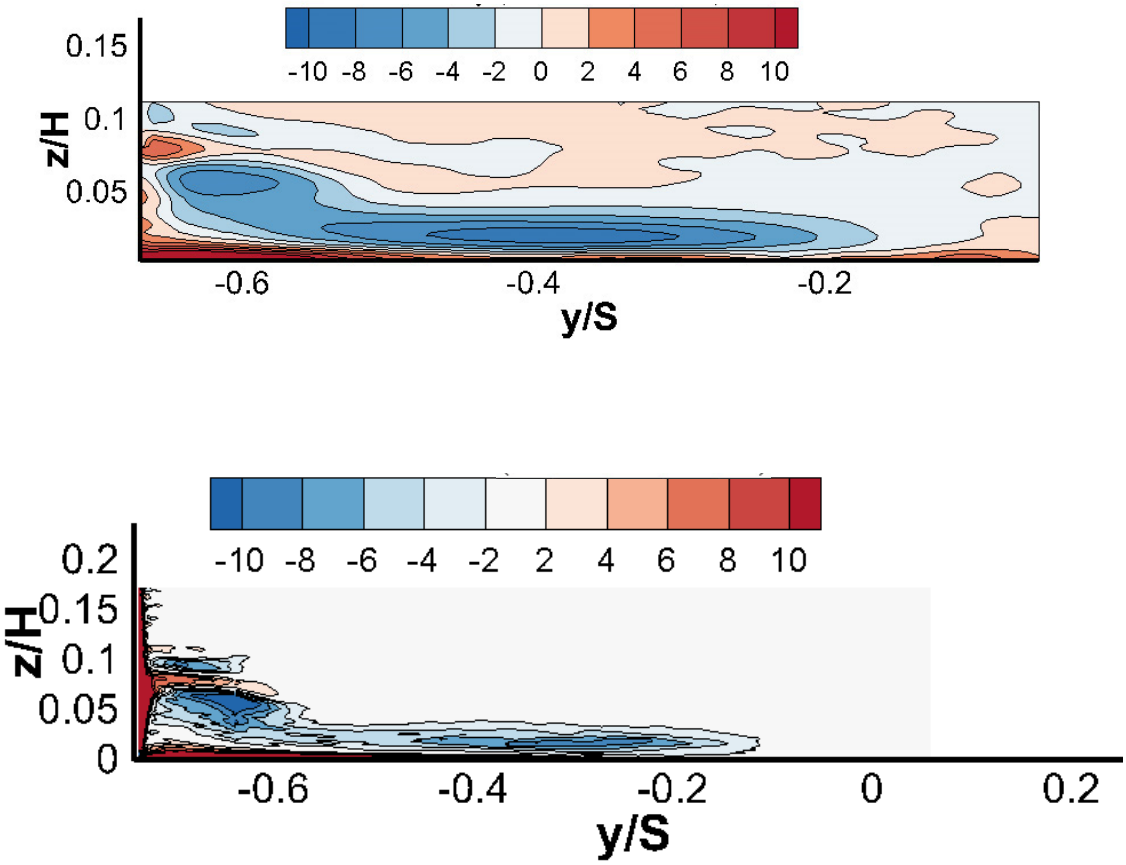

Figure 56: 85% Cx Non-Dimensional X-Vorticity Comparison: SPIV (top), ILES (bottom)

To begin, Figure 57 is a simplified schematic of a sample plane in which the velocity data has been collected. In Figure 57 it can be seen how the streamwise flow is not normal to the measurement plane but rather exits at the angle, α, which is approximately 58°. This flow angle is caused by the turning of the turbine blades. Because the flow exits at an angle non-normal to the measurement plane, chosen based upon previous research[15], [21], [22] and tunnel limitations, the calculation of vorticity in the streamwise, or secondary, direction is difficult to accomplish.

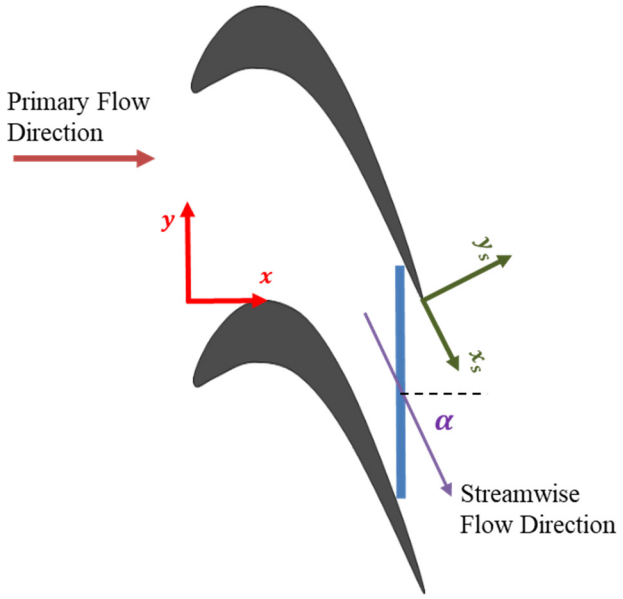

Figure 57. Simplified Streamwise Vorticity

However, calculation of vorticity in the primary, or x, direction is directly achievable from the SPIV data. Secondary flow theory states that secondary vorticity can be calculated using the Equation (14)[68].

$$\omega_{x_s} = \omega_x \cos\alpha + \omega_y \sin\alpha \qquad \textbf{(14)}$$

where α is the primary turning angle for the flow of interest. The difficulty with using this equation is finding the component vorticity in the *y*-direction. The calculation of this y-component has been presented in literature for some transonic flow conditions[68]–[70]. The equations presented by Perdichizzi[69], and later Taremi[70], require the use of the speed of sound and a natural log of a total pressure term to calculate the the y-vorticty. Gregory-Smith[68] conversely, presents a much simpler version for finding the y-vorticity

based on a simplified Helmholtz Equation. The Equation presented is shown here as Equation (15)

$$u\omega_y - v\omega_x = \left[\frac{1}{\rho}\frac{\partial p_o}{\partial z}\right] \quad \textbf{(15)}$$

where u and v are the flow velocity in the x and y direction respectively.

Solving for y-vorticity yields Equation 16.

$$\omega_y = \frac{1}{u}\left[\frac{1}{\rho}\frac{\partial p_o}{\partial z} + v\omega_x\right] \quad \textbf{(16)}$$

Gregory-Smith cites the incompressible Helmholtz equation as the starting point for the derivation of Equation (16). However, the author has derived a similar equation starting with the *Gromeka-Lamb* form of the Navier-Stokes equations presented in the textbook by Granger[71] shown in Equation 17.

$$\frac{\partial \boldsymbol{V}}{\partial t} + \boldsymbol{\omega} \times \boldsymbol{V} = \boldsymbol{g} - \boldsymbol{\nabla}\left(\frac{p}{\rho} + \frac{V^2}{2}\right) - \nu(\boldsymbol{\nabla} \times \boldsymbol{\omega}) \quad \textbf{(17)}$$

where **g** is the gravity vector, and ν is the dynamic viscosity. The entire derivation can be seen in Appendix C but only the critical components will be highlighted in the subsequent discussion.

Initial assumptions of steady, incompressible and inviscid flow with a negligible effect of gravity were made to simplify the *Gromeka-Lamb* to:

$$\boldsymbol{\omega} \times \boldsymbol{V} = -\frac{1}{\rho}\nabla\left(p + \rho\frac{V^2}{2}\right) \quad \textbf{(18)}$$

Using the definition of total pressure Equation 18 simples to:

$$\boldsymbol{V} \times \boldsymbol{\omega} = \frac{1}{\rho}\nabla p_o \quad \textbf{(19)}$$

Investigating only the z-component of velocity following the expansion of the left hand side of the equation and application of the gradient yields the Helmholtz equation presented in Gregory-Smith.

$$u\omega_y - v\omega_x = \frac{1}{\rho}\frac{\partial p_o}{\partial z}$$

However, taking a separate approach yields an interesting result. Following the application of the previous assumptions Equation 17 can also be written as

$$\boldsymbol{V} \times \boldsymbol{\omega} = \nabla\left(\frac{p}{\rho} + \frac{V^2}{2}\right) \quad \textbf{(20)}$$

Appling the definition of the speed of sound, the perfect gas law and a gradient identity, Equation (20) becomes

$$\boldsymbol{V} \times \boldsymbol{\omega} = \nabla\left(\frac{a^2}{\gamma}\right) + \nabla\left(\frac{V^2}{2}\right) \quad \textbf{(21)}$$

The use of the definition of total enthalpy yields

$$\nabla h = \nabla h_o - \nabla\left(\frac{V^2}{2}\right) = \nabla(c_p T) \quad \textbf{(22)}$$

Again using the speed of sound, the definition of total enthalpy and combining equations it can be shown that

$$\nabla\left(\frac{c_p a^2}{\gamma R}\right) = -\nabla\left(\frac{V^2}{2}\right) \quad \textbf{(23)}$$

Using Equation (23), Equation (21) becomes

$$\boldsymbol{V} \times \boldsymbol{\omega} = \nabla\left(\frac{a^2}{\gamma}\right) + \nabla\left(-\frac{c_p a^2}{\gamma R}\right) \quad \textbf{(24)}$$

The definition of $c_p = \frac{\gamma R}{\gamma - 1}$ gives

$$\boldsymbol{V} \times \boldsymbol{\omega} = \nabla\left(\frac{a^2}{\gamma}\right) - \nabla\left(\frac{\gamma R a^2}{\gamma R(\gamma - 1)}\right) \quad \textbf{(25)}$$

Canceling terms and recombining the RHS produces

$$\boldsymbol{V} \times \boldsymbol{\omega} = \nabla\left(\frac{-a^2}{\gamma(\gamma - 1)}\right) \quad \textbf{(26)}$$

Focusing only on the z-component again and expanding the LHS yields

$$u\omega_y - v\omega_x = \frac{\partial}{\partial \mathrm{z}}\left(\frac{-a^2}{\gamma(\gamma - 1)}\right) \quad \textbf{(27)}$$

And, taking the speed of sound and ratio of specific heats as constant it can be shown that y-vorticity can be described by Equation (28).

$$\omega_y = \frac{v}{u}\omega_x \quad \textbf{(28)}$$

This equation only applies in areas where the flow can be assumed steady, incompressible and inviscid. But these assumptions will allow for the presentation of the streamwise vorticity in the SPIV measurement planes. In order to validate the accuracy and applicability of the previous derivation the previously discussed ILES solution will be used again.

Figure 58 though Figure 61 allow for a comparison of vorticities calculated in the 85% plane. Appendix D contains the figures for the 75% and 95% plane for additional reference. In the following figures in this section where the L2F profile is shown, the height of the solution is approximately 18% span, or z/H = 0.18.

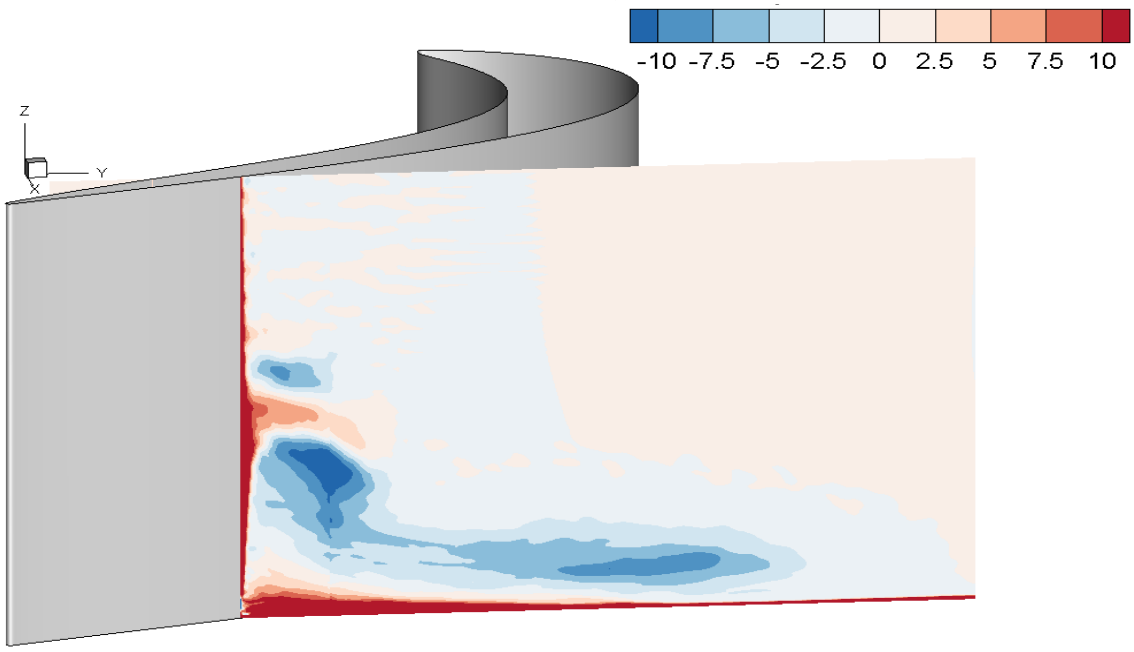

Figure 58. Actual Non-Dimensional Vorticity x-Direction, 85% Cx

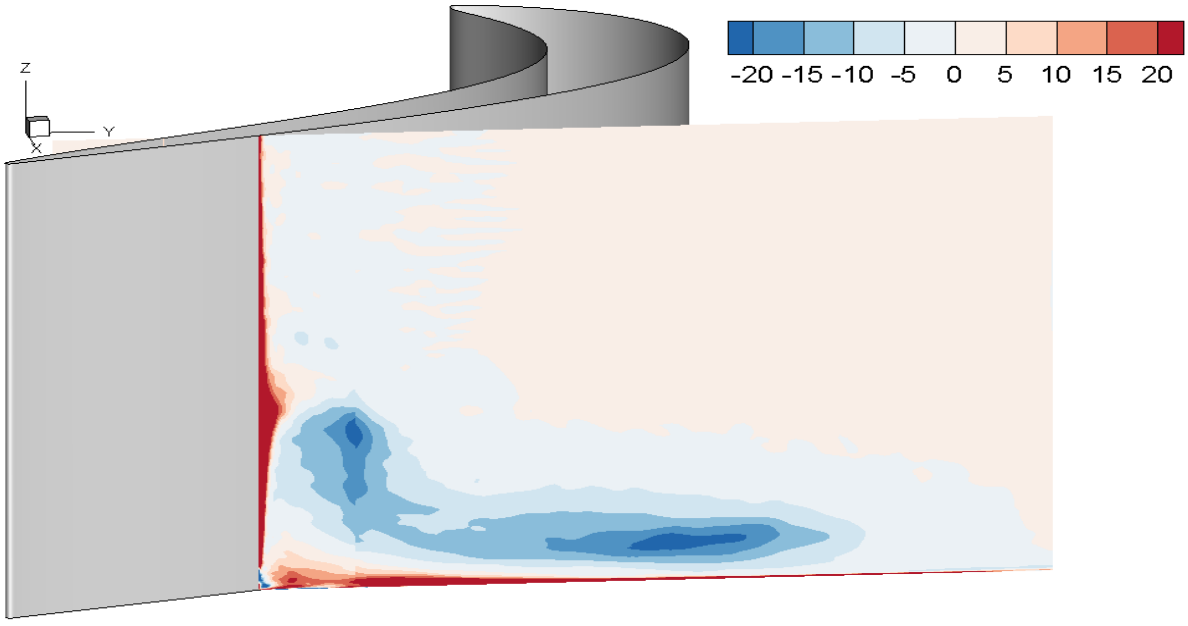

Figure 59. Actual Non-Dimensional Vorticity Secondary Direction, 85% Cx

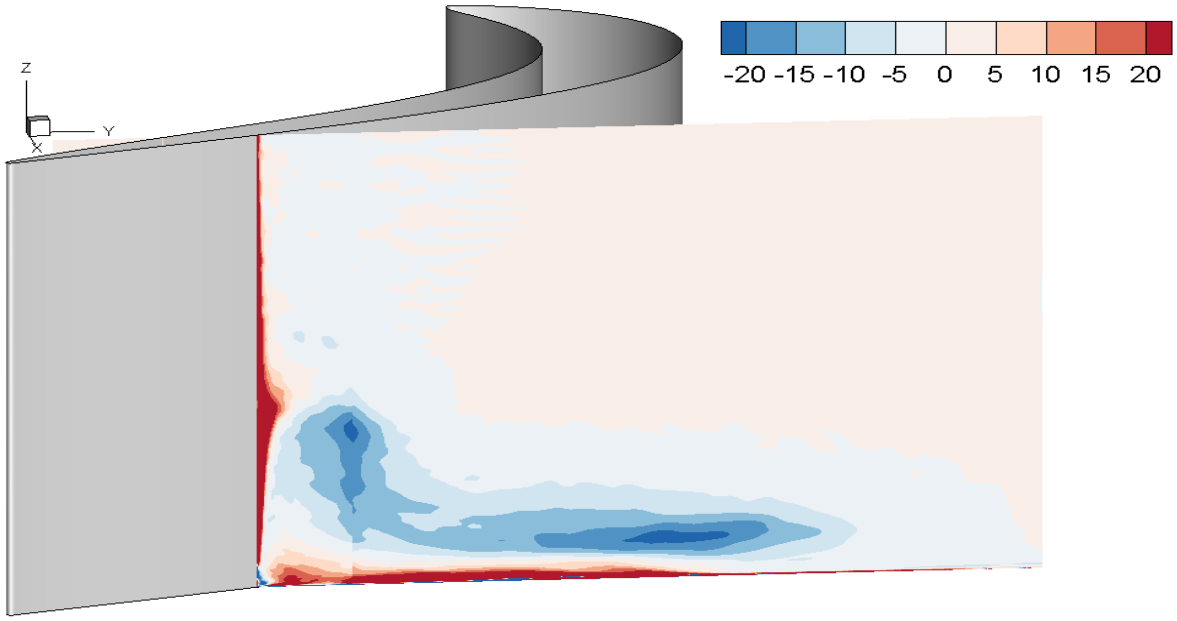

Figure 60. Direct Helmholtz Non-Dimensional Vorticity Secondary Direction, 85% Cx

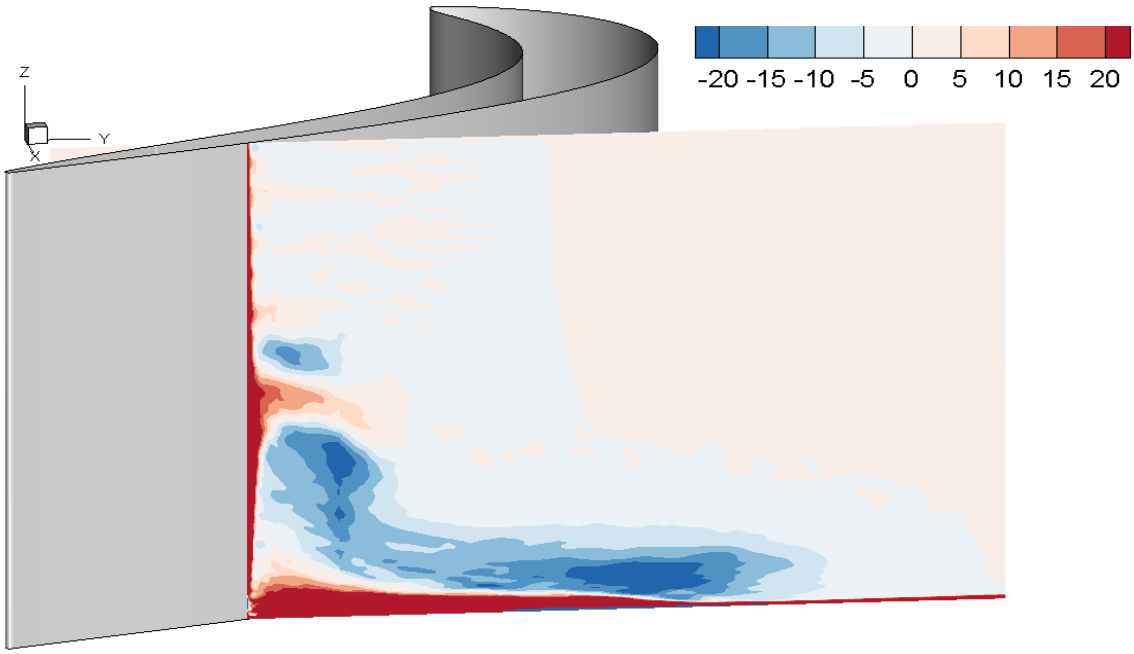

Figure 61. Simplified Helmholtz Non-Dimensional Vorticity Secondary Direction, 85% Cx

Comparison will start with Figure 58, which gives the plot of vorticity that is directly calculated from the ILES solution normal to the measurement plane. This vorticity is the same as what would be calculated directly from the SPIV data. These vorticity maps have been non-dimensionalized by dividing by the incoming velocity and multiplying by the axial chord length. The SPIV data will be non-demisionalized in a similar fashion. Note how the vorticity along the surface of the blade is oblong. The suction side corner separation vortex is what is shown along the blade of the figure, the endwall region shows the development of the pressure side leg of the horseshoe vortex. This optical phenomenon exists because of the angle at which the SSCSV is cut. If one is to consider the vortex as a cylinder, a non-normal cross section will appear as an oval when projected along the plane as opposed to the true circular area of a normal cross section. See Figure 62 for further clarification. The right hand cross section is the true secondary vorticity and the left hand cross section is a non-normal slice through the same cylinder. Ideally, the presentation of the true vorticity is desired as compared to one that is skewed based upon the measurement plane. A final point on Figure 58 is the magnitude of the vorticity and how the scale is half of that of the other figures. This difference in scale was chosen so that the underlying features may be seen.

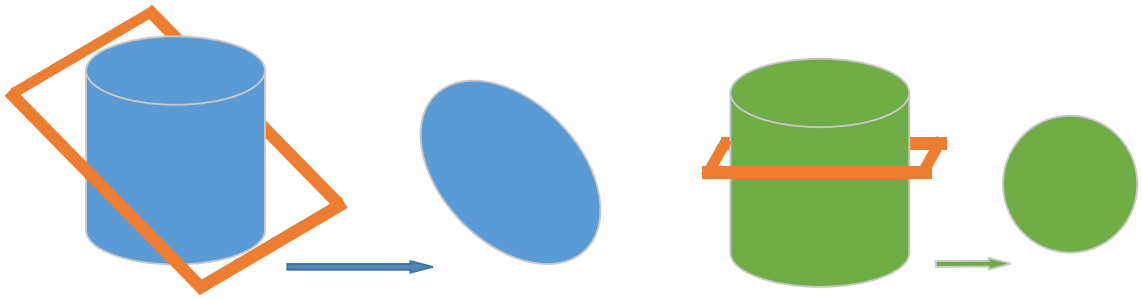

Figure 62. Non-Normal Slice of a Cylinder

Figure 59 is the plot of the true secondary vorticity, calculated directly from the ILES. Ideally this figure is what is desired to be presented, however, as previously discussed the calculation of this vorticity from experimental data is quite challenging. Note the circular shape of the SSCSV in this figure as opposed to the x-vorticity previously plotted and also how the magnitude of this vorticity is plotted as a double the magnitude as the x-direction plot.

Figure 60 is the secondary vorticity as calculated from finding the y-vorticity as presented by the relation using the Helmholtz equation provided by Gregory-Smith. Recall that this calculation requires the gradient in the z-direction of the total pressure but makes the assumptions of steady, inviscid, incompressible flow with a negligible gravity influence. Notice the circular shape of the SSCSV in this figure. The magnitudes of the Helmholtz calculation are quite similar to the true secondary vorticity previously calculated. It can be seen, how closely the assumption matches the true secondary vorticity. The devotions primarily occur in regions where the change in loss is the greatest. These regions are dominated by shear stresses which are caused by viscous forces. As such, when neglecting viscosity the Helmholtz assumption breaks down. Nonetheless, the usefulness of the Helmholtz calculation is evident.

Finally, Figure 61 is a plot of the simplified Helmholtz solution as presented here. This simplified solution calculates y-vorticity by scaling the x-vorticity by a ratio of the velocity components. Note how the general shape of the secondary vorticity plots calculated using this relation relates closely to the true vorticity plotted earlier. The relative magnitudes of the vorticities are also similar. It is worth noting the clear deviation along the endwall and above the SSCSV. Also the differences in regions of high viscous forces and locations where the total pressure changes are substantial. This calculation assumes that the total pressure does not change in the z direction. This assumption is likely the cause of some of the difference shown here

In an ideal scenario total pressure loss plots would be used in conjunction with the direct Helmholtz equation, but if total pressure measurements are unobtainable, or curve fits of the plots prove to be too computationally intensive, the simplified solution can be used to plot secondary vorticity. A plot of a simplified secondary vorticity, in place of direct x-vorticity produces maps of vorticity with values that are nearer in magnitude to the true secondary vorticity than merely the x-vorticity. Also, the simplified secondary vorticity provides a shape nearer to the actual vorticity as compared to the x-vorticity.

4.4 - Results of Average SPIV Data

In order to describe the use of vorticity as an acceptable means of locating the vortical structures found within the passage, Figure 63 is used as a reference. Figure 63 is a plot of the baseline x-direction vorticity and non-dimensional secondary velocity vectors in each measurement plane. The secondary velocity vectors were calculated using Equation (29) as presented by Marks et al [21].

$$V_s = u\cos\alpha + v\sin\alpha \quad \textbf{(29)}$$

Where V_s is the secondary velocity, u is the streamwise component of velocity, v is the pitchwise component of velocity and α is gas exit angle. The calculation of the secondary velocity allows for a clear presentation of the direction of the fluid rotation and helps alleviate some of the previously discussed viewing angle projection issues. The key features of each plane have been labeled to further discussion in the following section. The regions of positive vorticity are due to separation along the surface of the L2F profile and are not the focus of the present study.

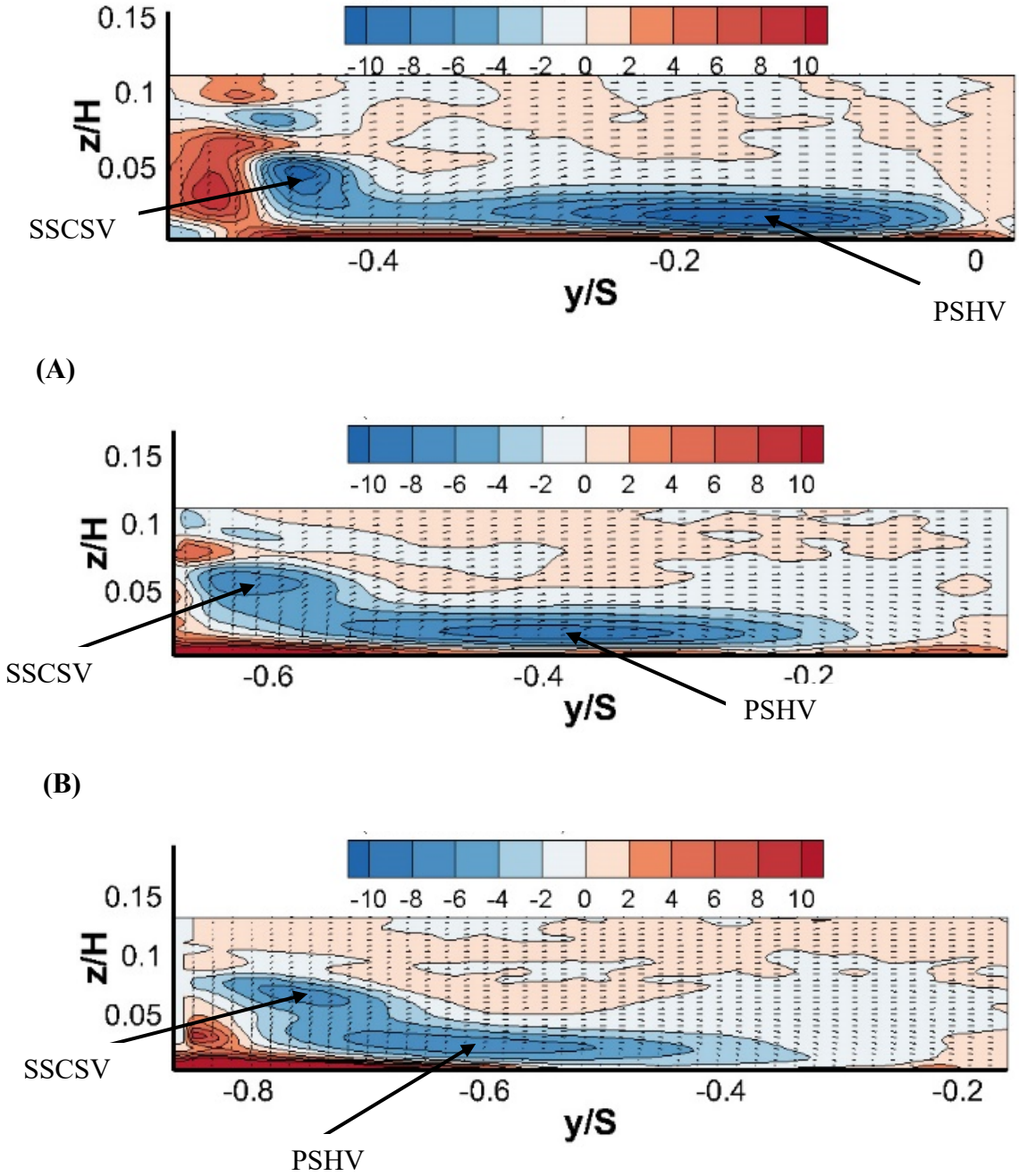

Figure 63. X - Vorticity and Secondary Velocity in 75% Cx Plane (A), 85% Cx Plane (B), and 95% Cx Plane (C)

Note in Figure 63 the way that the velocity vectors wrap around the large regions of high magnitude negative vorticity. This vorticity is characteristic of the location of the pressure side leg of the horseshoe vortex and will be used in subsequent plots to locate the vortex's average location. Given the way that the velocity vectors closely resemble the vorticity maps the use of vorticity is sufficient for locating the vortices. In subsequent figures, the velocity vectors will not be presented for the sake of clarity.

In the previous section, ILES data was used to show the usability of a simplified Helmholtz method to calculate y-vorticity and subsequent secondary vorticity. This method has been used here and the baseline condition is presented in Figure 64. However, for completeness, the x-vorticity and the full Helmholtz secondary vorticity have also been calculated and the baseline conditions are shown in Figure 65 and Figure 66 respectively.

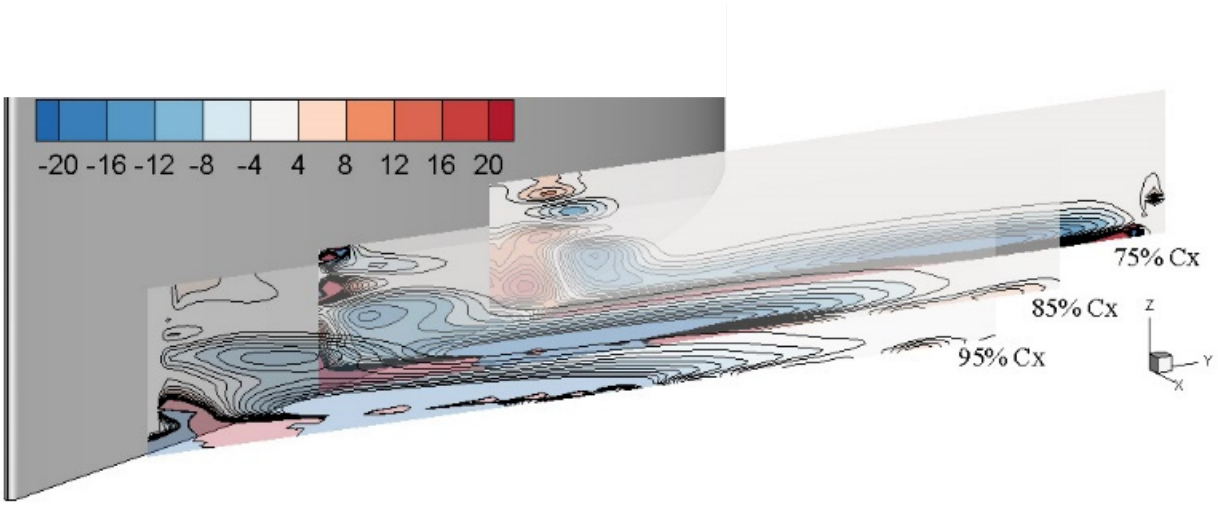

Figure 64. Baseline - Simplified Helmholtz Secondary Vorticity

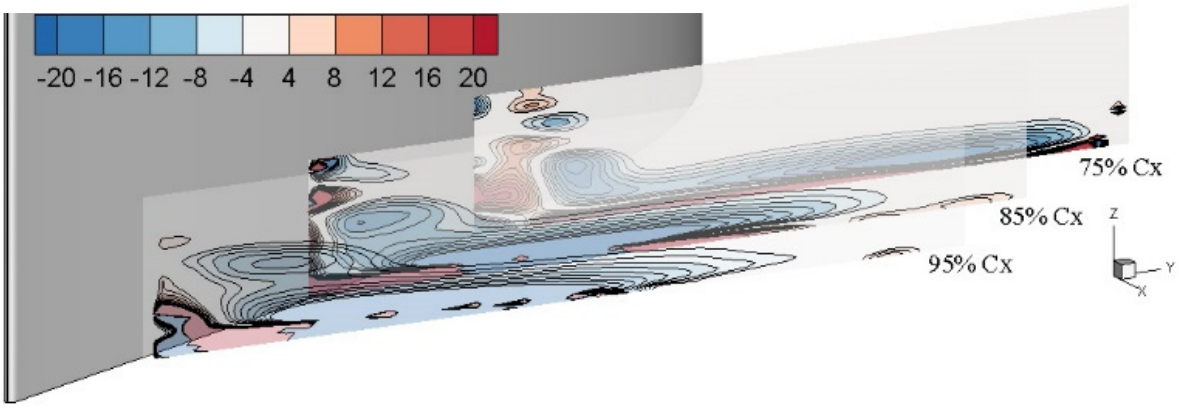

Figure 65.Baseline - Helmholtz Secondary Vorticity

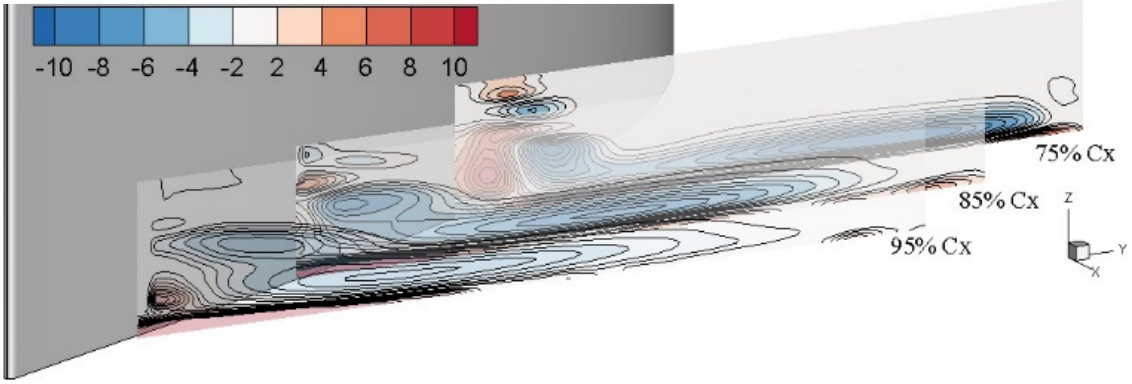

Figure 66.Baseline - X-Vorticity

As with the previous ILES discussion, the simplified Helmholtz assumption presents an adequate representation of the true secondary vorticity without requiring an intrusive pressure loss measurement or difficult bi-cubic spline fit of discrete experimental data and subsequent derivation. Note in Figure 64 and Figure 65 there are no major differences that occur in locations of the flow that are of interest in the present study. The differences between the results of these two calculation methods may not be worth the

additional effort required. However, should the reader desire to see the full Helmholtz calculated vorticities, they have been included in Appendix E for reference. The calculation of these vorticities used the previously discussed pressure loss measurements in conjunction with the current SPIV data to calculate the y-vorticity using Equation 16 and then the secondary vorticity using Equation 14.

Also included in Appendix E are figures similar to Figure 67. Figure 67 is a graphical representation of the scaling factor (SF) added to the x-vorticity in the Helmholtz calculation. This factor is found as the right hand side of Equation (16). For reference, $SF = \frac{1}{\rho * u}\left(\frac{\partial p_o}{\partial z}\right)$. Like vorticity, this factor has units of 1/s so is non-dimensionalized by the incoming velocity and the axial chord length.

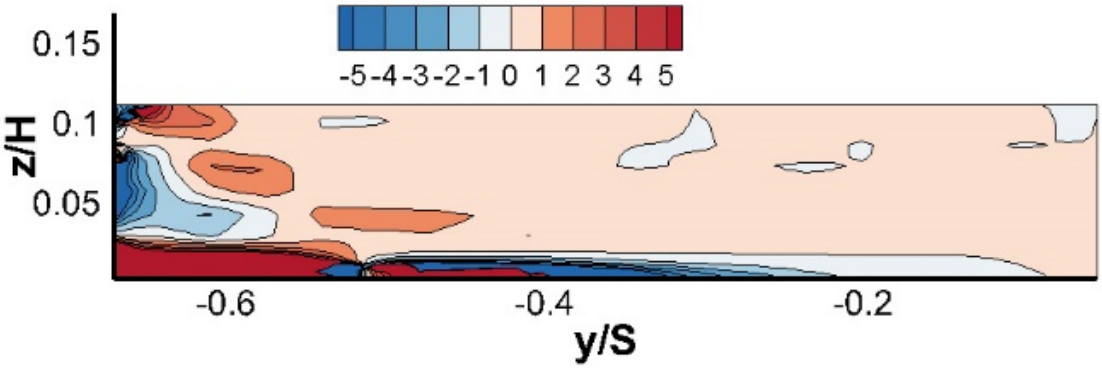

Figure 67. Helmholtz Non-Dimensional Total Pressure Scaling Factor for Baseline at 85% Cx

Notice how the highest magnitudes of the scaling factor are in regions of high pressure gradients and in areas that, for the most part, are not influencing the flow features

of interest. The location of high magnitude scaling factor is either below the location of the pressure side leg of the horseshoe vortex or left of the suction side corner separation vortex.

Finally, the use of the simplified Helmholtz computation provides a truer representation of the magnitude of the vorticity as compared to simply the x-vorticity components. Note how in Figure 66 the magnitude of the vorticity is approximately half of the vorticities in either of the Helmholtz calculations. Again, as with the Helmholtz calculations previously discussed, the x-vorticities are included in Appendix F for reference.

In order to concisely discuss the effects of endwall forcing figures similar to Figure 64 will be used. This whole passage figure allows for the presentation of the location of the pressure side leg of the horseshoe vortex as it travels throughout the passage and therefore allows for easy comparison of the effectiveness of each blowing case on shifting the vortex's location and strength. For study of individual planes of data see Appendix G. The individual plots of the separate vorticity calculation procedures can also be found in their respective appendices.

Now, moving to the comparison of the simplified Helmholtz secondary vorticities, Figure 68 shows a map of vorticity throughout the passage for the 22 Hz Pulsed Jet case. In Figure 68 note the location of the pressure side leg of the horseshoe vortex in planes presented. The PSHV appears to have shifted location slightly when compared to the vortex was in the baseline case. In the 75% plane the PSHV has shifted 11.8% span towards the suction surface. There has also been a reduction in PSHV strength of 12% as well. Further details regarding the vortices present in the 75% Cx plane can be found in Table 12. The

magnitudes presented in Table 12 are the non-dimensionalized Simplified Helmholtz Magnitudes.

Table 12. 75% Cx vortex locations and Simplified Helmholtz Magnitudes

Forcing Case	SSCSV			PSHV			Separation		
	y/S	z/H	Mag.	y/S	z/H	Mag.	y/S	z/H	Total (mm)
Baseline	-0.450	0.046	-18.182	-0.146	0.013	-25.323	-0.303	0.033	60.264
22 Hz	-0.443	0.042	-14.559	-0.264	0.015	-22.272	-0.178	0.026	37.174
65 Hz	-0.440	0.038	-14.653	-0.280	0.010	-24.429	-0.160	0.028	34.575
45.7 SLPM	-0.438	0.037	-14.462	-0.283	0.014	-22.347	-0.154	0.023	32.118
68.7 SLPM	-0.439	0.033	-15.924	-0.321	0.013	-20.740	-0.118	0.020	25.444

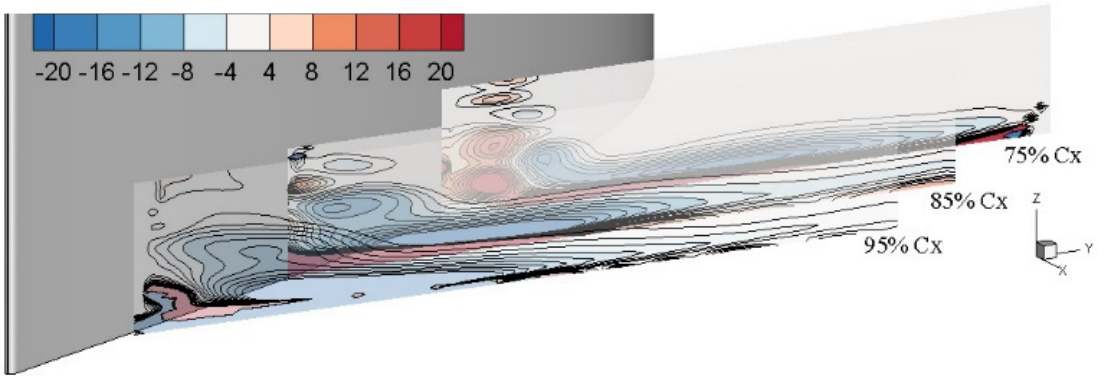

Figure 68. 22 Hz Pulsed Jets – Non-Dimensional Simplified Helmholtz Secondary Vorticity

Figure 69 is a presentation of the 65 Hz blowing case. Similar to the 22 Hz case, there has been significant changes to the location and strength of the pressure side leg of

the horseshoe vortex. The vortex has shifted towards the suction surface by 13.3%. In Figure 69 it can be clearly seen in the 85% plane the motion of the PSHV towards the suction surface. This trend extends throughout the passage. Further, the region of vorticity relating to the mixing region of the PSHV and SSCSV is noticeably smaller in the 95% plane which coincides with the loss reported previously. However the vorticity magnitude in the 75% plane has only reduced 3.5%. See Table 12 for details of the vortices in the 75% plane. Given that the data presented is the time average of an unsteady event, the reduction in magnitude may be a result of less fluctuation of the PSHV when the 65 Hz forcing is applied. However, without analyzing the high-speed data a conclusive statement on that possibility cannot be made.

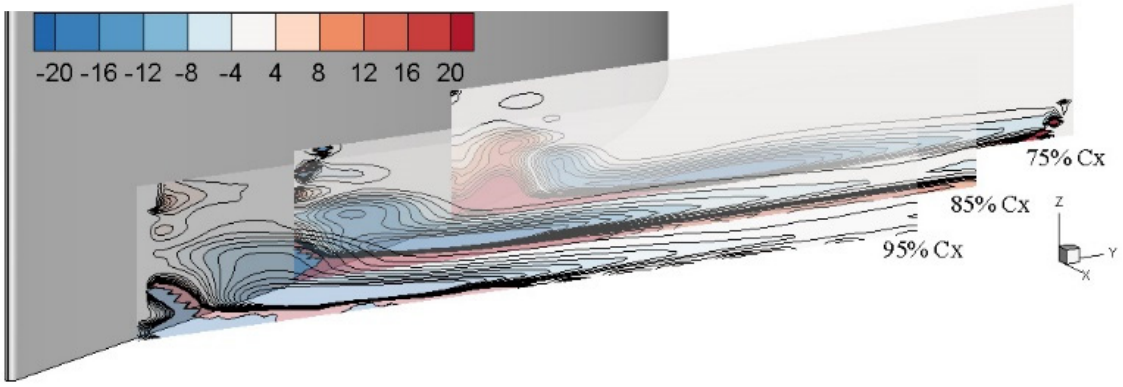

Figure 69. 65 Hz Pulsed Jets - Non-Dimensional Simplified Helmholtz Secondary Vorticity

Moving onto the steady cases, Figure 70 is a plot of the low momentum steady jet case. In Figure 70 it can be seen that similar effects as the 22 Hz pulsed case are produced. The location and strength of the PSHV is slightly affected with the vortex shifting slightly,

13.7% pitch, towards the suction surface and slightly off the endwall, 1.3%. These observations overlap with the conclusion of the minimal loss reduction in the 45.7 SLPM case.

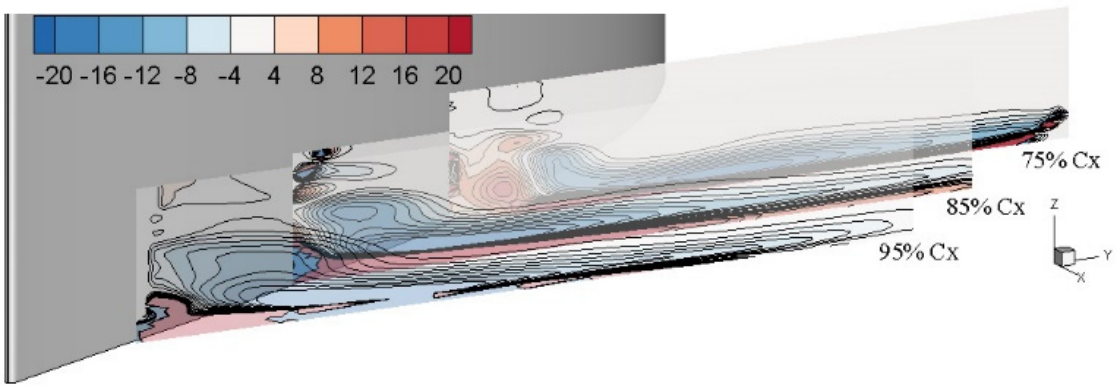

Figure 70. 45.7 SLPM Steady Jets - Non-Dimensional Simplified Helmholtz Secondary Vorticity

The final forcing case to be studied here is shown in Figure 71. This figure is a plot of the 68.7 SLPM steady forcing case. The conclusions to be drawn from Figure 71 are similar to the conclusions of the 65 Hz pulsed case. It can be seen in each plane the considerable difference in pressure side leg of the horseshoe vortex location. Further the strength and signature of the PSHV in the 95% plane is nearly indistinguishable from the SSCSV. The location and strength of the vortices shown in Figure 71 again match the conclusions from the pressure loss study that the 68.7 SLPM steady forcing case is an effective means for redirecting and reducing the strength of the endwall vortices. See Table 12 for additional vortex values for the 75 Cx plane.

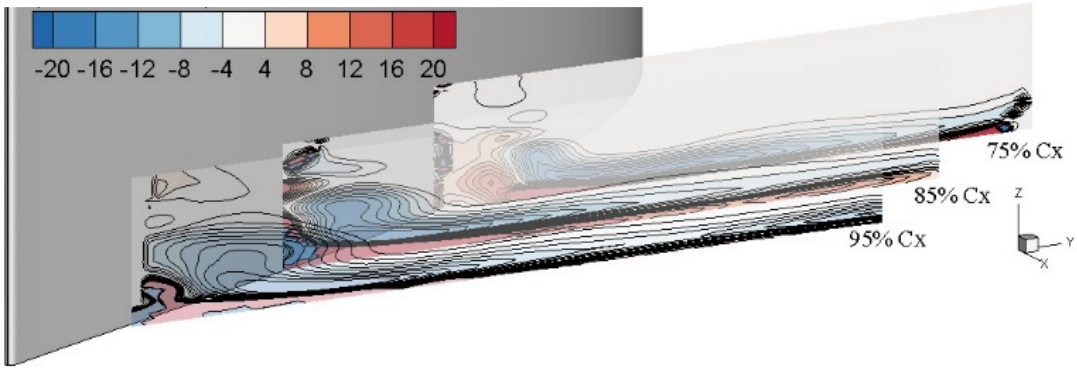

Figure 71. 68.7 SLPM Steady Jets - Simplified Helmholtz Secondary Vorticity

As a secondary look at the location of the pressure side leg of the horseshoe vortex, shown in Figure 72, shows a net effect of the application of localized endwall forcing is a shifting of the PSHV towards the suction surface. However, unlike the pressure loss measurements in the previous section, there are no conclusive observations that can be made about the height of the PSHV from the endwall in the 75% plane.

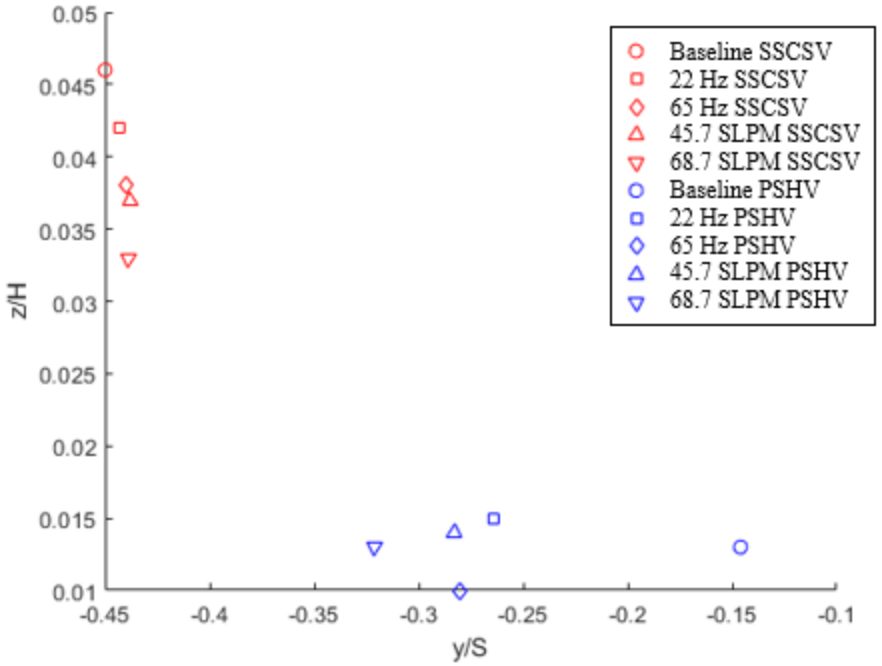

Figure 72. Location of Vortices in 75% Cx SPIV

Finally, when plotting the separation of the SSCSV and the PSHV a general trend can be seen in Figure 73. This trend shows that as the vortices, on average are closer to each other, the resulting magnitudes of the PSHV reduces. However, the outlier case here is again the 65 Hz and additional research into the high-speed data should be performed to conclusive state why the 65 Hz case is an outlier. However, the separation of the SSCSV and the PSHV can clearly be seen to decrease with the application of endwall normal active flow control.

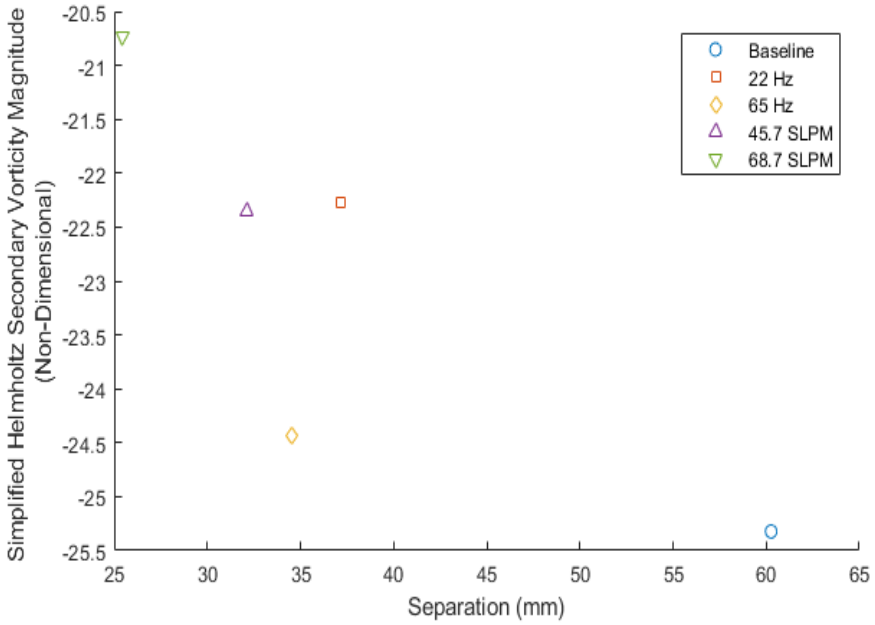

Figure 73. Separation of SSCSV and PSHV v. PSHV Vorticity Magnitude

V. Conclusions and Recommendations

Conclusions of Research

The purpose of this research was to investigate the effectiveness of pulsed and steady endwall normal jets in manipulating the strength and location of the pressure side leg of horseshoe vortex originating at the leading edge of the high-lift L2F turbine blade profile, and the passage vortex that forms following the interaction of this PSHV with a corner separation vortex from the suction surface of the L2F profile. The hypothesized effect of endwall normal pulsing was a reduction in strength of the endwall vortices and an overall reduction of pressure loss within the passage. The following discussion summarizes the conclusions drawn from the present study, which was conducted in a linear cascade low-speed wind tunnel.

In order to further understand the effects of the localized endwall forcing, a firm understanding of the baseline operation case is necessary. It was previously postulated that the passage vortex oscillates within a specific frequency range. The present research sought to further confirm the oscillation of the pressure side leg of the horseshoe vortex. Spectral analysis was performed using thin-film sensors placed along the endwall of the passage and spectral averages, ranging in number from 10 to 400, were collected and averaged to provide a power spectral density to show the time averaged oscillation frequency of the PSHV. This portion of the study concluded that the oscillation of the PSHV occurs in a frequency band centered near 22 Hz confirming previous research, which was based only upon 12 spectral sample averages, of the flow phenomena present.

With the knowledge of the pressure side leg of the horseshoe vortex natural oscillation centered near 22 Hz, pulsed and steady jet forcing was applied to the passage in order to manipulate the PSHV with the goal of reducing overall pressure loss. Pulsed frequencies chosen were 22 Hz, due to the natural oscillation of the PSHV, and 65 Hz, based upon previous research that showed an optimum frequency of 65 Hz for reducing pressure loss in the same low speed wind tunnel configuration. The pulsed flow control cases applied had an average mass flow rate of 40.1 SLPM for the 22 Hz case and 44.7 SLPM for the 65 Hz case. Steady jet forcing with mass flows of 45.7 SLPM and 68.7 SLPM were also collected. These values were chosen to coincide with the average mass flow of the 65 Hz forcing case pulsed condition. The pulsed and steady jet endwall normal forcing was applied in a localized area on the endwall approximately 7% axial chord downstream of the leading edge of the L2F profile located along a previously defined PSHV liftoff line.

Total pressure loss measurements were collected at three out-of-plane locations: 150%, 125% and 105% axial chord and three in-passage locations: 95%, 85% and 75% axial chord. Consistent with prior research, the total pressure measurements were used in conjunction with the incoming total pressure and incoming dynamic pressure to calculate a total pressure loss coefficient. The mapping of this total pressure loss coefficient was used to provide an understanding and net effect of the location of the vortical endwall structures they travels though and downstream of the passage for each forcing case.

Forcing cases of 65 Hz pulsed jet flow control, approximately three times the natural frequency of the flow features present in this experimental set up, and 68.7 SLPM steady jet flow control led to the largest reduction in strength of the passage vortex. Each

of these cases significantly altered the location of the passage vortex by forcing the feature off from the endwall and towards the suction surface of the adjacent blade. The manipulation of the passage vortex allowed for a reduction of total pressure loss of 2.2 % in the 65 Hz pulsed jet case, 1.8% in the 68.7 SLPM steady jet case, 0.3% in the 45.7 SLPM steady jet case and no change in the 22 Hz pulsed jet case.

Close inspection of the pressure loss map suggested that the loss reduction created by the manipulation of the passage vortex was partially counteracted by additional endwall adjacent losses generated by the forcing of jets normal to the axial flow direction.

In order to further investigate the effects of endwall normal forcing on the endwall vortices stereoscopic particle image velocimetry was implemented. Planes of data were chosen to correspond to the location and orientation of the in-passage pressure maps. From these planes the average velocity components were used in order to map vorticity as a means of locating the PSHV, SSCSV, and resultant PV as they traveled through the passage.

All three velocity components were measured in the three in-passage planes. The velocity values compared reasonably well with previous Implicit Large Eddy Simulation investigations of the same blade profiles and flow conditions. From the three collected in-plane component velocities, the component of vorticity normal to the measurement plane was directly determined. However, due to the large secondary flow components present in the passage, it is preferred to find the vorticity component in the secondary direction. After consulting the literature a method was found whereby the secondary component of vorticity could be estimated. Two types of estimation was applied, one using the incompressible Helmholtz equation and a second which implemented a simplification of the pressure term

present in the Helmholtz equation. Significantly, the later approach was not clearly articulated in the investigated literature, so it was derived from the *Gromeka-Lamb* expression as part of the current research effort. While the derivation may be helpful in future efforts, it was found though comparison with the aforementioned CFD-based study that the simplified method yielded adequate results.

The conclusions drawn from the average of high-speed PIV average data showed the application of active flow control plays a significant role in the strength and location of the endwall flow features present in the passage of a high-lift linear cascade. There appeared to also be a relation between the separation of the SSCSV and the PSHV and the magnitude of the PSHV. However, the outlier case of 65 Hz was seen to have minimal effect on strength of the PSHV and further study of the high-speed data may provide insight into the location of the PSHV. In the study the motion of the vortex was shown by the location of the center of the greatest magnitude vorticities traveling nearer to the suction surface and higher off the endwall. The 22 Hz pulsed and 45.7 SLPM steady cases again showed less benefit than their higher mass flow and greater frequency counterparts.

Recommendations for Future Research

While this study aimed to provide further information regarding the effects of endwall normal forcing on the strength and location of a vortical endwall structures there are still questions that can be answered in further research. Such work may be performed by investigating the high-speed instantaneous velocity data collected using SPIV or adding a third camera and studying this flow field using a new tomographic PIV approach. Further,

loss reduction may be increased by optimizing the location and direction of the endwall forcing.

In this present study, only the average and standard deviation components of velocity from the high-speed SPIV data were used, by investigating the high-speed data it may be possible to further detail the oscillation of the passage vortex and investigate exactly how the endwall jets effect the behavior of the vortical structures. By studying the time histories of the vortices present within the passage it may be possible to further understand the near-time-accurate effects that the application of endwall normal jets has on the strength and location of vortical endwall structures.

Finally, the present research has shown that localized forcing of a PSHV is an effective means for reducing the strength and location of vortical loss features present in LPT's, however, by optimizing the forcing location and angle of the jets it may be possible to reduce the loss that is generated by the normal forcing of the endwall jets.

Appendix A – Spectral Analysis

This appendix contains the resultant power spectral density (PSD) plots from all of the Spectral Analysis test performed in this research effort. The appendix is separated into two sections focusing on the passage sensors and the leading edge sensors respectively.

Passage Sensors:

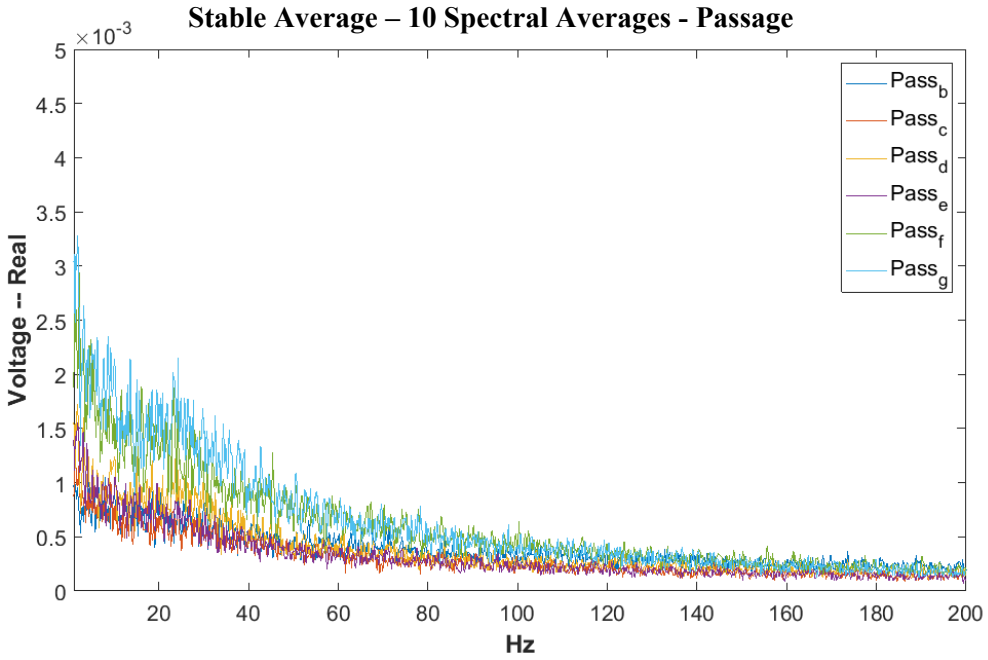

Figure 74. In-Passage Hot-film PSD, 10 Averages, 0-.005V v. 0-200 Hz

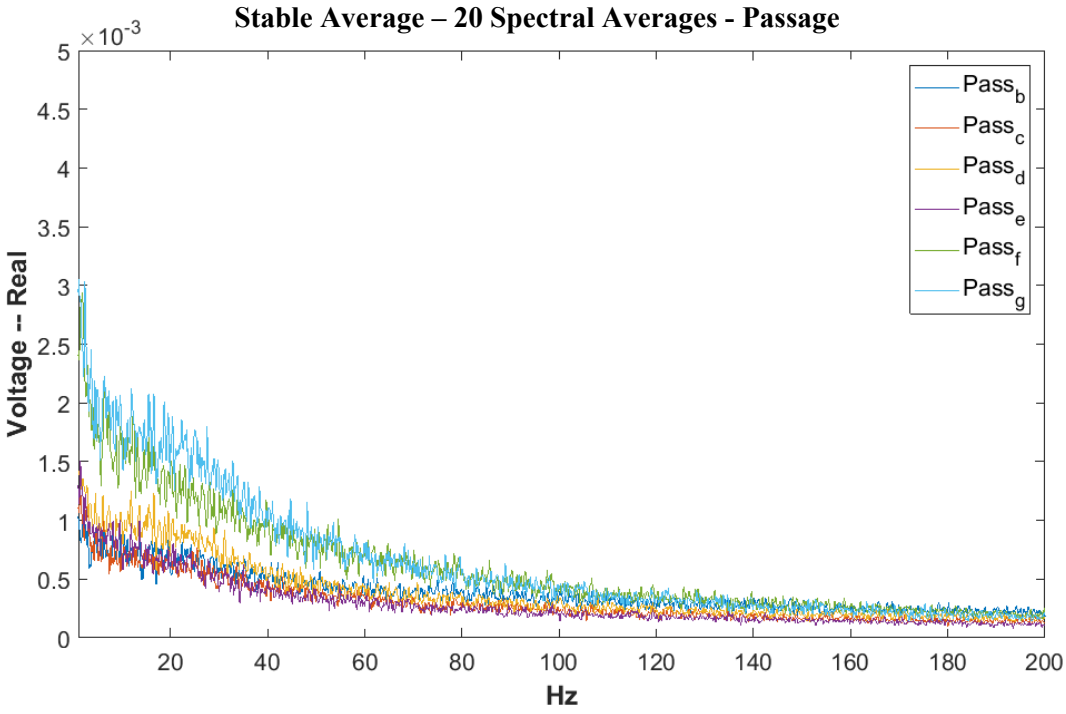

Figure 75. In-Passage Hot-film PSD, 20 Averages, 0-.005V v. 0-200 Hz

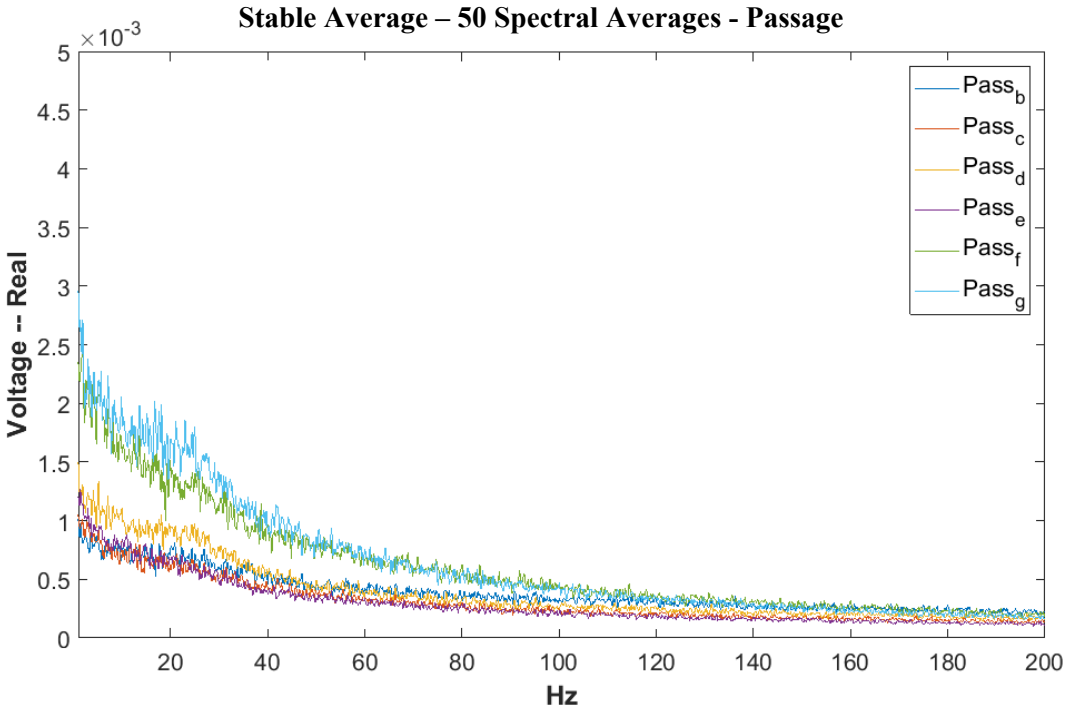

Figure 76. In-Passage Hot-film PSD, 50 Averages, 0-.005V v. 0-200 Hz

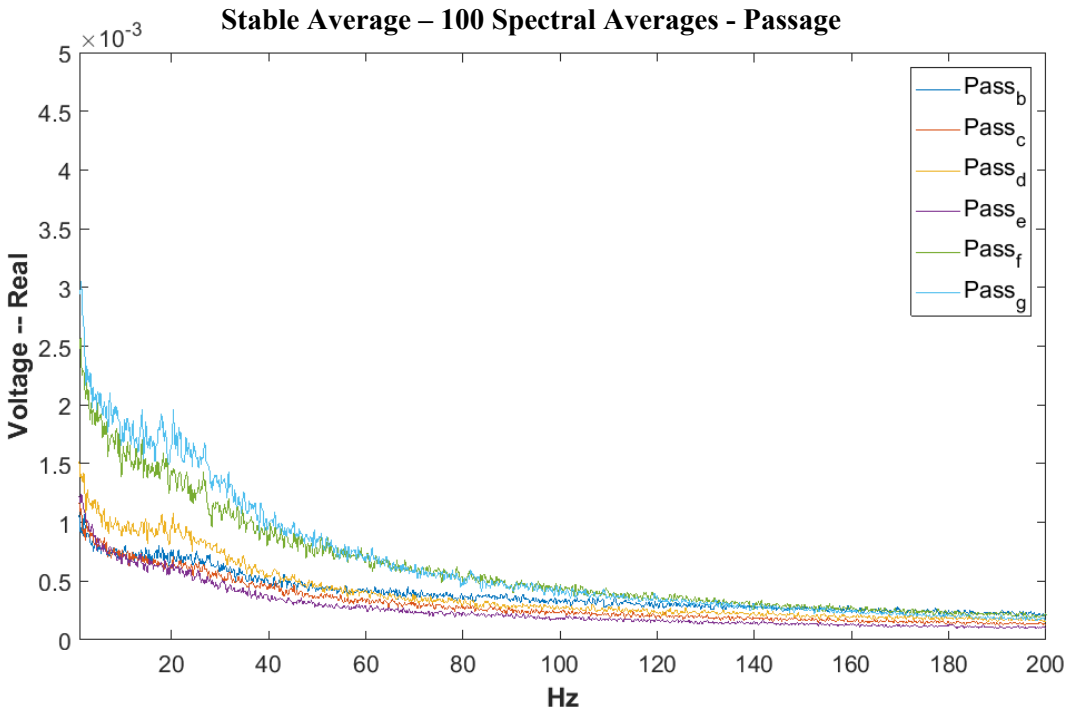

Figure 77. In-Passage Hot-film PSD, 100 Averages, 0-.005V v. 0-200 Hz

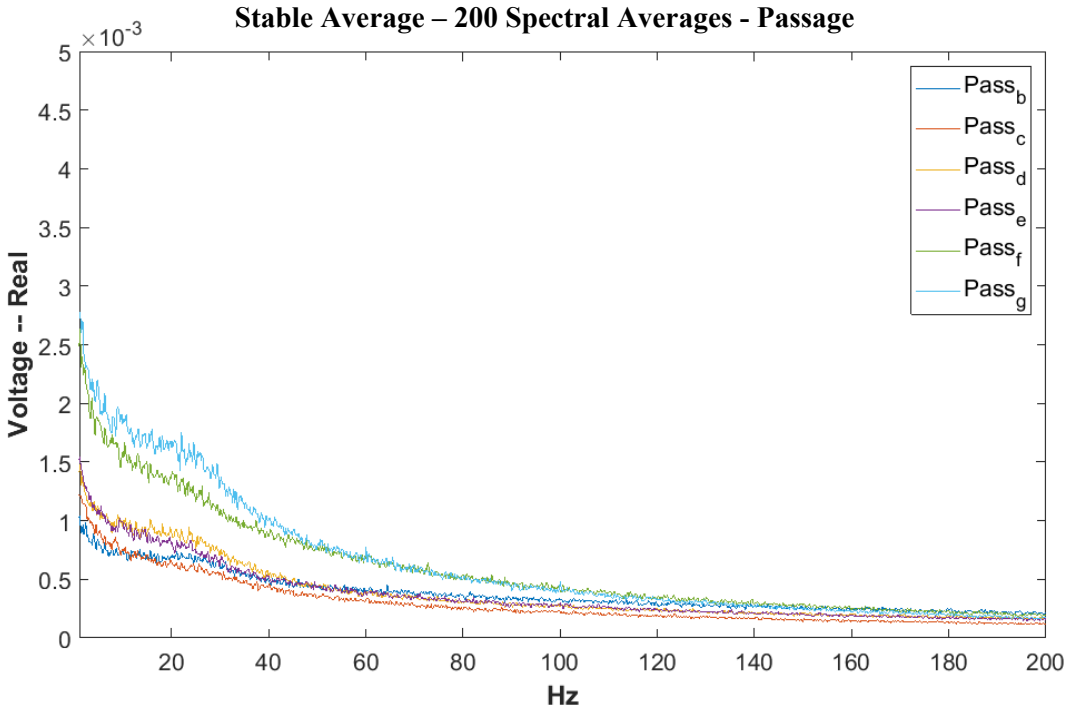

Figure 78. In-Passage Hot-film PSD, 200 Averages, 0-.005V v. 0-200 Hz

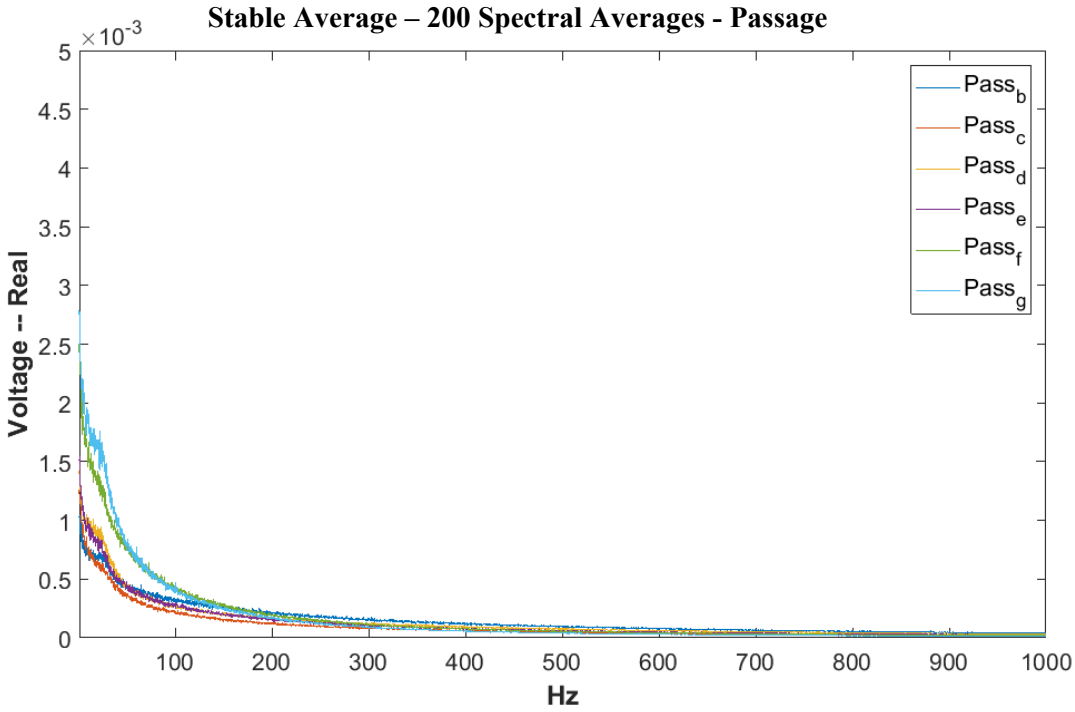

Figure 79. In-Passage Hot-film PSD, 200 Averages, 0-.005V v. 0-1000 Hz

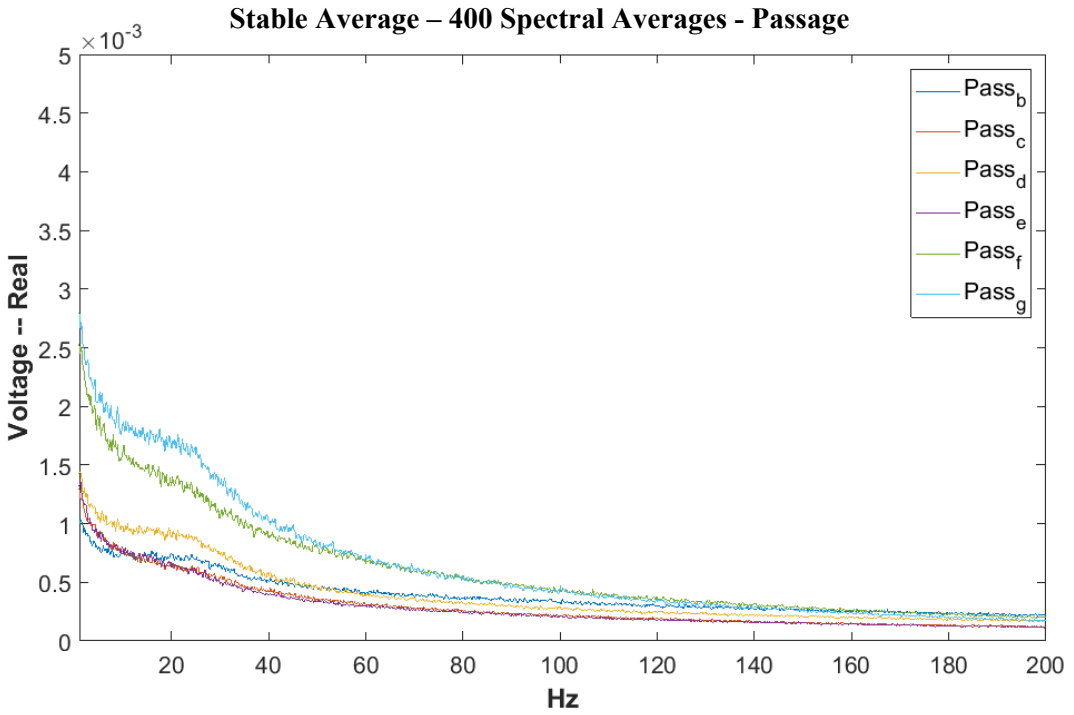

Figure 80. In-Passage Hot-film PSD, 400 Averages, 0-.005V v. 0-200 Hz

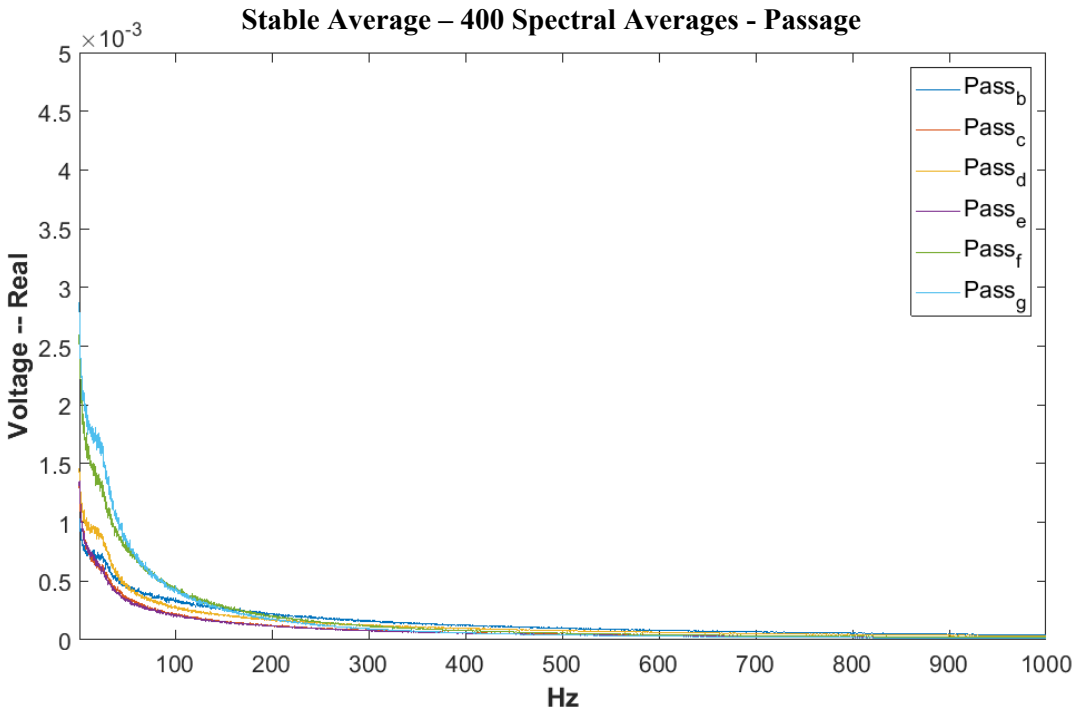

Figure 81. In-Passage Hot-film PSD, 400 Averages, 0-.005V v. 0-1000 Hz

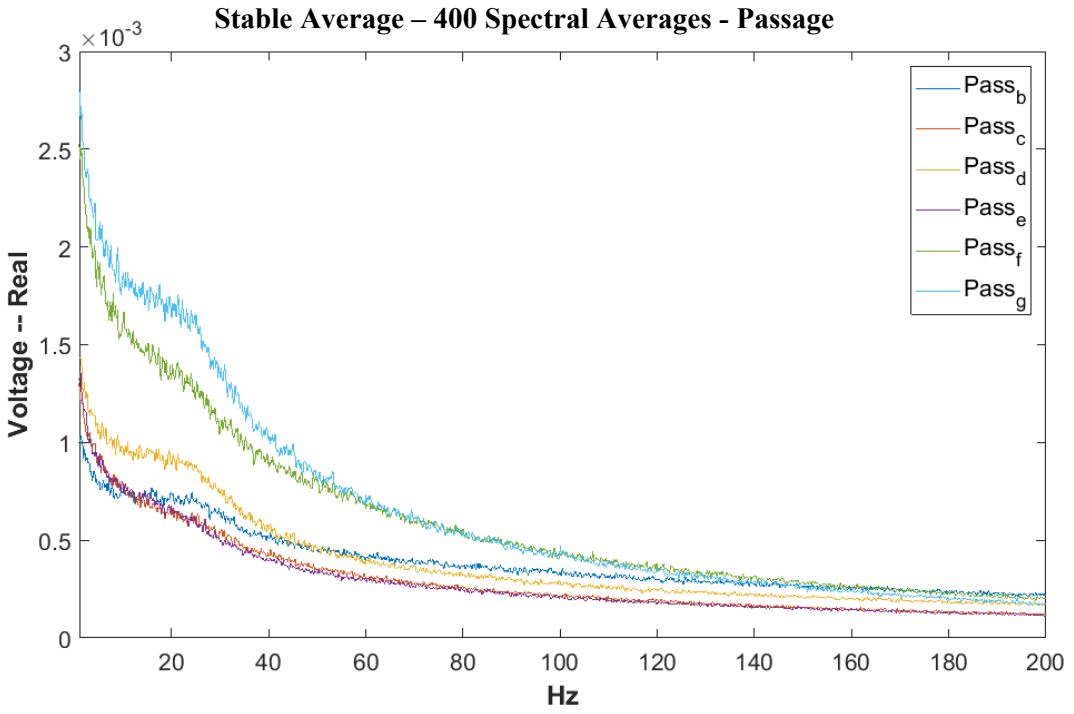

Figure 82. In-Passage Hot-film PSD, 400 Averages, 0-.003V v. 0-200 Hz

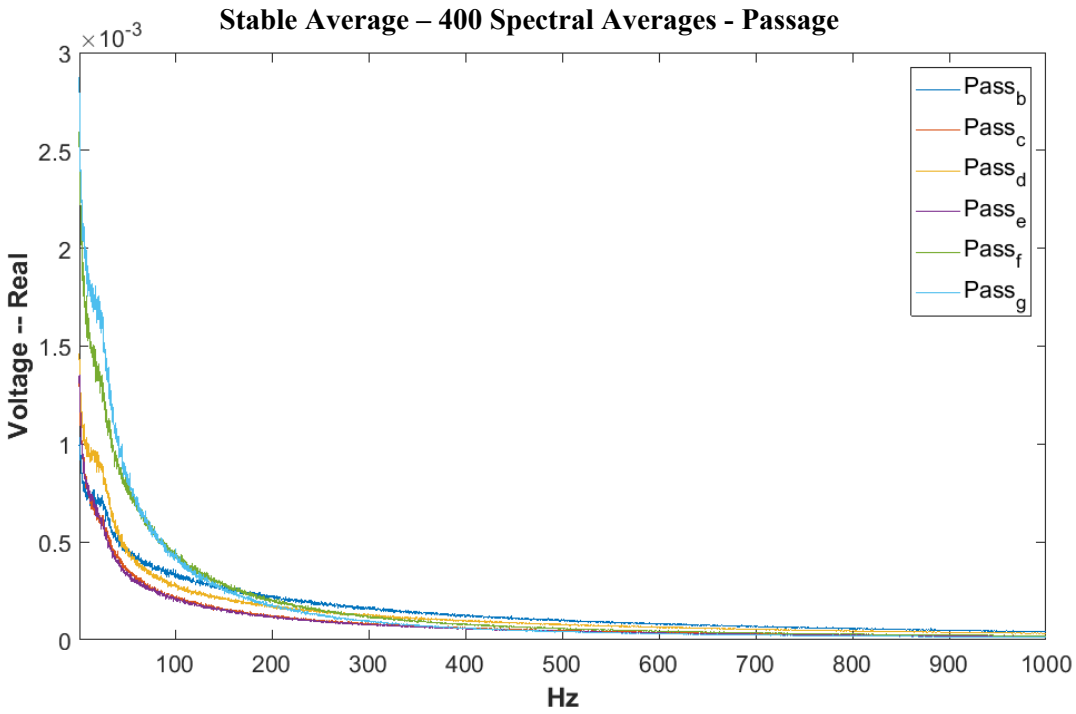

Figure 83. In-Passage Hot-film PSD, 400 Averages, 0-.003V v. 0-1000 Hz

Leading Edge Sensors:

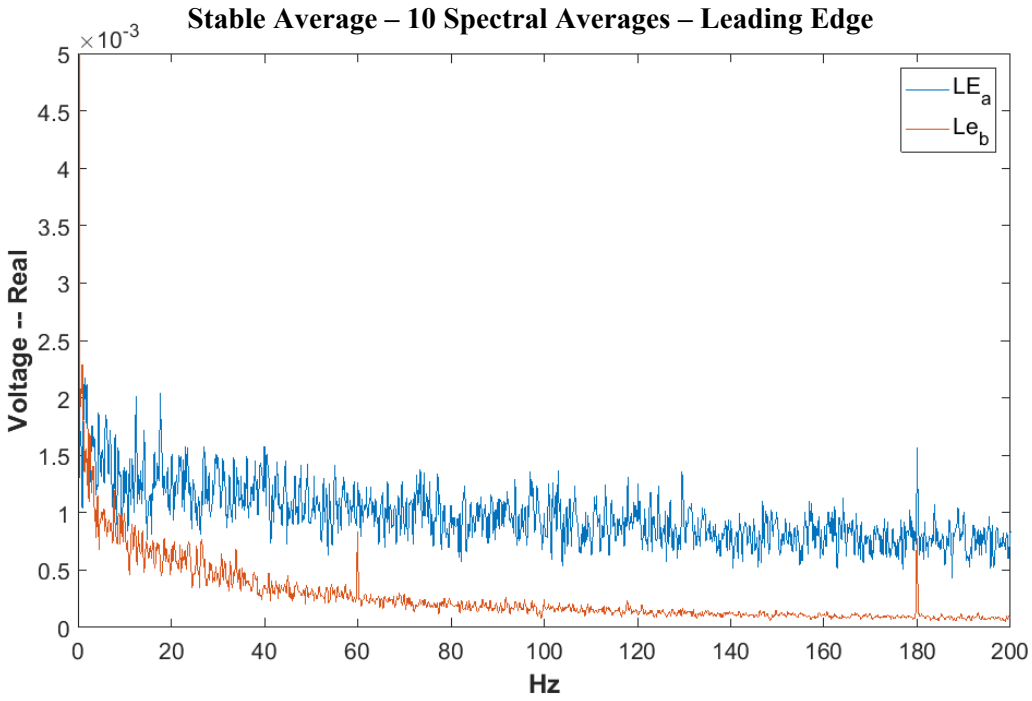

Figure 84. Leading Edge Hot-film PSD, 10 Averages, 0-.005V v. 0-200 Hz

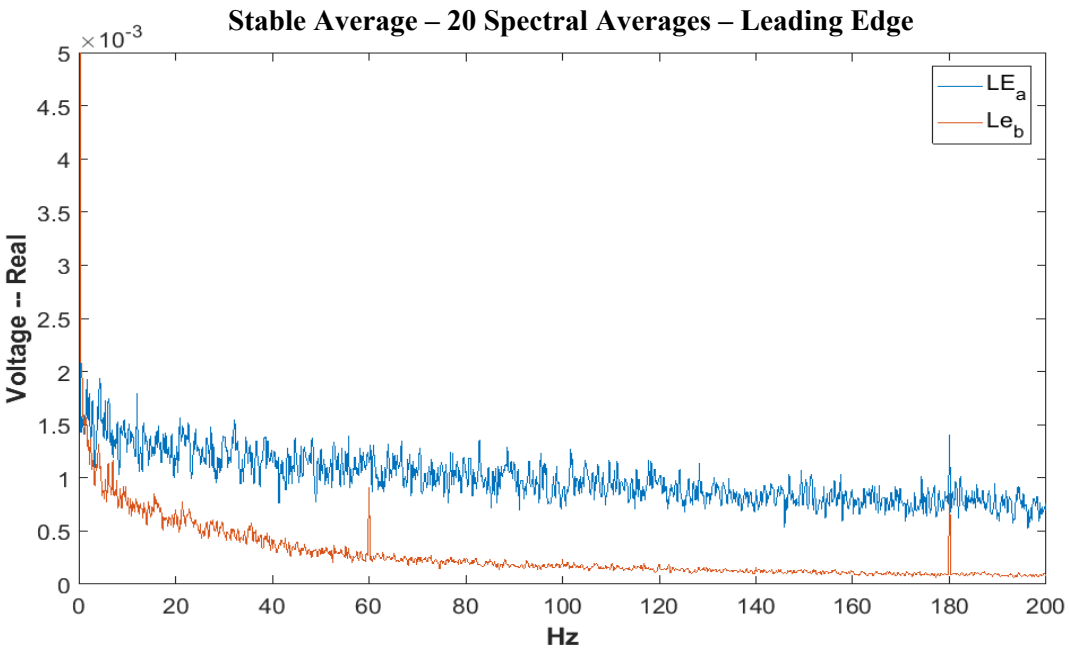

Figure 85. Leading Edge Hot-film PSD, 20 Averages, 0-.005V v. 0-200 Hz

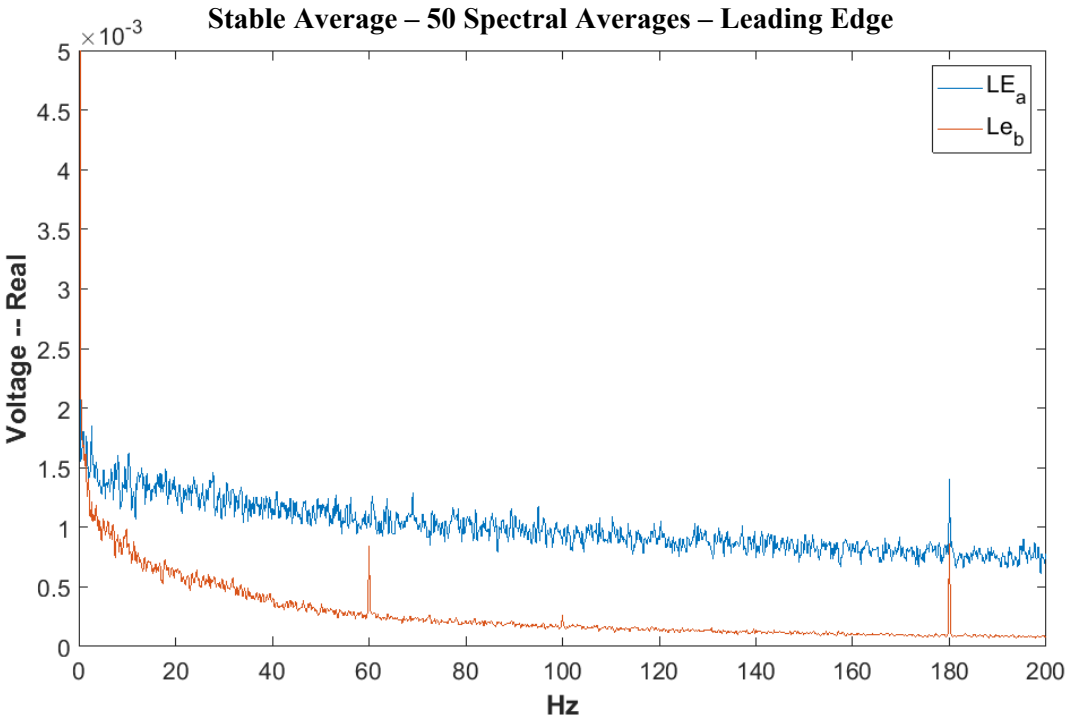

Figure 86. Leading Edge Hot-film PSD, 50 Averages, 0-.005V v. 0-200 Hz

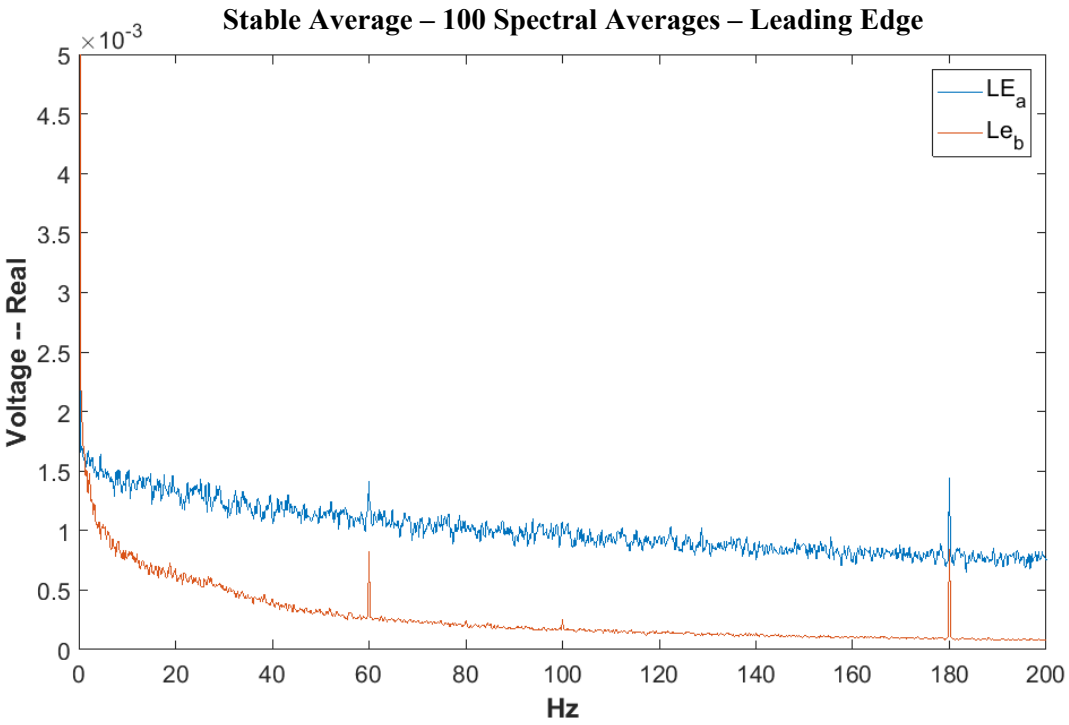

Figure 87. Leading Edge Hot-film PSD, 100 Averages, 0-.005V v. 0-200 Hz

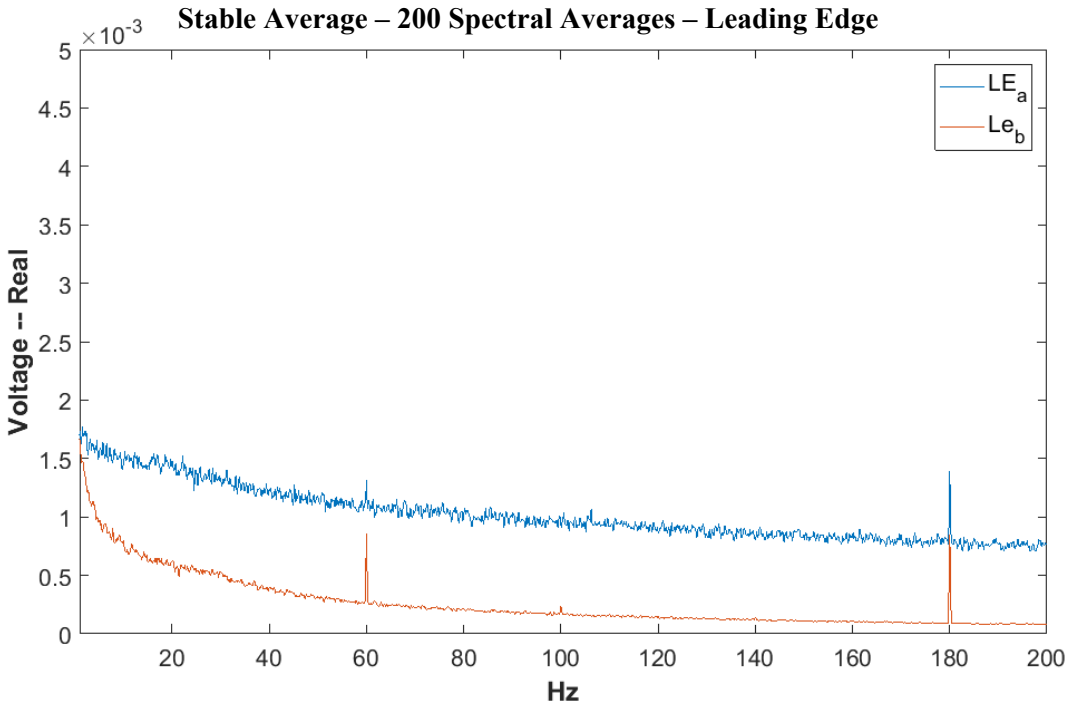

Figure 88. Leading Edge Hot-film PSD, 200 Averages, 0-.005V v. 0-200 Hz

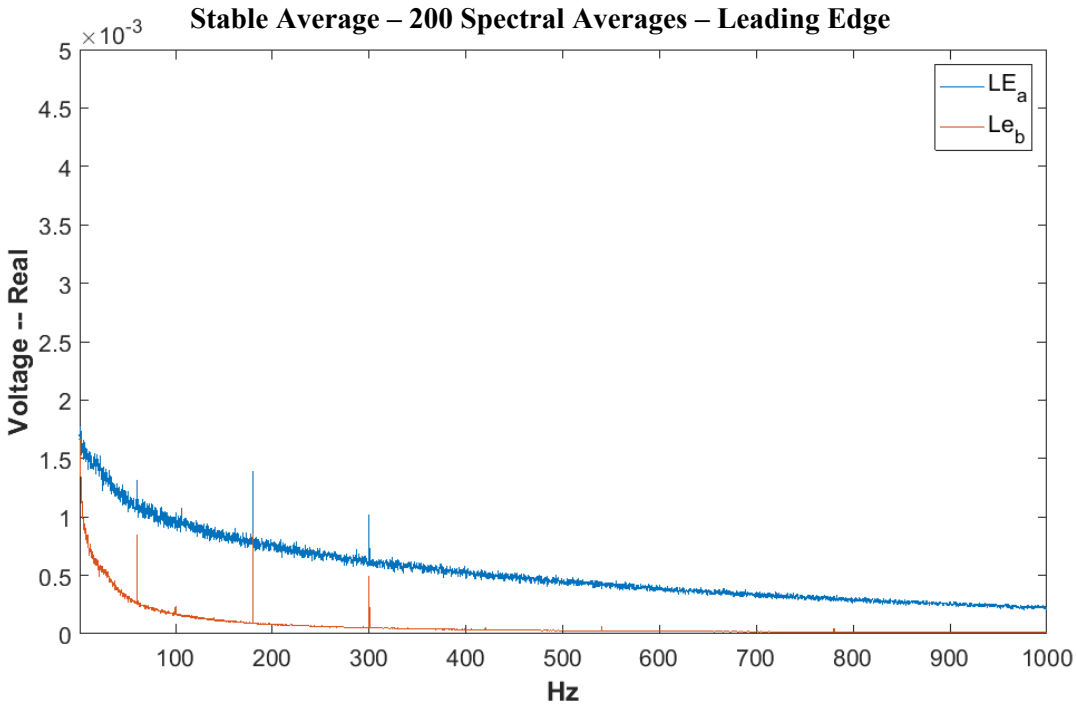

Figure 89. Leading Edge Hot-film PSD, 200 Averages, 0-.005V v. 0-1000 Hz

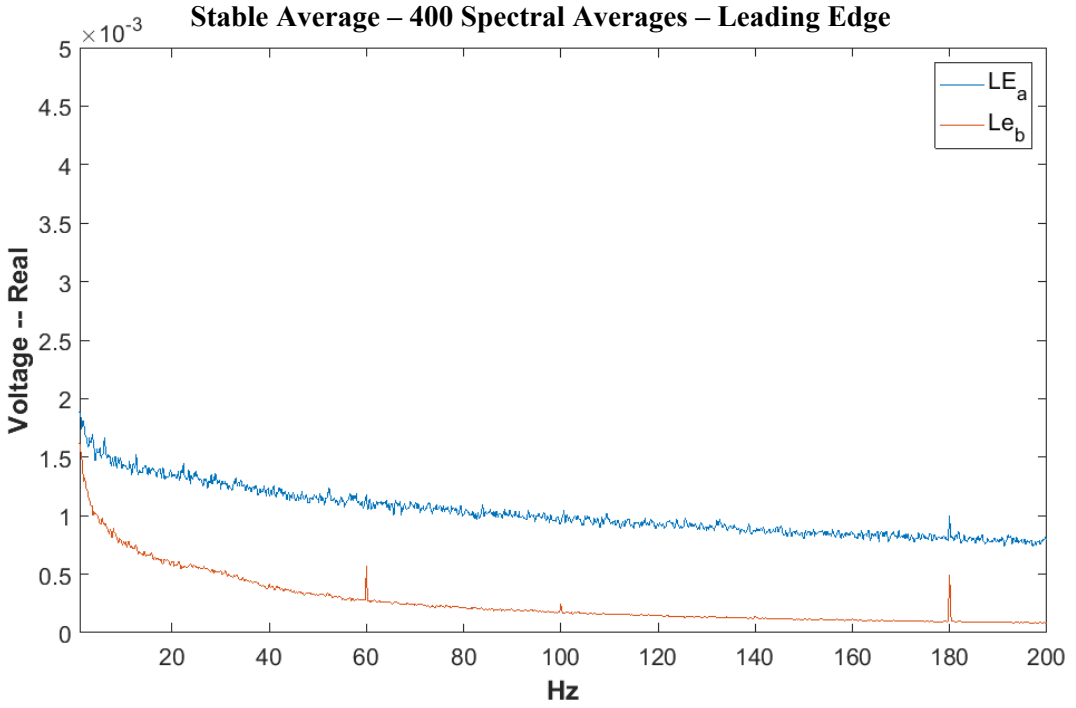

Figure 90. Leading Edge Hot-film PSD, 400 Averages, 0-.005V v. 0-200 Hz

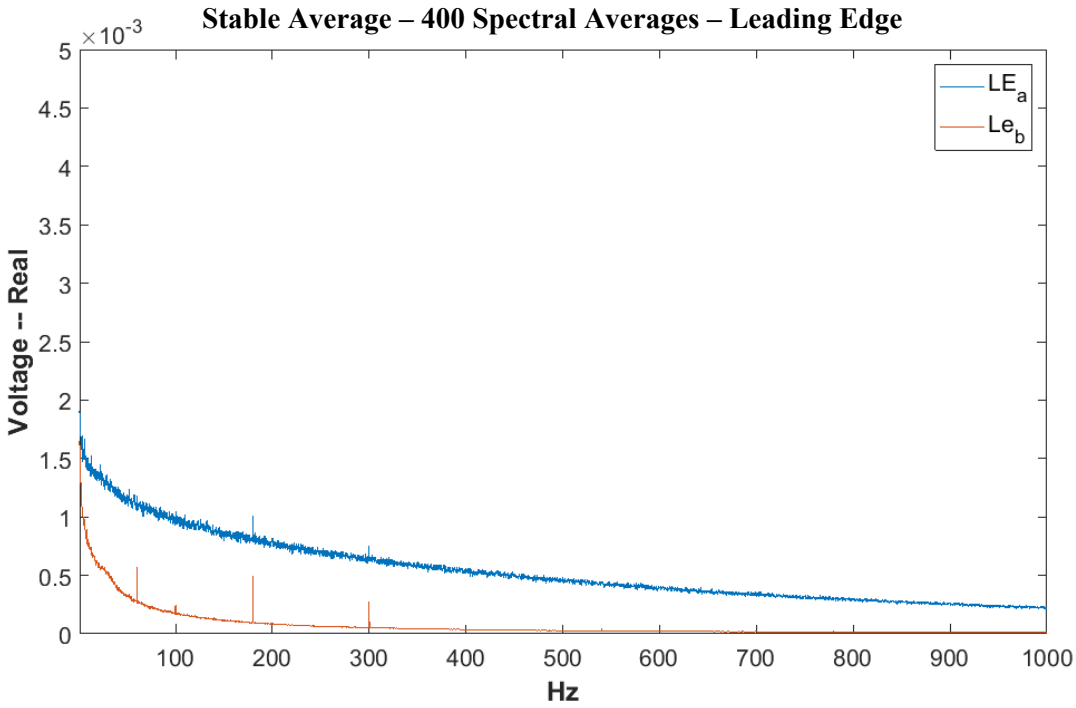

Figure 91. Leading Edge Hot-film PSD, 400 Averages, 0-.005V v. 0-1000 Hz

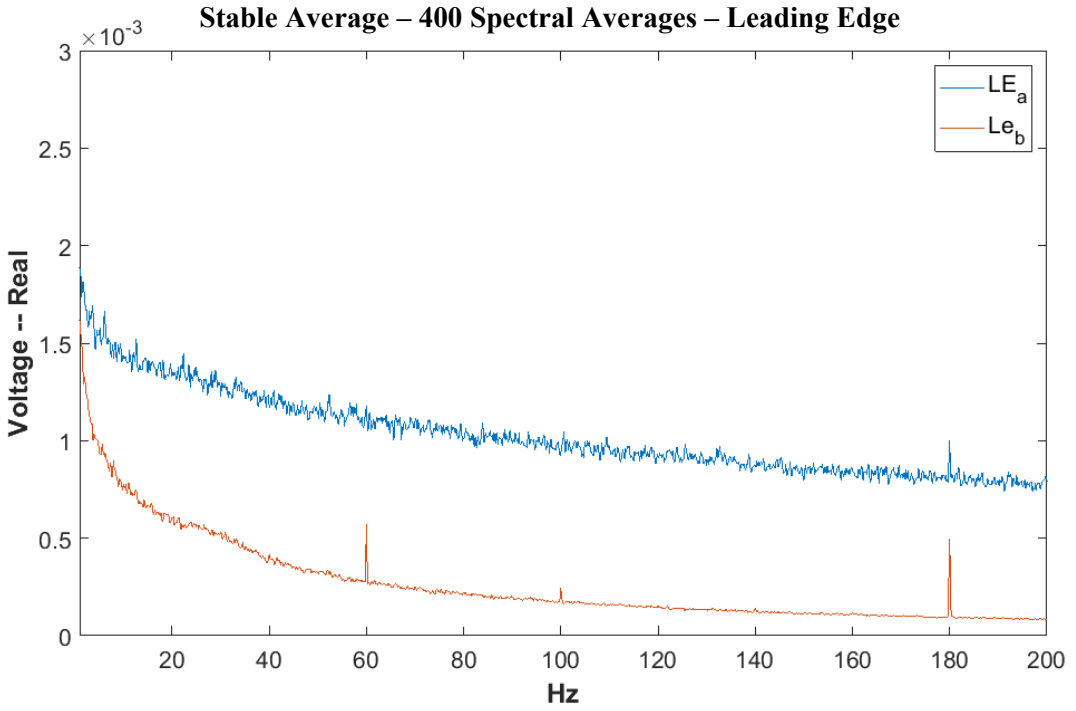

Figure 92. Leading Edge Hot-film PSD, 400 Averages, 0-.005V v. 0-200 Hz

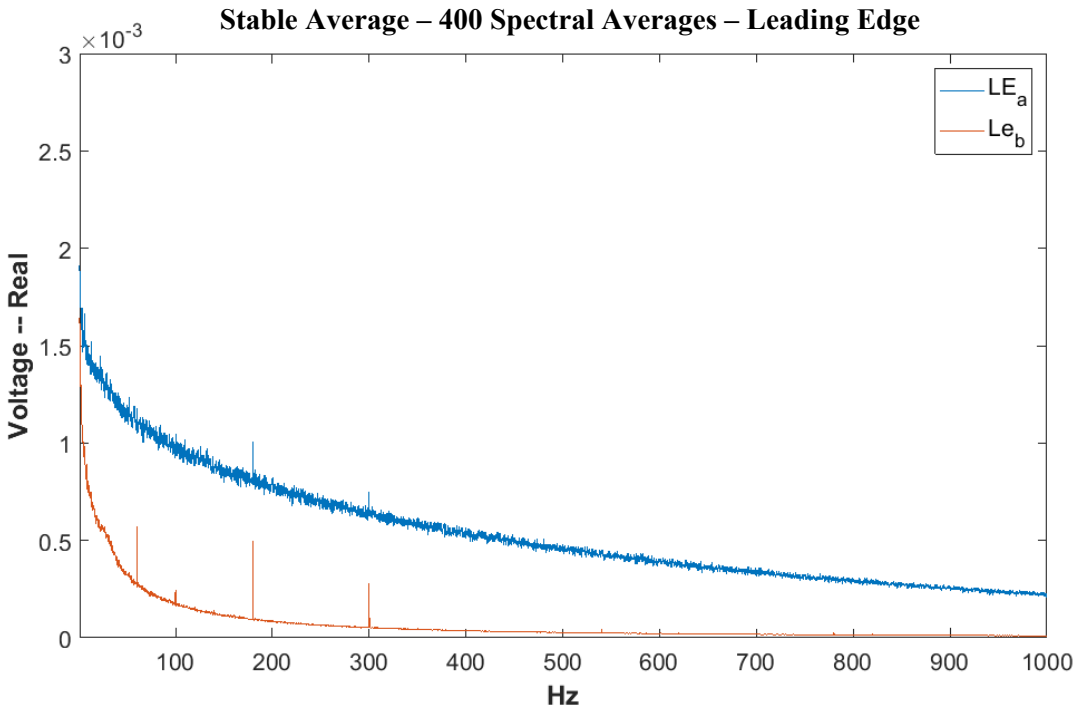

Figure 93. Leading Edge Hot-film PSD, 400 Averages, 0-.005V v. 0-1000 Hz

Under Tunnel Sensor:

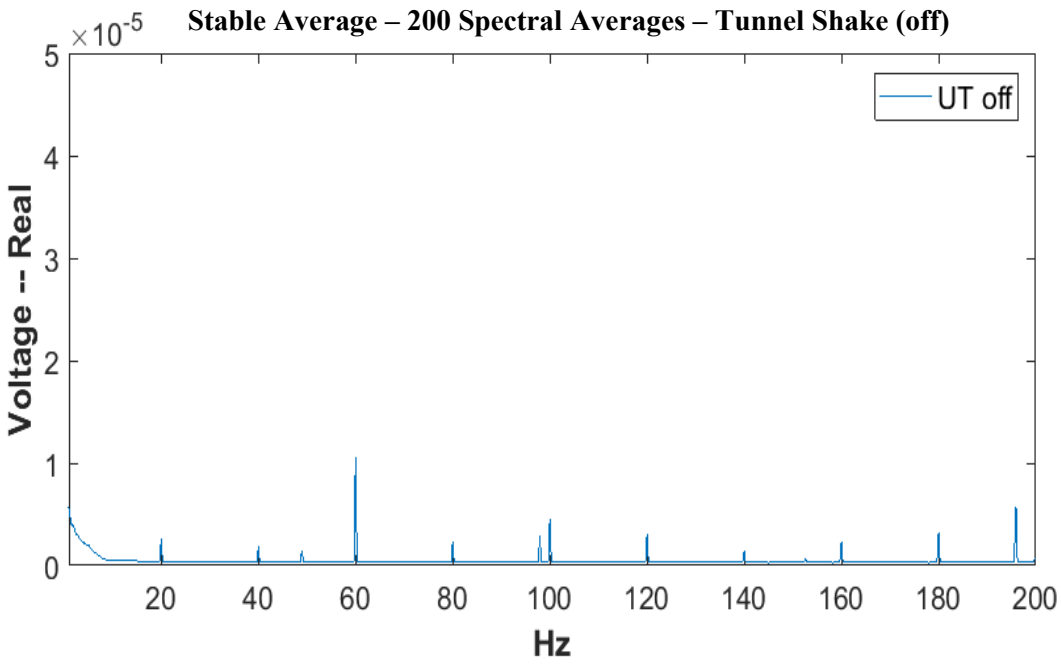

Figure 94. Under Tunnel Hot-film PSD, 200 Averages, 0-.005V v. 0-200 Hz, Tunnel Off

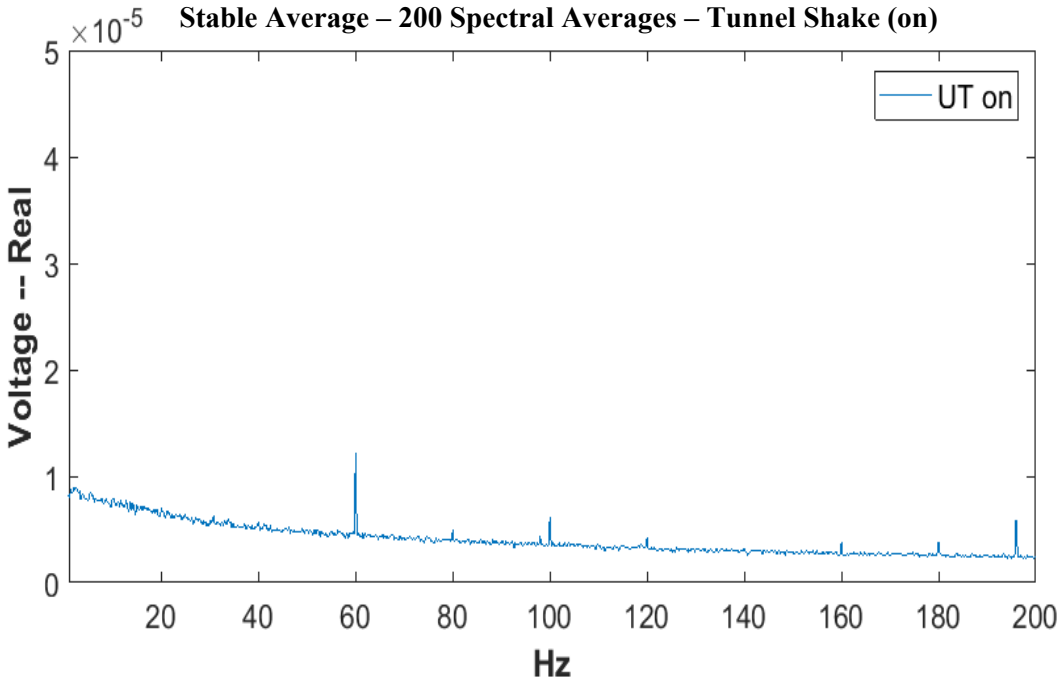

Figure 95. Under Tunnel Hot-film PSD, 200 Averages, 0-.005V v. 0-200 Hz, Tunnel On

Subtracted Data:

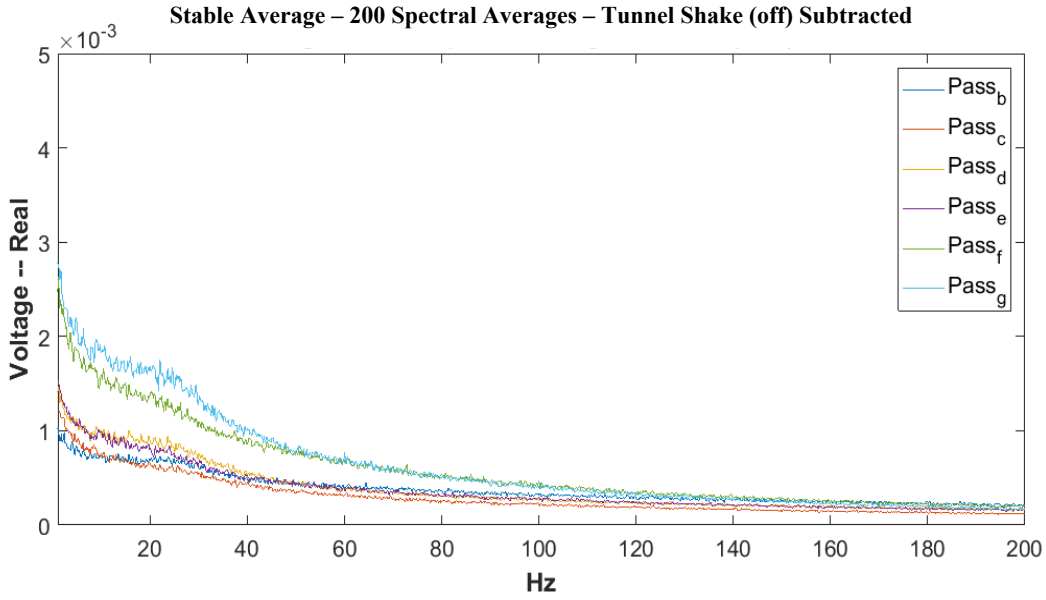

Figure 96. Under Tunnel Hot-film Corrected PSD, 200 Averages, 0-.005V v. 0-200 Hz, Tunnel Off

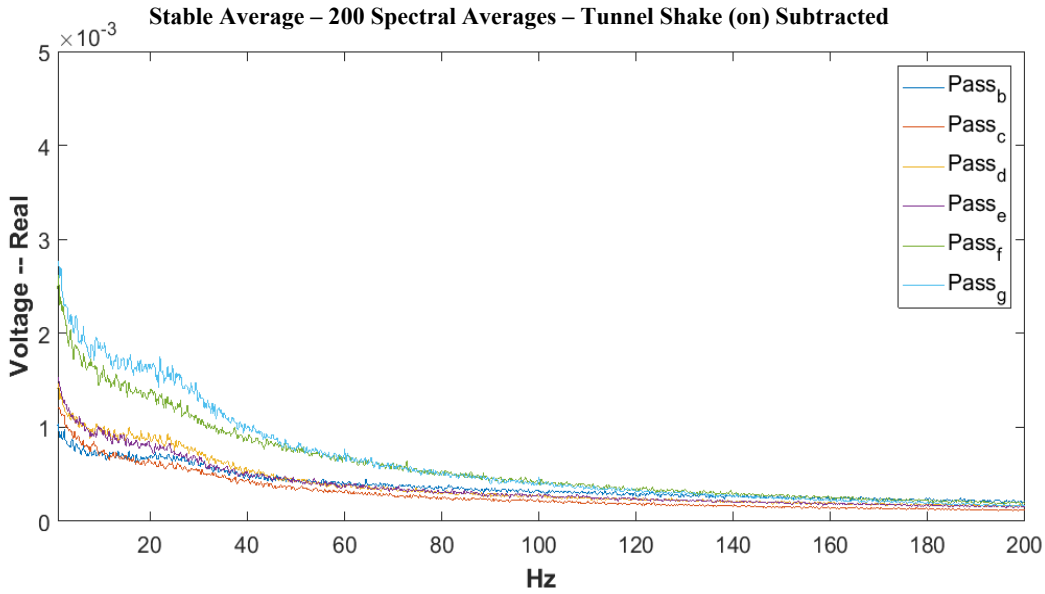

Figure 97. Under Tunnel Hot-film Corrected PSD, 200 Averages, 0-.005V v. 0-200 Hz, Tunnel On

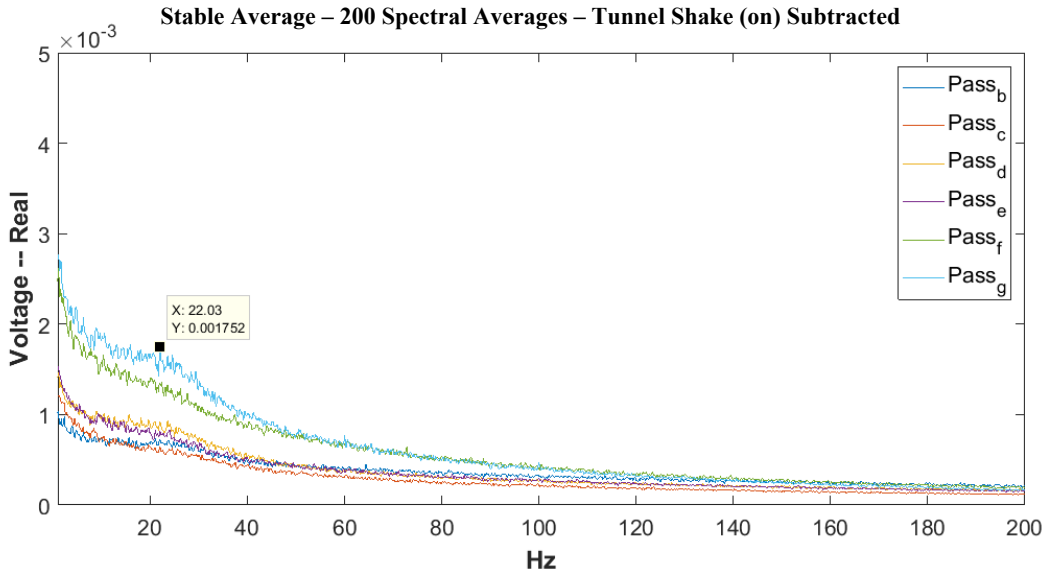

Figure 98. Under Tunnel Hot-film Corrected PSD, 200 Averages, 0-.005V v. 0-200 Hz, Peak Verification

The low frequency signal, below 3-5 Hz, was thought to be due to the vibrations of the tunnel. In order to test this hypothesis the sensor mounted below the passage was used and an average of 200 spectral averages was collected. It was observed that the magnitude of the shake of the tunnel was not the cause of the low frequency signal. Figure 99 is a side by side comparison of the sample series of the original 200 sample set and with the tunnel vibration signal subtracted.

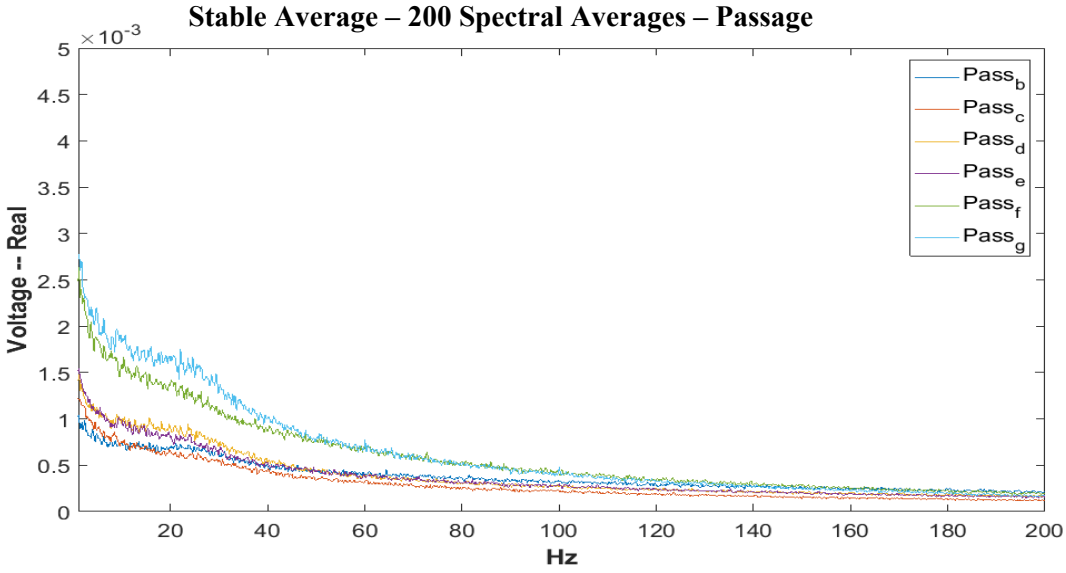

(A)

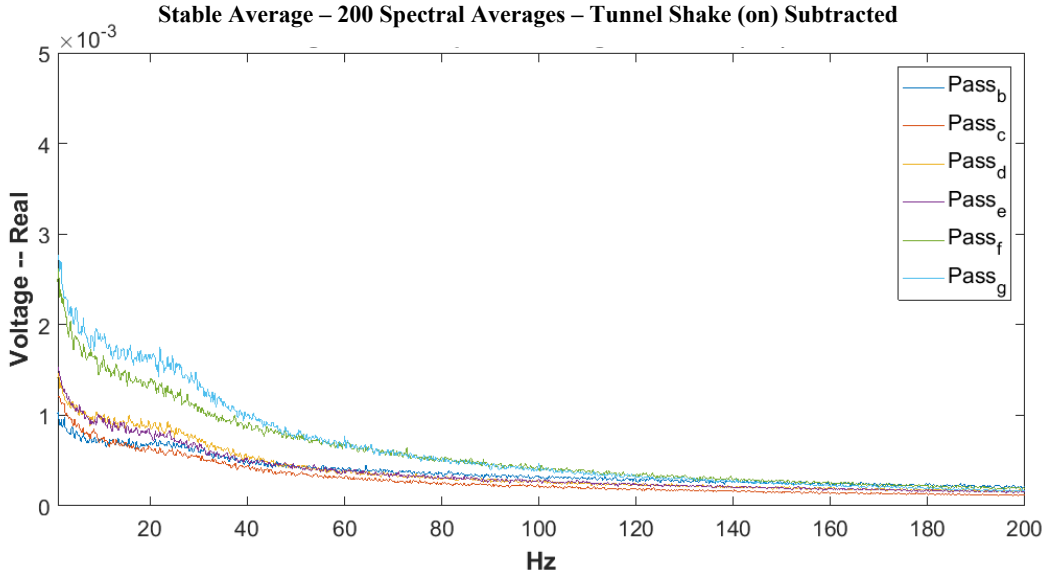

(B)

Figure 99. Comparison of 200 Stable averages with (B) and without (A) tunnel shake subtracted

It is not known at this time what causes the high magnitude for the signal in the range of f =3 to 5 Hz.

Appendix B – Total Pressure Loss

Appendix B contains all of the pressure loss measurements that have been collected in this endeavor. The measurements are laid out based upon forcing frequency and plane location. Plots are presented from 150% to 75% for each specific forcing case. Following the presentation of all of the individual plots, the in-passage, out-of-passage, and global maps are shown for the baseline and each forcing case. Finally, a collection of pitchwise, area averaged loss coefficient maps are shown for a selection of cases.

Individual Pressure Loss Plots:

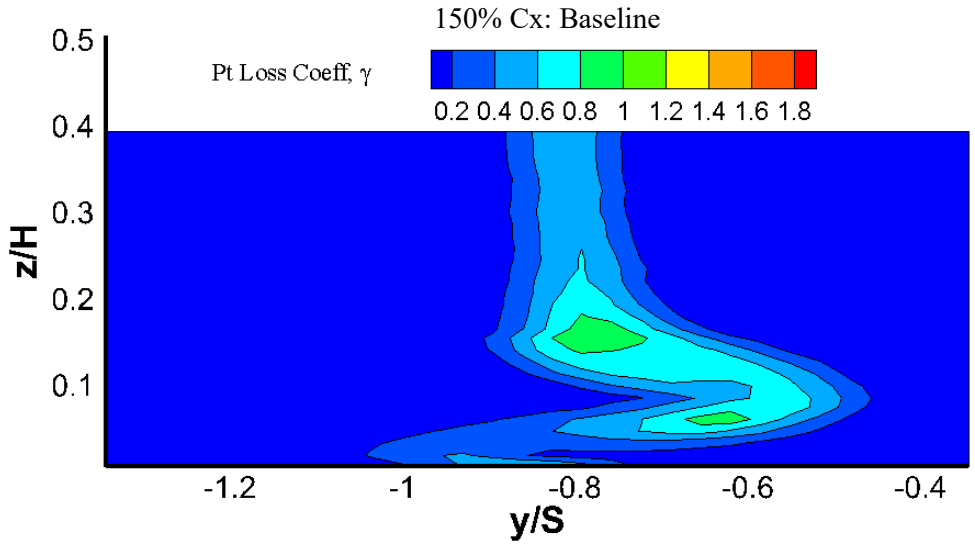

Figure 100. Baseline 150% Cx Total Pressure Loss Map

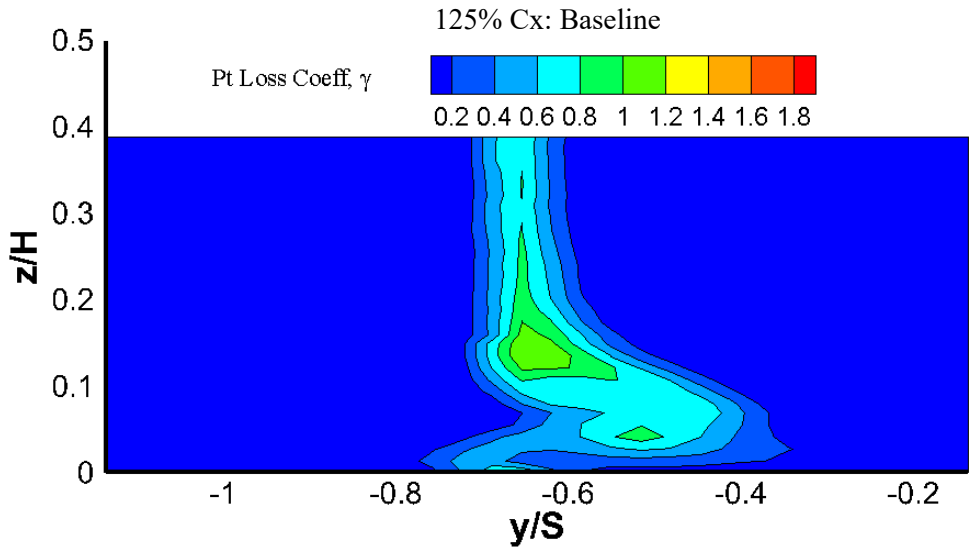

Figure 101. Baseline 125% Cx Total Pressure Loss Map

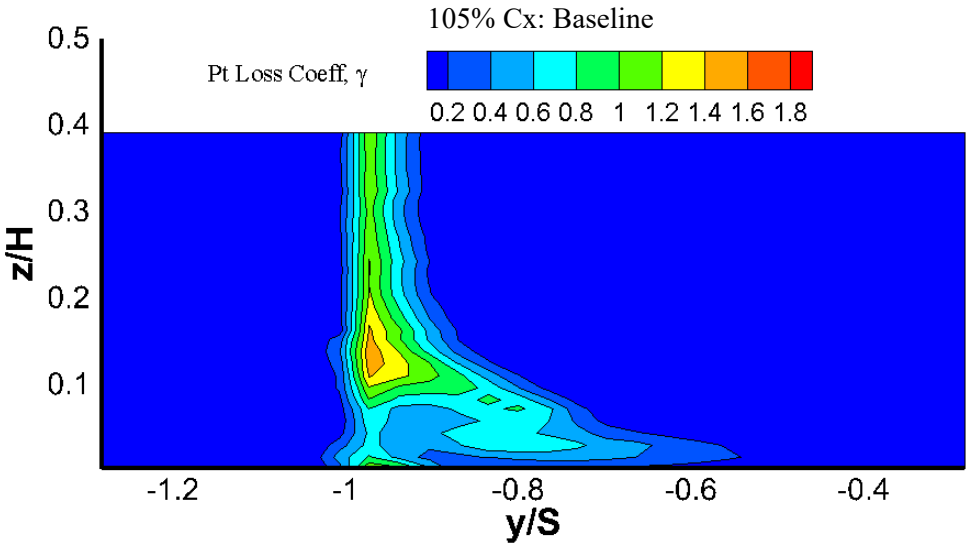

Figure 102. Baseline 105% Cx Total Pressure Loss Map

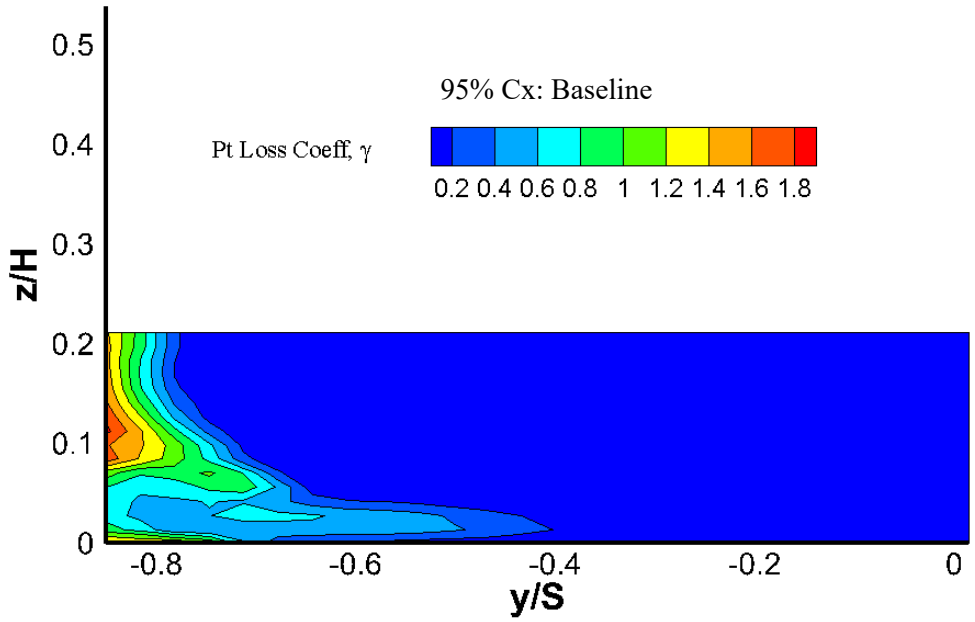

Figure 103. Baseline 95% Cx Total Pressure Loss Map

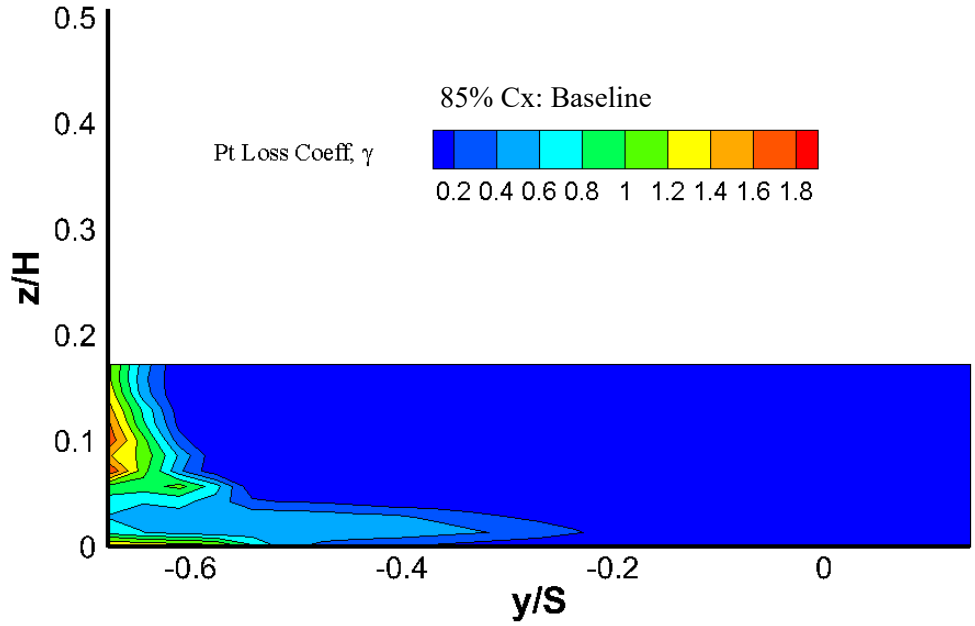

Figure 104. Baseline 85% Cx Total Pressure Loss Map

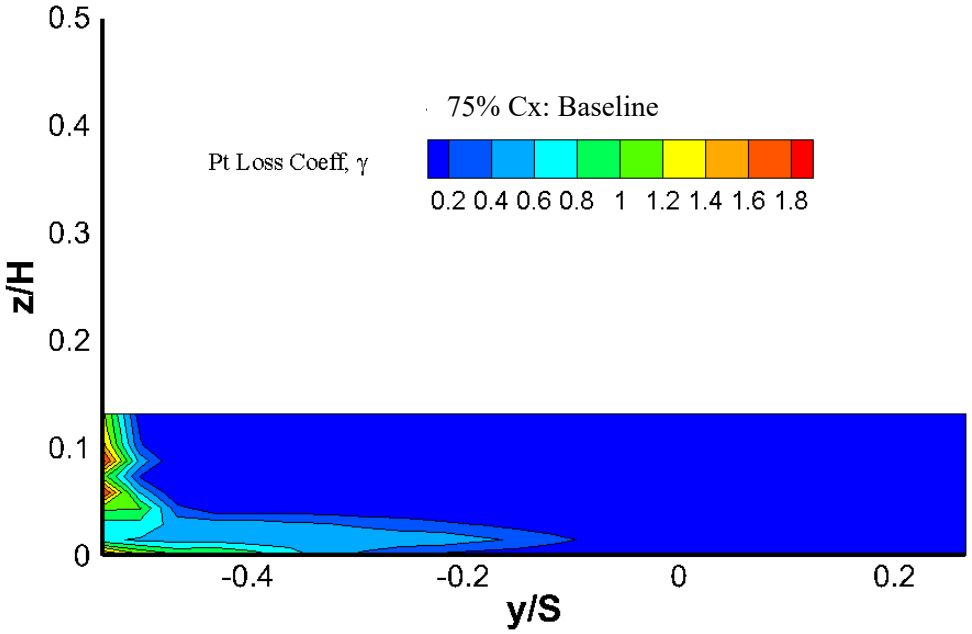

Figure 105. Baseline 75% Cx Total Pressure Loss Map

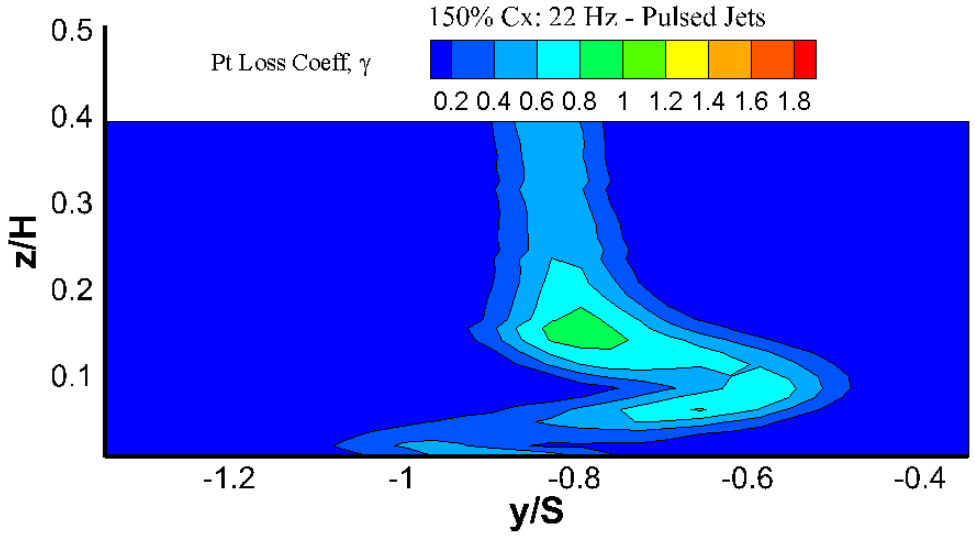

Figure 106. 22 Hz Pulsed Jets 150% Cx Total Pressure Loss Map

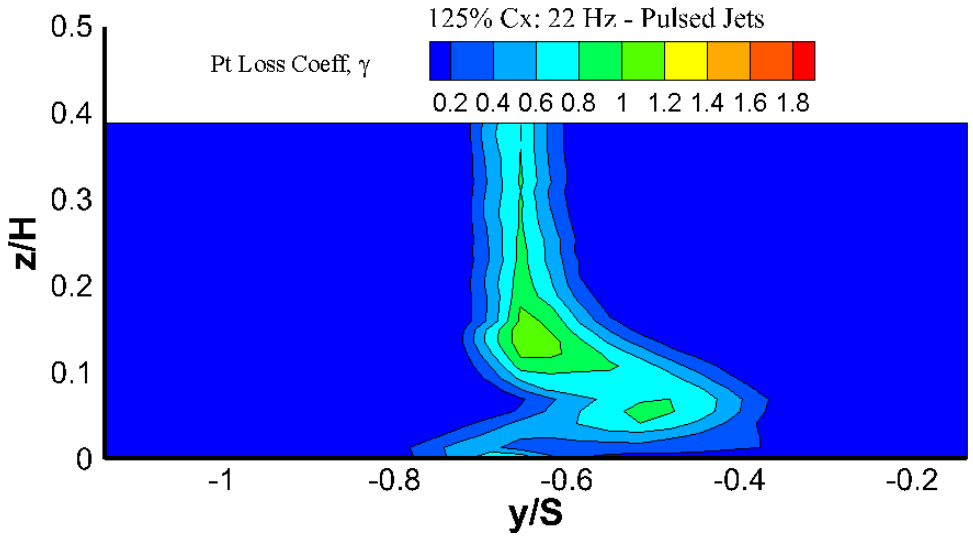

Figure 107. 22 Hz Pulsed Jets 125% Cx Total Pressure Loss Map

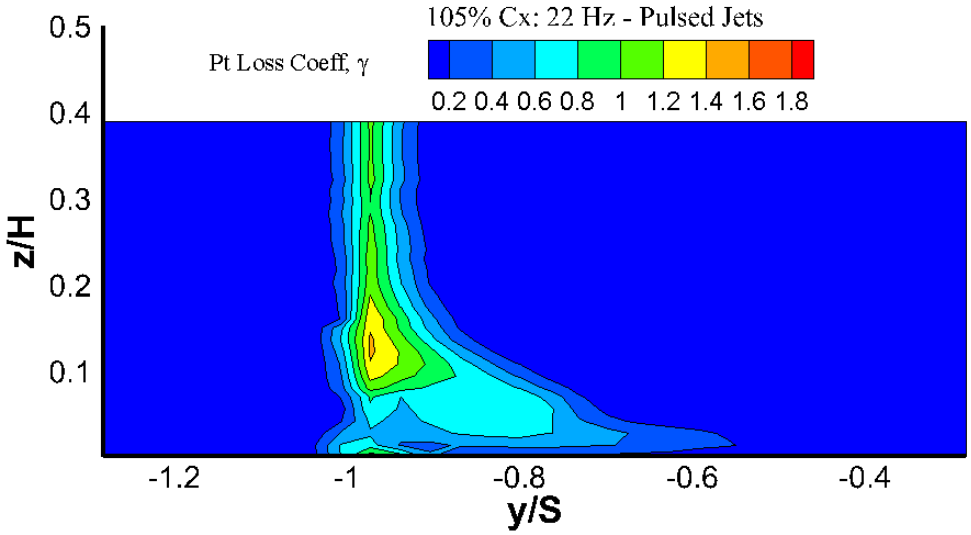

Figure 108. 22 Hz Pulsed Jets 105% Cx Total Pressure Loss Map

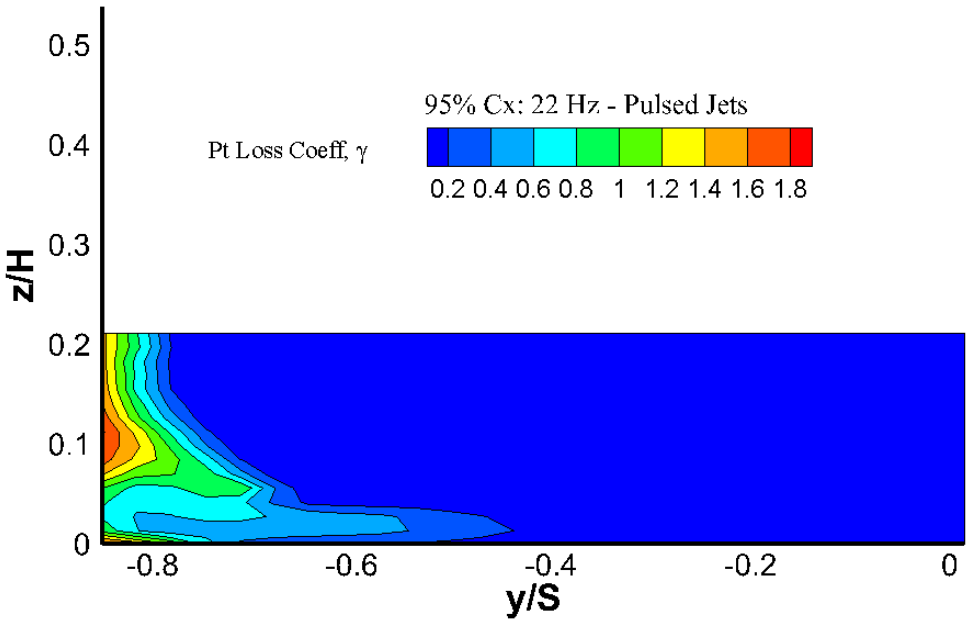

Figure 109. 22 Hz Pulsed Jets 95% Cx Total Pressure Loss Map

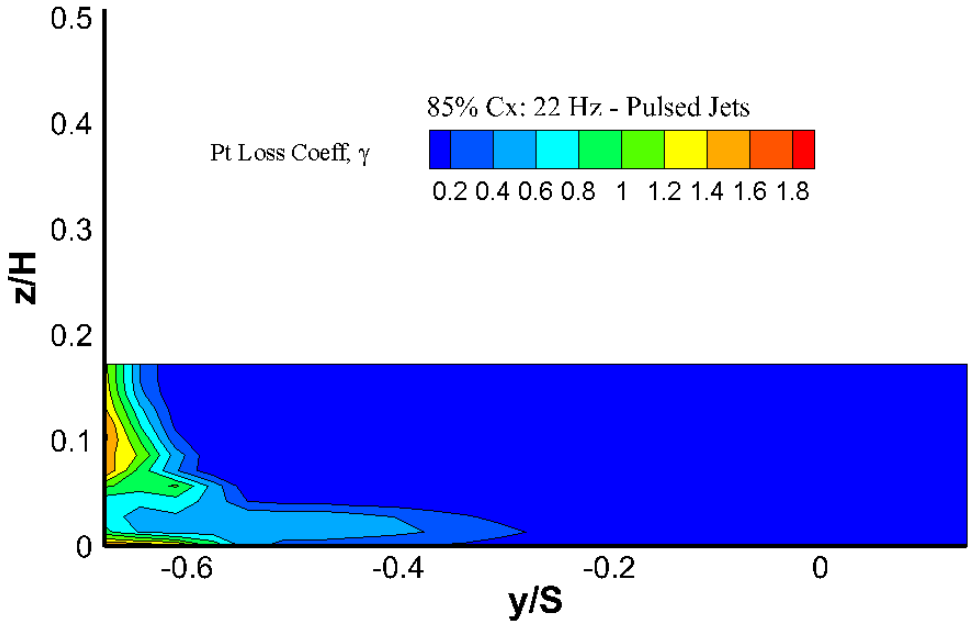

Figure 110. 22 Hz Pulsed Jets 85% Cx Total Pressure Loss Map

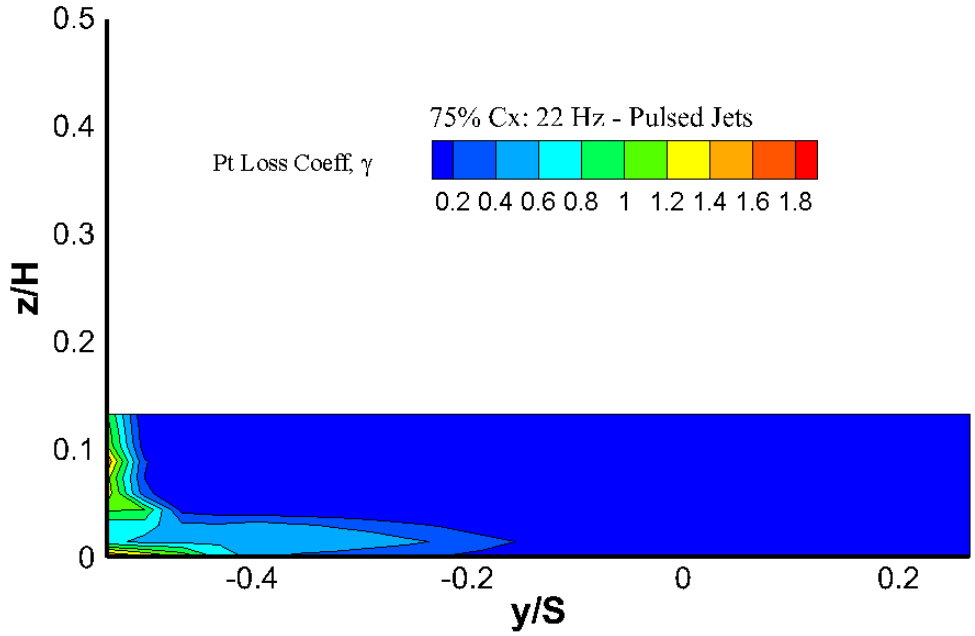

Figure 111. 22 Hz Pulsed Jets 75% Cx Total Pressure Loss Map

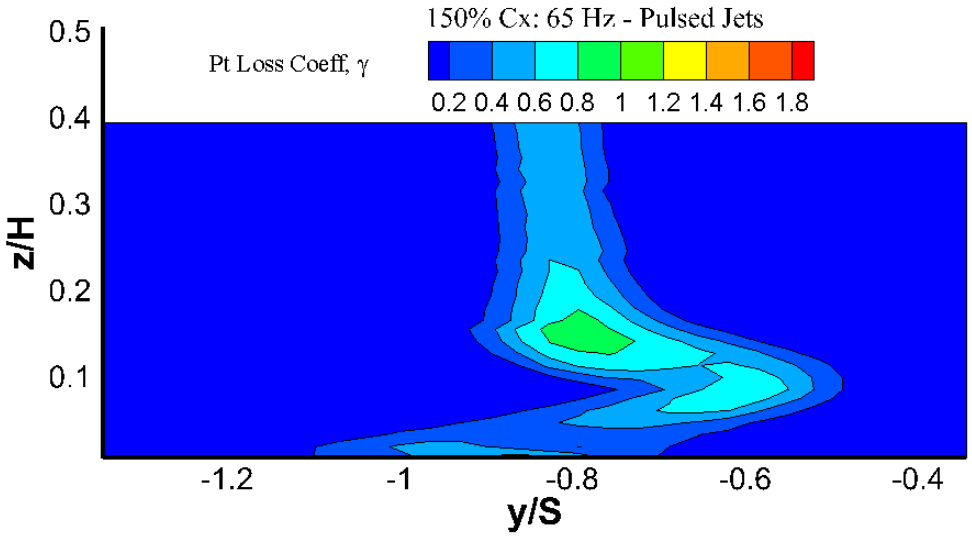

Figure 112. 65 Hz Pulsed Jets 150% Cx Total Pressure Loss Map

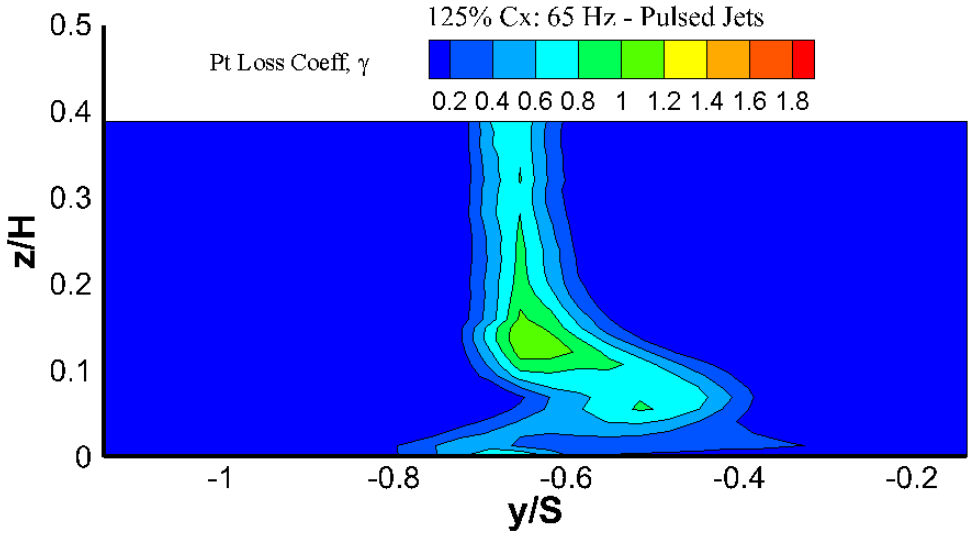

Figure 113. 65 Hz Pulsed Jets 125% Cx Total Pressure Loss Map

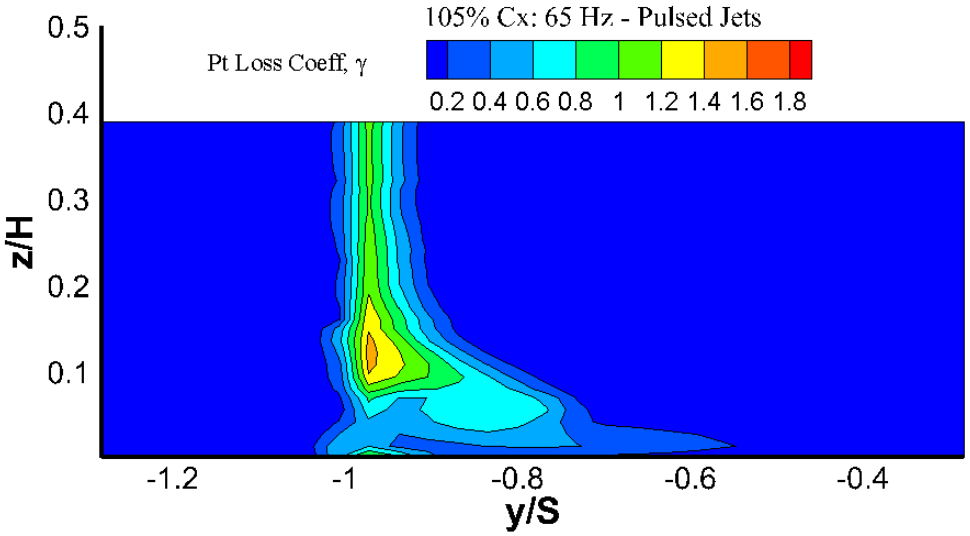

Figure 114. 65 Hz Pulsed Jets 105% Cx Total Pressure Loss Map

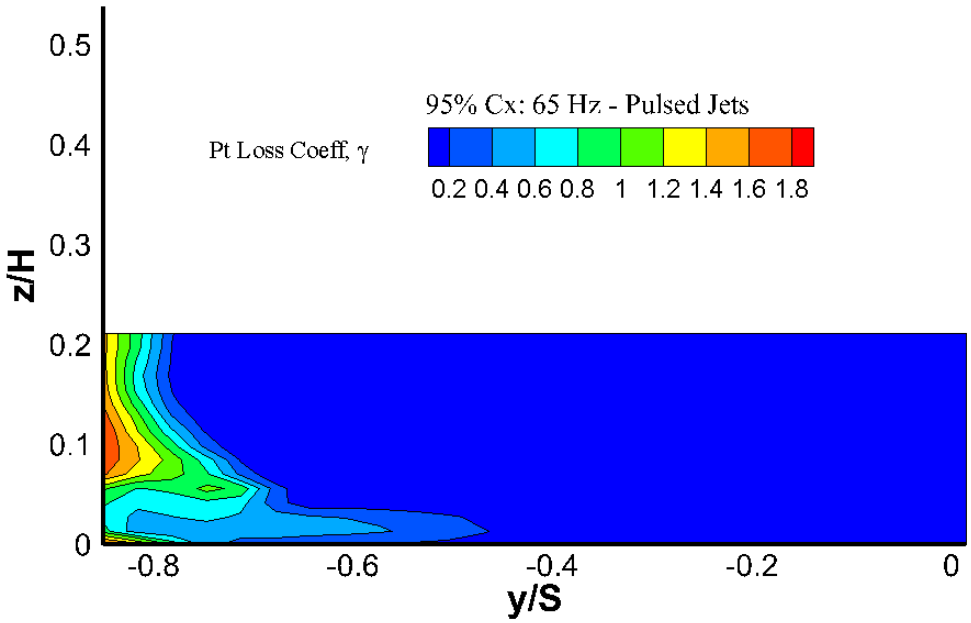

Figure 115. 65 Hz Pulsed Jets 95% Cx Total Pressure Loss Map

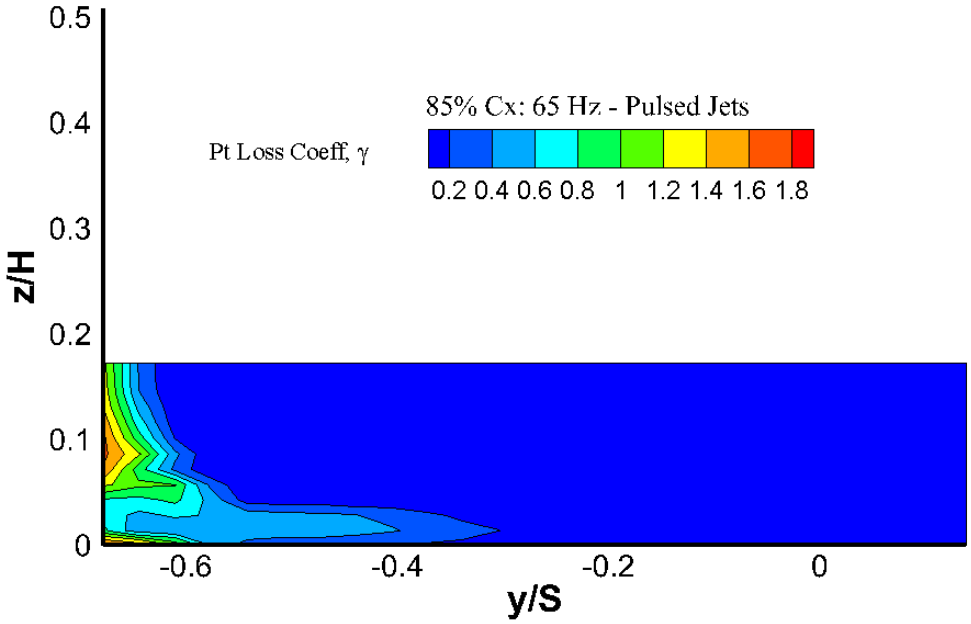

Figure 116. 65 Hz Pulsed Jets 85% Cx Total Pressure Loss Map

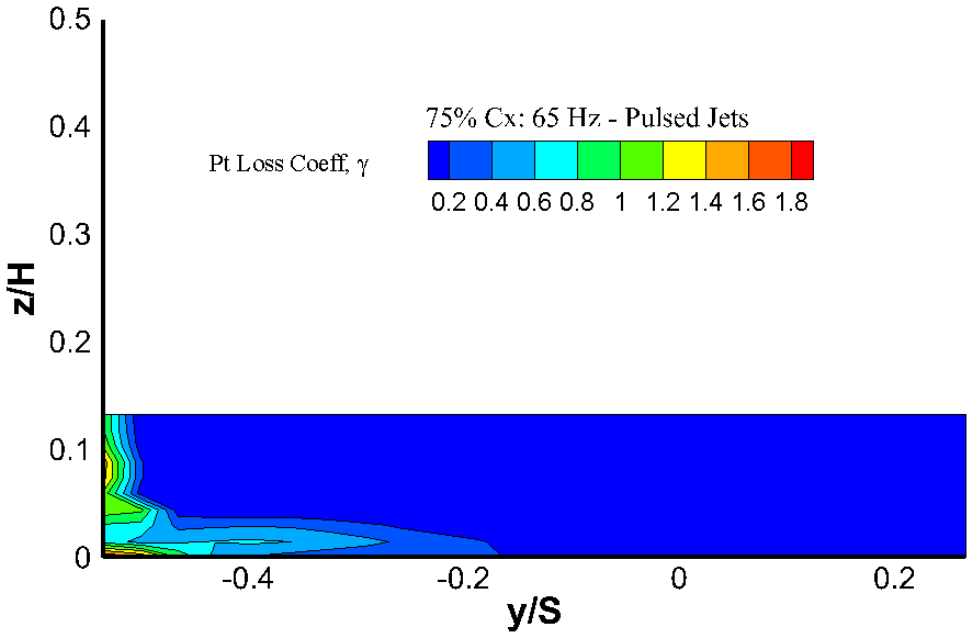

Figure 117. 65 Hz Pulsed Jets 75% Cx Total Pressure Loss Map

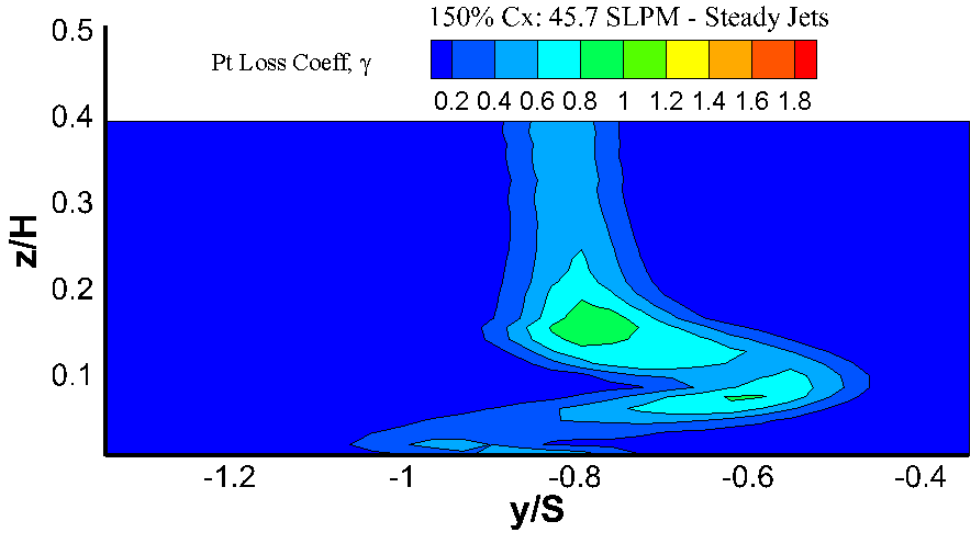

Figure 118. 45.7 SLPM Steady Jets 150% Cx Total Pressure Loss Map

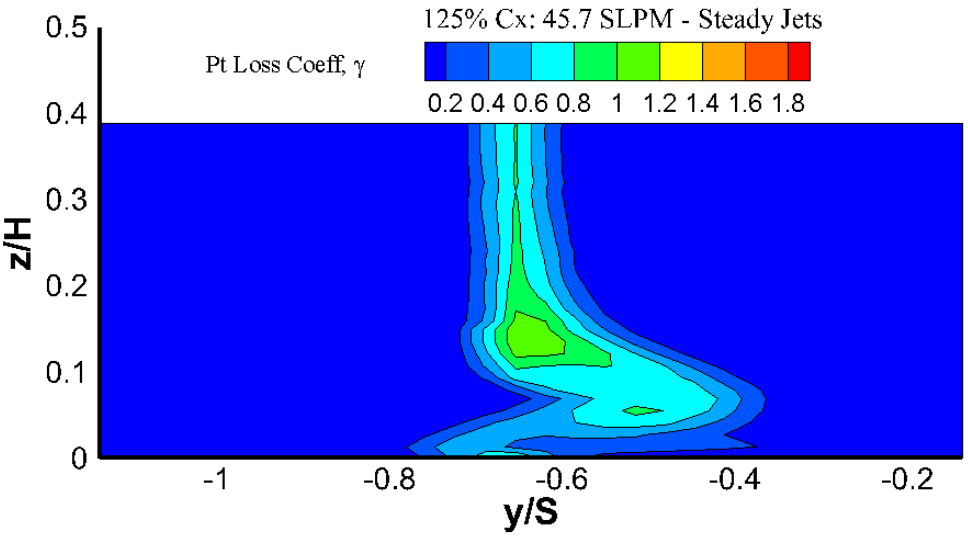

Figure 119. 45.7 SLPM Steady Jets 125% Cx Total Pressure Loss Map

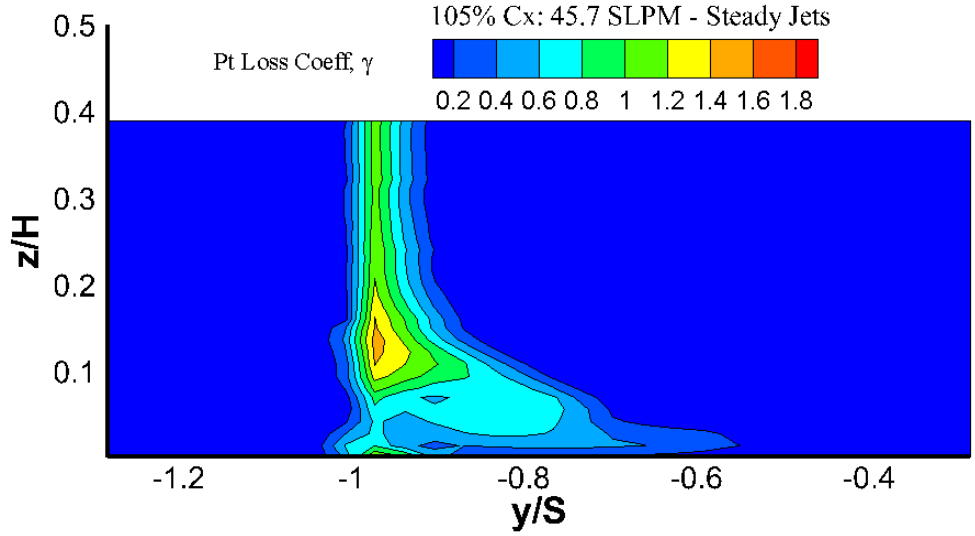

Figure 120. 45.7 SLPM Steady Jets 105% Cx Total Pressure Loss Map

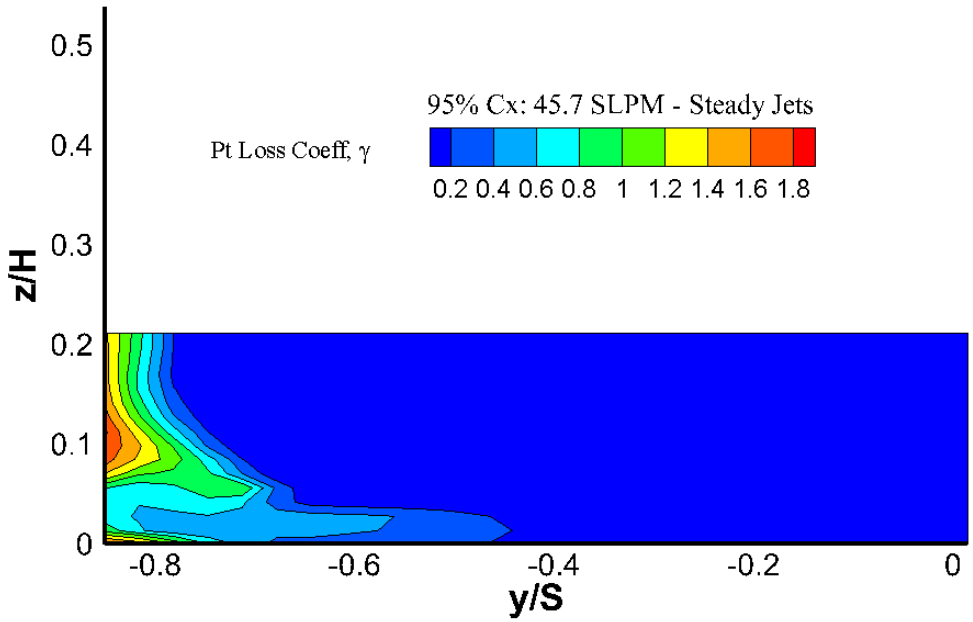

Figure 121. 45.7 SLPM Steady Jets 95% Cx Total Pressure Loss Map

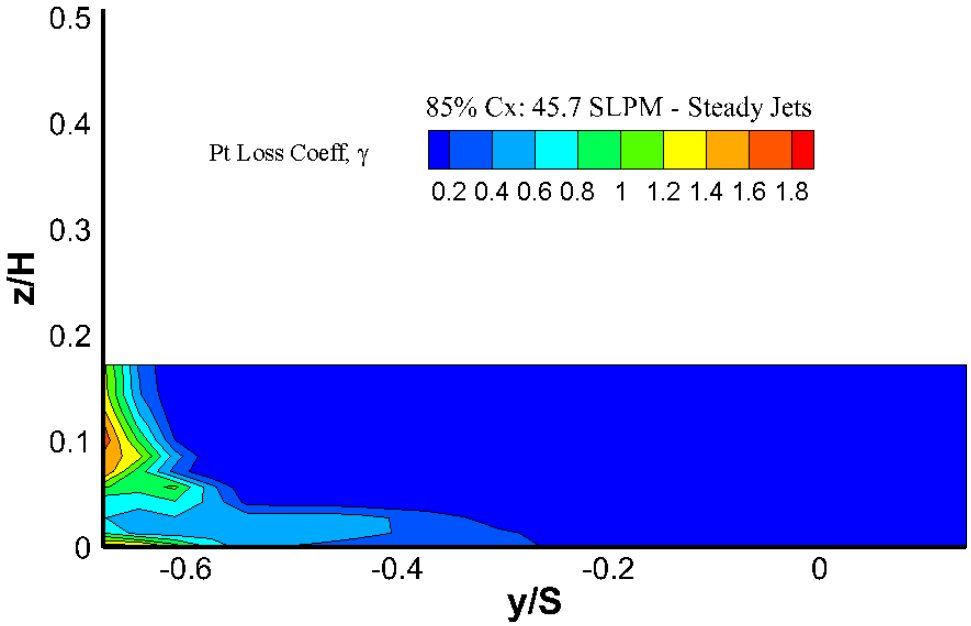

Figure 122. 45.7 SLPM Steady Jets 85% Cx Total Pressure Loss Map

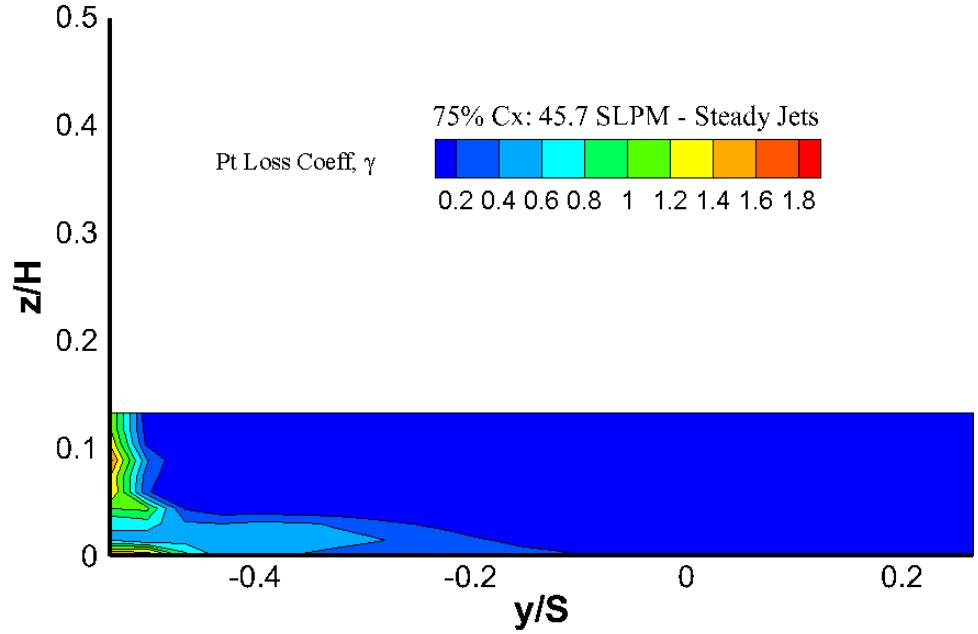

Figure 123. 45.7 SLPM Steady Jets 75% Cx Total Pressure Loss Map

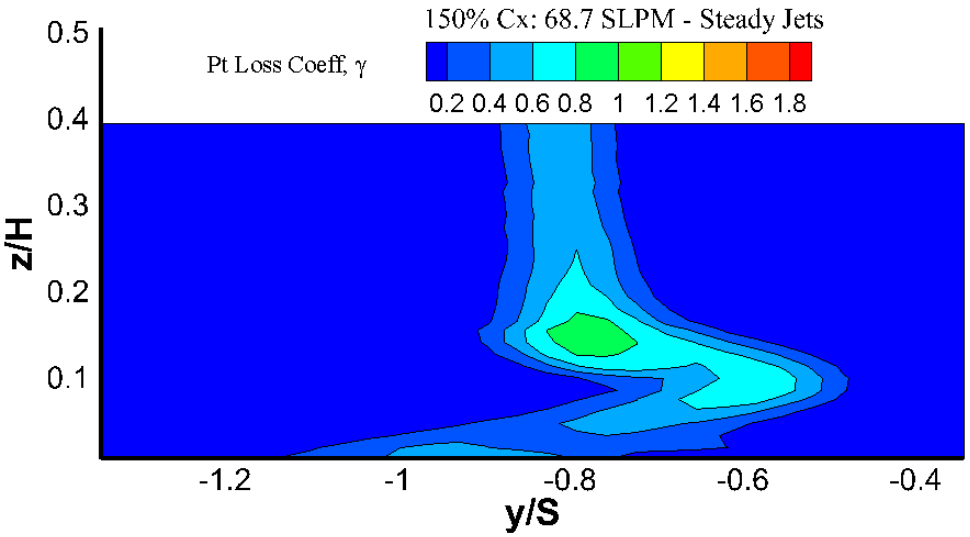

Figure 124. 68.7 SLPM Steady Jets 150% Cx Total Pressure Loss Map

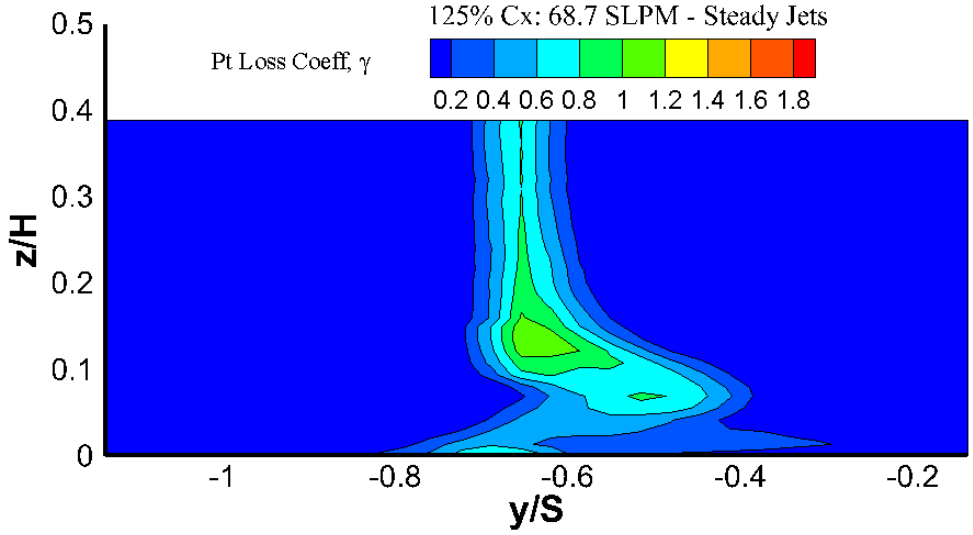

Figure 125. 68.7 SLPM Steady Jets 125% Cx Total Pressure Loss Map

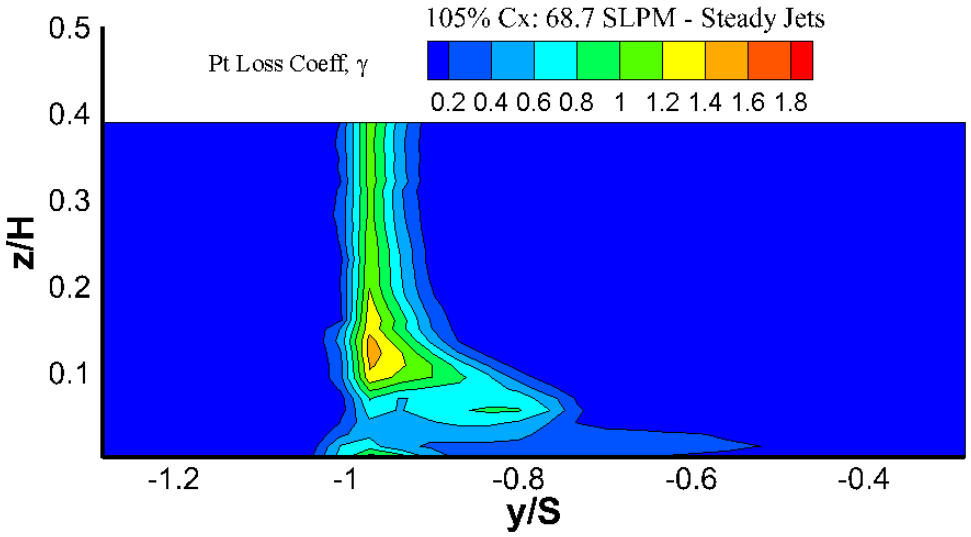

Figure 126. 68.7 SLPM Steady Jets 105% Cx Total Pressure Loss Map

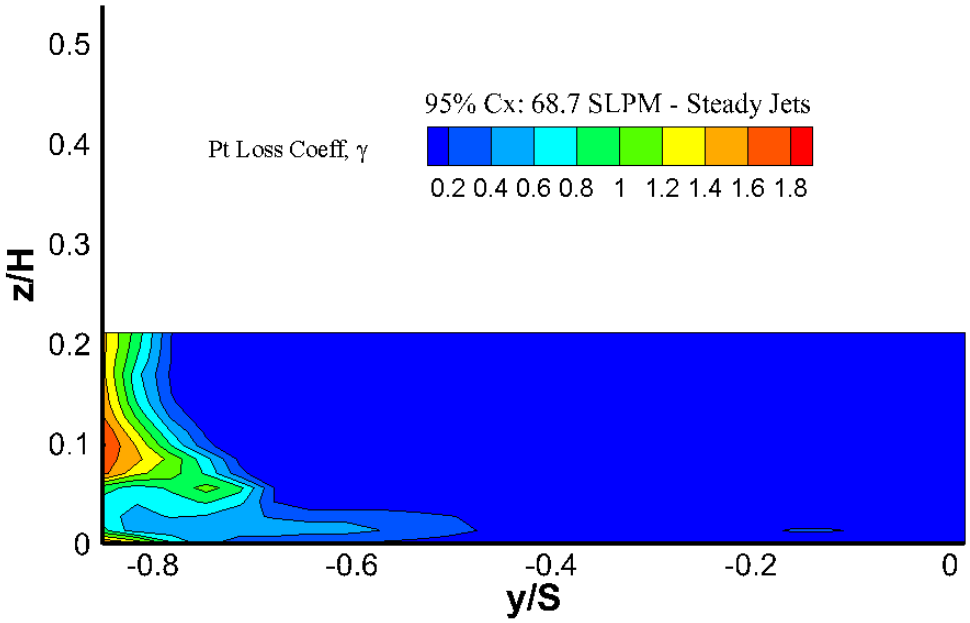

Figure 127. 68.7 SLPM Steady Jets 95% Cx Total Pressure Loss Map

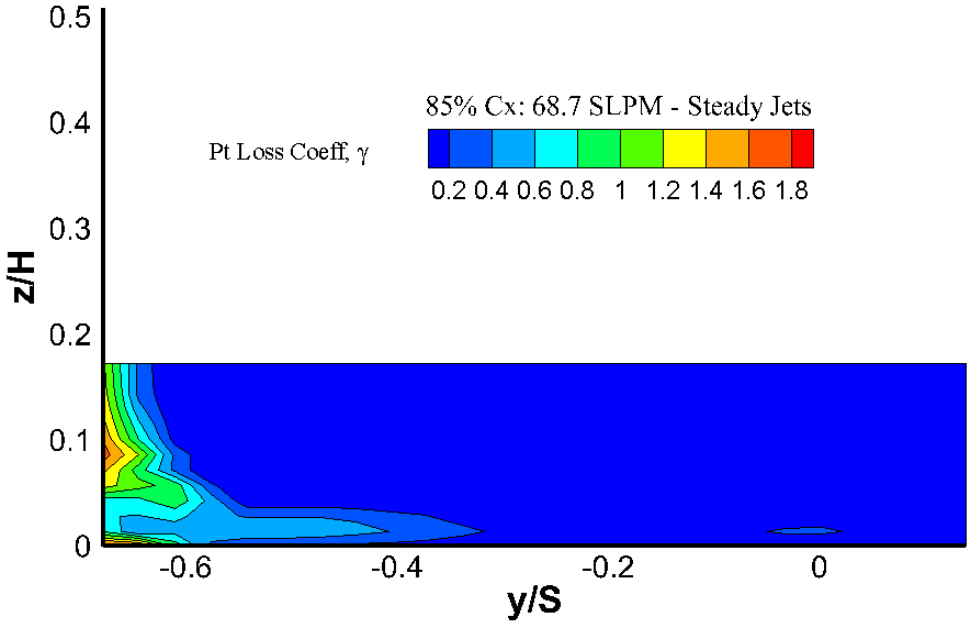

Figure 128. 68.7 SLPM Steady Jets 85% Cx Total Pressure Loss Map

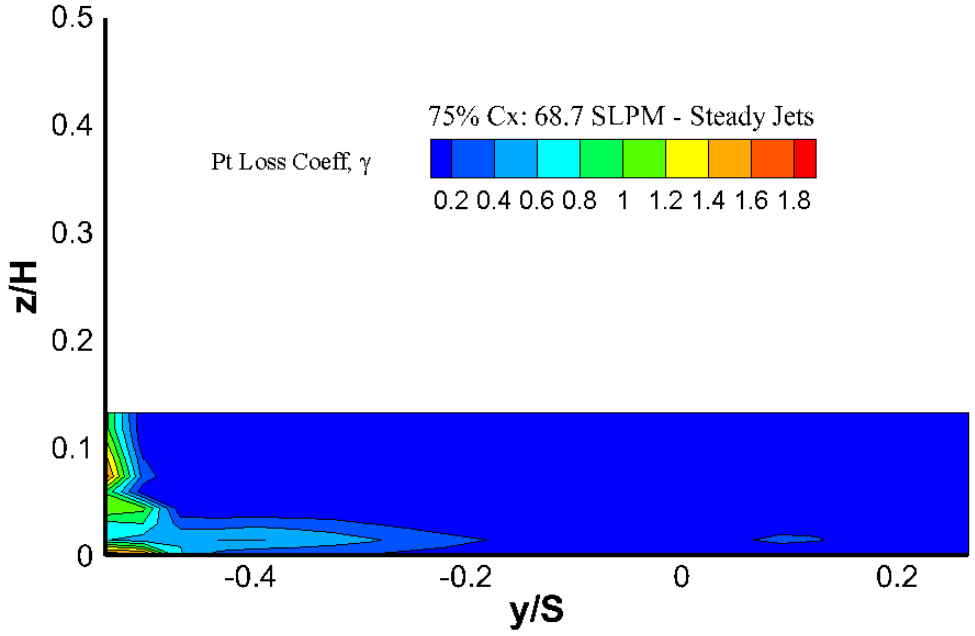

Figure 129. 68.7 SLPM Steady Jets 75% Cx Total Pressure Loss Map

Global Pressure Loss Mapping Plots:

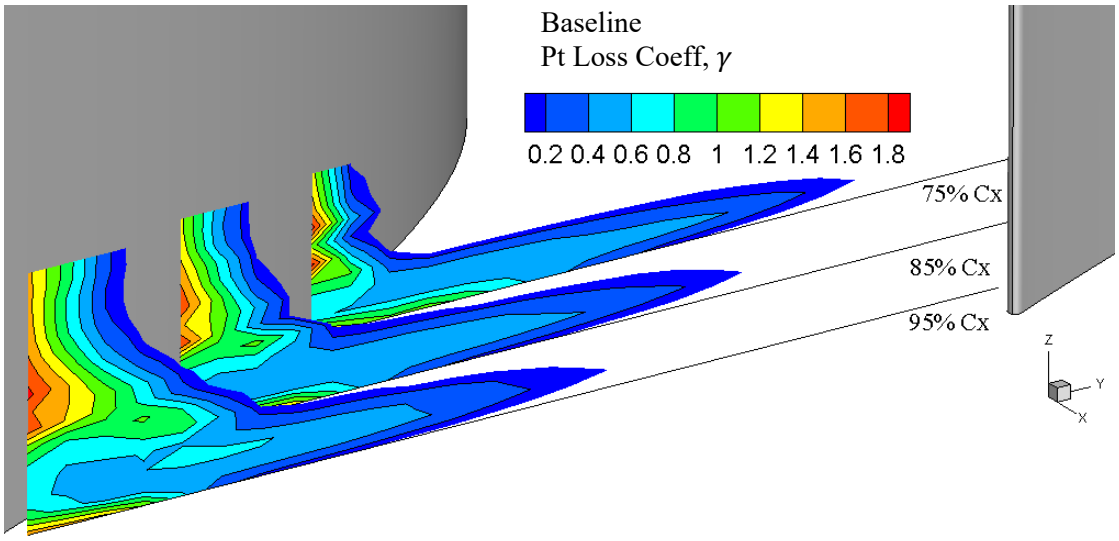

Figure 130. Baseline In-Passage Total Pressure Loss Map

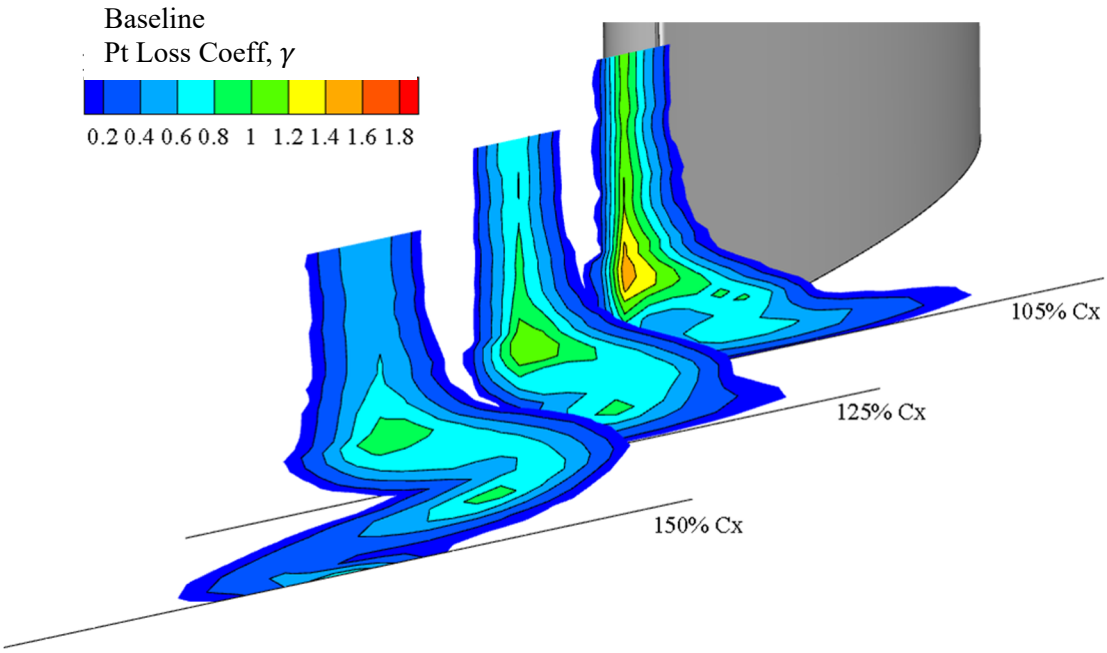

Figure 131. Baseline Out-of-Passage Total Pressure Loss Map

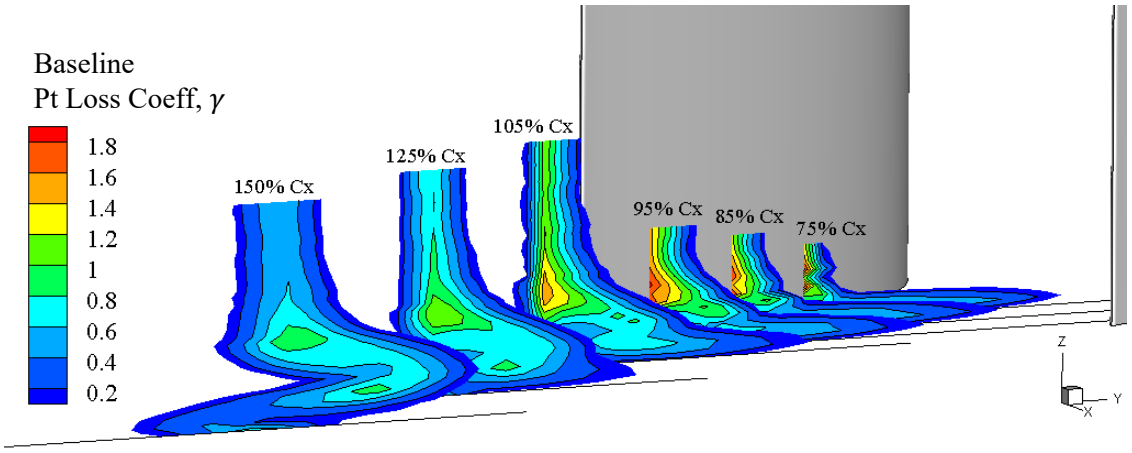

Figure 132. Baseline Global Total Pressure Loss Map

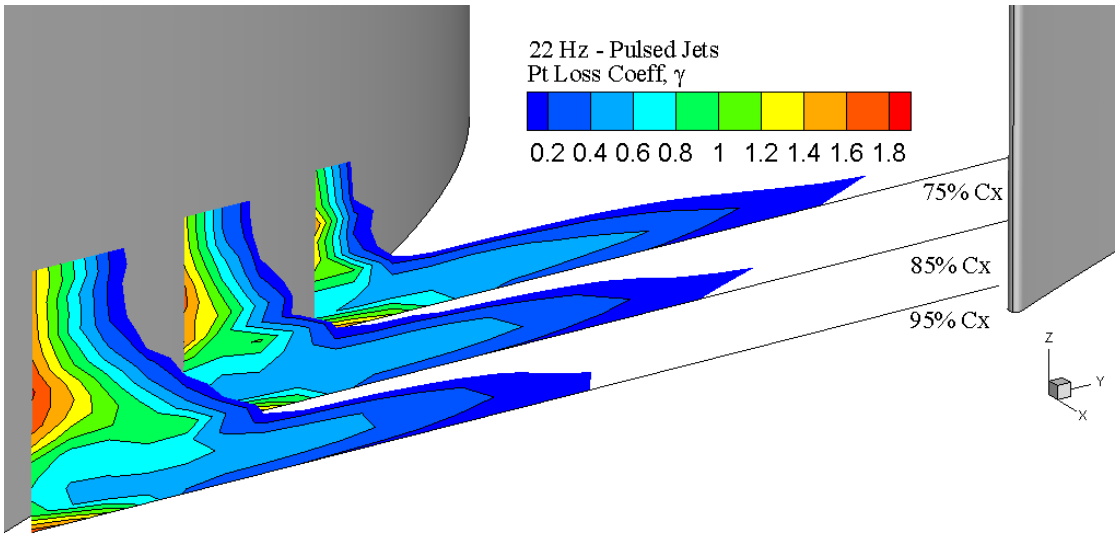

Figure 133. 22 Hz Pulsed In-Passage Total Pressure Loss Map

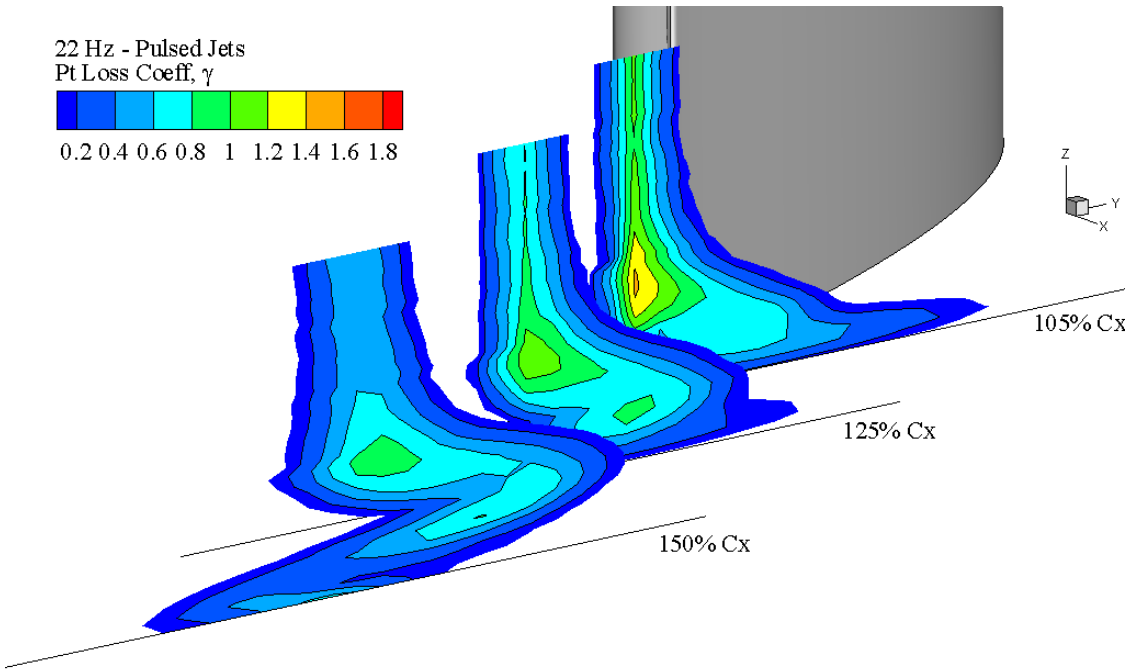

Figure 134. 22 Hz Pulsed Out-of-Passage Total Pressure Loss Map

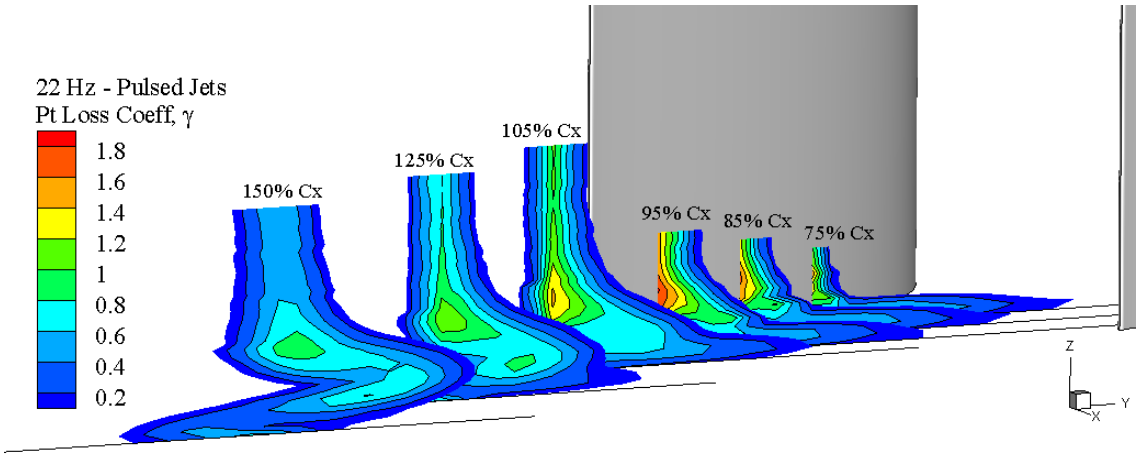

Figure 135. 22 Hz Pulsed Global Passage Total Pressure Loss Map

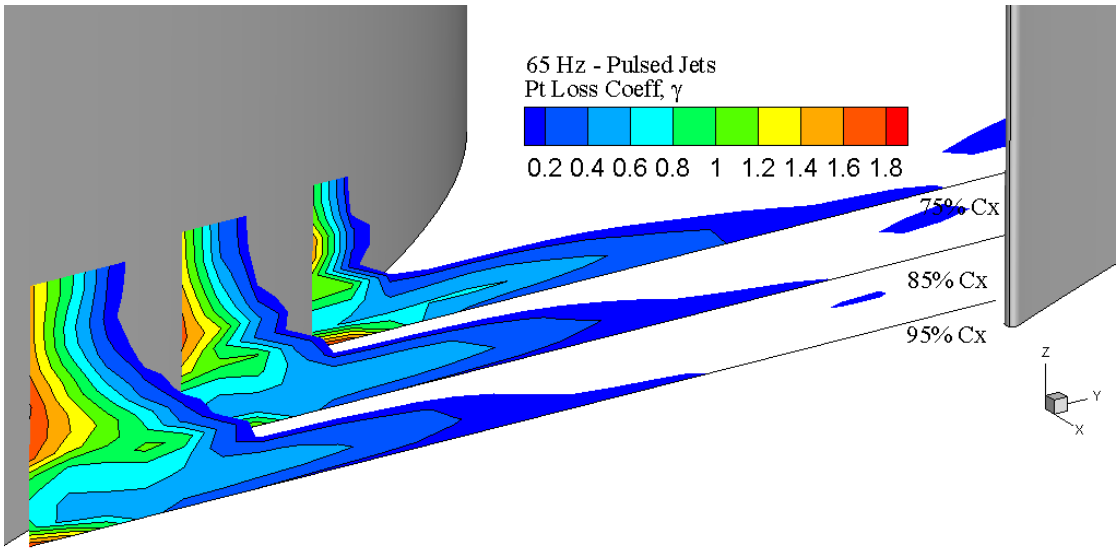

Figure 136. 65 Hz Pulsed In-Passage Total Pressure Loss Map

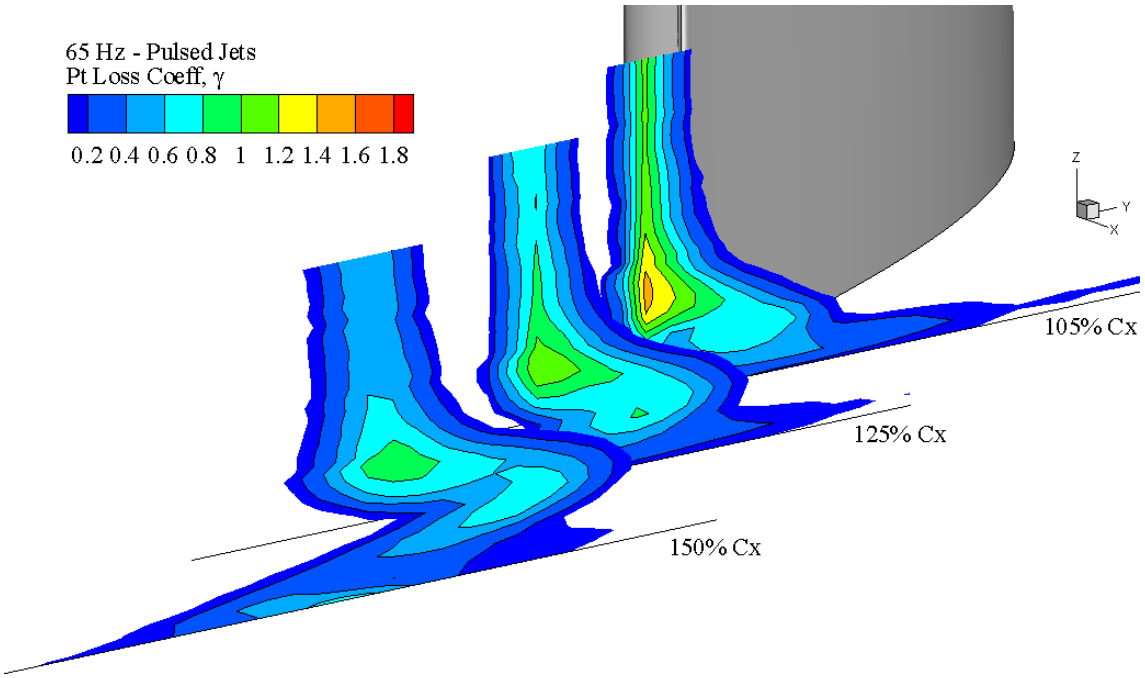

Figure 137. 65 Hz Pulsed Out-of-Passage Total Pressure Loss Map

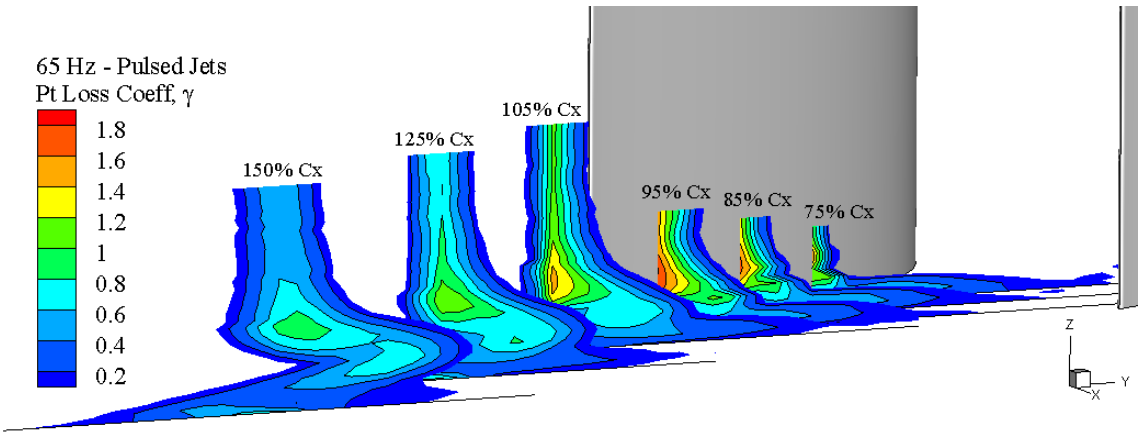

Figure 138. 65 Hz Pulsed Global Passage Total Pressure Loss Map

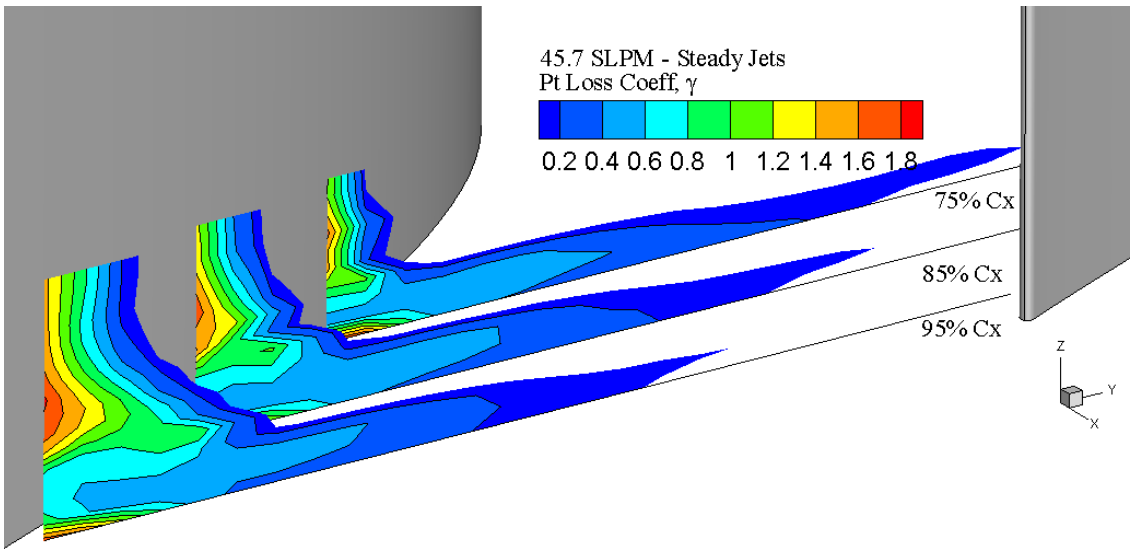

Figure 139. 45.7 SLPM Steady Jets In-Passage Total Pressure Loss Map

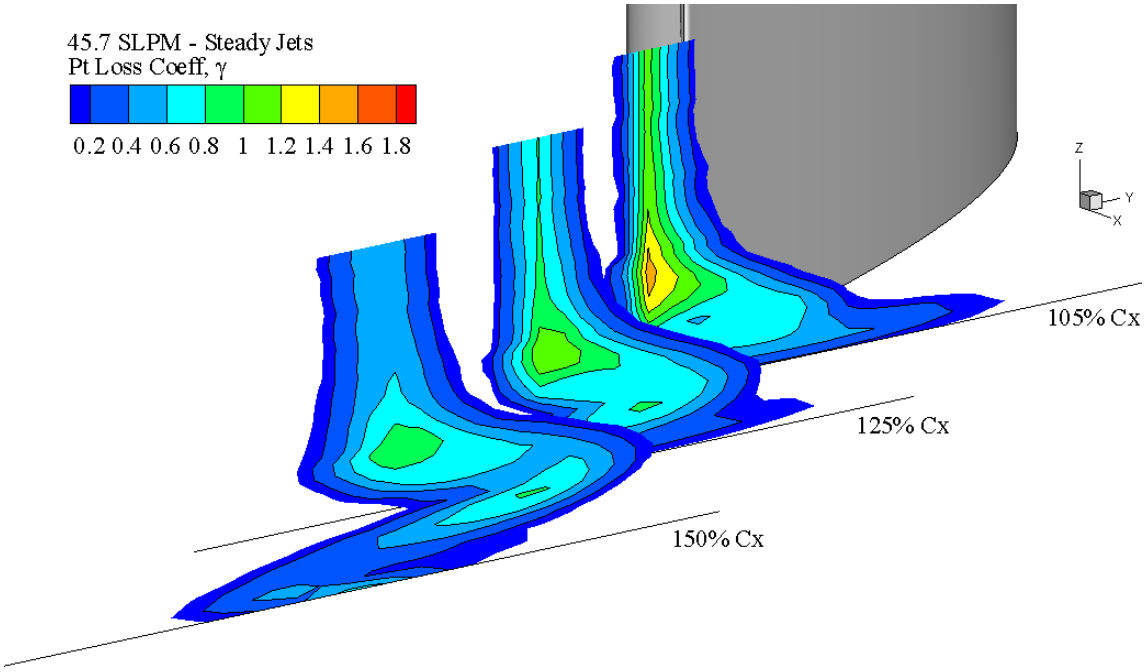

Figure 140. 45.7 SLPM Steady Jets Out-of-Passage Total Pressure Loss Map

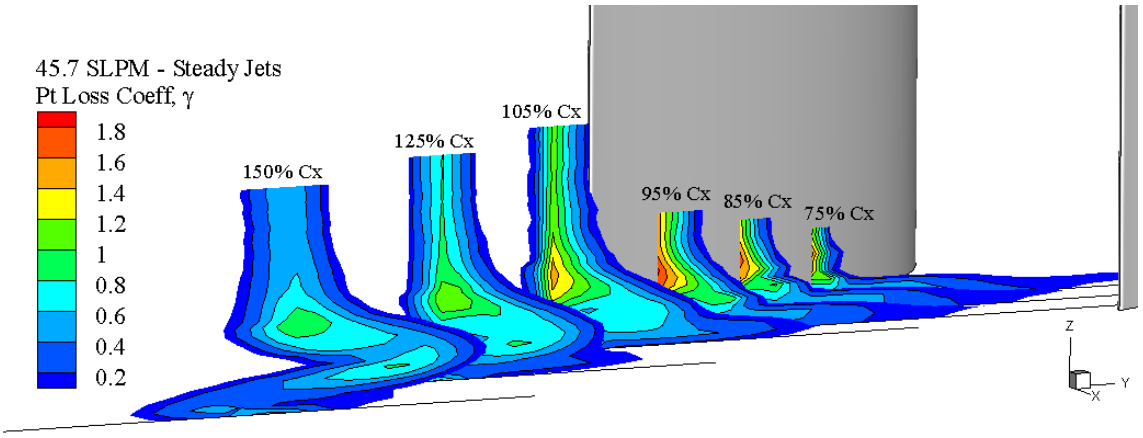

Figure 141. 45.7 SLPM Steady Jets Global Passage Total Pressure Loss Map

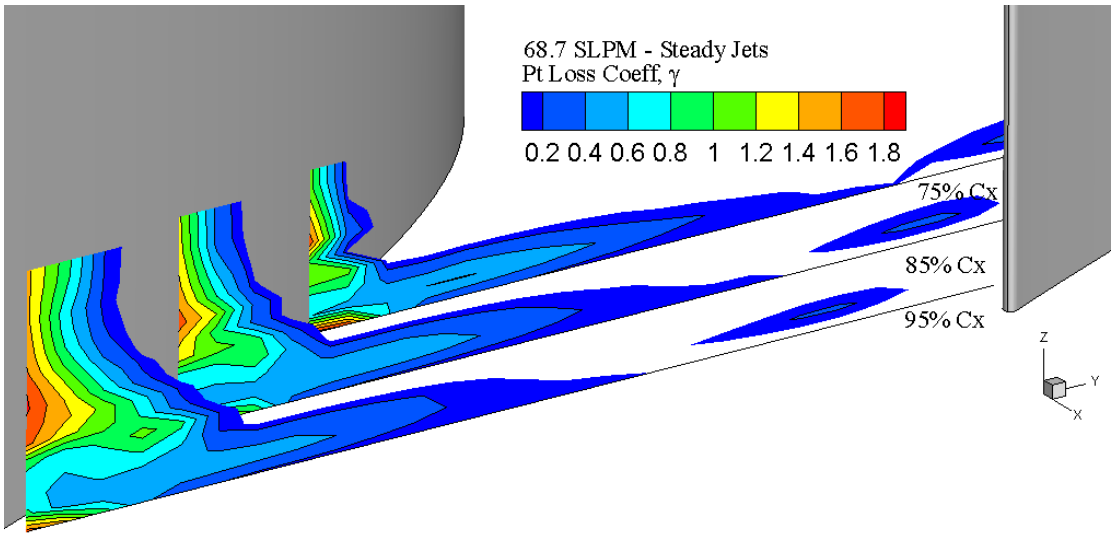

Figure 142. 68.7 SLPM Steady Jets In-Passage Total Pressure Loss Map

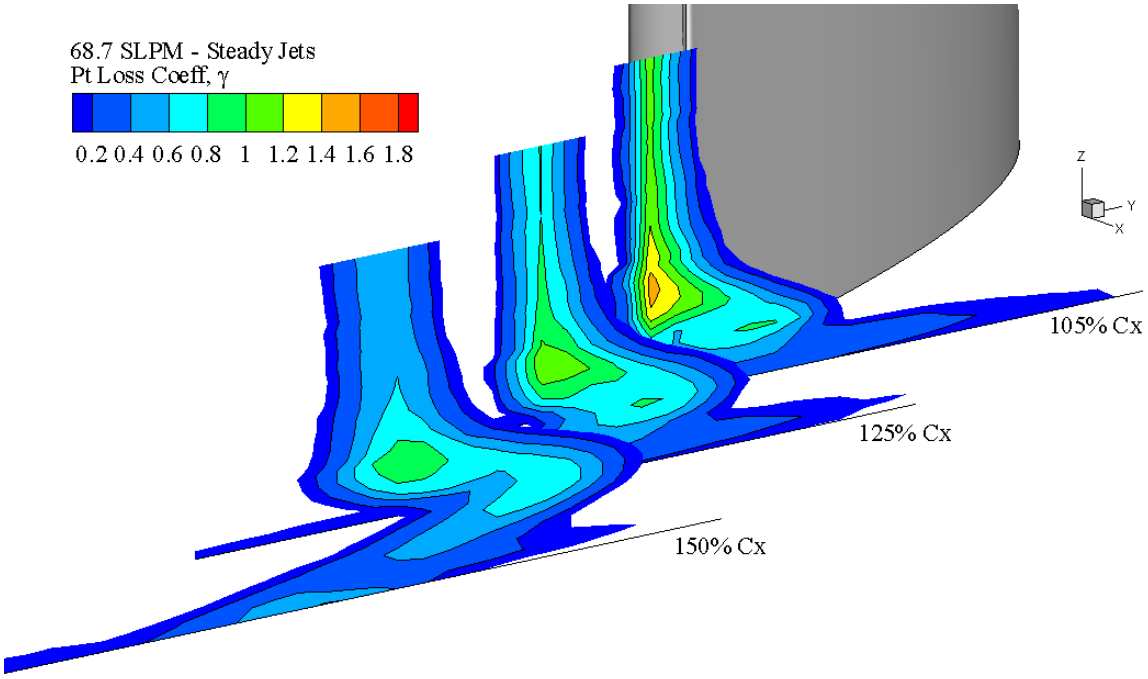

Figure 143. 68.7 SLPM Steady Jets Out-of-Passage Total Pressure Loss Map

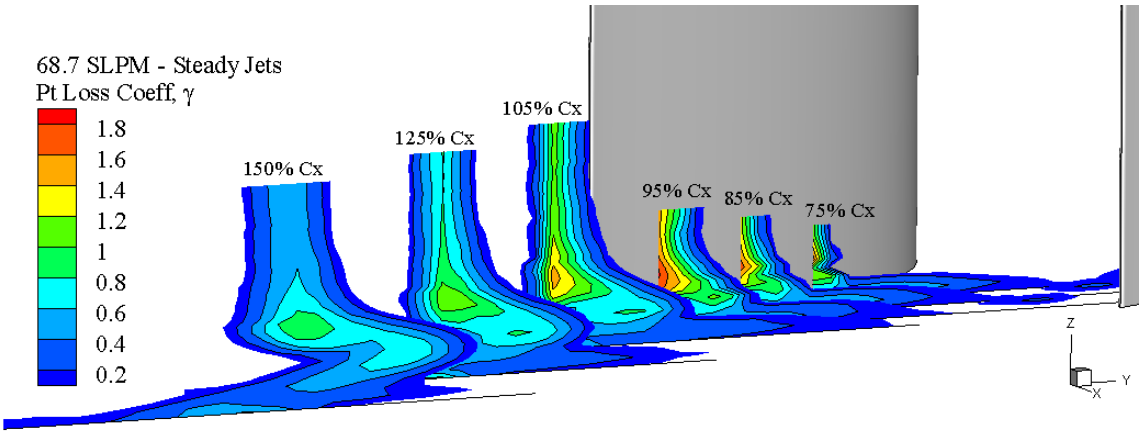

Figure 144. 68.7 SLPM Steady Jets Global Passage Total Pressure Loss Map

Pitchwise Area-Averaged Loss Comparison Plots:

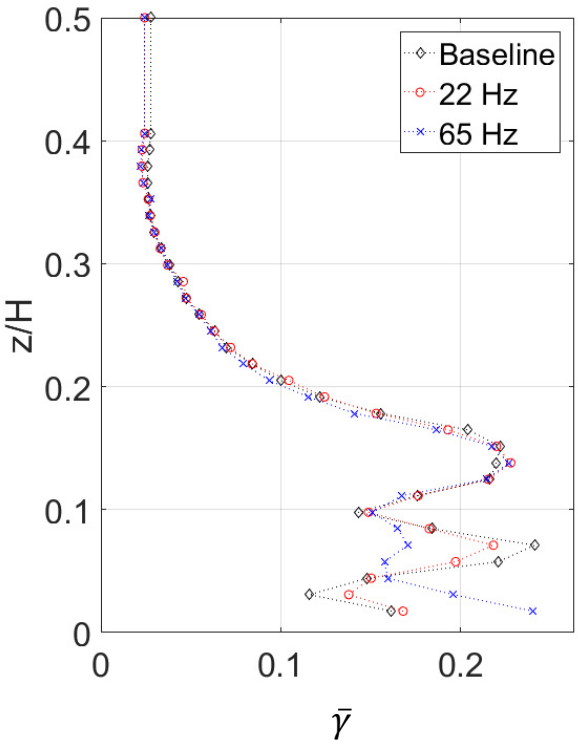

Figure 145. Pulsed Jet Pitchwise Area-Averaged Loss Comparison

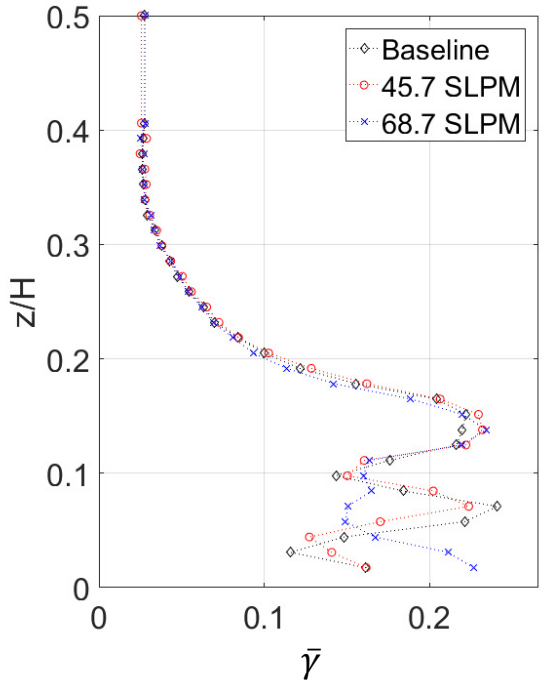

Figure 146. Steady Jet Pitchwise Area-Averaged Loss Comparison

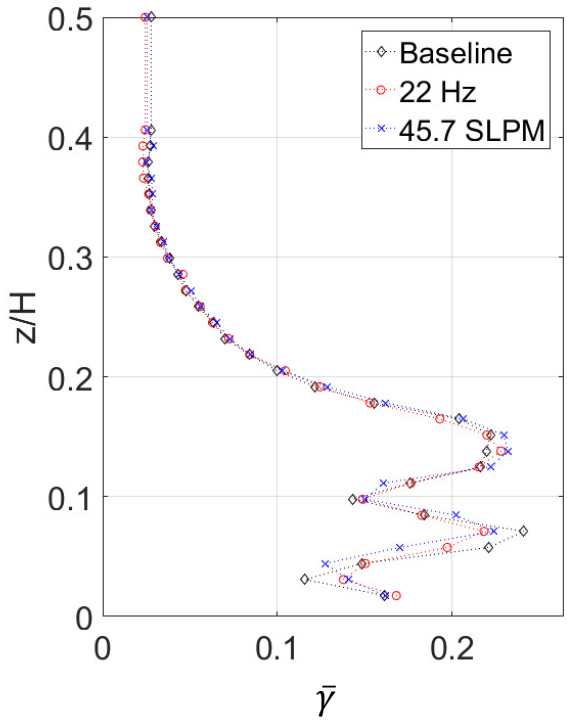

Figure 147. 22 Hz Pulsed - 45.7 SLPM Steady Jet Pitchwise Area-Averaged Loss Comparison

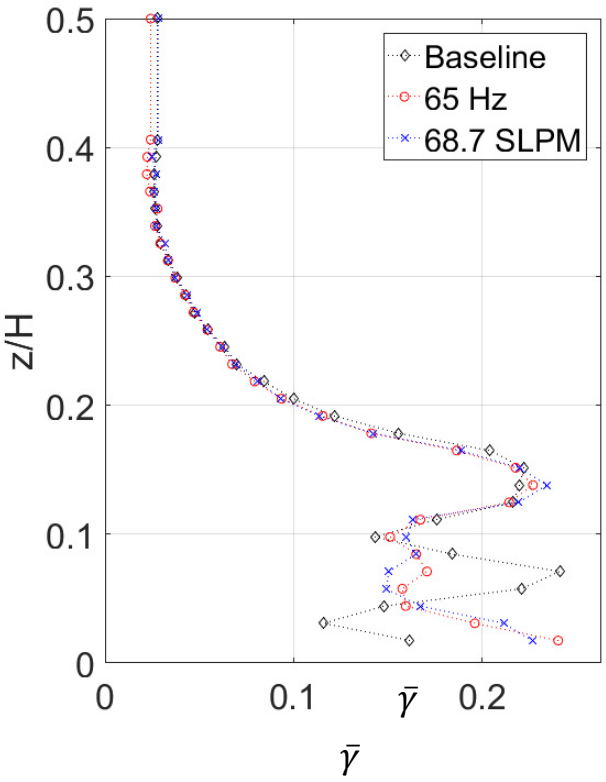

Figure 148. 65 Hz Pulsed - 68.7 SLPM Steady Jet Pitchwise Area-Averaged Loss Comparison

Appendix C – Streamwise Vorticity Derivation

Appendix C steps through the derivation of streamwise vorticity as first presented by Gregory-Smith[68]. Following that derivation, new assumptions are added and a derivation is preformed that had not seen in present literature.

Gregory-Smith[68] provides an approximation for finding streamwise vorticity as being derived from the incompressible Helmholtz equation.

$$\omega_y = \frac{1}{u}\left[\frac{1}{\rho}\frac{\partial p_o}{\partial z} + v\omega_x\right] \quad (1)$$

This derivation can be verified ab initio beginning with the *Gromeka-Lamb* form of the Navier-Stokes equations presented in Granger[71].

$$\frac{\partial \boldsymbol{V}}{\partial t} + \boldsymbol{\omega} \times \boldsymbol{V} = \boldsymbol{g} - \boldsymbol{\nabla}\left(\frac{p}{\rho} + \frac{V^2}{2}\right) - \nu(\boldsymbol{\nabla} \times \boldsymbol{\omega}) \quad (2)$$

Assuming steady, incompressible, inviscid and a negligible effect of gravity the *Gromeka-Lamb* equation simplifies to

$$\boldsymbol{\omega} \times \boldsymbol{V} = -\frac{1}{\rho}\nabla\left(p + \rho\frac{V^2}{2}\right) \quad (3)$$

A vector identity switches the sign on the RHS of the equation

$$\boldsymbol{V} \times \boldsymbol{\omega} = \frac{1}{\rho}\nabla\left(p + \rho\frac{V^2}{2}\right) \quad (4)$$

The definition of total pressure is then applied to the RHS

$$\boldsymbol{V} \times \boldsymbol{\omega} = \frac{1}{\rho}\nabla p_o \quad (5)$$

Expanding the LHS

$$\left(u\hat{\imath} + v\hat{\jmath} + w\hat{k}\right) \times \left(\omega_x\hat{\imath} + \omega_y\hat{\jmath} + \omega_z\hat{k}\right) = \frac{1}{\rho}\nabla p_o \tag{6}$$

Then examining the z-component of velocity yields

$$u\omega_y - v\omega_x = \frac{1}{\rho}\nabla p_o \tag{7}$$

Application of the z-component of the gradient gives

$$u\omega_y - v\omega_x = \frac{1}{\rho}\frac{\partial p_o}{\partial z} \tag{8}$$

A final simplification yields the aforementioned Helmholtz equation.

$$\omega_y = \frac{1}{u}\left[\frac{1}{\rho}\frac{\partial p_o}{\partial z} + v\omega_x\right]$$

However, if one is focus upon the RHS with the same previous assumptions one finds

$$\boldsymbol{V} \times \boldsymbol{\omega} = \nabla\left(\frac{p}{\rho} + \frac{V^2}{2}\right) \tag{9}$$

Application the definition of the speed of sound, the perfect gas law yields

$$a^2 = \gamma RT = \gamma\frac{p}{\rho} \tag{10}$$

$$\frac{p}{\rho} = \frac{a^2}{\gamma} \tag{11}$$

$$\boldsymbol{V} \times \boldsymbol{\omega} = \nabla\left(\frac{a^2}{\gamma} + \frac{V^2}{2}\right) \tag{12}$$

Because the RHS consists of scalars the gradient can be factored through

$$\boldsymbol{V} \times \boldsymbol{\omega} = \nabla\left(\frac{a^2}{\gamma}\right) + \nabla\left(\frac{V^2}{2}\right) \tag{13}$$

An assumption of constant enthalpy provides the following derivation

$$h \equiv h_o - \frac{V^2}{2} \quad \textbf{(14)}$$

$$\nabla h = \nabla h_o - \nabla\left(\frac{V^2}{2}\right) \quad \textbf{(15)}$$

Because total enthalpy is constant equation 15 simplifies to

$$\nabla h = -\nabla\left(\frac{V^2}{2}\right) \quad \textbf{(16)}$$

A similar definition of enthalpy shows

$$\nabla h = \nabla\left(c_p T\right) \quad \textbf{(17)}$$

Using the previously defined speed of sound it can be shown

$$T = \frac{a^2}{\gamma R} \quad \textbf{(18)}$$

Combing equations 16-18 gives

$$\nabla\left(\frac{c_p a^2}{\gamma R}\right) = -\nabla\left(\frac{V^2}{2}\right) \quad \textbf{(19)}$$

Therefore, assuming constant enthalpy and substituting equation 18 into equation 13 one finds

$$\boldsymbol{V} \times \boldsymbol{\omega} = \nabla\left(\frac{a^2}{\gamma}\right) + \nabla\left(-\frac{c_p a^2}{\gamma R}\right) \quad \textbf{(20)}$$

Substitution of the definition of $c_p = \frac{\gamma R}{\gamma - 1}$ gives

$$\boldsymbol{V} \times \boldsymbol{\omega} = \nabla\left(\frac{a^2}{\gamma}\right) - \nabla\left(\frac{\gamma R a^2}{\gamma R(\gamma - 1)}\right) \quad \textbf{(21)}$$

Canceling terms the RHS becomes

$$\boldsymbol{V} \times \boldsymbol{\omega} = \nabla\left(\frac{a^2}{\gamma}\right) - \nabla\left(\frac{a^2}{(\gamma - 1)}\right) \quad \textbf{(22)}$$

Recombining the RHS and simplifying yields

$$\boldsymbol{V} \times \boldsymbol{\omega} = \nabla\left(\frac{-a^2}{\gamma(\gamma - 1)}\right) \quad \textbf{(23)}$$

Applying the cross product and taking only the z-term leaves

$$u\omega_y - v\omega_x = \frac{\partial}{\partial \mathrm{z}}\left(\frac{-a^2}{\gamma(\gamma - 1)}\right) \quad \textbf{(24)}$$

Finally, since the speed of sound and the ratio of specific heats can be assumed constant

$$u\omega_y - v\omega_x = 0 \quad \textbf{(24)}$$

Therefore, it has been shown that, when assuming steady, incompressible and inviscid flow an approximation for the streamwise velocity, denoted ω_y can be represented as:

$$\omega_y = \frac{v}{u}\omega_x \quad \textbf{(25)}$$

Appendix D – ILES Simulations

Appendix D contains figures created from the baseline ILES CFD solution of Gross et al. [58] in an effort to further defend the use of the previous derivations described in Appendix D.

ILES Vorticity Calculations:

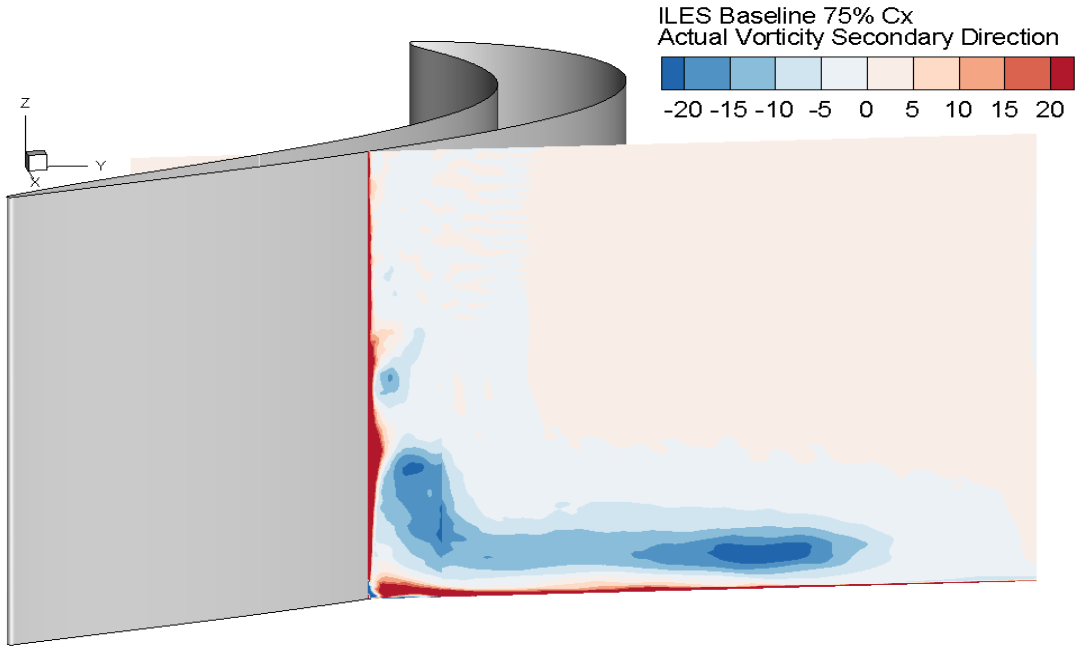

Figure 149. ILES Baseline, Actual Vorticity x-Direction 75% Cx

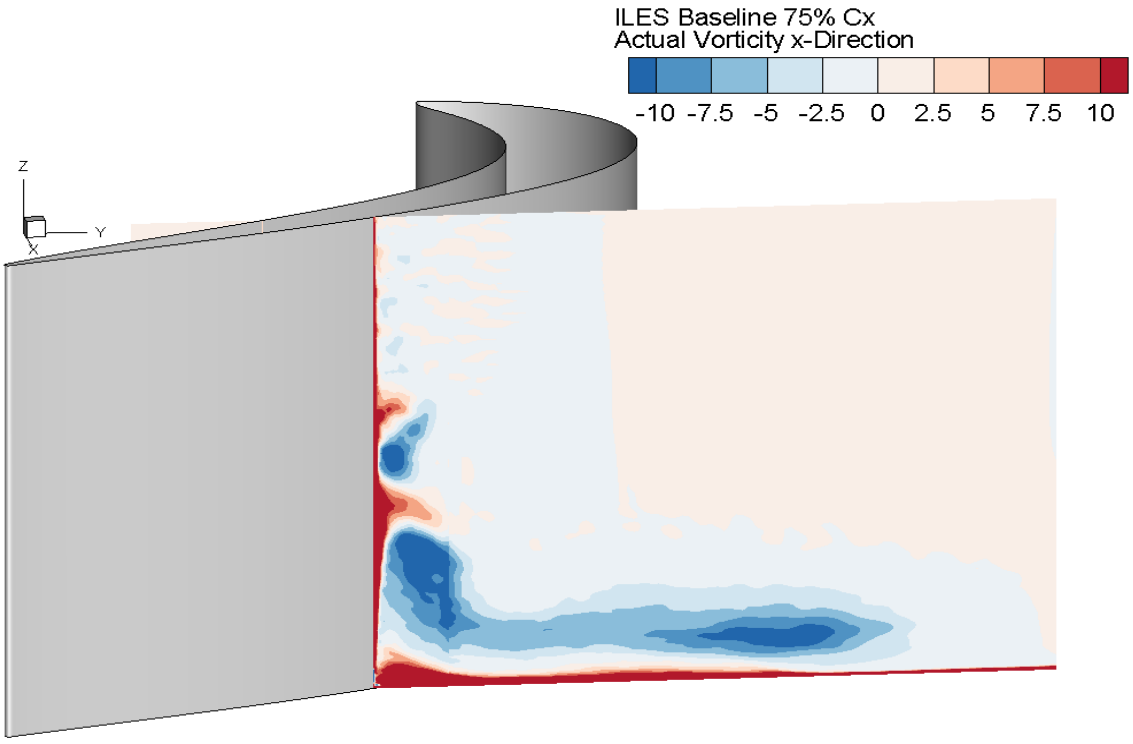

Figure 150. ILES Baseline, Actual Vorticity x-Direction 75% Cx (Corrected Scale)

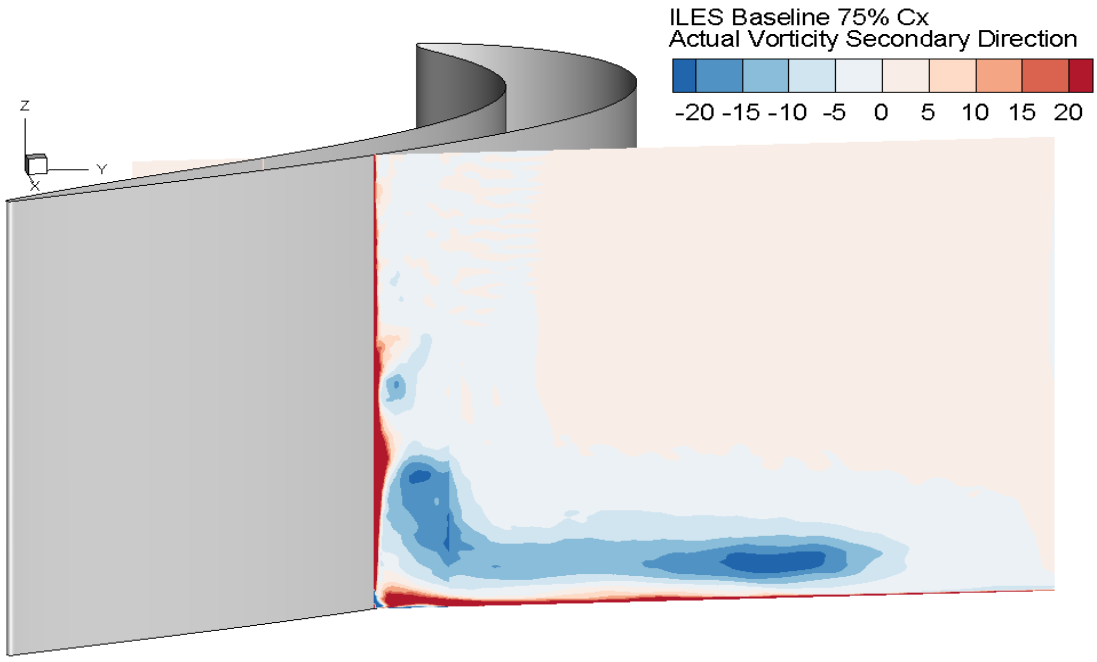

Figure 151. ILES Baseline, Actual Secondary Vorticity 75% Cx

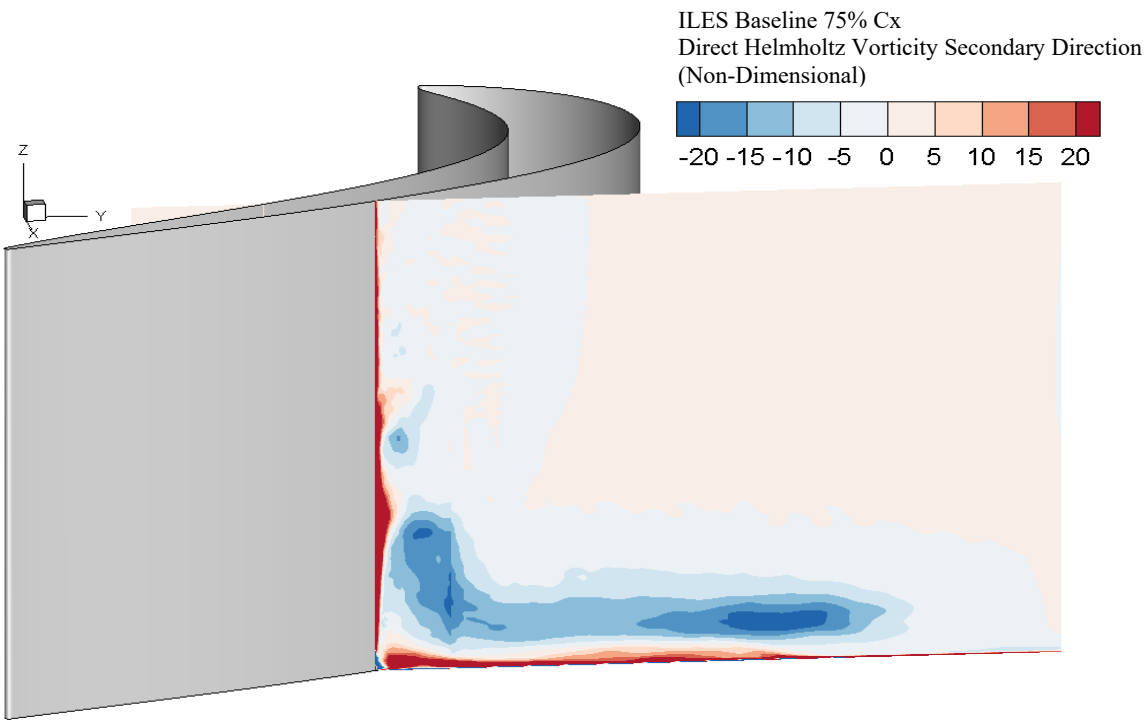

Figure 152. ILES Baseline, Direct Helmholtz Secondary Vorticity 75% Cx

ILES Baseline 75% Cx
Simplified Helmholtz Vorticity Secondary Direction

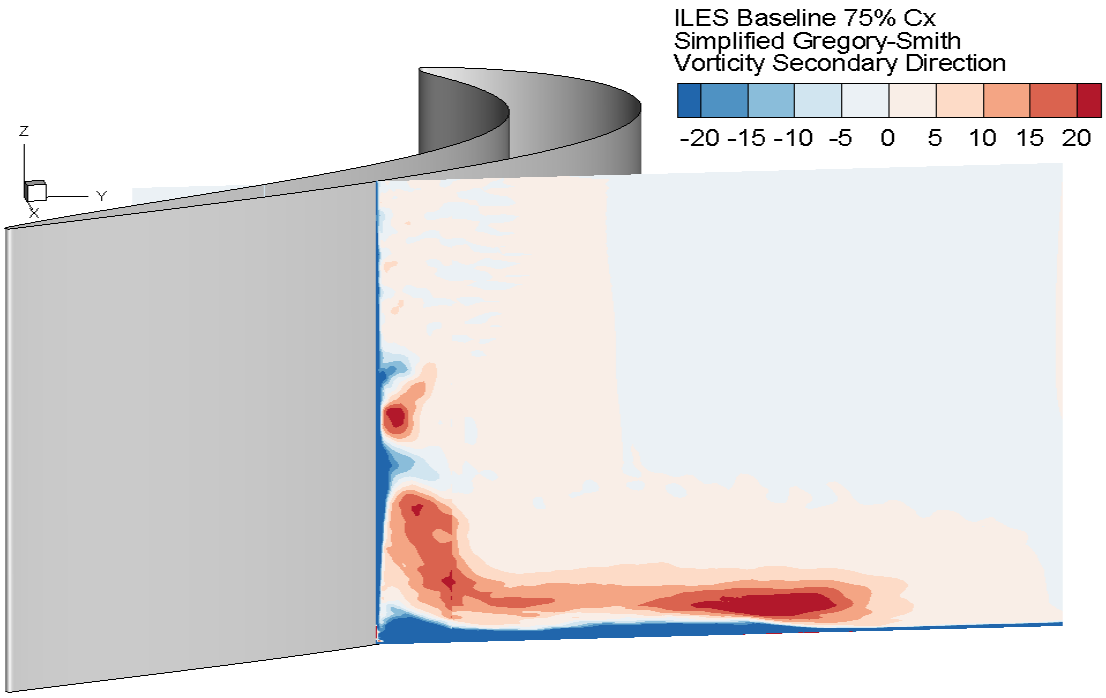

Figure 153. ILES Baseline, Simplified Helmholtz Secondary Vorticity 75% Cx

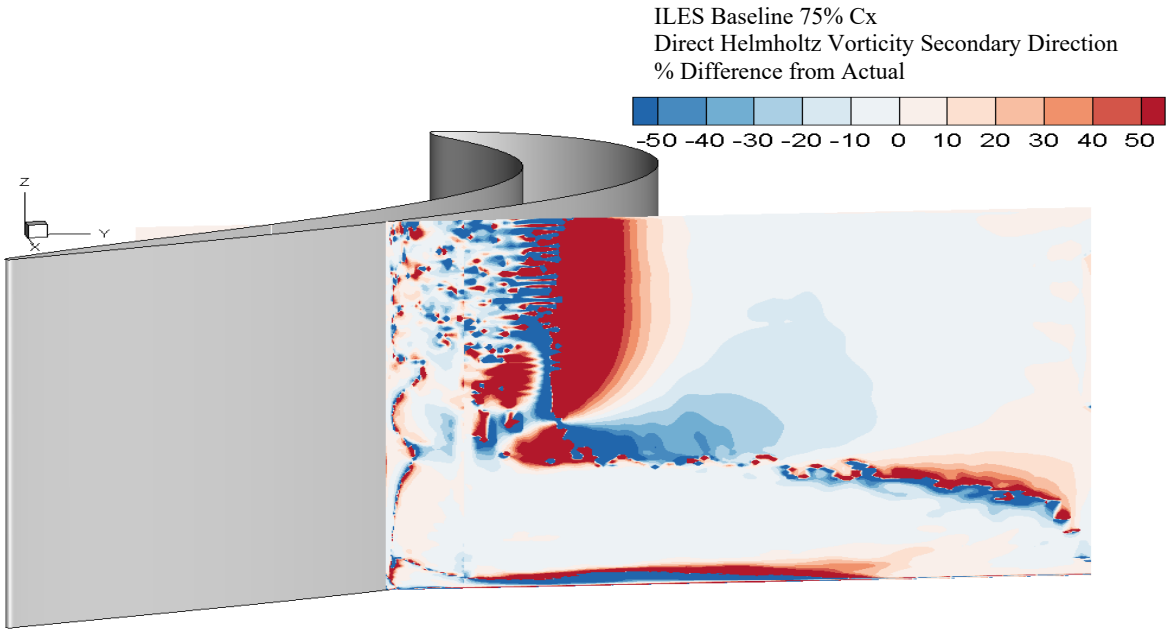

Figure 154. ILES Baseline, Comparison of Actual to Direct Helmholtz Secondary Vorticity 75% Cx

ILES Baseline 75% Cx
Simplified Helmholtz Vorticity Secondary Direction
% Difference from Actual

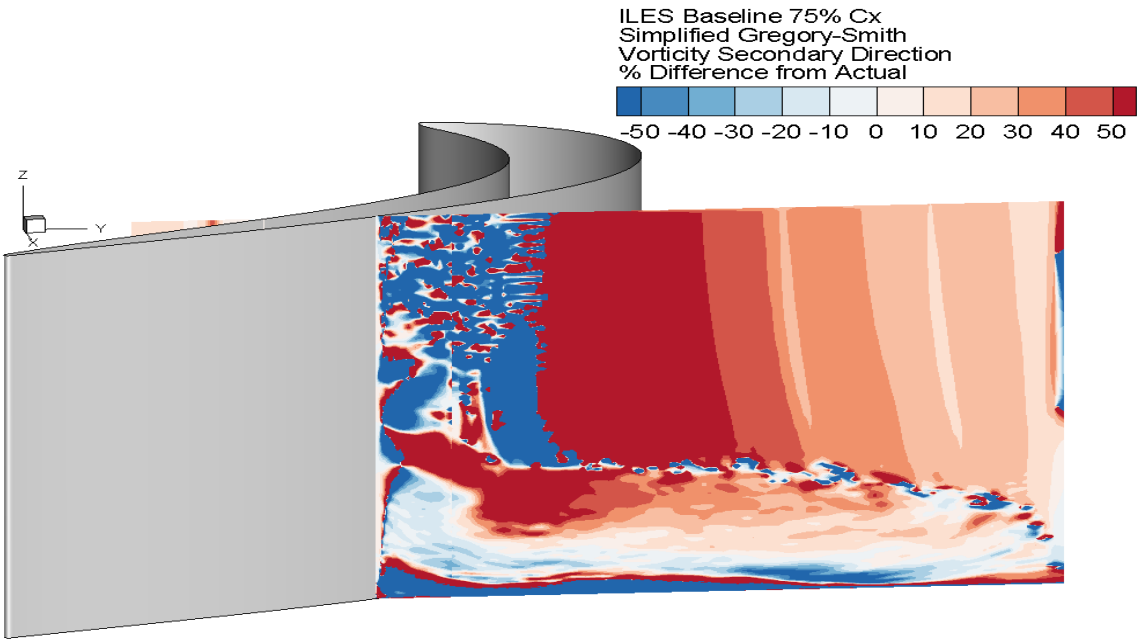

Figure 155. ILES Baseline, Comparison of Actual to Simplified Direct Helmholtz Secondary Vorticity 75% Cx

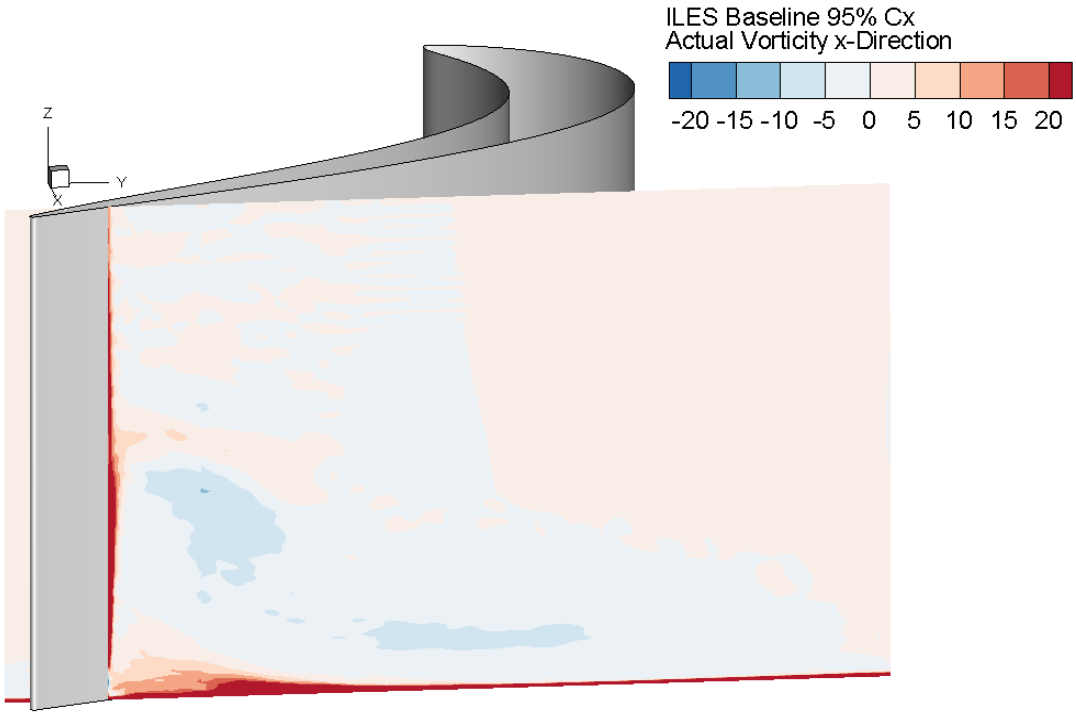

Figure 156. ILES Baseline, Actual Vorticity x-Direction 95% Cx

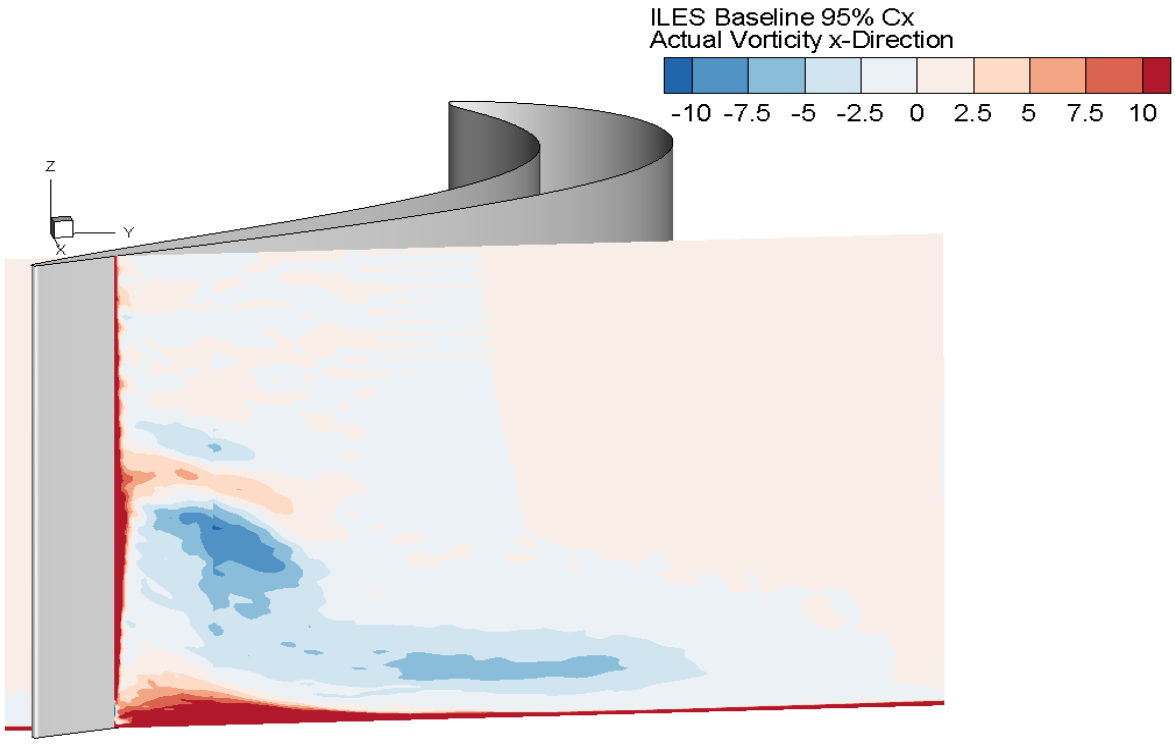

Figure 157. ILES Baseline, Actual Vorticity x-Direction 95% Cx (Corrected Scale)

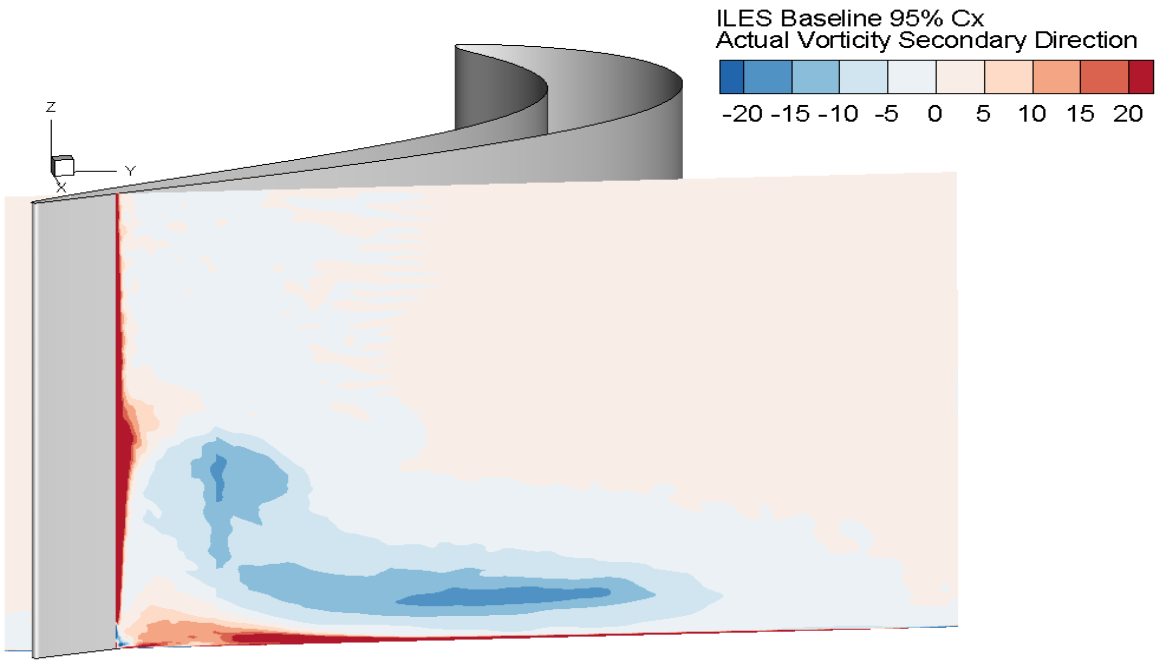

Figure 158. ILES Baseline, Actual Secondary Vorticity 95% Cx

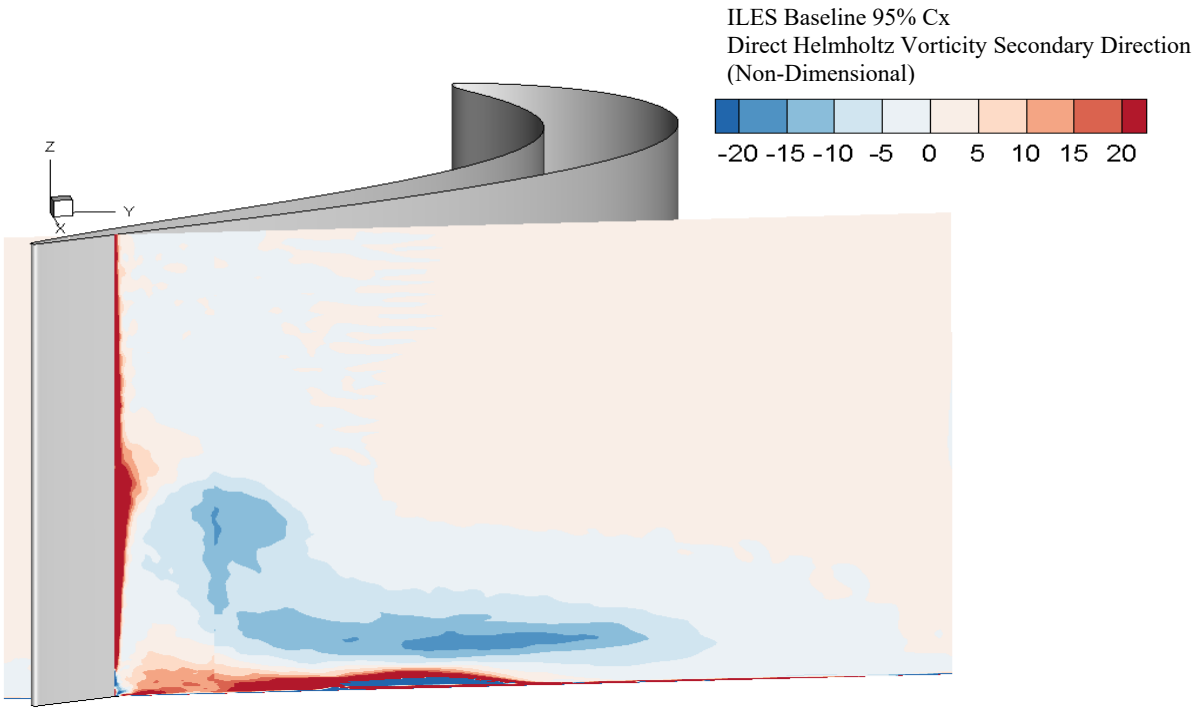

Figure 159. ILES Baseline, Direct Helmholtz Secondary Vorticity 95% Cx

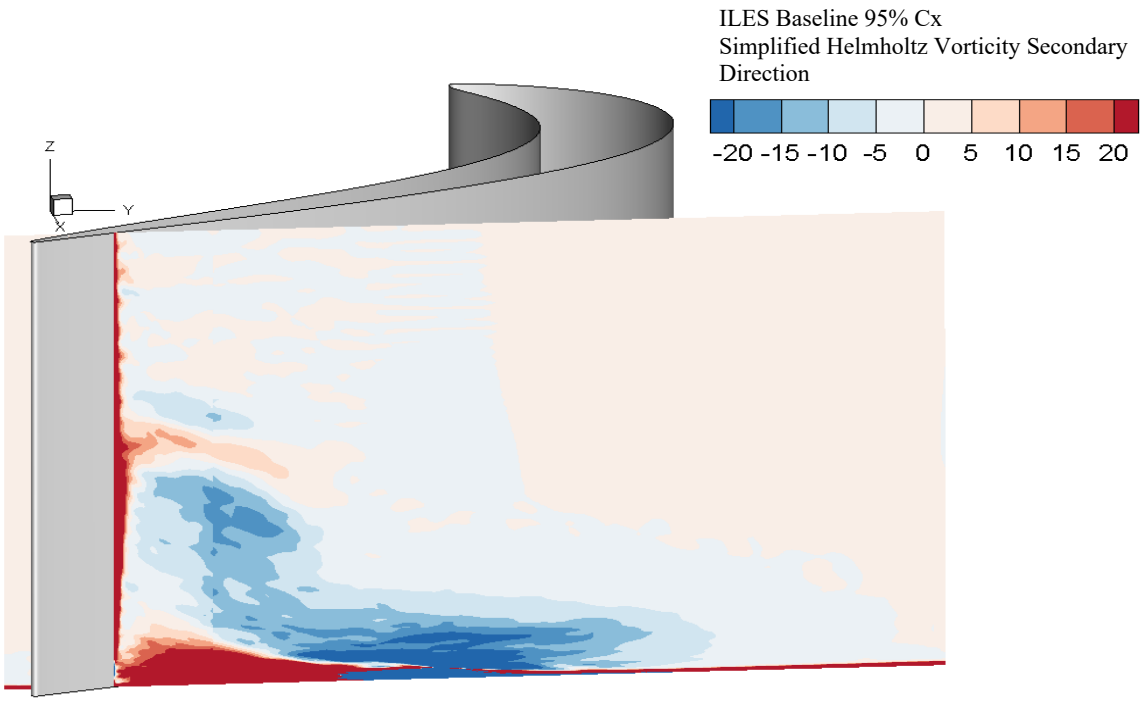

Figure 160. ILES Baseline, Simplified Helmholtz Secondary Vorticity 95% Cx

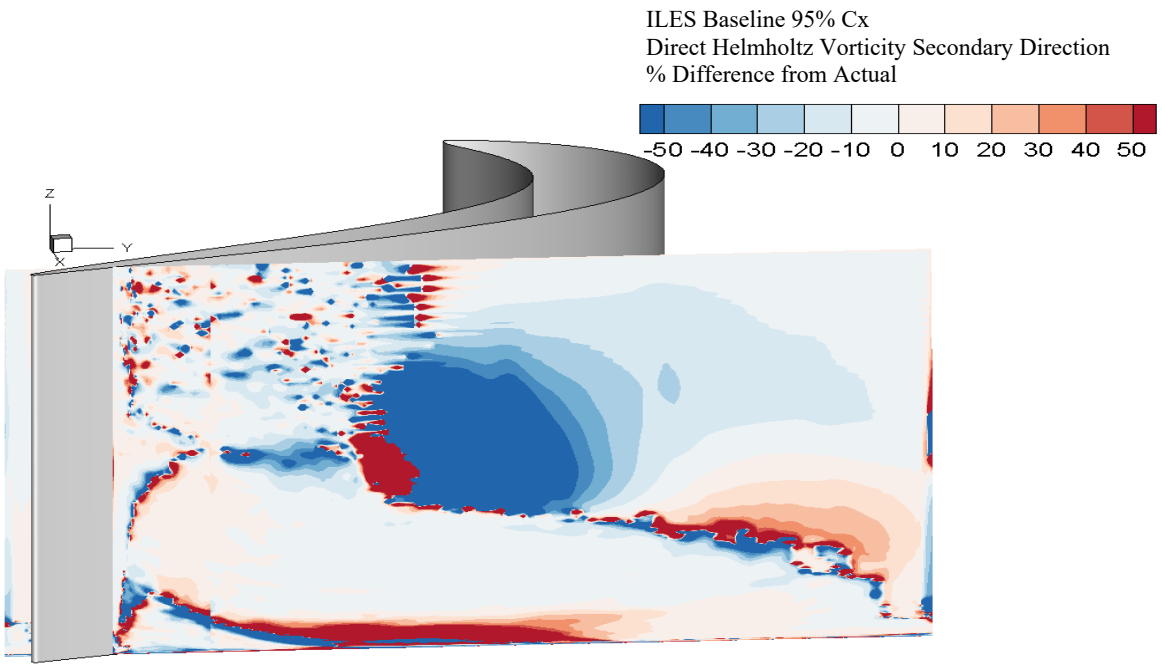

Figure 161. ILES Baseline, Comparison of Actual to Direct Helmholtz Secondary Vorticity 95% Cx

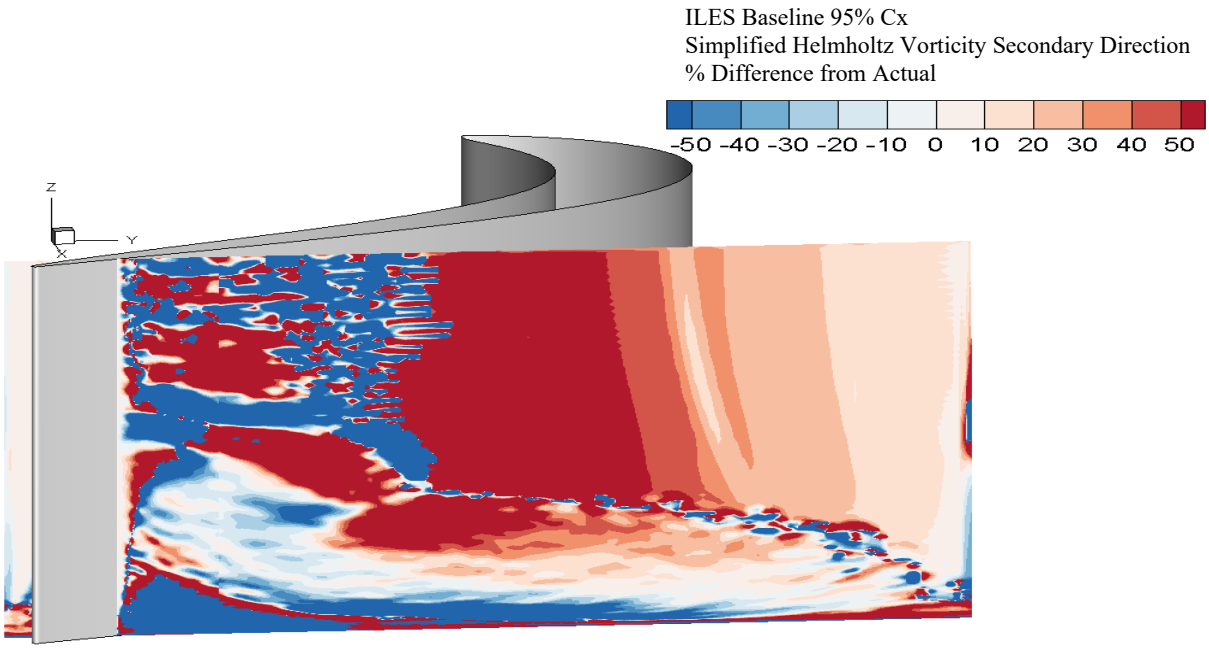

Figure 162. ILES Baseline, Comparison of Actual to Simplified Direct Helmholtz Secondary Vorticity 95% Cx

Appendix E – SPIV Helmholtz Secondary Vorticity

Appendix E contains all of the average SPIV data collected and processed using the direct Helmholtz method to calculate the secondary vorticities. The global maps are shown first for each test case followed by each individual plot. Finally, this appendix contains the scaling factor for the simplified Helmholtz derivation previously discussed in Appendix C

Global Vorticity Mapping Plots:

Baseline
Helmholtz Vorticity Secondary Direction
(Non-Dimensional)

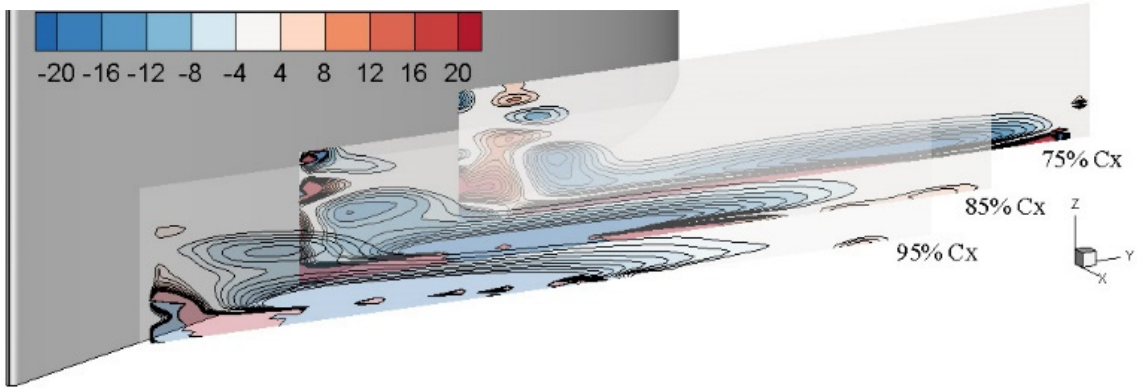

Figure 163. Baseline Helmholtz Secondary Vorticity In-Passage Map

22 Hz – Pulsed Jets
Helmholtz Vorticity Secondary Direction
(Non-Dimensional)

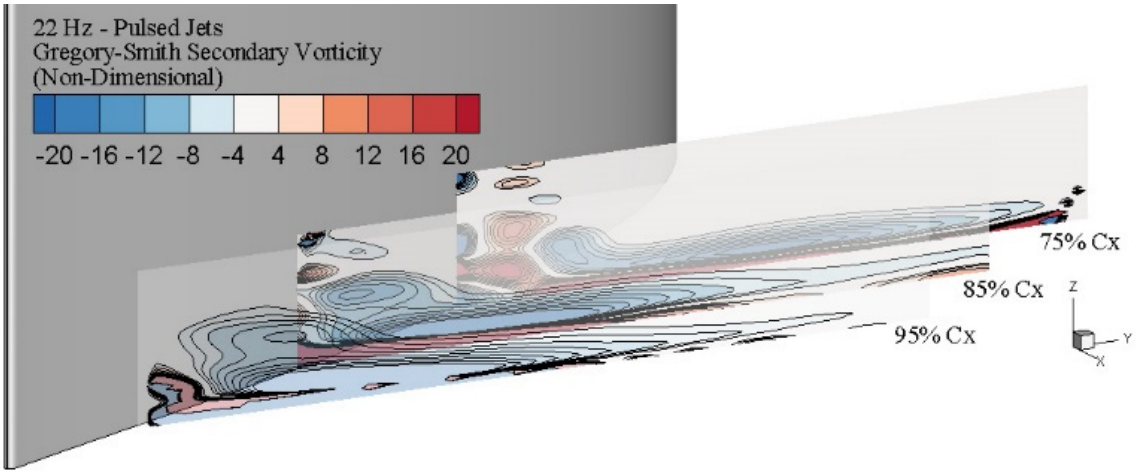

Figure 164. 22 Hz Pulsed Jets Helmholtz Secondary Vorticity In-Passage Map

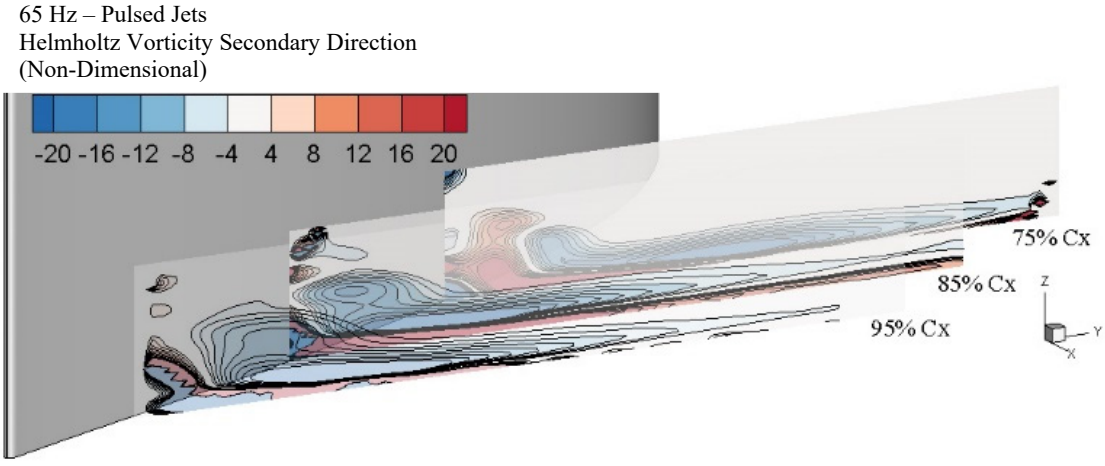

Figure 165. 65 Hz Pulsed Jets Helmholtz Secondary Vorticity In-Passage Map

45.7 SLPM – Steady Jets
Helmholtz Vorticity Secondary Direction
(Non-Dimensional)

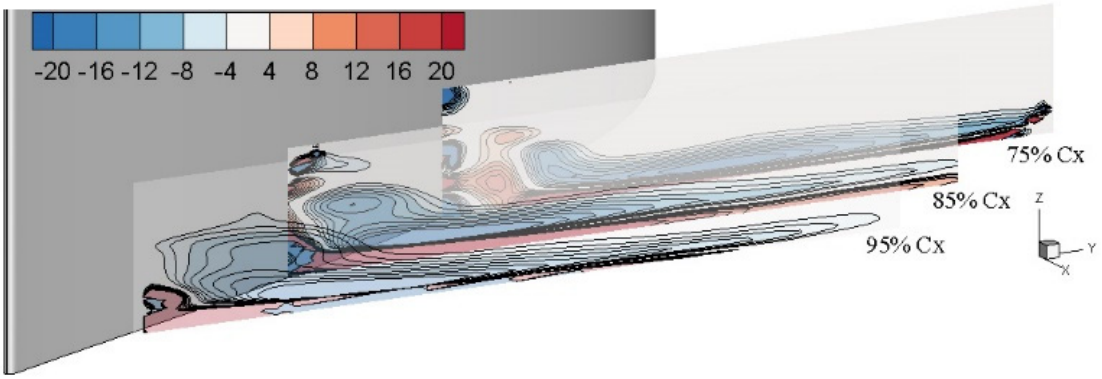

Figure 166. 45.7 SLPM Steady Jets Helmholtz Secondary Vorticity In-Passage Map

68.7 SLPM – Steady Jets
Helmholtz Vorticity Secondary Direction
(Non-Dimensional)

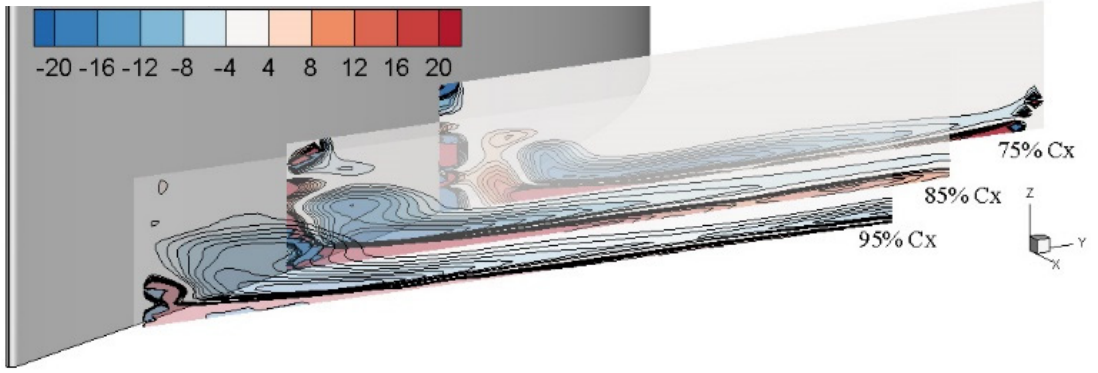

Figure 167. 68.7 SLPM Steady Jets Helmholtz Secondary Vorticity In-Passage Map

Individual Vorticity Mapping Plots:

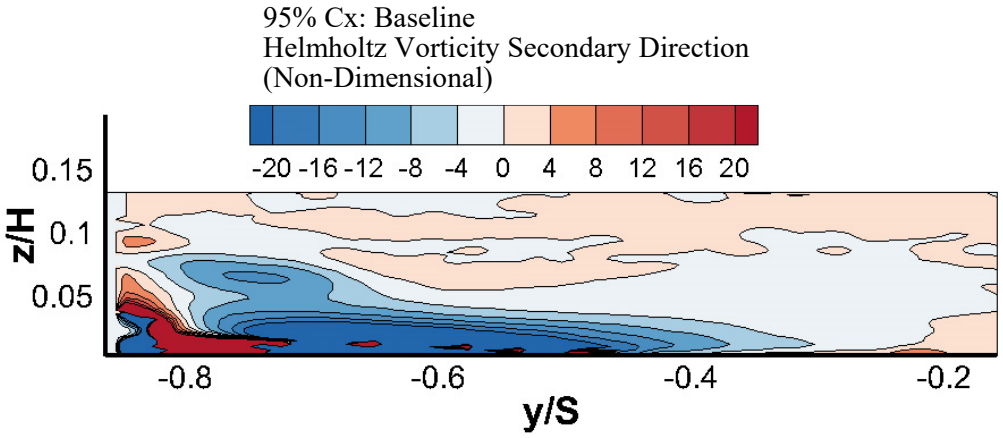

Figure 168. Helmholtz Secondary Vorticity - Baseline 95% Cx

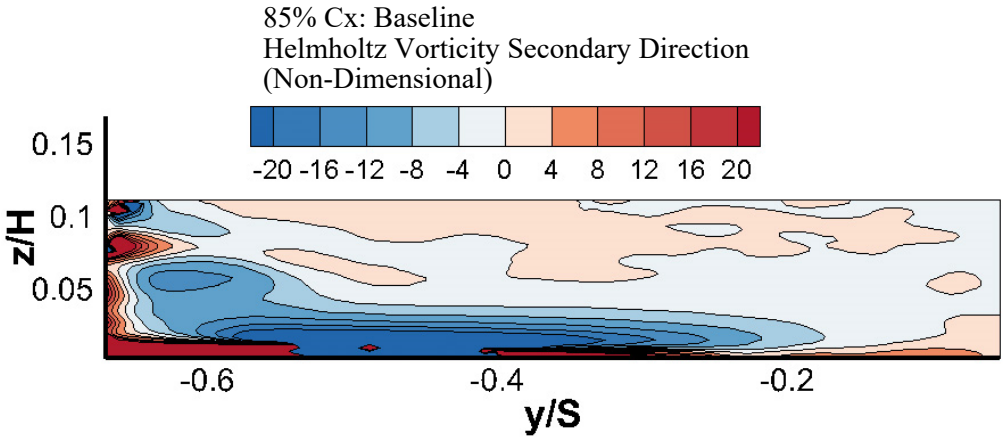

Figure 169. Helmholtz Secondary Vorticity - Baseline 85% Cx

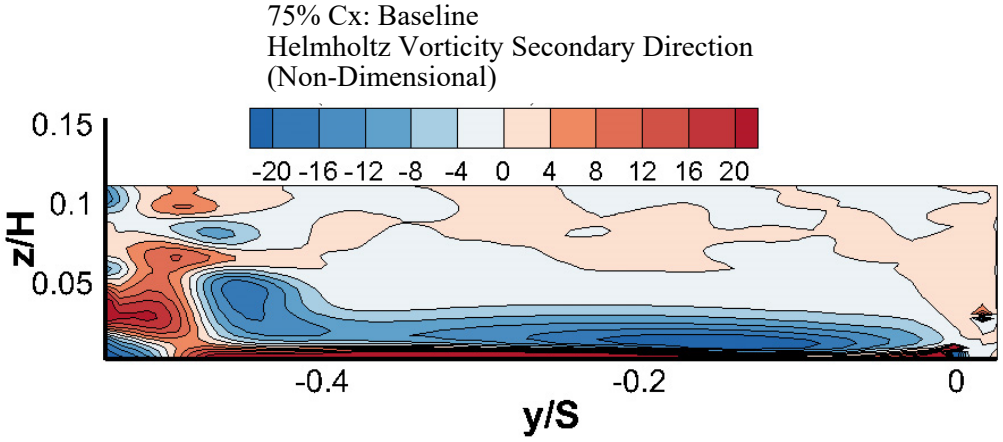

Figure 170. Helmholtz Secondary Vorticity - Baseline 75% Cx

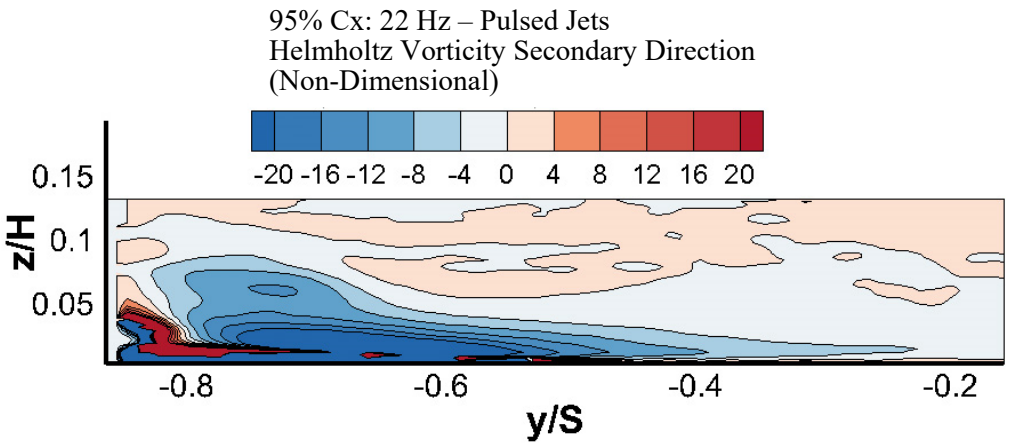

Figure 171. Helmholtz Secondary Vorticity - 22 Hz Pulsed Jets 95% Cx

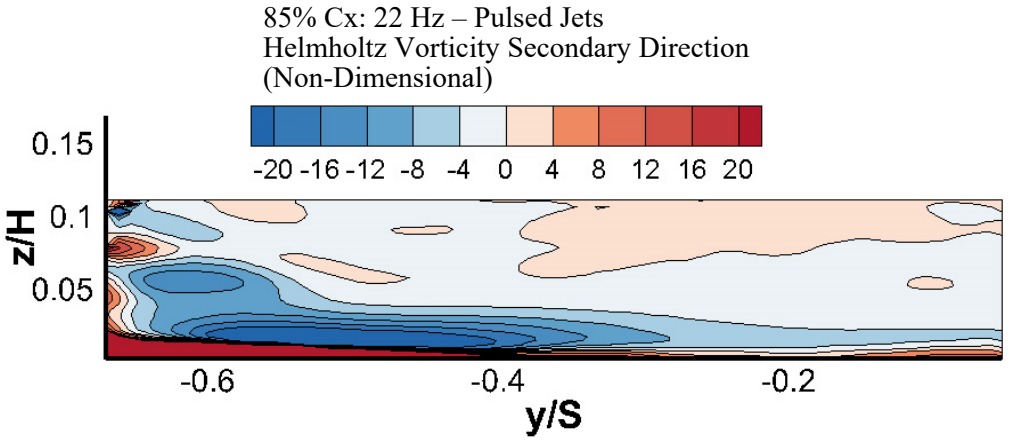

Figure 172. Helmholtz Secondary Vorticity - 22 Hz Pulsed Jets 85% Cx

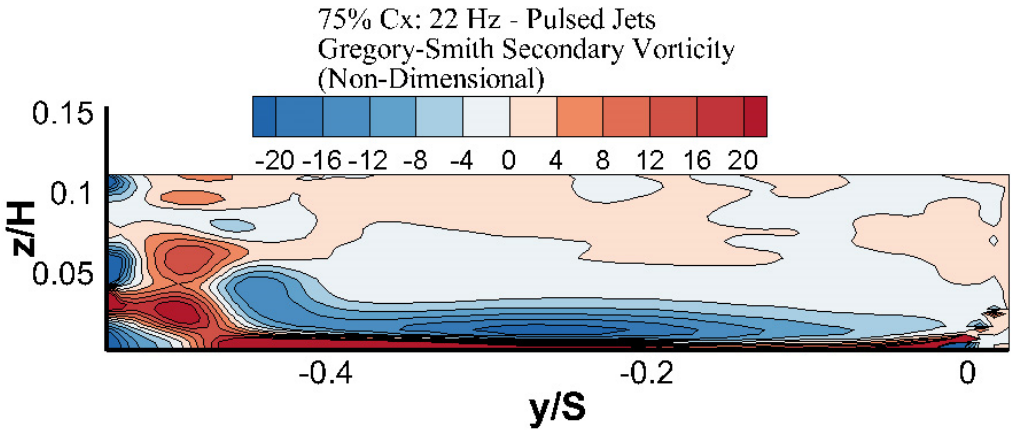

Figure 173. Helmholtz Secondary Vorticity - 22 Hz Pulsed Jets 75% Cx

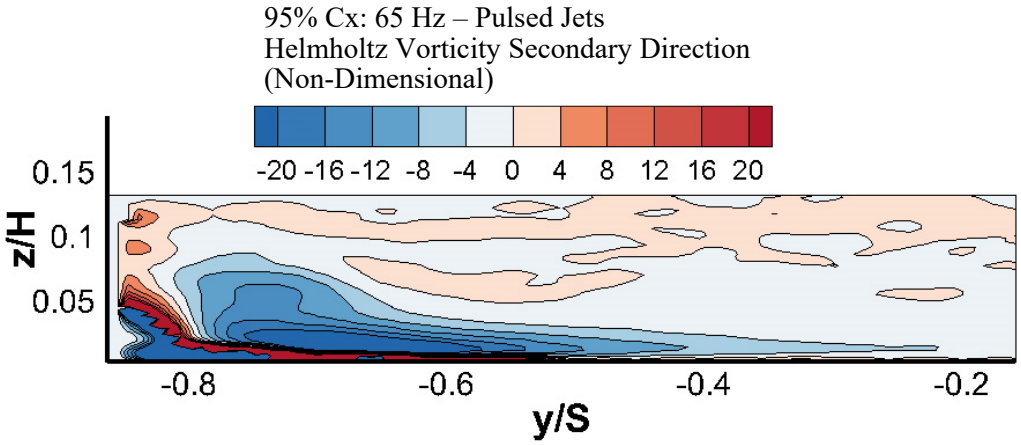

Figure 174. Helmholtz Secondary Vorticity - 65 Hz Pulsed Jets 95% Cx

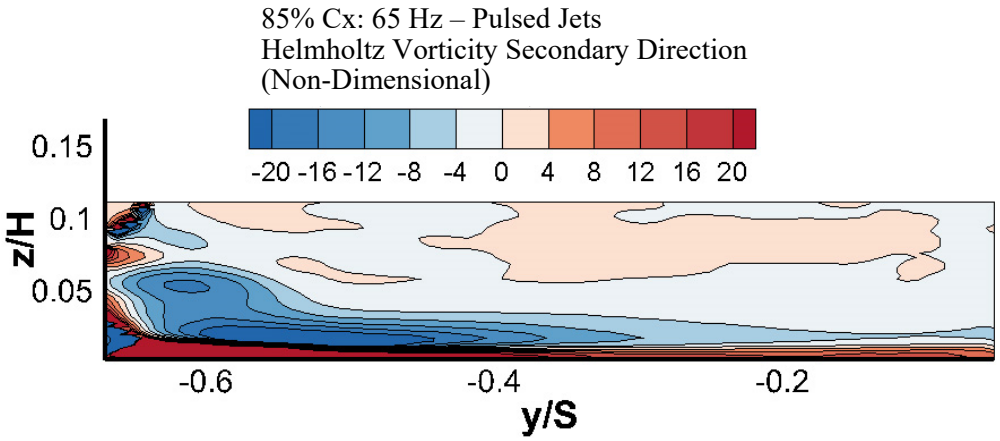

Figure 175. Helmholtz Secondary Vorticity - 65 Hz Pulsed Jets 85% Cx

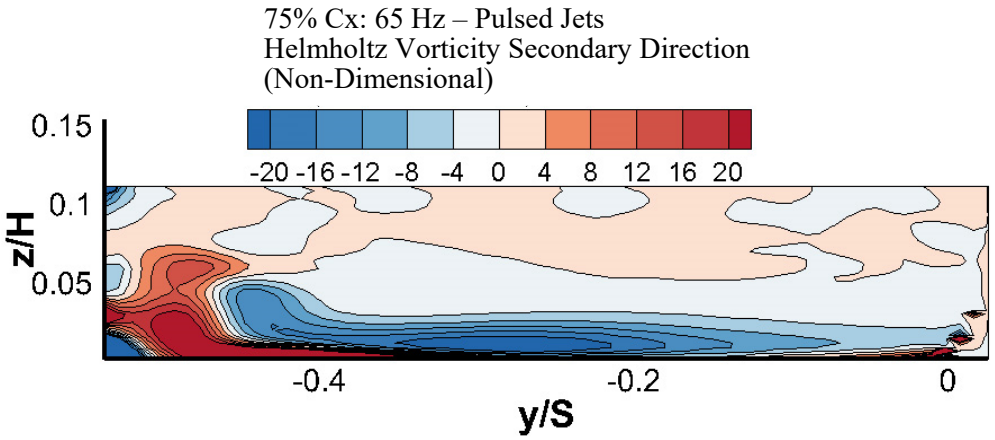

Figure 176. Helmholtz Secondary Vorticity - 65 Hz Pulsed Jets 75% Cx

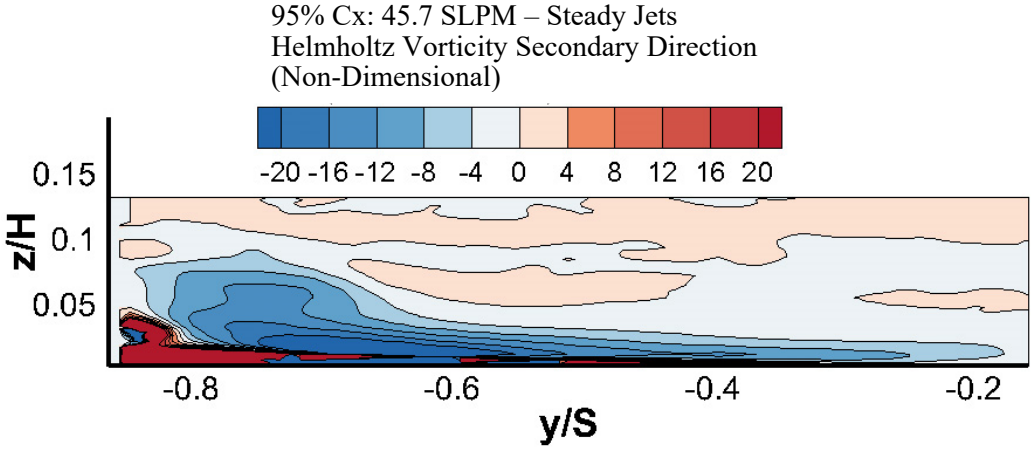

Figure 177. Helmholtz Secondary Vorticity - 45.7 SLPM Steady Jets 95% Cx

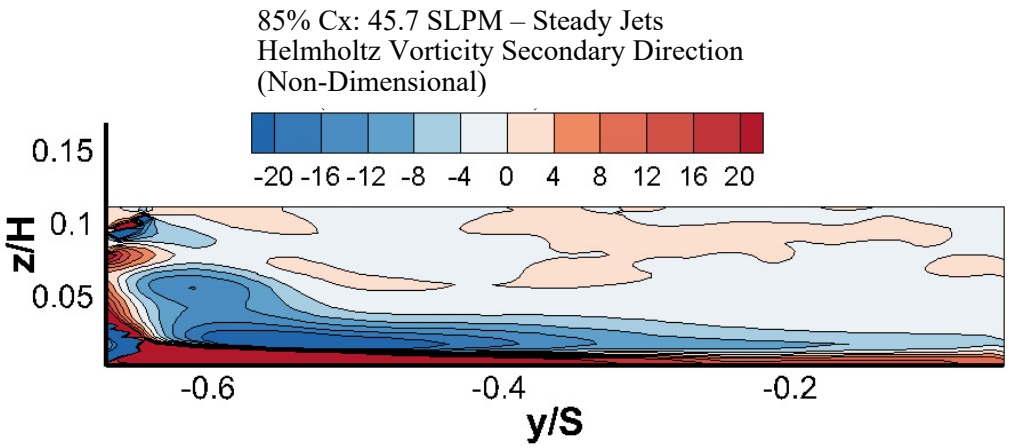

Figure 178. Helmholtz Secondary Vorticity - 45.7 SLPM Steady Jets 85% Cx

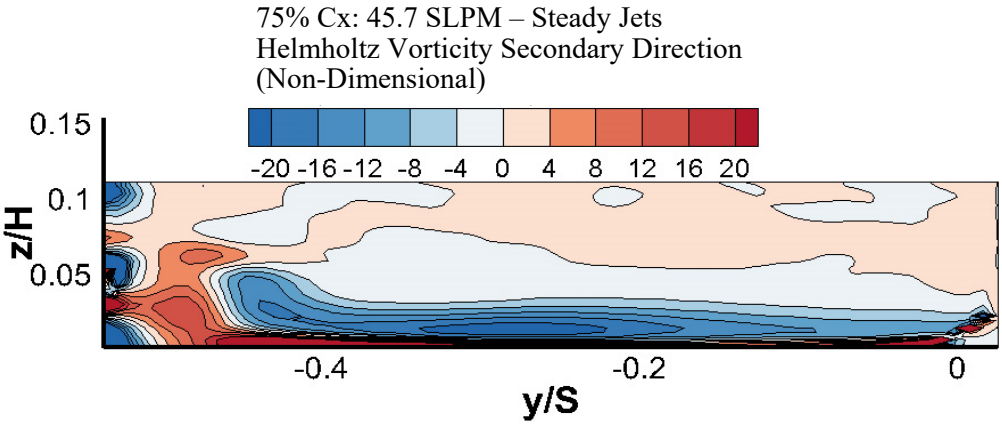

Figure 179. Helmholtz Secondary Vorticity - 45.7 SLPM Steady Jets 75% Cx

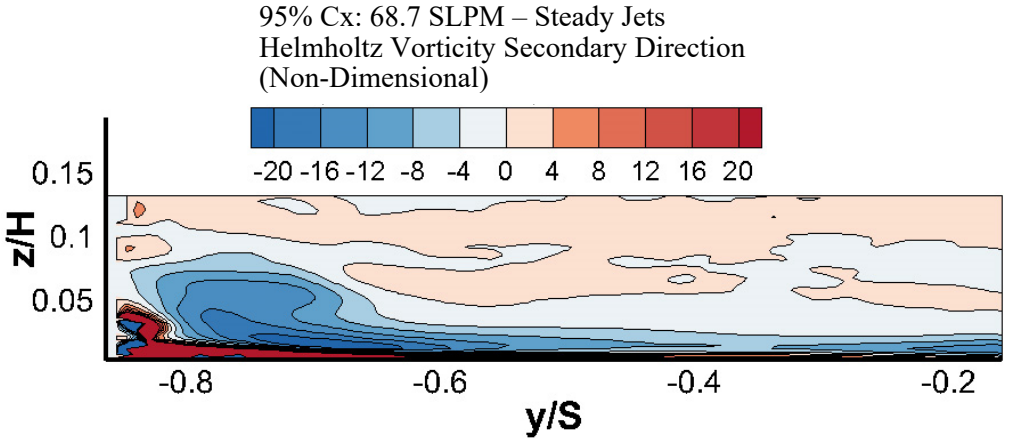

Figure 180. Helmholtz Secondary Vorticity - 68.7 SLPM Steady Jets 95% Cx

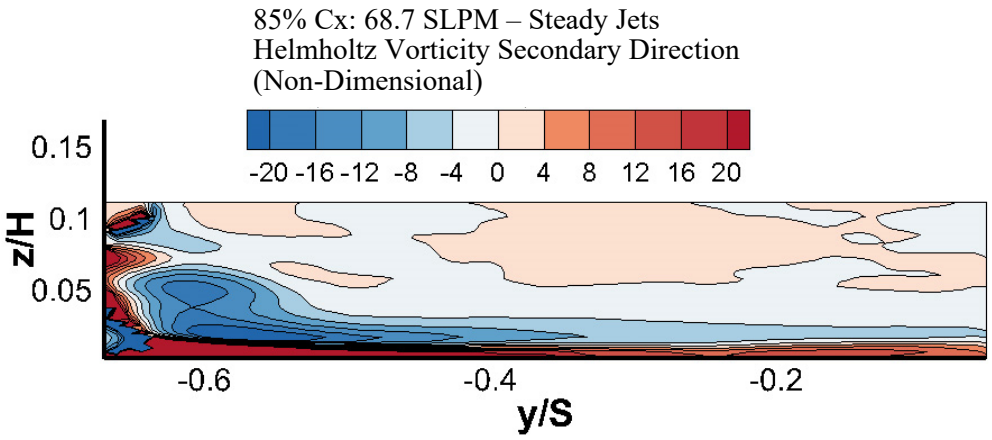

Figure 181. Helmholtz Secondary Vorticity - 68.7 SLPM Steady Jets 85% Cx

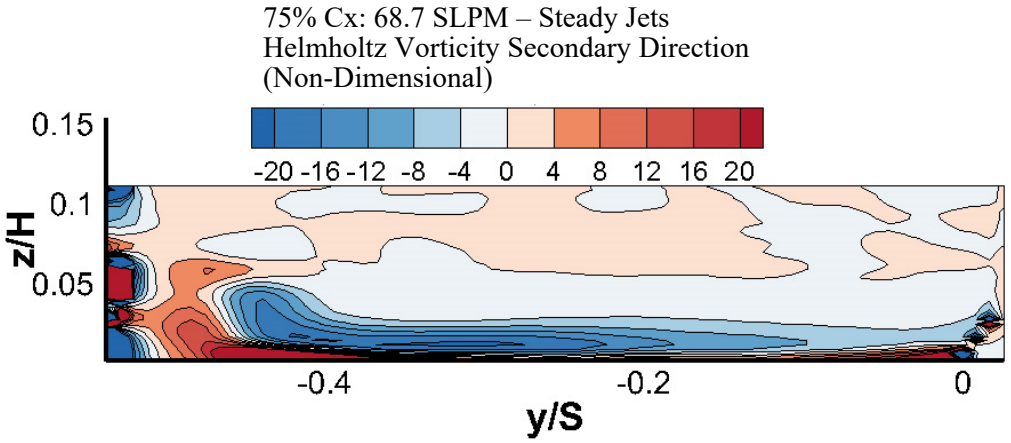

Figure 182. Helmholtz Secondary Vorticity - 68.7 SLPM Steady Jets 75% Cx

Scaling Factor Mapping Plots: $\boldsymbol{Scaling\ Fator = \frac{1}{rho*u}\left(\frac{\partial p_o}{\partial z}\right)}$

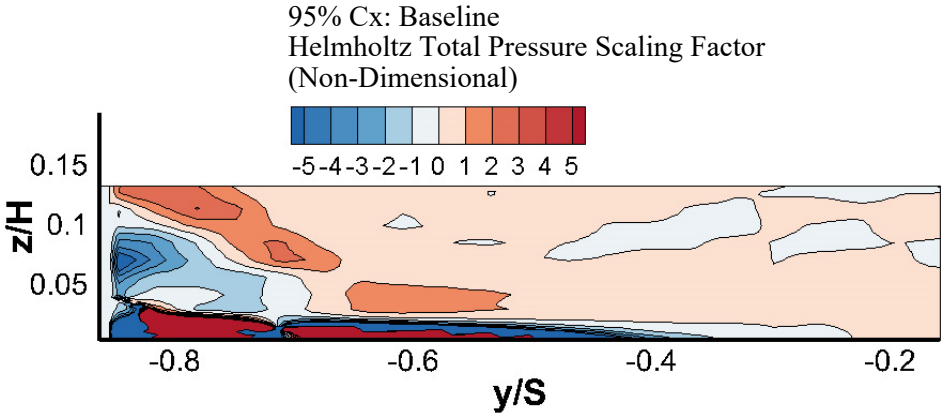

Figure 183. Helmholtz Total Pressure Scaling Factor - Baseline 95% Cx

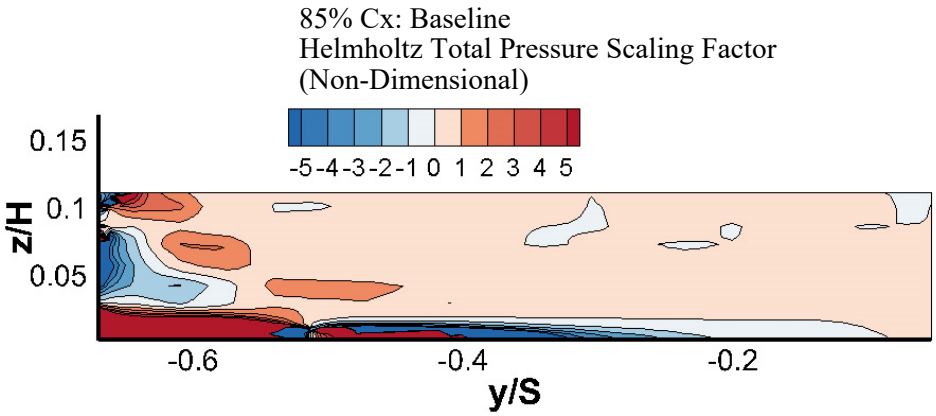

Figure 184. Helmholtz Total Pressure Scaling Factor - Baseline 85% Cx

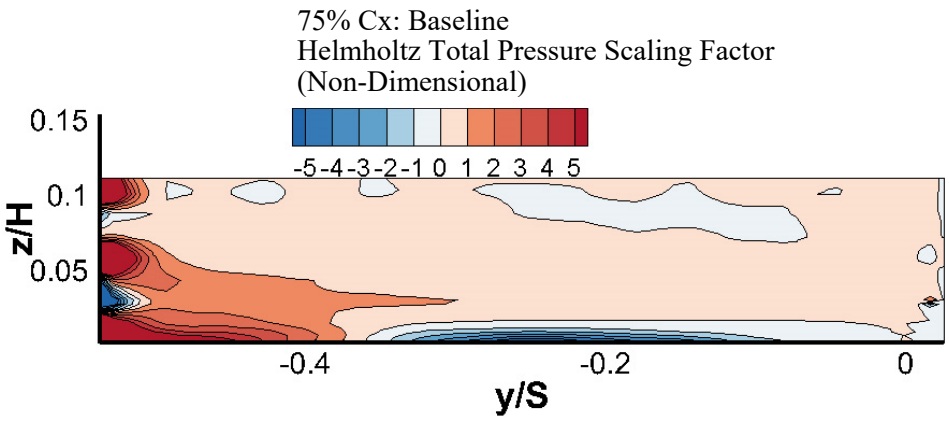

Figure 185. Helmholtz Total Pressure Scaling Factor - Baseline 75% Cx

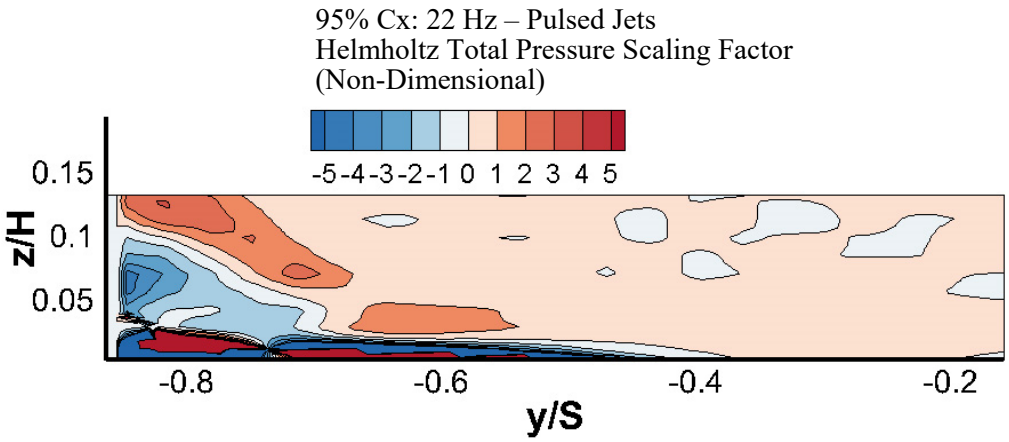

Figure 186. Helmholtz Total Pressure Scaling Factor - 22 Hz Pulsed Jets 95% Cx

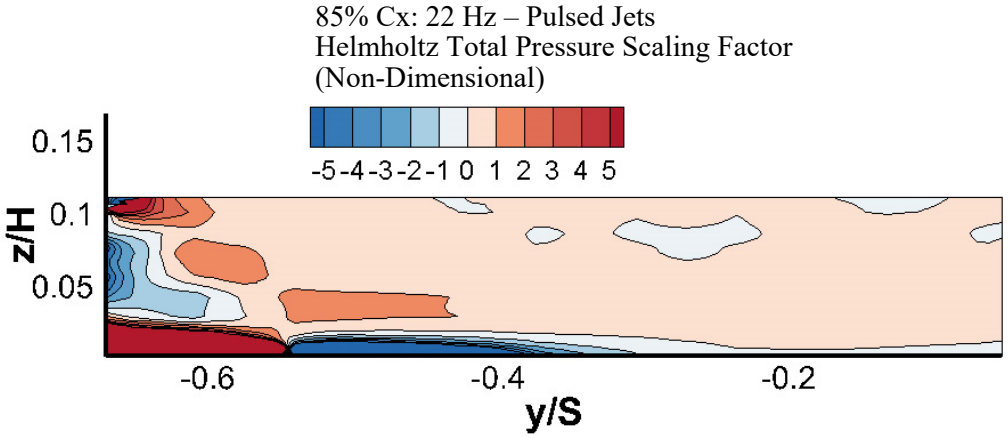

Figure 187. Helmholtz Total Pressure Scaling Factor - 22 Hz Pulsed Jets 85% Cx

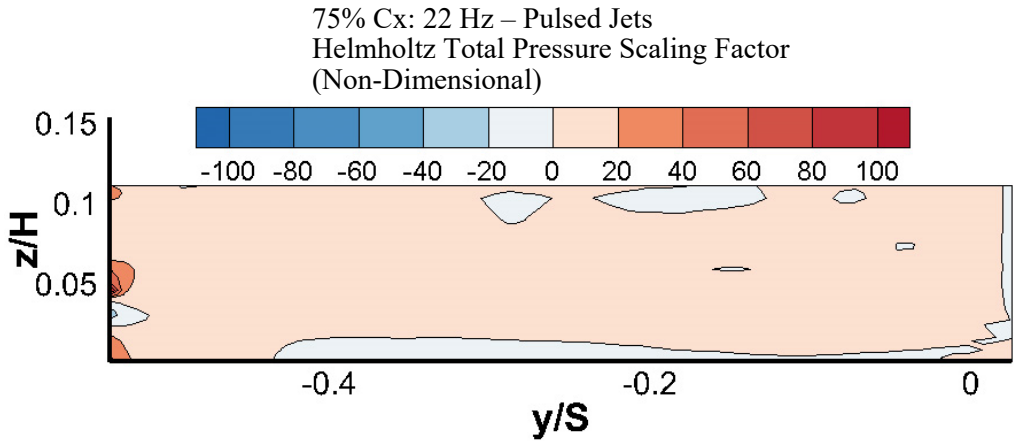

Figure 188. Helmholtz Total Pressure Scaling Factor - 22 Hz Pulsed Jets 75% Cx

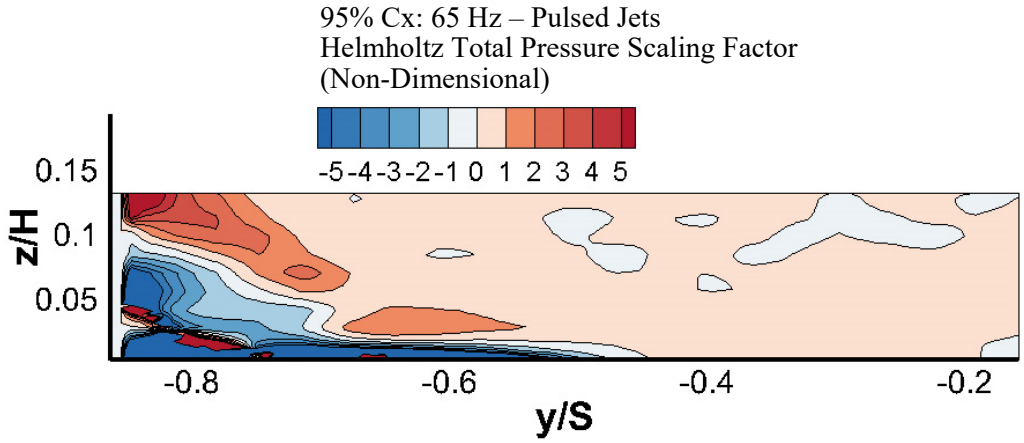

Figure 189. Helmholtz Total Pressure Scaling Factor - 65 Hz Pulsed Jets 95% Cx

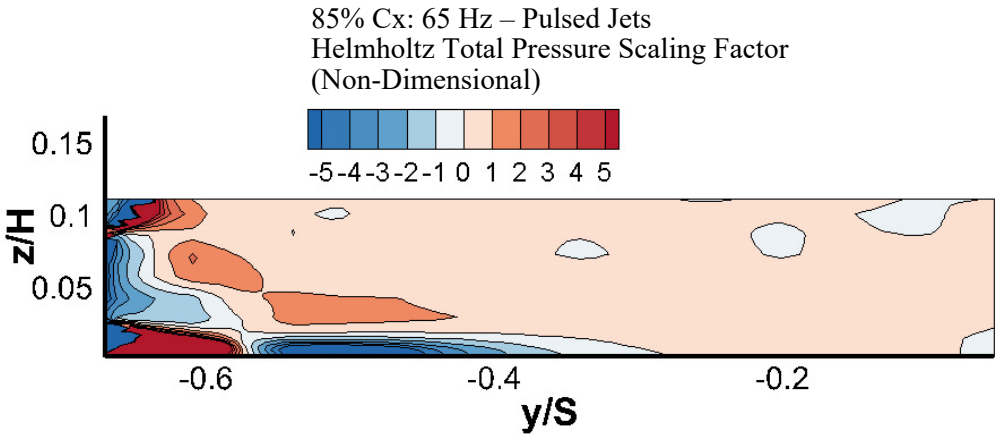

Figure 190. Helmholtz Total Pressure Scaling Factor - 65 Hz Pulsed Jets 85% Cx

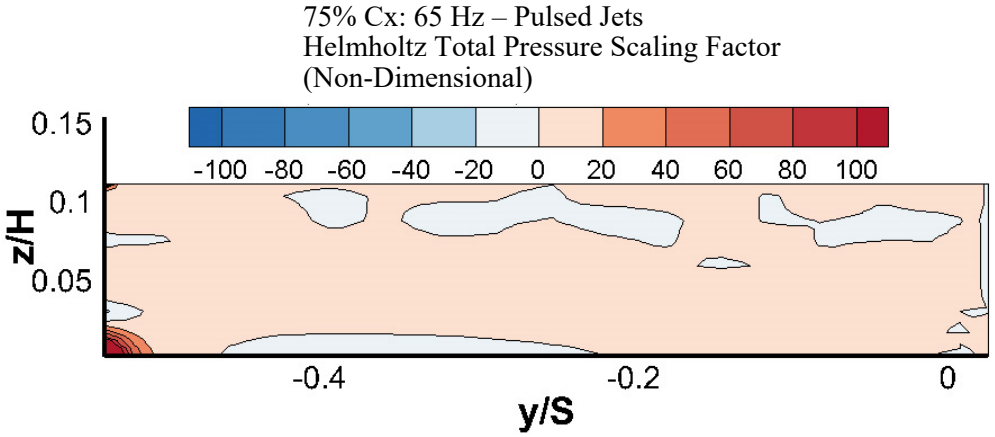

Figure 191. Helmholtz Total Pressure Scaling Factor - 65 Hz Pulsed Jets 75% Cx

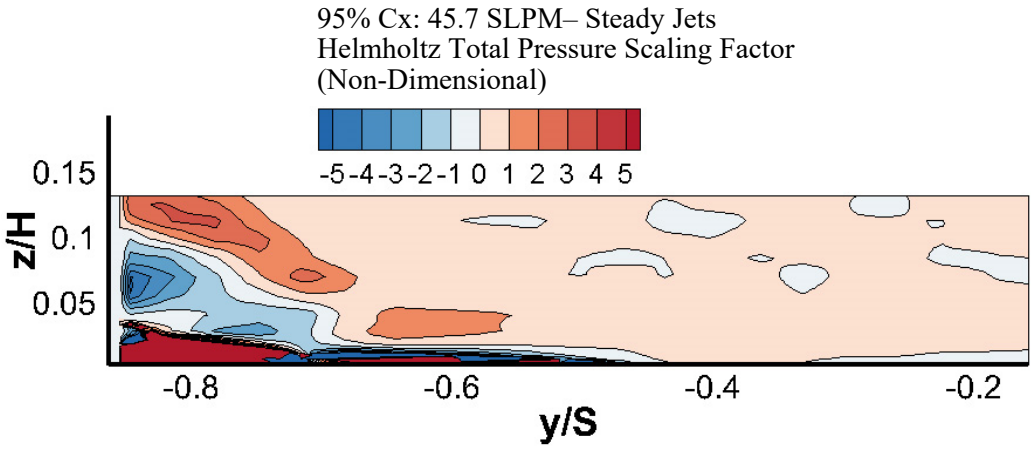

Figure 192. Helmholtz Total Pressure Scaling Factor - 45.7 SLPM Steady Jets 95% Cx

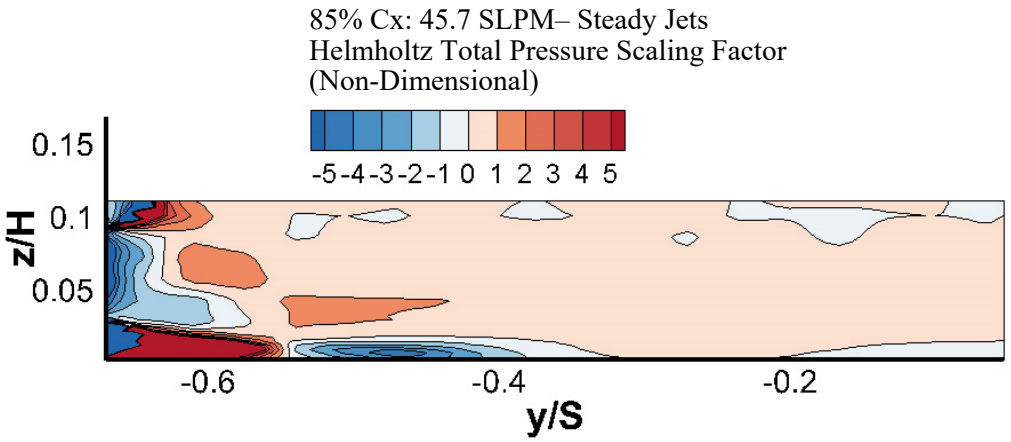

Figure 193. Helmholtz Total Pressure Scaling Factor - 45.7 SLPM Steady Jets 85% Cx

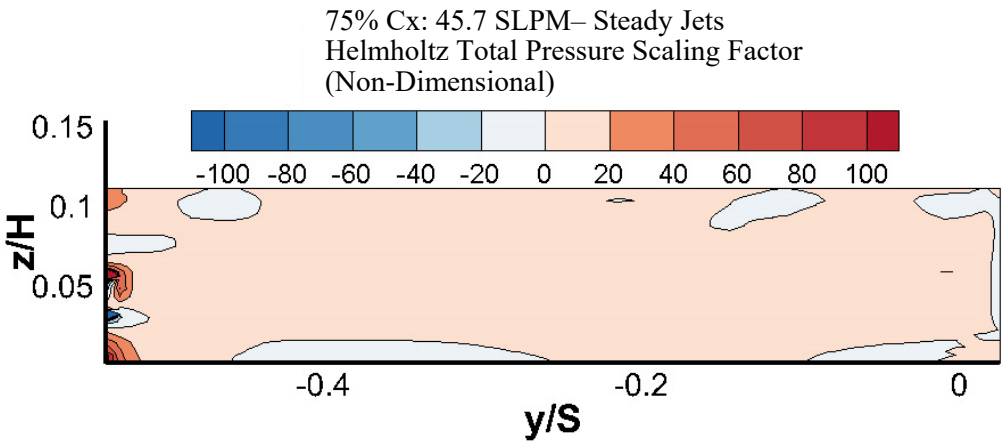

Figure 194. Helmholtz Total Pressure Scaling Factor - 45.7 SLPM Steady Jets 75% Cx

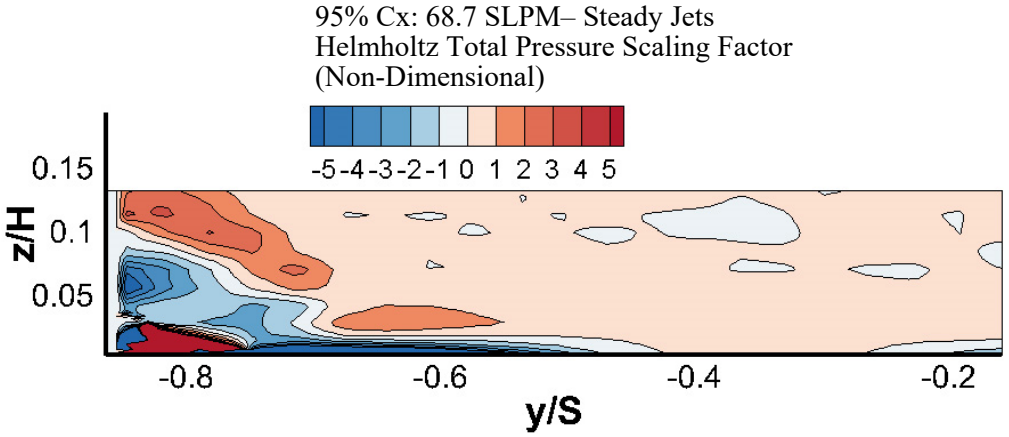

Figure 195. Helmholtz Total Pressure Scaling Factor - 68.7 SLPM Steady Jets 95% Cx

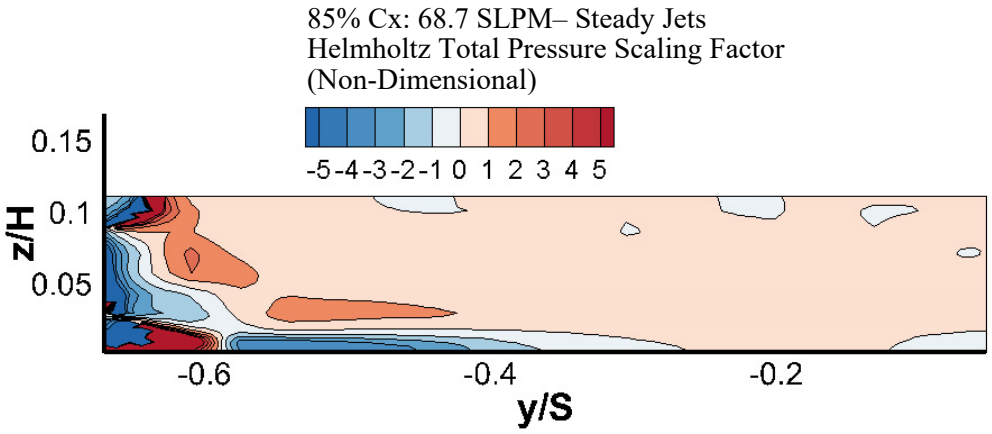

Figure 196. Helmholtz Total Pressure Scaling Factor - 68.7 SLPM Steady Jets 85% Cx

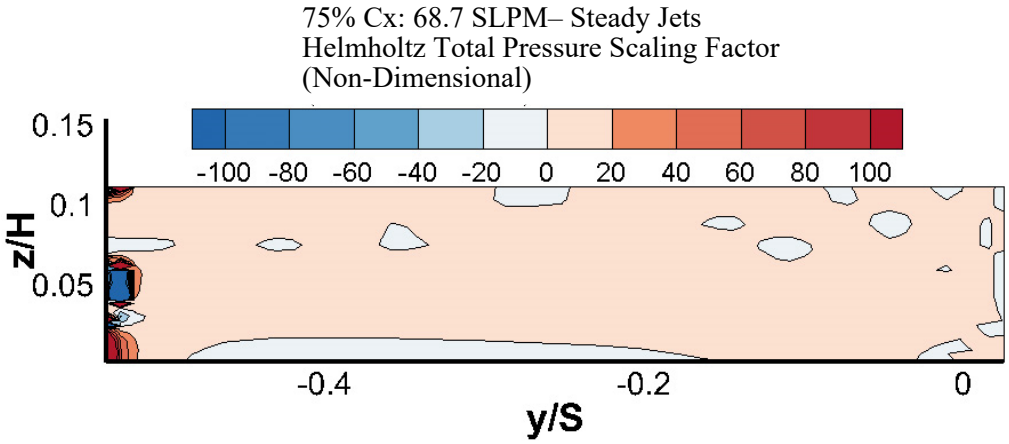

Figure 197. Helmholtz Total Pressure Scaling Factor - 68.7 SLPM Steady Jets 75% Cx

Appendix F – SPIV X-Direction Vorticity

Appendix F contains all of the average SPIV data collected and processed presenting the x component of vorticity normal to the measurement plane of interest. The global maps are shown first for each test case followed by each individual plot.

Global Vorticity Mapping Plots:

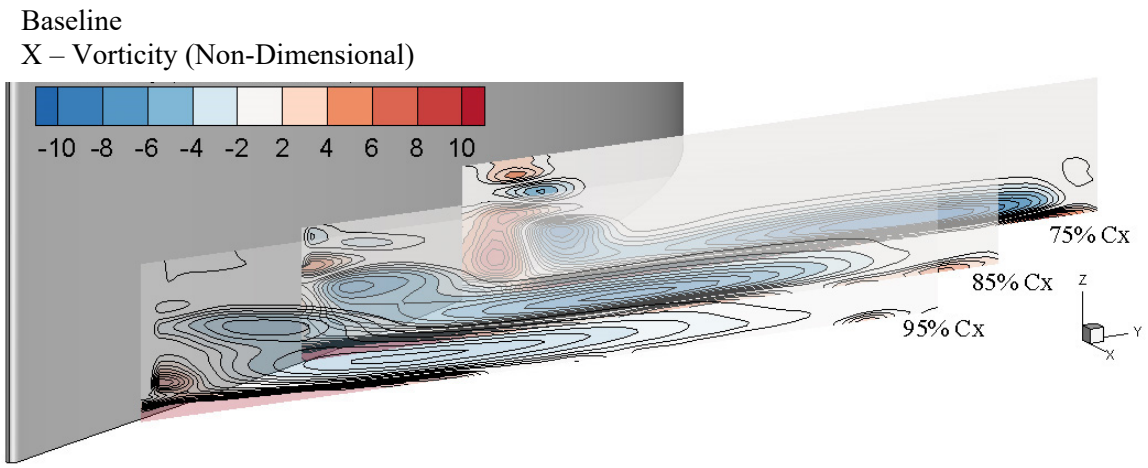

Figure 198. Baseline X-Direction Vorticity In-Passage Map

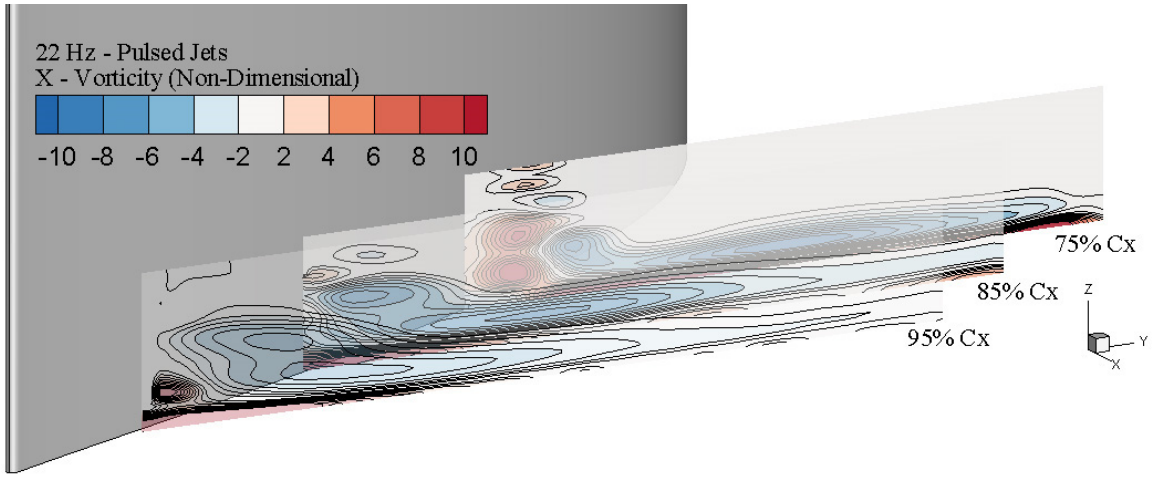

Figure 199. 22 Hz Pulsed Jets X-Direction Vorticity In-Passage Map

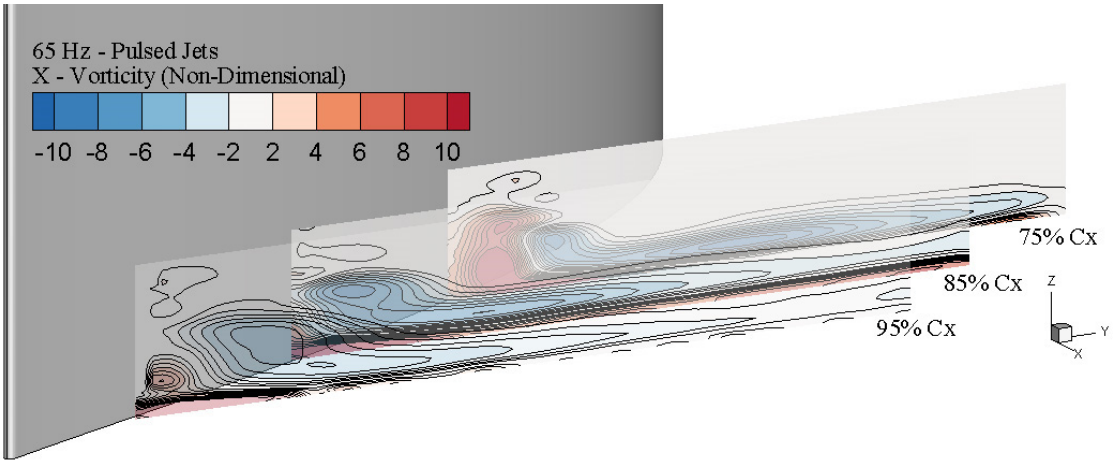

Figure 200. 65 Hz Pulsed Jets X-Direction Vorticity In-Passage Map

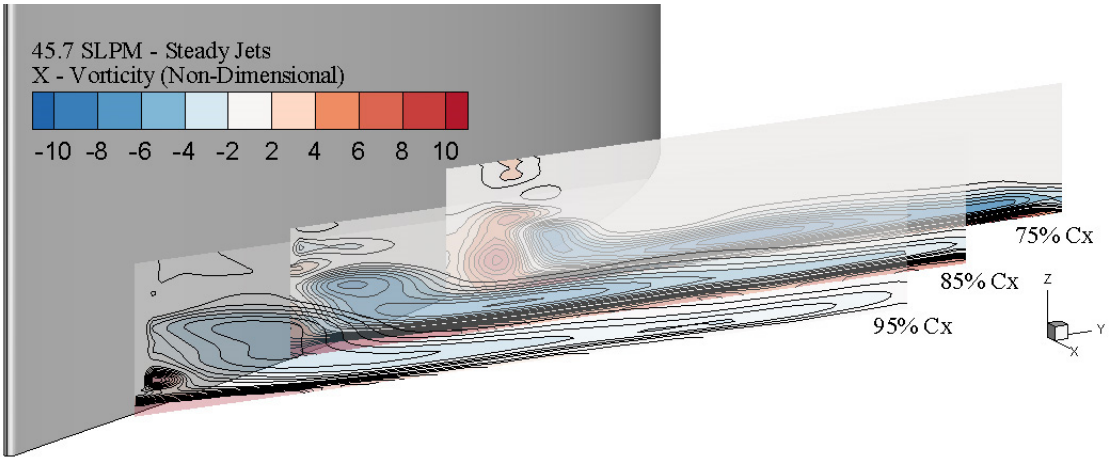

Figure 201. 45.7 SLPM Steady Jets X-Direction Vorticity In-Passage Map

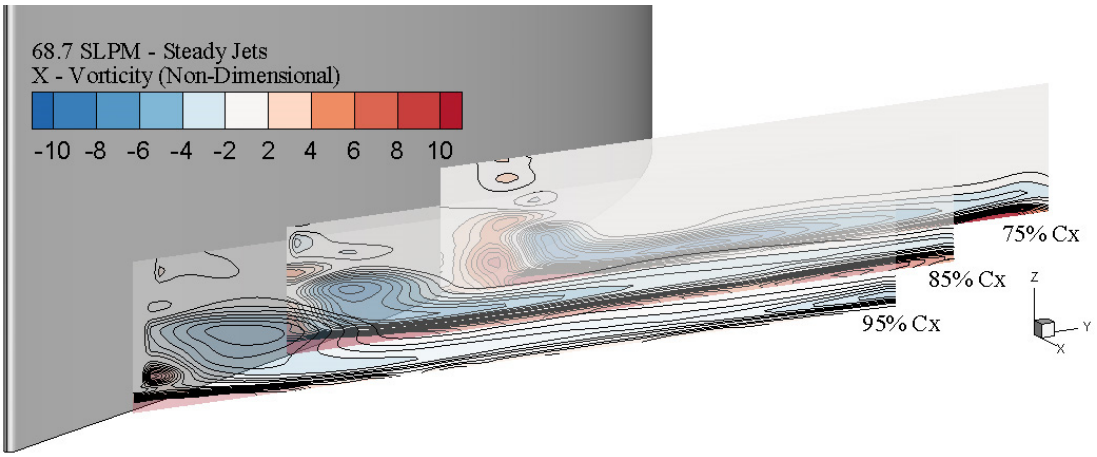

Figure 202. 68.7 SLPM Steady Jets X-Direction Vorticity In-Passage Map

Individual Vorticity Mapping Plots:

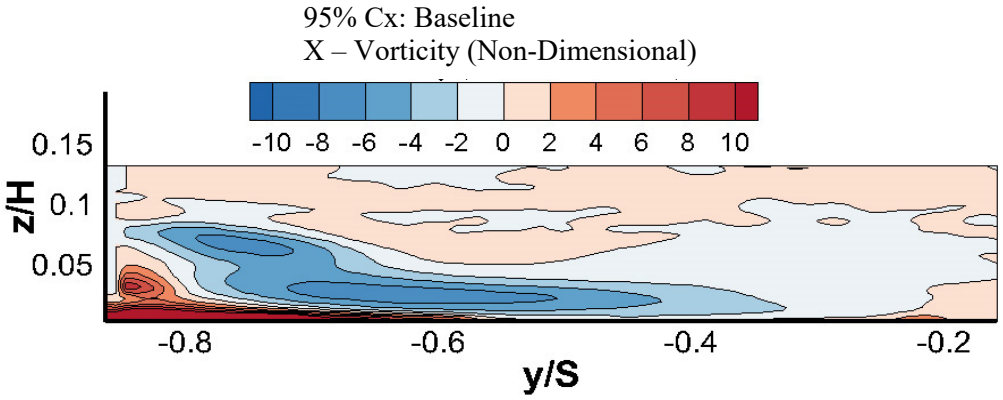

Figure 203. x – Vorticity - Baseline 95% Cx

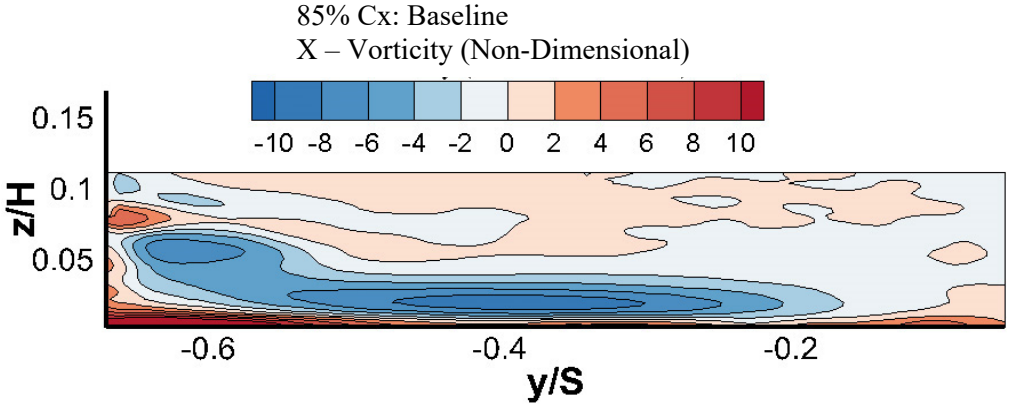

Figure 204. x – Vorticity - Baseline 85% Cx

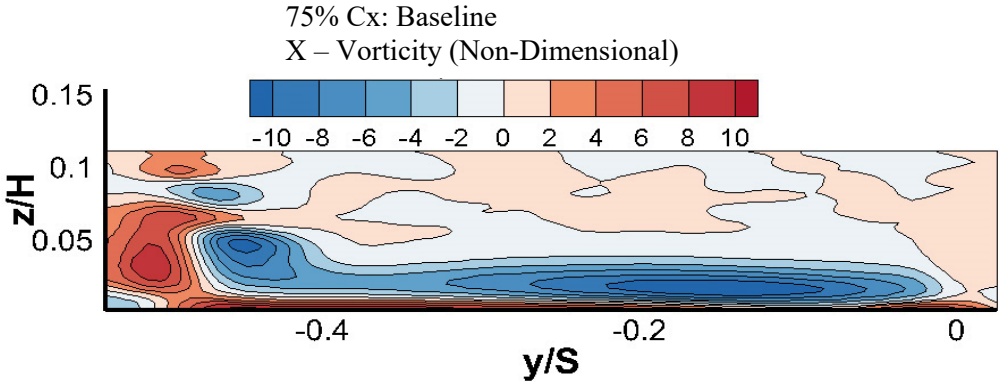

Figure 205. x – Vorticity - Baseline 75% Cx

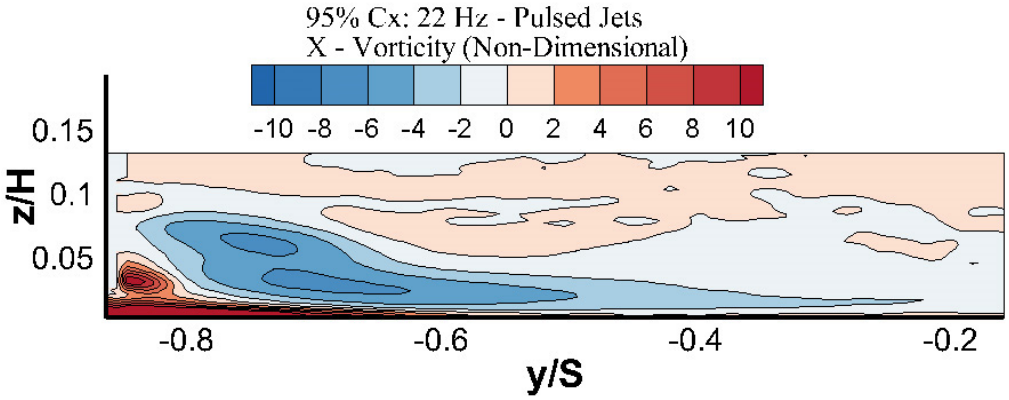

Figure 206. x – Vorticity - 22 Hz Pulsed Jets 95% Cx

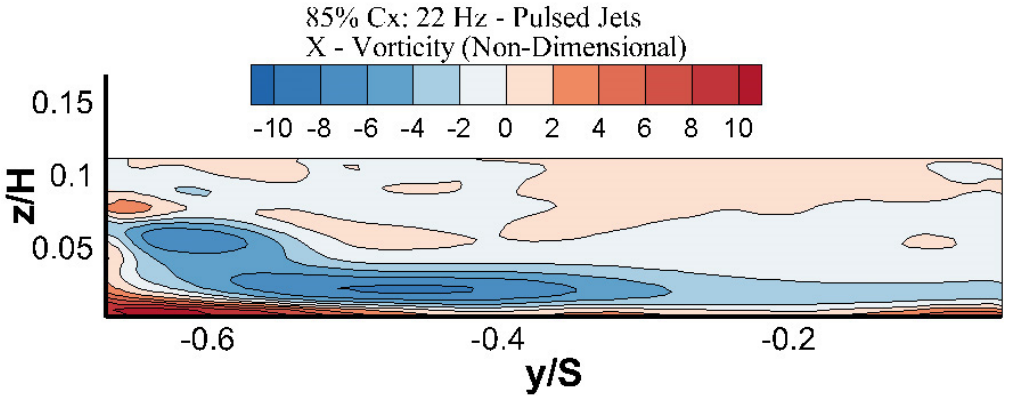

Figure 207. x – Vorticity - 22 Hz Pulsed Jets 85% Cx

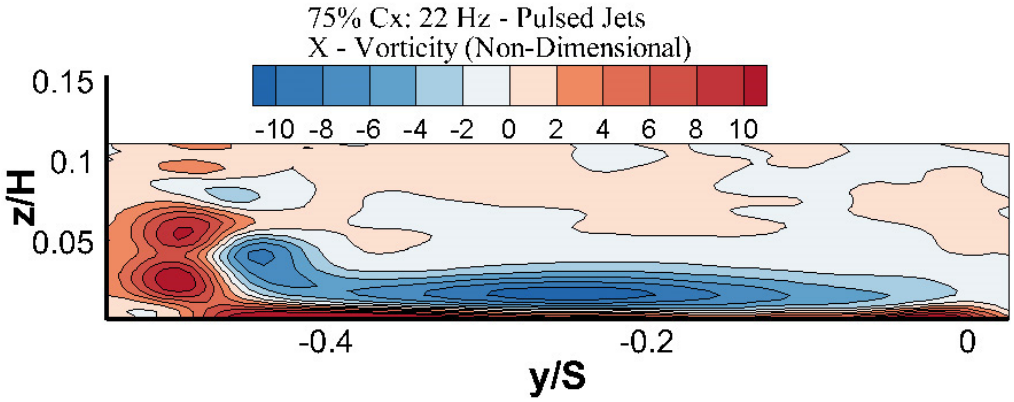

Figure 208. x – Vorticity - 22 Hz Pulsed Jets 75% Cx

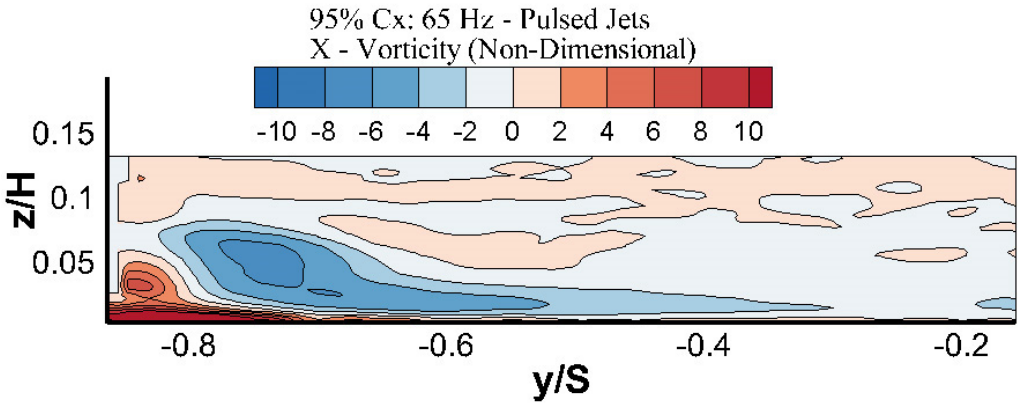

Figure 209. x – Vorticity - 65 Hz Pulsed Jets 95% Cx

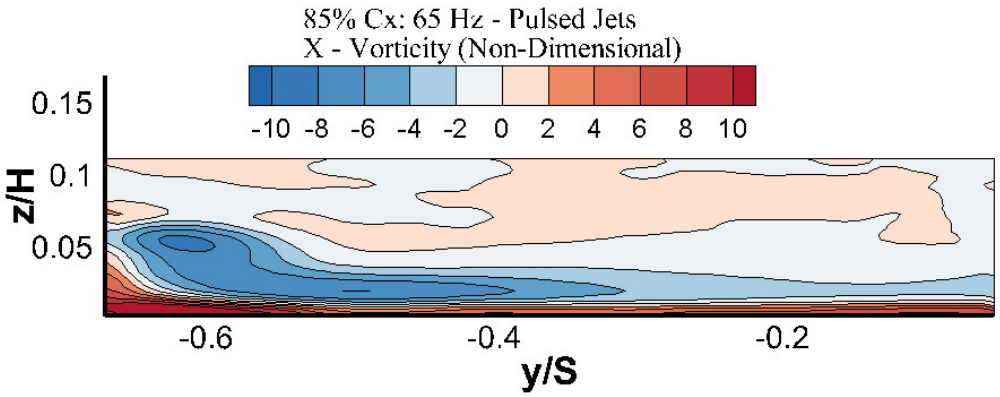

Figure 210. x – Vorticity - 65 Hz Pulsed Jets 85% Cx

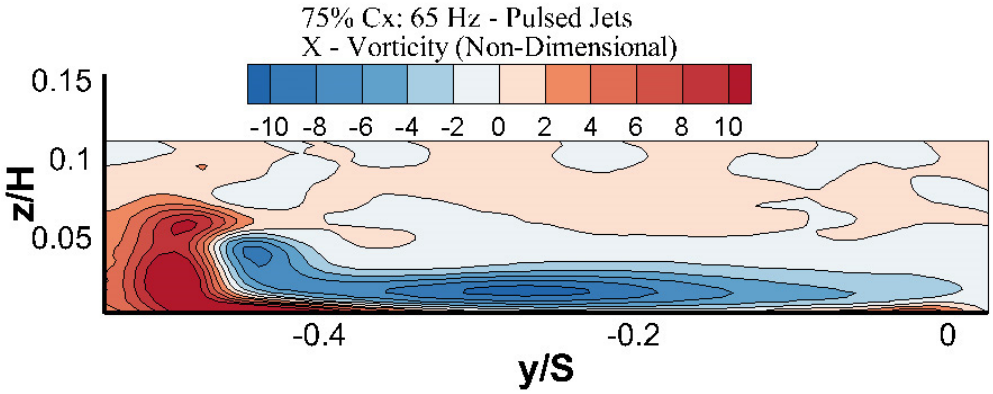

Figure 211. x – Vorticity - 65 Hz Pulsed Jets 75% Cx

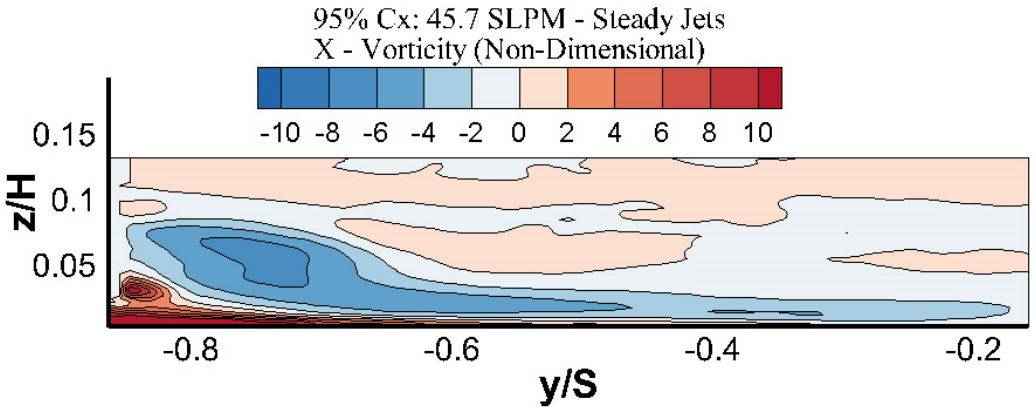

Figure 212. x – Vorticity - 45.7 SLPM Steady Jets 95% Cx

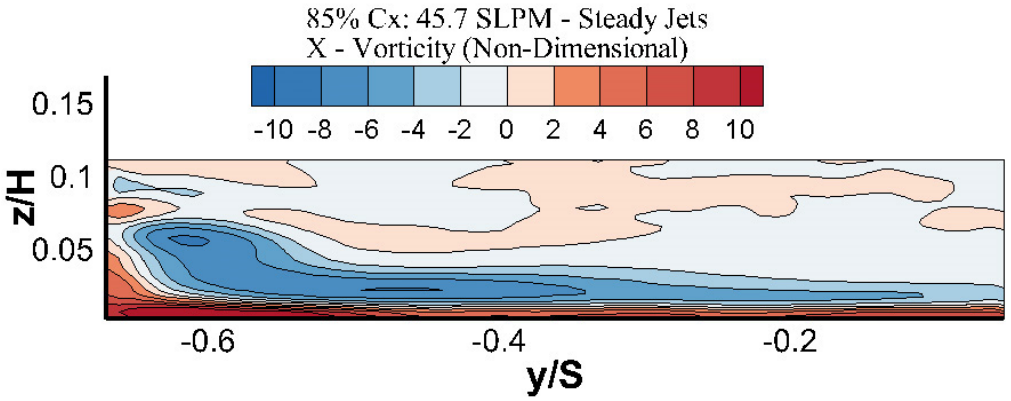

Figure 213. x – Vorticity - 45.7 SLPM Steady Jets 85% Cx

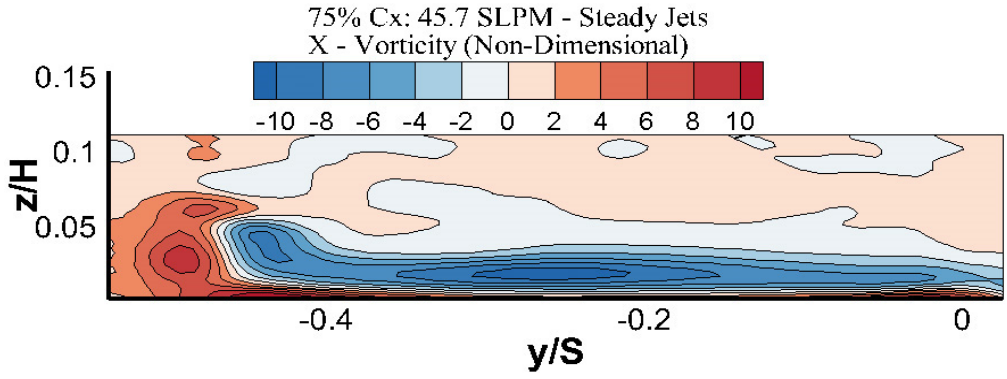

Figure 214. x – Vorticity - 45.7 SLPM Steady Jets 75% Cx

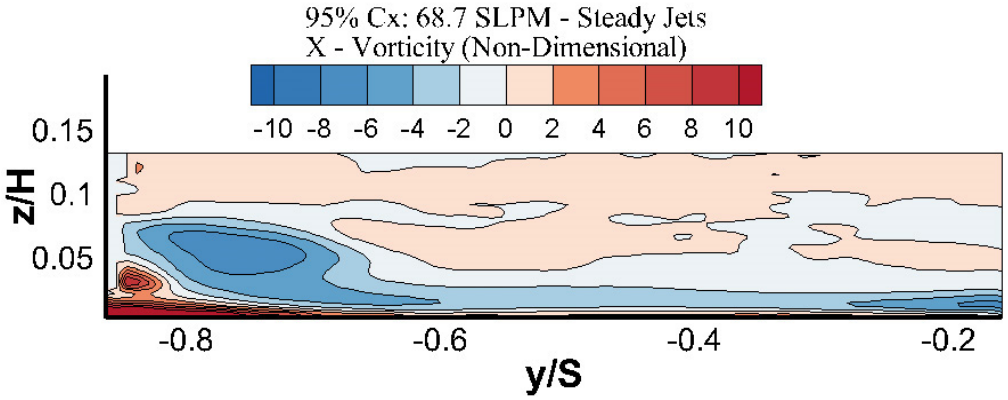

Figure 215. x – Vorticity - 68.7 SLPM Steady Jets 95% Cx

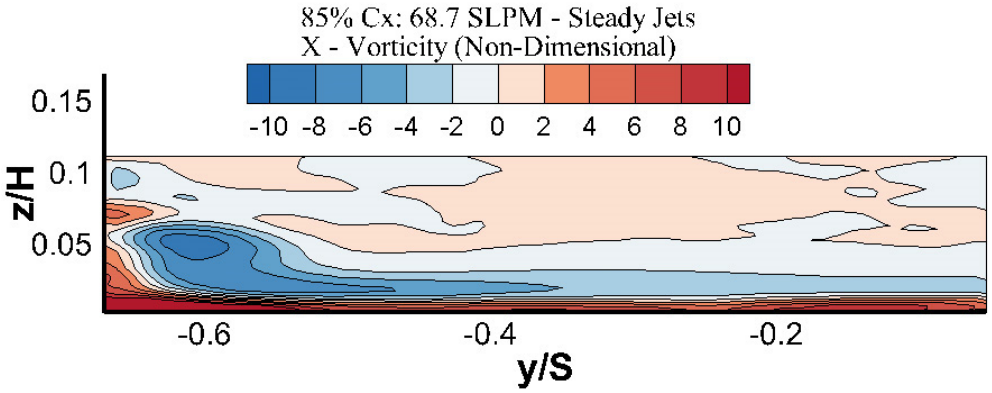

Figure 216. x – Vorticity - 68.7 SLPM Steady Jets 85% Cx

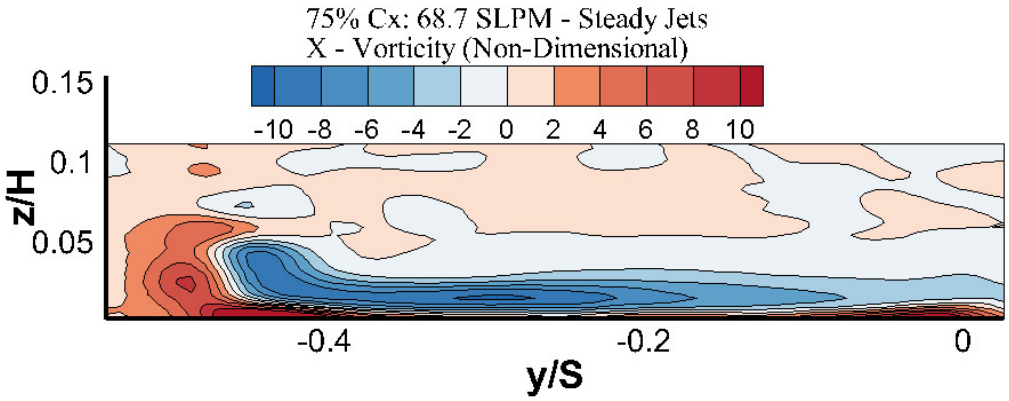

Figure 217. x – Vorticity - 68.7 SLPM Steady Jets 75% Cx

Appendix G – Additional SPIV Simplified Helmholtz Secondary Vorticity

Appendix G contains all of the average SPIV data collected and processed using the Simplified Helmholtz method to calculate the secondary vorticities. The individual plots for each test case is shown in each measurement plane.

Individual Vorticity Mapping Plots:

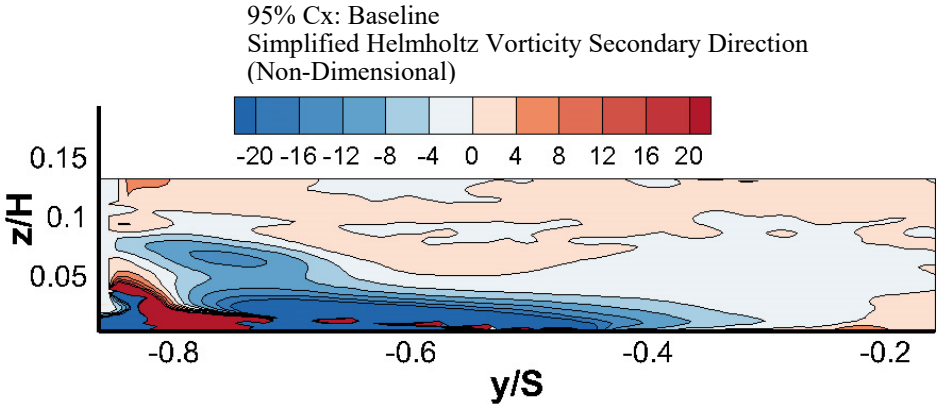

Figure 218. Simplified Helmholtz Secondary Vorticity - Baseline 95% Cx

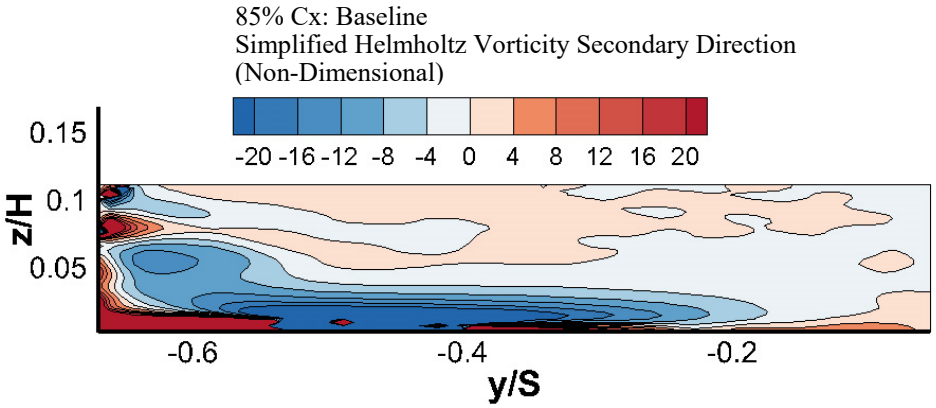

Figure 219. Simplified Helmholtz Secondary Vorticity - Baseline 85% Cx

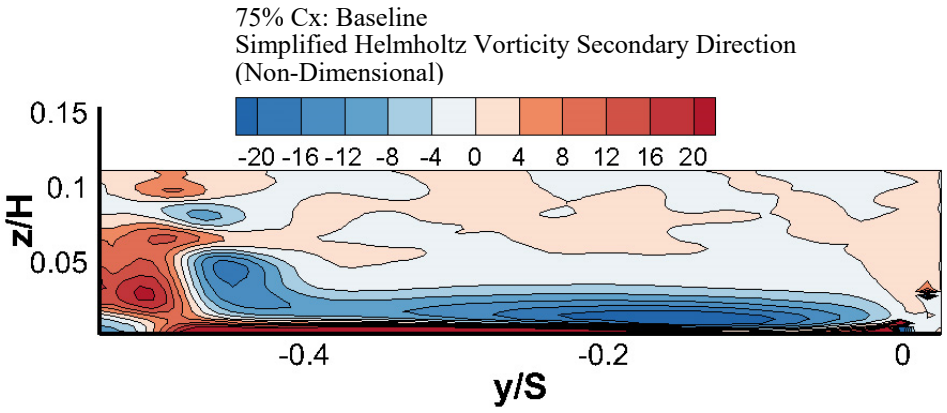

Figure 220. Simplified Helmholtz Secondary Vorticity - Baseline 75% Cx

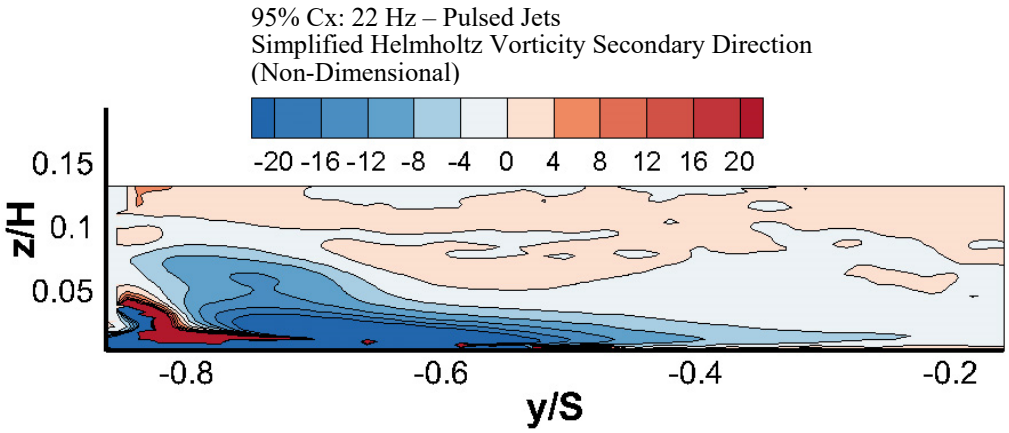

Figure 221. Simplified Helmholtz Secondary Vorticity - 22 Hz Pulsed Jets 95% Cx

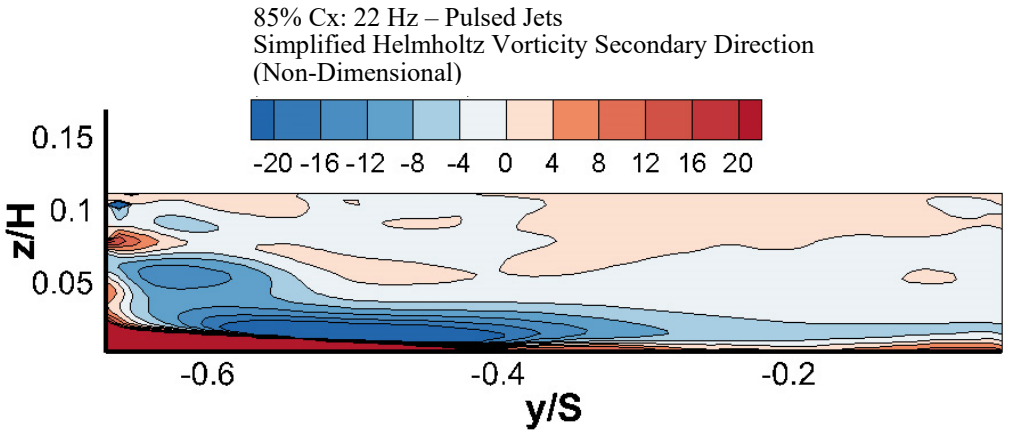

Figure 222. Simplified Helmholtz Secondary Vorticity - 22 Hz Pulsed Jets 85% Cx

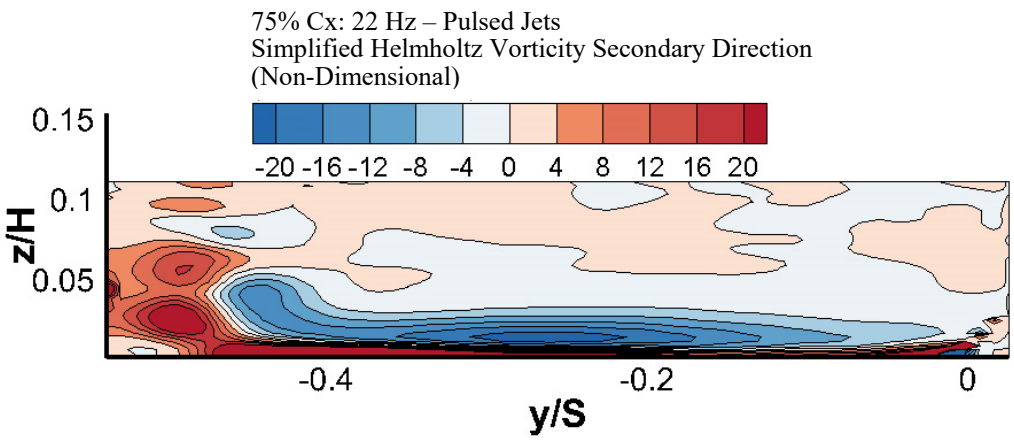

Figure 223. Simplified Helmholtz Secondary Vorticity - 22 Hz Pulsed Jets 75% Cx

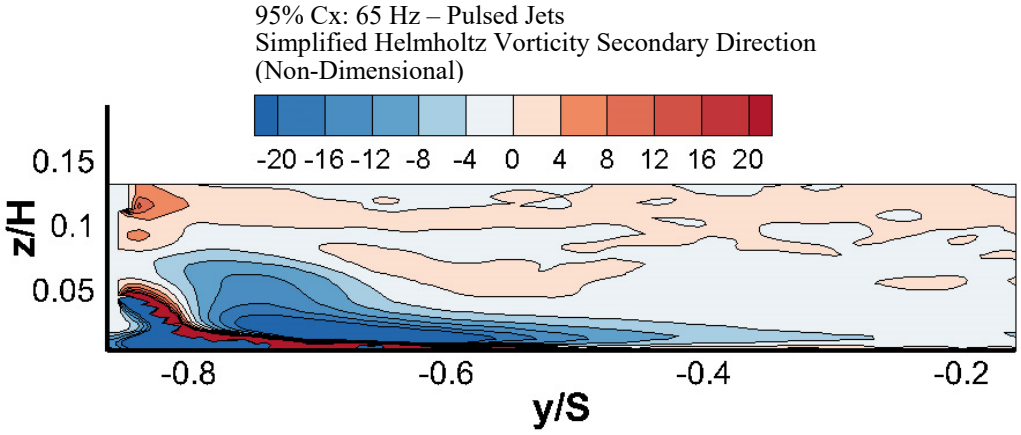

Figure 224. Simplified Helmholtz Secondary Vorticity - 65 Hz Pulsed Jets 95% Cx

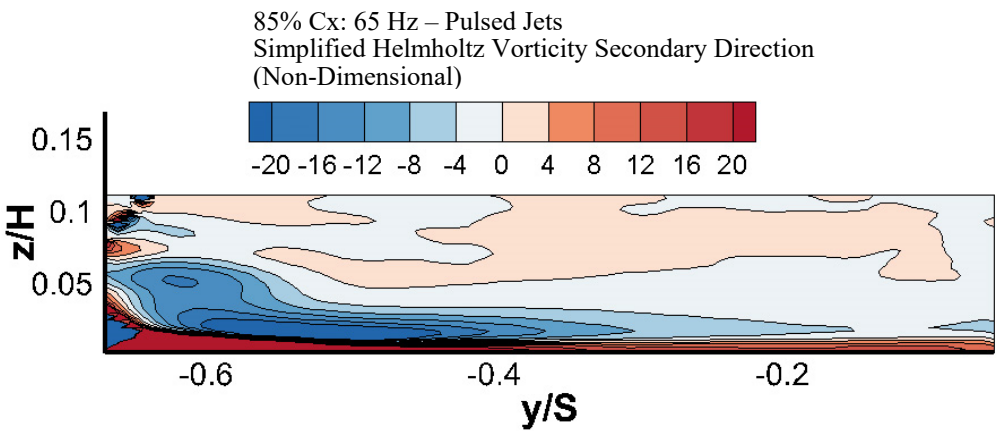

Figure 225. Simplified Helmholtz Secondary Vorticity - 65 Hz Pulsed Jets 85% Cx

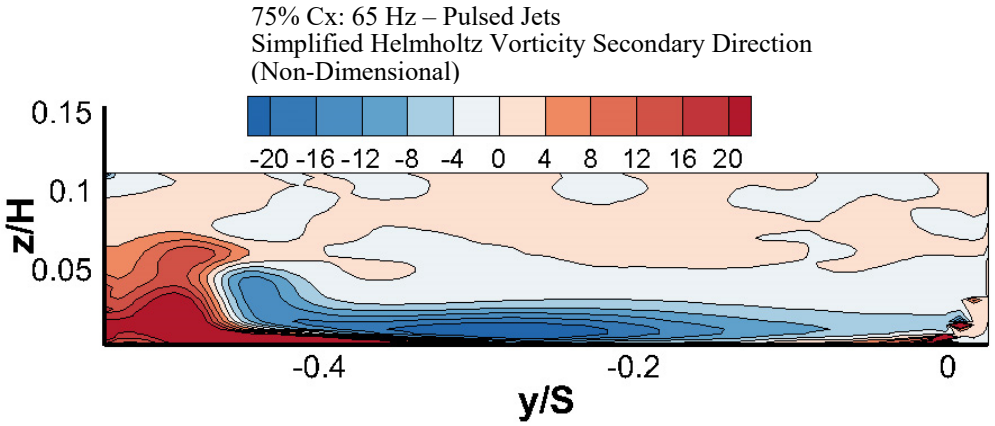

Figure 226. Simplified Helmholtz Secondary Vorticity - 65 Hz Pulsed Jets 75% Cx

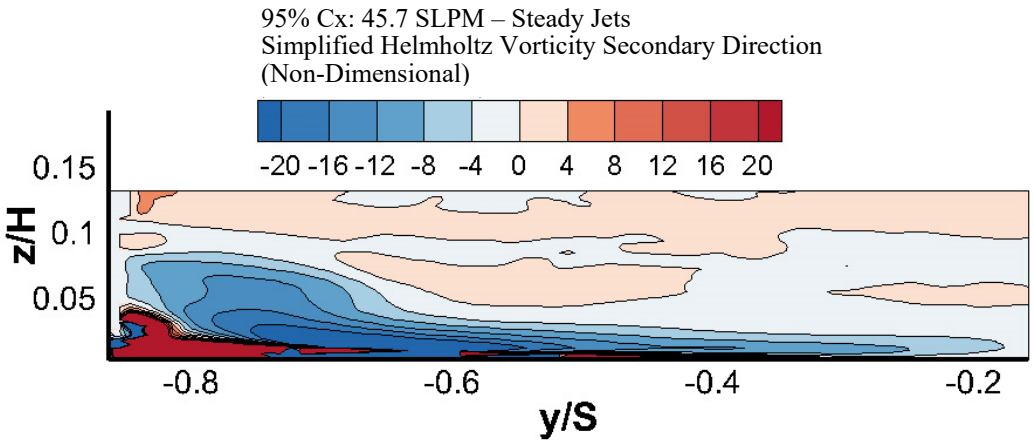

Figure 227. Simplified Helmholtz Secondary Vorticity - 45.7 SLPM Steady Jets 95% Cx

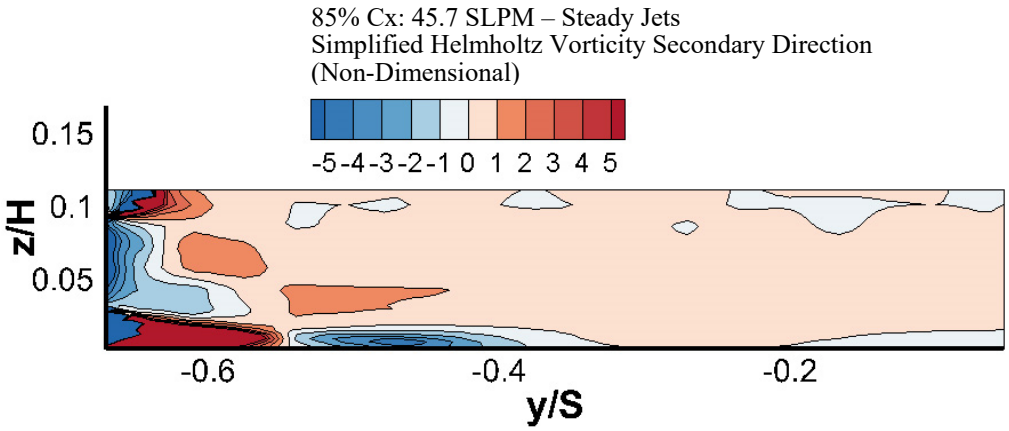

Figure 228. Simplified Helmholtz Secondary Vorticity - 45.7 SLPM Steady Jets 85% Cx

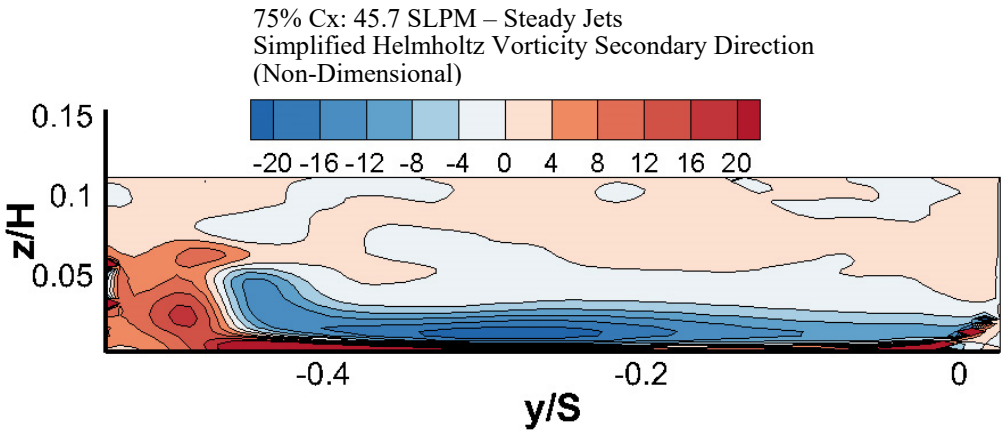

Figure 229. Simplified Helmholtz Secondary Vorticity - 45.7 SLPM Steady Jets 75% Cx

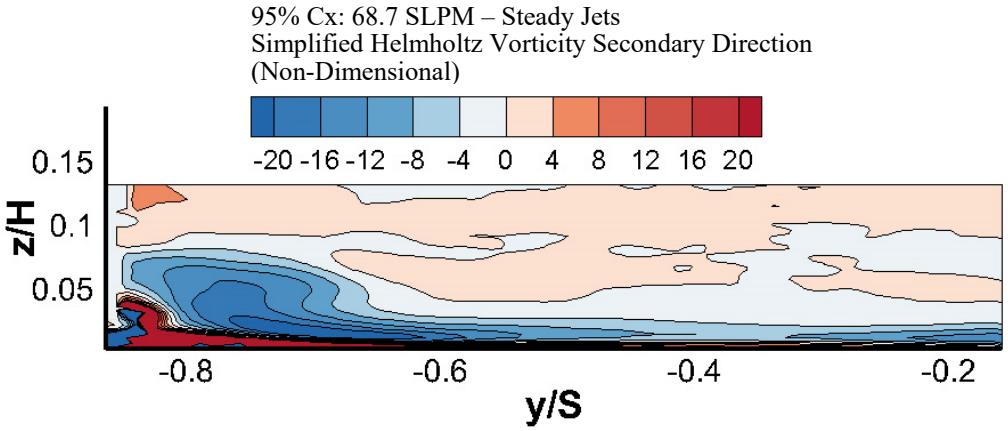

Figure 230. Simplified Helmholtz Secondary Vorticity - 68.7 SLPM Steady Jets 95% Cx

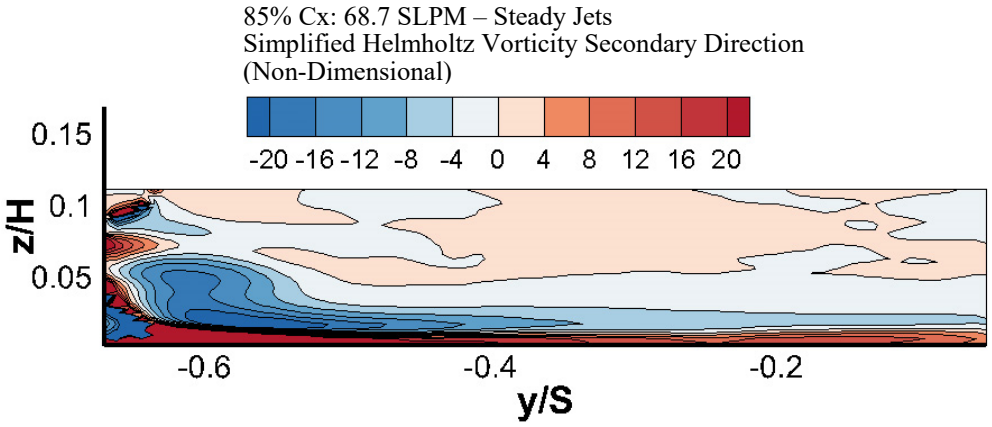

Figure 231. Simplified Helmholtz Secondary Vorticity - 68.7 SLPM Steady Jets 85% Cx

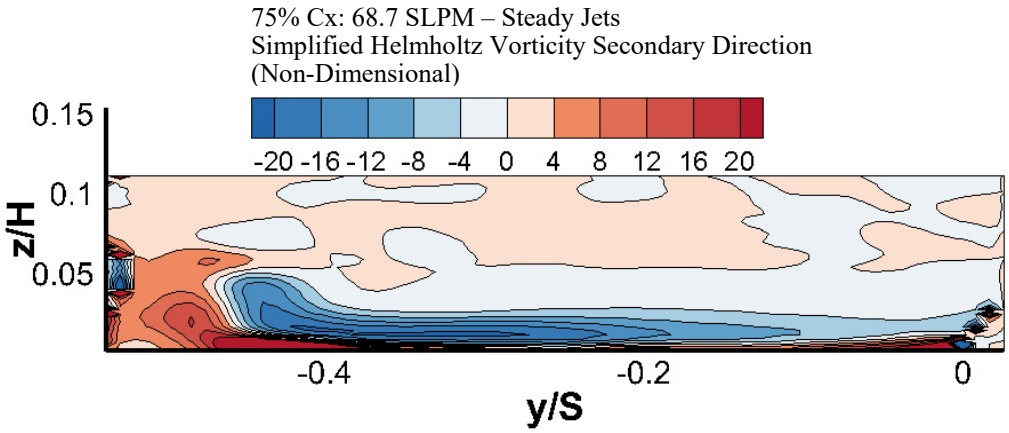

Figure 232. Simplified Helmholtz Secondary Vorticity - 68.7 SLPM Steady Jets 75% Cx

Appendix H – Additional SPIV Error Analysis

Appendix H presents a brief discussion of SPIV error associated in this research effort. Figure 233 shows the standard deviation of velocity in the 85% plane for the Baseline case, Figure 234 shows the standard deviation of velocity for the 65 Hz pulsed case and finally Figure 235 shows the standard deviation of velocity for the 68.7 SLPM cases.

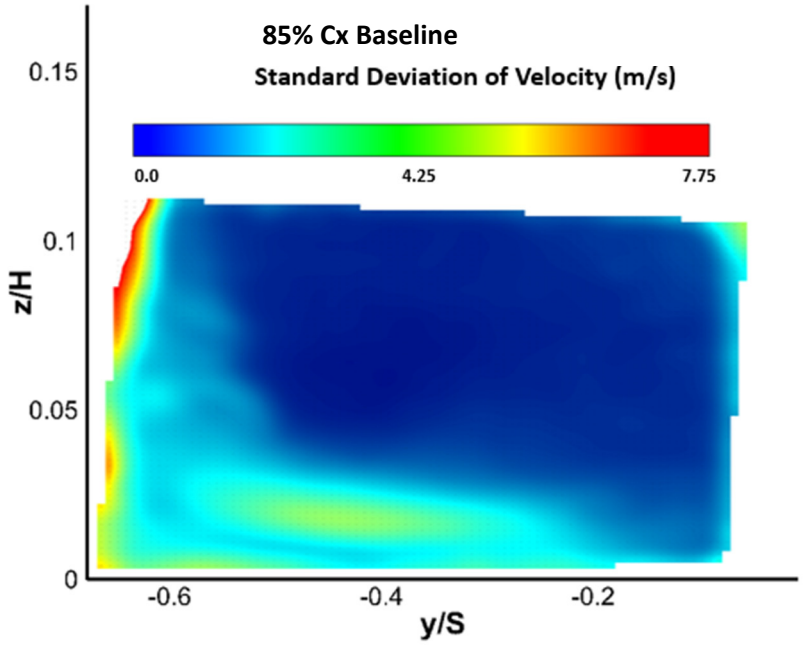

Figure 233. 85% Cx Baseline Standard Deviation of Velocity

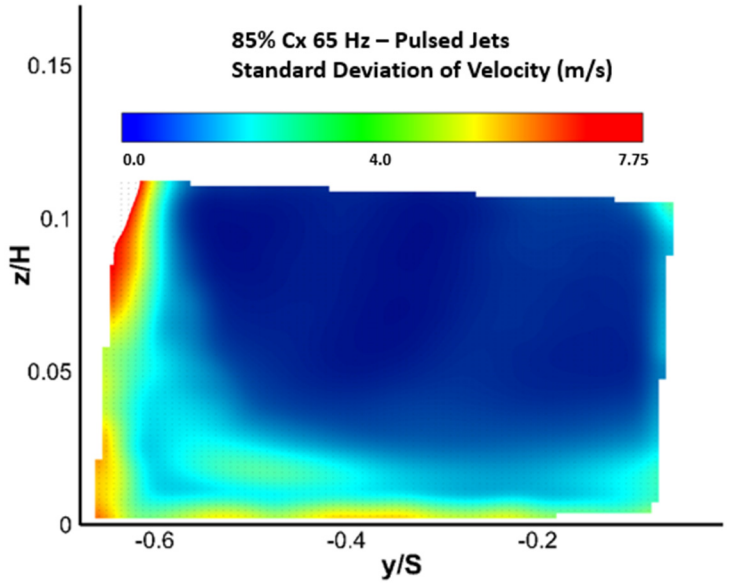

Figure 234. 85% Cx 65 Hz – Pulsed Jets Standard Deviation of Velocity

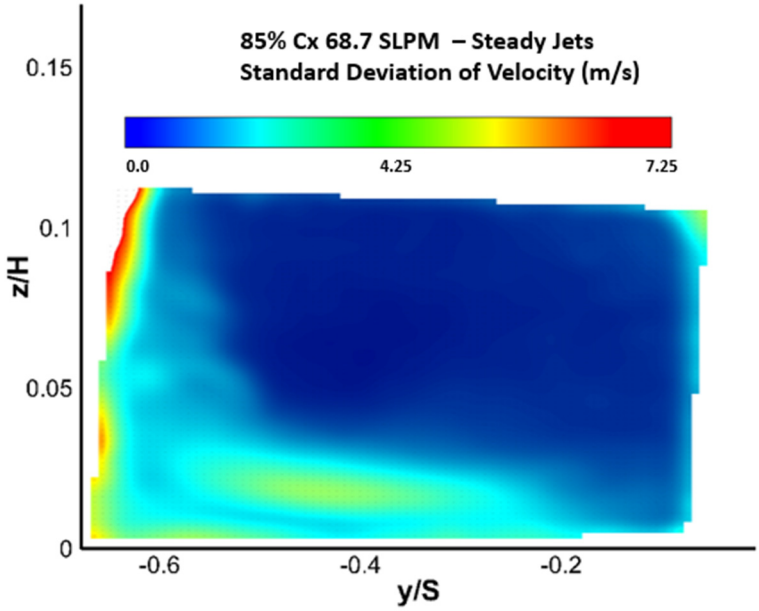

Figure 235. 85% Cx 68.7 SLPM - Steady Jets Standard Deviation of Velocity

Note in all plots of the standard deviation of velocity the regions of the flow that are not of direct interest in this report, that tis the areas where the passage and separation

vortices are not present, the standard deviation of velocity is on the order of 0.75 m/s. This velocity, in the 85% plane for instance, results in a deviation of approximately 3.5% with a given local flow velocity of 19.5 m/s. The fluctuation in velocity is representative of the freestream turbulence intensity of 3% found in the LSWT. The pixel displacements for the three representative cases are shown in Figure 236 for the Baseline case, Figure 237 for the 65 Hz case and Figure 238 for the 68.7 SLPM case. Pixel displacements between 5 and 8 pixels were desired for the given flow conditions.

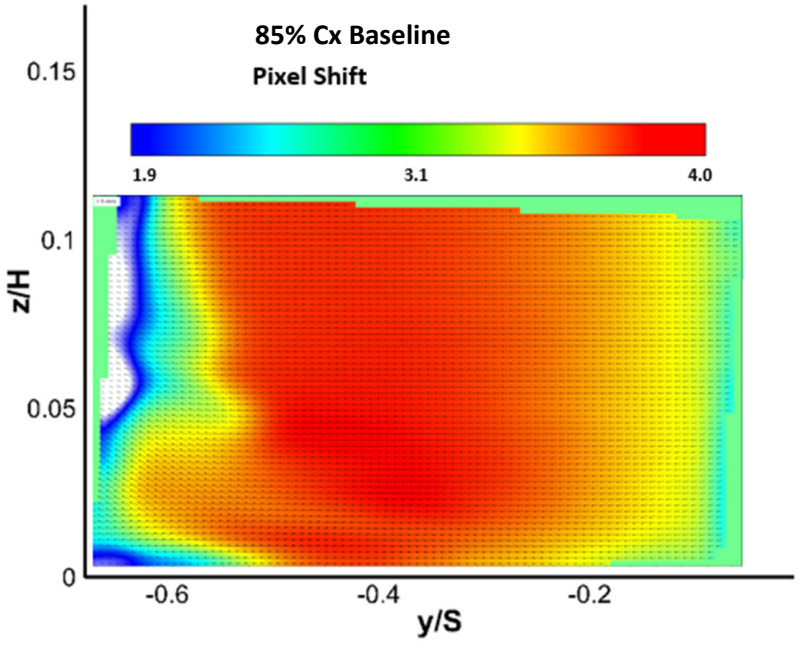

Figure 236. 85% Cx Baseline Pixel Shift

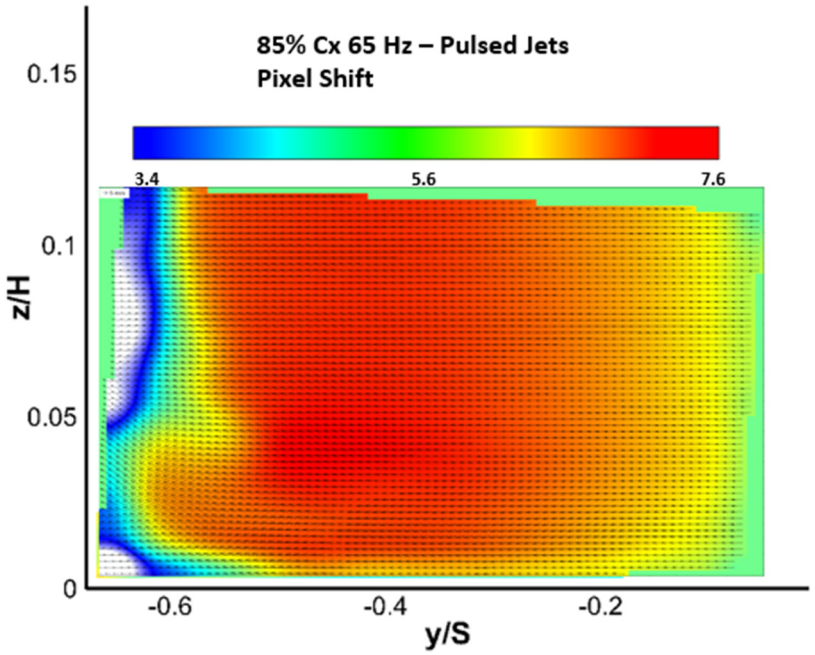

Figure 237. 85% Cx 65 Hz - Pulsed Jets Pixel Shift

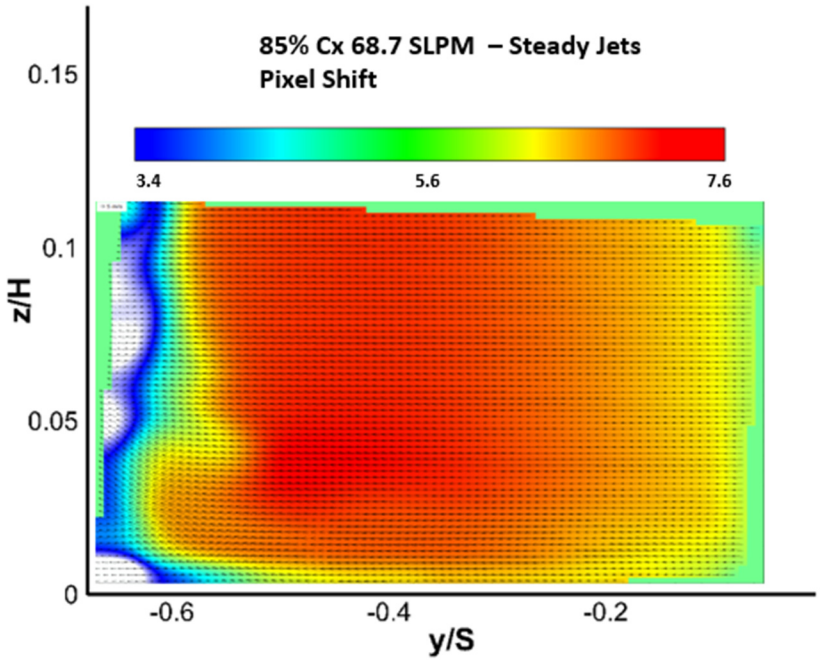

Figure 238. 85% Cx 68.7 SLPM - Pulsed Jets Pixel Shift

The time between images changed between planes based upon the local flow velocities. The *dt's* for each plane were 20 μsec, 40 μsec, and 35 μsec for the 95%, 85% and 75% planes respectively. The Baseline 85% Cx case was an anomaly though with a *dt* of 20 μsec. As a final check of the reliability of the data the correlation values for the representative cases can be seen in the following figures. Figure 239 shows the correlation value for the 0 Hz case, Figure 240 shows the correlation value for the 65 Hz case and Figure 241 shows the 68.7 SLPM forcing case value. For this study, a data set was considered acceptable if the correlation value for the majority of the sample space was above 0.6.

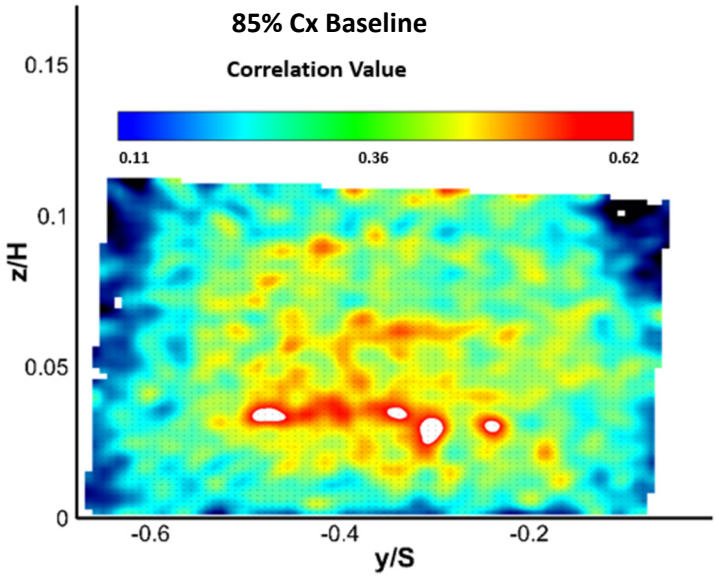

Figure 239. 85% Cx Baseline Correlation Value

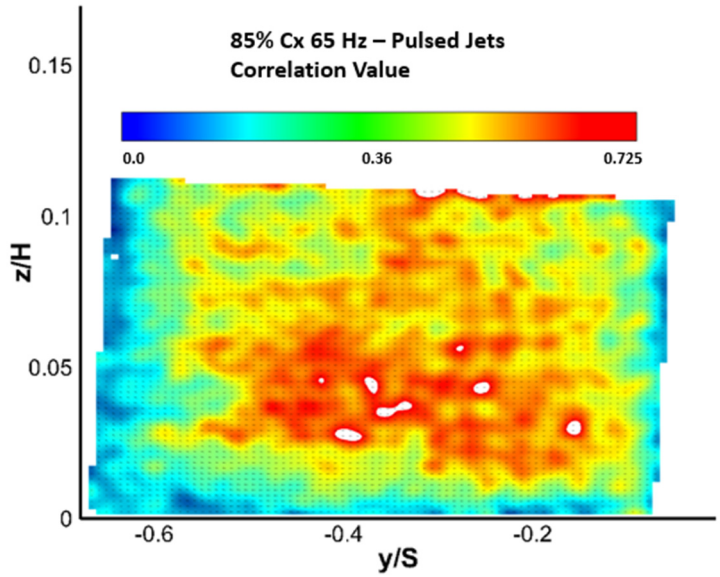

Figure 240. 85% Cx 65 Hz - Pulsed Jets Correlation Value

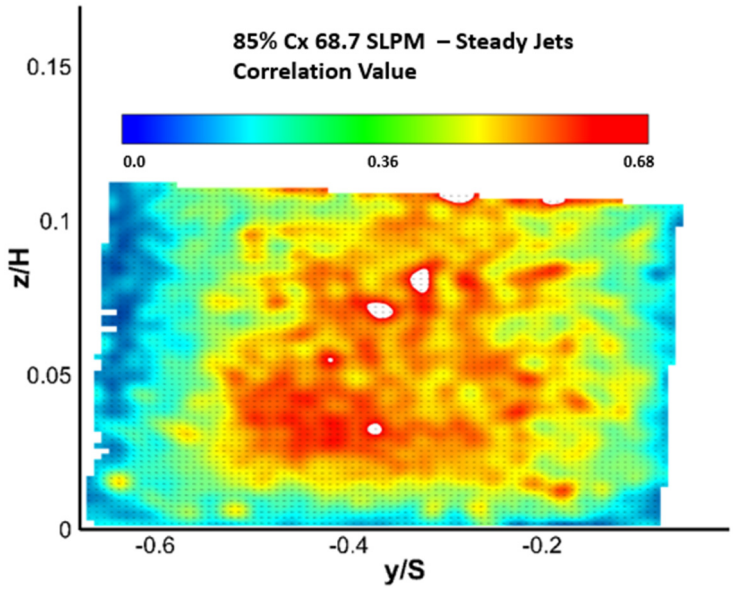

Figure 241. 85% Cx 68.7 SLPM - Steady Jets Correlation Value

Bibliography

[1] K. Palt, “McDonnell Douglas / Boeing C-17 Globemaster III Heavy Military Transport Aircraft,” 2017. [Online]. Available: http://www.flugzeuginfo.net/acdata_php/acdata_7474_en.php%0A. [Accessed: 20-Aug-2011].

[2] U.S. Department of Transportation Federal Avation Administration, “U.S. Department of Transportation Federal Avation Administration Type Certificate Data Sheet E17NE,” 2014.

[3] United Technologies Corporation - Pratt & Whitney Division, “JT9D Engine.” [Online]. Available: http://www.pw.utc.com/products-and-services/products/commercial-engines/JT9D-Engine/. [Accessed: 12-Nov-2018].

[4] D. Rutherford, “Size Matters for Aircraft Fuel Efficiency. Just Not in the Way That You Think.,” *International Council on Clean Transportation*, 2018. [Online]. Available: https://www.theicct.org/blog/staff/size-matters-for-aircraft-fuel-efficiency. [Accessed: 12-Nov-2018].

[5] D. T. Mattingly, Jack; Heiser, William H.; Pratt, *Aircraft Engine Design 2nd Edition*. 2002.

[6] R. J. Howell, Hodson, H. P., Schulte, V., Stieger, R. D., Schiffer, Heinz-Peter, Haselbach, F.Harvey, N. W., “Boundary Layer Development in the BR710 and BR715 LP Turbines—The Implementation of High-Lift and Ultra-High-Lift Concepts,” *J. Turbomach.*, vol. 124, no. 3, p. 385-392, 2002.

[7] T. J. Praisner, Grover, E. A., Knezevici, D. C., Popovic, I., Sjolander, S. A., Clark, J. P., Sondergaard, R., “Toward the Expansion of Low-Pressure-Turbine Airfoil Design Space,” *J. Turbomach.*, vol. 135, no. 6, p. 061007, Sep. 2013.

[8] M. McQuilling, “Design and Validation of a High-Lift Low-Pressure Turbine Blade,” Air Force Institute of Technology, 2007.

[9] E. M. Lyall, “Effects of Front-Loading and Stagger Angle on Endwall Losses of High Lift Low Pressure Turbine Vanes,” Air Force Institute of Technology, 2012.

[10] E. M. Lyall, P. I. King, J. P. Clark, and R. Sondergaard, “Endwall Loss Reduction of High Lift Low Pressure Turbine Airfoils Using Profile Contouring—Part I: Airfoil Design,” *J. Turbomach.*, vol. 136, no. 8, p. 081005, Jan. 2014.

[11] O. P. Sharma, K. A. Belford, and R. H. Ni, “Three-Dimensional Turbopump Flowfield Analysis,” 1992.

[12] O. P. Sharma and T. L. Butler, “Predictions of Endwall Losses and Secondary Flows in Axial Flow Turbine Cascades,” *J. Turbomach.*, vol. 109, no. 2, 1987.

[13] J. Bons, S. Benton, C. Bernardini, and M. Bloxham, “Active Flow Control for Low-Pressure Turbines,” *AIAA Journal*, vol. 56, no. 7, pp. 2687–2698, 2018.

[14] E. Veley, C. Marks, R. Anthony, R. Sondergaard, and M. Wolff, “Unsteady Flow Measurements in a Front Loaded Low Pressure Turbine Passage,” in *2018 AIAA Aerospace Sciences Meeting*, 2018, p. 10.2514/6.2018-2124.

[15] P. S. Bear, “On the Experimental Evaluation of Loss Production and Recustion in a Highly Loaded Low Pressure Turbine Cascade,” Wright State University, 2016.

[16] J. A. Dickel, C. Marks, J. Clark, R. Sondergaard, and M. Wolff, “Non-Axisymmetric Endwall Contouring of Front-Loaded High-Lift Low Pressure Turbines,” in *2018 AIAA Aerospace Sciences Meeting*, 2018, p. 10.2514/6.2018-2125.

[17] N. Fletcher, C. Marks, R. Petrie, R. Sondergaard, and M. Wolff, “Experimental Investigation of Endwall Flow Control for Front Loaded Turbine Blades,” in *2018 Joint Propulsion Conference*, 2018, p. 10.2514/6.2018-4436.

[18] M. T. Maybury, “Technology Horizons: A Vision for Air Force Science and Technology 2010-30,” *Air Sp. Power J.*, no. April, pp. 3–30, 2012.

[19] E. M. Curtis, H. P. Hodson, M. R. Banieghbal, J. D. Denton, R. J. Howell, and N. W. Harvey, “Development of Blade Profiles for Low-Pressure Turbine Applications,” *J. Turbomach.*, vol. 119, no. 3, pp. 531–538, 1997.

[20] J. T. Schmitz Schmitz, J. T., Perez, E., Morris, S. C., Corke, T. C., Clark, J. P., Koch, P. J., Puterbaugh, S. L., “Highly Loaded Low-Pressure Turbine: Design, Numerical, and Experimental Analysis,” *J. Propuls. Power*, vol. 32, no. 1, pp. 142–152, 2016.

[21] C. R. Marks, R. Sondergaard, P. S. Bear, and M. Wolff, “Reynolds Number Effects on the Secondary Flow of Profile Contoured Low Pressure Turbines,” in *54th AIAA Aerospace Sciences Meeting*, 2016, p. 10.2514/6.2016-0114.

[22] P. Bear, M. Wolff, A. Gross, C. R. Marks, and R. Sondergaard, “Experimental

Investigation of Total Pressure Loss Development in a Highly Loaded Low-Pressure Turbine Cascade," *J. Turbomach.*, vol. 140, p. 031003, 2018.

[23] M. H. Donovan, M. Wolff, C. R. Marks, R. Sondergaard, and E. Veley, "Periodic Forcing of an Endwall Vortex in a Highly Loaded Low Pressure Turbine," in *AIAA Scitech 2019 Forum*, 2019, no. January, p. 10.2514/6.2019-0621.

[24] J. P. Bons, L. C. Hansen, J. P. Clark, P. J. Koch, and R. Sondergaard, "Designing Low-Pressure Turbine Blades With Integrated Flow Control," in *Volume 3: Turbo Expo 2005, Parts A and B*, 2005, pp. 1079–1091.

[25] J. Cornish, III, "Vortex Flows," in *Applied Aerodynamics Conference*, 1983, p. AIAA-83-1812.

[26] D. Küchemann, "Report on the I.U.T.A.M. Symposium on Concentrated Vortex Motions in Fluids," *J. Fluid Mech.*, vol. 21, no. 01, Jan. 1965.

[27] W. A. Eckerle and L. S. Langston, "Measurements of a Turbulent Horseshoe Vortex Formed Around a Cylinder," 1986.

[28] Cummings, Russel M, Mason, Williiam H, Morton, Scott A Mcdaniel, David R., *Applied Computational Aerodynamics*.

[29] E. Veley, C. Marks, R. Anthony, R. Sondergaard, N. Fletcher, and M. Wolff, "Unsteady Flow Measurements in a Low Pressure Turbine Passage using Surface Mounted Thin Film Sensors," in *53rd AIAA/SAE/ASEE Joint Propulsion Conference*, 2017, p. 10.2514/6.2017-4825.

[30] S. Harrison, "Secondary Loss Generation in a Linear Cascade of High-Turning Turbine Blades," *Vol. 1 Turbomach.*, vol. 112, no. October 1990, pp. 618–624, 1989.

[31] T. Kawai and T. Adachi, "Effects of Blade Boundary Layer Fences on Secondary Flow and Losses in a Turbine Cascade.," *Trans. Japan Soc. Mech. Eng. Ser. B*, vol. 54, no. 505, pp. 2484–2491, 1988.

[32] S. Anders, W. Sellers III, and A. Washburn, "Active Flow Control Activities at NASA Langley," in *2nd AIAA Flow Control Conference*, 2004, p. 2004-2623.

[33] T. Kawai, S. Shinoki, and T. Adachi, "Secondary Flow Control and Loss Reduction in a Turbine Cascade Using Endwall Fences," *JSME Int. Journal. Ser. 2, Fluids Eng. Heat Transf. Power, Combust. Thermophys. Prop.*, vol. 32, no. 3,

pp. 375–387, 1989.

[34] T. Kawai, S. Shinoki, and T. Adachi, “Visualization Study of Three-Dimensional Flows in a Turbine Cascade Endwall Region,” *JSME Int. Journal. Ser. 2, Fluids Eng. Heat Transf. Power, Combust. Thermophys. Prop.*, vol. 33, no. 2, pp. 256–264, 1990.

[35] J. T. Chung, T. W. Simon, and J. Buddhavarapu, “Three-Dimensional Flow Near the Blade/Endwall Junction of a Gas Turbine: Application of a Boundary Layer Fence,” in *Volume 4: Heat Transfer; Electric Power; Industrial and Cogeneration*, 1991, vol. 113, p. 91-GT-45.

[36] J. T. Chung and T. W. Simon, “Effectiveness of the Gas Turbine Endwall Fences in Secondary Flow Control at Elevated Freestream Turbulence Levels,” in *International Gas Turbine and Aeroengine Congress and Exposition*, 1993, p. 10.1115/93GT051.

[37] N. V Aunapu, R. J. Volino, K. A. Flack, and R. M. Stoddard, “Secondary Flow Measurements in a Turbine Passage With Endwall Flow Modification,” *J. Turbomach.*, vol. 122, no. 4, pp. 651–658, 2000.

[38] Y. J. Moon and S. R. Koh, “Counter-Rotating Streamwise Vortex Formation in the Turbine Cascade with Endwall Fence,” *Comput. Fluids*, vol. 30, no. 4, pp. 473–490, 2001.

[39] M. Govardhan and K. N. Kumar, “Secondary Flow Loss Reduction in a Turbine Cascade with a Linearly Varied Height Etreamwise Endwall Fence,” *Int. J. Rotating Mach.*, vol. 2011, p. 10.1155/2011/352819, 2011.

[40] H. Sauer, H. Wolf, “Influencing the Secondary Flow in Turbine Cascades by the Modification of the Blade Leading Edge,” in *Proceedings 2nd European Conference on Turbomachinery*, 1997.

[41] H. Sauer, R. Müller, and K. Vogeler, “Reduction of Secondary Flow Losses in Turbine Cascades by Leading Edge Modifications at the Endwall,” *J. Turbomach.*, vol. 123, no. 2, p. 207, 2001.

[42] O. Mannerfelt, “Ship hull and vessel with such a hull,” US6058864A.

[43] G. I. Mahmood and S. Acharya, “Experimental Investigation of Flow Structure and Nusselt Number in a Low-Speed Linear Blade Passage With and Without Leading-Edge Fillets,” *J. Heat Transfer*, vol. 127, no. 5, 2005.

[44] A. T. Lethander, K. A. Thole, G. Zess, and J. Wagner, "Optimizing the Vane-Endwall Junction to Reduce Adiabatic Wall Temperatures in a Turbine Vane Passage," *Vol. 5 Turbo Expo 2003, Parts A B*, vol. 20, no. 6, pp. 711–721, 2003.

[45] J. C. Hartland, D. G. Gregory-Smith, N. W. Harvey, and M. G. Rose, "Nonaxisymmetric Turbine End Wall Design: Part II—Experimental Validation," *J. Turbomach.*, vol. 122, pp. 286–293, 2000.

[46] A. E. Deich, M. E., and Zaryankin, "'Methods of Increasing the Efficiency of Turbine Stages," *Teploenergetica*, vol. No. 2, pp. 18–24, 1960.

[47] N. W. Harvey, M. G. Rose, M. D. Taylor, S. Shahpar, J. Hartland, and D. G. Gregory-Smith, "Nonaxisymmetric Turbine End Wall Design: Part I - Three-Dimensional Linear Design System," *J. Turbomach.*, vol. 122, pp. 278–285, 2000.

[48] D. C. Knezevici, S. A. Sjolander, T. J. Praisner, E. Allen-Bradley, and E. A. Grover, "Measurements of Secondary Losses in a High-Lift Front-Loaded Turbine Cascade With the Implementation of Non-Axisymmetric Endwall Contouring," *Vol. 7 Turbomachinery, Parts A B*, vol. 132, pp. 965–977, 2009.

[49] T. J. Praisner, E. Allen-Bradley, E. A. Grover, D. C. Knezevici, and S. A. Sjolander, "Application of Nonaxisymmetric Endwall Contouring to Conventional and High-Lift Turbine Airfoils," *J. Turbomach.*, vol. 135, no. 6, p. 061006, Sep. 2013.

[50] K. McManus, H. Legner, and S. Davis, "Pulsed Vortex Generator Jets for Active Control of Flow Separation," in *Fluid Dynamics Conference*, 1994, p. 10.2514/6.1994-2218.

[51] J. P. Bons, R. Sondergaard, and R. B. Rivir, "Turbine Separation Control Using Pulsed Vortex Generator Jets," *J. Turbomach.*, vol. 123, no. 2, pp. 198–206, 2001.

[52] R. Sondergaard, R. B. Rivir, and J. P. Bons, "Control of Low-Pressure Turbine Separation Using Vortex-Generator Jets," *J. Propuls. Power*, vol. 18, no. 4, pp. 889–895, 2002.

[53] D. P. Rizzetta and M. R. Visbal, "Numerical Study of Active Flow Control for a Transitional Highly Loaded Low-Pressure Turbine," 2006, vol. 128, no. 5, p. 10.1115/1.2238877.

[54] J. P. Bons, R. Sondergaard, and R. B. Rivir, "The Fluid Dynamics of LPT Blade Separation Control Using Pulsed Jets," *J. Turbomach.*, vol. 124, no. 1, pp. 77–85,

2002.

[55] S. I. Benton, J. P. Bons, and R. Sondergaard, “Secondary Flow Loss Reduction Through Blowing for a High-Lift Front-Loaded Low Pressure Turbine Cascade,” *J. Turbomach.*, vol. 135, no. 2, p. 021020, 2013.

[56] S. I. Benton, C. Bernardini, J. P. Bons, and R. Sondergaard, “Parametric Optimization of Unsteady End Wall Blowing on a Highly Loaded Low-Pressure Turbine,” *J. Turbomach.*, vol. 136, no. 7, p. 071013, 2014.

[57] A. Gross, C. Marks, and R. Sondergaard, “Numerical Simulations of Active Flow Control for Highly Loaded Low-Pressure Turbine Cascade,” 2017, p. 10.25146.2017-1460.

[58] A. Gross, S. Romero, C. Marks, and R. Sondergaard, “Numerical Investigation of Low-Pressure Turbine Endwall Flows,” in *54th AIAA Aerospace Sciences Meeting*, 2016, p. 10.2514/6.2016-0331.

[59] E. Veley, “Measurement of Unsteady Characteristics of Endwall Vorticies,” Wright State University, 2017.

[60] Agilent Technologies, “The Fundamentals of Signal Analysis.” 2000.

[61] R. J. Adrian, “Uses, Analysis and Interpretation of PIV Data,” 1999, p. 10.2514/6.1999-3753.

[62] R. J. Adrian, “Twenty Years of Particle Image Velocimetry,” *Exp. Fluids*, vol. 39, no. 2, pp. 159–169, 2005.

[63] S. J. Beresh, “Comparison of PIV Data Using Multiple Configurations and Processing Techniques,” *Exp. Fluids*, vol. 47, no. 6, pp. 883–896, 2009.

[64] P. A. Gulotta, M. F. Reeder, C. R. Hoskins, and B. J. Hagen, “Particle Image Velocimetry Particle-Response Study in the AFRL Mach 3 Tunnel,” *55th AIAA Aerosp. Sci. Meet.*, p. 10.2514/6.2017-0474, 2017.

[65] LaVision, “13 Stereoscopic PIV,” in *Product-Manual for DaVis 8.4*, Gottingen: LaVision GmbH, 2017, pp. 121–135.

[66] B. H. Timmins, B. W. Wilson, B. L. Smith, and P. P. Vlachos, “A Method for Automatic Estimation of Instantaneous Local Uncertainty in Particle Image Velocimetry Measurements,” *Exp. Fluids*, vol. 53, no. 4, pp. 1133–1147, 2012.

[67] C. W. H. van Doorne, J. Westerweel, and F. T. M. Nieuwstadt, “Measurement Uncertainty of Stereoscopic-PIV for Flow with Large Out-of-plane Motion,” *Particle Image Velocimetry: Recent Improvements*, no. 1999. pp. 213–227, 2004.

[68] D. G. Gregory-Smith, C. P. Graves, and J. a. Walsh, “Growth of Secondary Losses and Vorticity in an Axial Turbine Cascade,” *J. Turbomach.*, vol. 110, p. 10.1115/1.3262163, 1988.

[69] A. Perdichizzi, “Mach Number Effects on Secondary Flow Development Downstream of a Turbine Cascade,” *Vol. 1 Turbomach.*, vol. 112, no. October 1990, pp. 643–651, 1989.

[70] F. Taremi, S. A. Sjolander, and T. J. Praisner, “Application of Endwall Contouring to Transonic Turbine Cascades: Experimental Measurements at Design Conditions,” *J. Turbomach.*, vol. 135, no. 1, p. 061006, Oct. 2012.

[71] R. A. Granger, *Fluid Mechanics*. 1985.

REPORT DOCUMENTATION PAGE

Form Approved
OMB No. 074-0188

1. REPORT DATE *(DD-MM-YYYY)*	2. REPORT TYPE	3. DATES COVERED *(From – To)*
21-03-2012	Master's Thesis	January 2018 – March 2019

TITLE AND SUBTITLE

Investigation of Endwall Vortex Manipulation In High Lift Turbines Caused By Active Endwall Forcing

5a. CONTRACT NUMBER

5b. GRANT NUMBER

5c. PROGRAM ELEMENT NUMBER

6. AUTHOR(S)

Babcock, Horatio J., Second Lieutenant, USAF

5d. PROJECT NUMBER
JON 19Y218C

5e. TASK NUMBER

5f. WORK UNIT NUMBER

7. PERFORMING ORGANIZATION NAMES(S) AND ADDRESS(S)
Air Force Institute of Technology
Graduate School of Engineering and Management (AFIT/ENY)
2950 Hobson Way, Building 640
WPAFB OH 45433-8865

8. PERFORMING ORGANIZATION REPORT NUMBER
AFIT-ENY-MS-19-M-202

9. SPONSORING/MONITORING AGENCY NAME(S) AND ADDRESS(ES)
Air Force Research Laboratory Aerospace Systems Directorate
1950 5th St. B20252 R11 WPAFB OH 45433
(937) 785-66764, christopher.marks.6@us.af.mil
ATTN: Dr. Christopher Marks

10. SPONSOR/MONITOR'S ACRONYM(S)
AFRL/RQTT

11. SPONSOR/MONITOR'S REPORT NUMBER(S)

12. DISTRIBUTION/AVAILABILITY STATEMENT
DISTRUBTION STATEMENT A. APPROVED FOR PUBLIC RELEASE; DISTRIBUTION UNLIMITED.

13. SUPPLEMENTARY NOTES

14. ABSTRACT
With the increased demand for lighter, more fuel efficient, gas turbine engines, the impetus to reduce engine weight has become apparent. One approach to reduce this weight is to reduce the number of blades in the turbine. However, to maintain power output, each blade must be capable of supporting a greater amount of lift. While several high-lift turbine profiles have been detailed in literature, most of these profiles have increased endwall losses, despite their desirable mid-span characteristics. The current effort documents significant manipulation and reduction in strength of endwall flow features via active control. The localized low-momentum active forcing manipulation of the pressure side leg of the horseshoe vortex, formed at the leading edge of the turbine profile, has been shown to reduce overall pressure loss near the endwall in certain active flow control conditions. A combination of stereographic particle image velocimetry measurements at several planes throughout the passage, along with total pressure loss measurements within and beyond the passage, has led to a deeper understanding of the fluid dynamic mechanisms responsible for the reduction in endwall losses.

15. SUBJECT TERMS
Gas Turbine Engines, Turbomachinery, Fluid Dynamics, Active Flow Control,

16. SECURITY CLASSIFICATION OF:			17. LIMITATION OF ABSTRACT	18. NUMBER OF PAGES	19a. NAME OF RESPONSIBLE PERSON
a. REPORT	b. ABSTRACT	c. THIS PAGE			Dr. Mark Reeder, AFIT/ENY
U	U	U	UU	244	19b. TELEPHONE NUMBER *(Include area code)* (937) 255-6565, ext 4530 (NOT DSN) (Mark.Reeder@afit.edu)

Standard Form 298 (Rev. 8-98)
Prescribed by ANSI Std. Z39-18